

CHEMIA

3/2020

**STUDIA UNIVERSITATIS BABEȘ-BOLYAI
CHEMIA**

3/2020

EDITORIAL BOARD OF STUDIA UNIVERSITATIS BABEȘ-BOLYAI CHEMIA

ONORARY EDITOR:

IONEL HAIDUC – Member of the Romanian Academy

EDITOR-IN-CHIEF:

LUMINIȚA SILAGHI-DUMITRESCU

EXECUTIVE EDITOR:

CASTELIA CRISTEA

EDITORIAL BOARD:

PAUL ȘERBAN AGACHI, Babeș-Bolyai University, Cluj-Napoca, Romania

LIVAIN BREAU, UQAM University of Quebec, Montreal, Canada

HANS JOACHIM BREUNIG, Institute of Inorganic and Physical Chemistry,
University of Bremen, Bremen, Germany

JEAN ESCUDIE, HFA, Paul Sabatier University, Toulouse, France

ION GROSU, Babeș-Bolyai University, Cluj-Napoca, Romania

EVAMARIE HEY-HAWKINS, University of Leipzig, Leipzig, Germany

FLORIN DAN IRIMIE, Babeș-Bolyai University, Cluj-Napoca, Romania

FERENC KILAR, University of Pecs, Pecs, Hungary

BRUCE KING, University of Georgia, Athens, Georgia, USA

ANTONIO LAGUNA, Department of Inorganic Chemistry, ICMA, University
of Zaragoza, Zaragoza, Spain

JURGEN LIEBSCHER, Humboldt University, Berlin, Germany

KIERAN MOLLOY, University of Bath, Bath, UK

IONEL CĂTĂLIN POPESCU, Babeș-Bolyai University, Cluj-Napoca, Romania

CRISTIAN SILVESTRU, Babeș-Bolyai University, Cluj-Napoca, Romania

[http://chem.ubbcluj.ro/~studiachemia/;](http://chem.ubbcluj.ro/~studiachemia/)
studiachemia@chem.ubbcluj.ro
http://www.studia.ubbcluj.ro/serii/chemia/index_en.html

YEAR
MONTH
ISSUE

Volume 65 (LXV) 2020
SEPTEMBER
3

STUDIA UNIVERSITATIS BABEȘ-BOLYAI CHEMIA

3

ISSUE DOI:10.24193/subbchem.2020.3

STUDIA UBB EDITORIAL OFFICE: B.P. Hasdeu no. 51, 400371 Cluj-Napoca, Romania,
Phone + 40 264 405352

CUPRINS – CONTENT – SOMMAIRE – INHALT

Editorial: Professor Liana Maria Mureșan on His 65th Anniversary 7

LAURA AQUILANTE, MIHAELA NISTOR, STEFANIA TAORMINA,
MAREK ŠEBELA, IVO FRÉBORT, IONEL CĂTĂLIN POPESCU,
Determination of Biogenic Amines by Using Amperometric Biosensors
Based on Grass PEA Amine Oxidase and OAT Polyamine Oxidase 9

NICOLETA COTOLAN, GRAZIELLA LIANA TURDEAN, JULIETA
DANIELA CHELARU, Improving the Corrosion Resistance of Mild
Steel by Zinc-Graphene Oxide Coatings 23

MARIAN-IOSIF FRÎNCU, ENIKO COVACI, SORIN-AUREL DORNEANU,
PETRU ILEA, Selective Electroextraction of Base Metals from
Leaching Solutions Obtained During the Recycling of Waste Printed
Circuit Boards. I. Intensive Galvanostatic Electrodeposition of Copper 33

VITOR BONAMIGO MOREIRA, ALEX KRUMMENAUER, JANE ZOPPAS FERREIRA, HUGO MARCELO VEIT, ELAINE ARMELIN, ALVARO MENEGUZZI, Computational Image Analysis as an Alternative Tool for the Evaluation of Corrosion in Salt Spray Test.....	45
PÉTER MÁRTON, EMŐKE ALBERT, NORBERT NAGY, BORBÁLA TEGZE, GABRIELLA STEFÁNIA SZABÓ, ZOLTÁN HÓRVÖLGYI, Chemically Modified Chitosan Coatings: Wetting and Electrochemical Studies.....	63
LÁSZLÓ KISS, SÁNDOR KUNSÁGI-MÁTÉ, Estimation of the Usefulness of Glassy Carbon Electrode in Non-Aqueous Solvents Polarized to Higher Anodic Potentials	81
S. ANDRADA MĂICĂNEANU, HOREA BEDELEAN, Na ⁺ - NH ₄ ⁺ Cation Exchange Study on Treated Zeolitic Volcanic Tuff in Fixed Bed Column	89
ALEXANDRINA GUIDEA, AUGUSTIN C. MOȚ, COSTEL SÂRBU, Comprehensive Assessment of Antioxidant And Chelating Capacity of Some Biogenic Amines and Related Drugs.....	101
LETITIA PETRESCU, ANA-MARIA POSA, Investigation, Simulation and Comparison of Various Routes for Bioethanol Production	119
IOANA GOJA, ADELINA ULICI, MONICA CULEA, VASILE MUNTEANU, PAULA PODEA, The Influence of Geographic Location and Enzyme-Assisted Extraction on Essential Oils Composition of <i>Thymus Serpyllum</i> Growing Wild in Transylvania.....	135
ADRIAN PATRUT, ROXANA T. PATRUT, MICHAEL J. SLATER, LASZLO RAKOSY, DANIEL A. LÖWY, KARL F. VON REDEN, Radiocarbon Dating of the Historic Livingstone Tree at Chiramba, Mozambique	149
LUCIA TIMIȘ, ALEXANDRA AVRAM, MARIA GOREA, LILIANA BIZO, SANDA CÎMPEAN, RADU SEPTIMIU CÂMPIAN, Synthesis and Characterization of Nano Biotricalcium Silicate, as a Component of an Endodontic Sealer	157
COSMIN V. CRIȘAN, NICULINA D. HĂDADE, ION GROSU, ANDREEA P. CRIȘAN, ANAMARIA TEREÇ, A Straightforward Synthesis of Novel 1,3,5-Triazine-Based Macrocyclic Scaffolds.....	171
ALINA OANA RUSU (MOLDOVAN), MARIA IULIANA GRUIA, VIORICA LAZAR LORDEAN, DAN MIHU, The Correlation Between Reactive Oxygen Species and Antioxidants	181
METODI MLADENOV, SPASKA YANEVA, Determination of the Composition and Contamination with Heavy Metals of Soils from the Srebarna Lake Reserve.....	193

DANIJELA KOSTIC, BILJANA ARSIC, MILAN MITIC, SNEŽANA MITIC, MARIJA MARKOVIC, GORDANA, STOJANOVIC, Determination of Optimal Extraction Parameters of Polyphenols from <i>Forsythia Europaea</i> Degen & Bald. Bloom Using Response Surface Methodology	203
SIMONA VARVARA, ROXANA BOSTAN, MARIA POPA, LUIZA GAINA, FLORIN POPA, Doxepin as Corrosion Inhibitor for Copper in 3.5 Wt. % NaCl Solution	215
PETER RODIČ, INGRID MILOŠEV, Corrosion Resistance of Cerium-Conversion Coatings Formed from Cerium(III) Salts on Aluminium Alloy 7075-T6.....	227
LUIZA STINGESCU, CALIN CADAR, LIVIU COSMIN COTET, LUCIAN BAIA, KATA SASZET, KLARA MAGYARI, ALIN GRIG MIHIS, CARMEN IOANA FORT, MALVINA STROE, ELENA MATEI, ANDREEA NILA, ION ANGHEL, MONICA BAIA, MIHAELA BAIBARAC, VIRGINIA DANCIU, Morphological and Structural Investigation of the Poly(Vinyl Chloride) / Graphene Oxide Composites	244

Studia Universitatis Babes-Bolyai Chemia has been selected for coverage in Thomson Reuters products and custom information services. Beginning with V. 53 (1) 2008, this publication is indexed and abstracted in the following:

- Science Citation Index Expanded (also known as SciSearch®)
- Chemistry Citation Index®
- Journal Citation Reports/Science Edition

EDITORIAL

Professor Liana Maria Mureșan on His 65th Anniversary



Professor Liana Maria Mureșan was born on May 3rd, 1954. In 1977 she graduated from University “Babes-Bolyai” of Cluj-Napoca as a chemist. In 1992 she received her PhD degree in Chemistry, under the supervision of the distinguished Professor Liviu Oniciu.

In 1977 she started to work as chemist at “Intreprinderea de Cazane Mici și Arzatoare” Cluj-Napoca. Starting in 1981, as researcher at “Institutul de Energetica Chimica și Biochimica” (Cluj-Napoca branch), Liana Maria Mureșan was interested by fuel cells and metals electrodeposition / electrorefining research fields.

In 1986, she begins a successful academic career at University Babeș-Bolyai, Cluj-Napoca. As Teaching Assistant (1986), Assistant Professor (1990), Associate Professor (1997) and Professor (2002) at the Faculty of Chemistry and Chemical Engineering Cluj-Napoca, Liana Maria Mureșan was teaching “Electrochemistry” for undergraduate and graduate programs. Her research interest was constantly focused on metals electrodeposition, corrosion, and chemically modified electrodes. From 2016, Professor Liana Maria Mureșan is heading the “Center for Electrochemical Research and Nonconventional Materials” at the Department of Chemical Engineering, Faculty of Chemistry and Chemical Engineering.

In addition to over 120 scientific papers and 4 invention patents, Professor Liana Maria Mureșan co-authored 4 books, 5 book-chapters, and managed numerous grants and research projects. She counts more than 130 participations to scientific conferences with lectures, posters and oral communications. The results obtained during the research grants she coordinated, have substantially contributed to better understanding of metal nanocomposites electrodeposition and their application anticorrosive coatings.

The quality of research performed by Professor Liana Maria Mureșan (Hirsch Index 20) allowed her to develop a broad network of scientific collaborations, being invited as researcher or visiting professor at many European universities such as: University “Pierre et Marie Curie”, Paris, France (1990-1991, 1996, 1999 and 2005); University “Eotvos Lorand”, Budapest, Hungary (1993); University “Joseph Fourier”, ENSEE Grenoble, France (1996); Free University, Brussels, Belgium (1999); Cagliari University, Italy (2017); Pisa University, Italy (2018).

Professor Liana Maria Mureșan was one of the founders of the Graduate School at the Department of Physical Chemistry. At the same time, she was an active member of the academic community serving as the head of the Department of Physical Chemistry (2008-2012).

This issue of *Studia Universitas Babeș-Bolyai Chemia* is dedicated to Professor Liana Maria Mureșan in recognition of her achievements within the academic community. The intention of the editors was to bring together contributions from the circle of her coworkers, scientists that developed common scientific interests during more than 30 years.

Now, at this anniversary moment, we – the colleagues of the Electrochemistry group, as well as all the colleagues and researchers of the Faculty of Chemistry and Chemical Engineering of the Babeș-Bolyai University, express Professor Liana Maria Mureșan their appreciation for her entire activity, along with the best wishes for a long life of successful future achievements!

Prof. emerit dr. Ionel Catalin POPESCU
Prof. emerit dr. eng. Petru ILEA
Prof. habil. dr. eng. Graziella Liana TURDEAN

Cluj-Napoca, July 2020

DETERMINATION OF BIOGENIC AMINES BY USING AMPEROMETRIC BIOSENSORS BASED ON GRASS PEA AMINE OXIDASE AND OAT POLYAMINE OXIDASE

LAURA AQUILANTE^{a,b,1}, MIHAELA NISTOR^{a,2}, STEFANIA TAORMINA^{a,3},
MAREK ŠEBELA^c, IVO FRÉBORT^c, IONEL CĂTĂLIN POPESCU^{b,*}

ABSTRACT. Grass pea amine oxidase (**GPAO**) and oat polyamine oxidase (**OPAO**) were immobilized along with horseradish peroxidase (HRP) and an Os-redox polymer (**Os-RP**) onto the surface of a graphite electrode by cross-linking with poly(ethyleneglycol) diglycidyl ether. The resulted reagentless amperometric biosensors were inserted in a flow injection setup and used as electrochemical detectors for the biogenic amines (**BA**) detection. Both biosensors were operated at low applied potential (-50 mV vs. Ag/AgCl, KCl_{0.1M}) where electrochemical interferences are minimal. The quantification of ten **BA** (tyramine, putrescine, cadaverine, histamine, cystamine, phenylethylamine, agmatine, tryptamine, spermine, and spermidine) either individual or in mixture (after a preliminary separation by using cation exchange chromatography) was reported. **G/(Os-RP)-HRP-GPAO** biosensor detected all ten BA, while **G/(Os-RP)-HRP-OPAO** biosensor detected only spermine and spermidine. Finally, a simple and low-cost method for free and acetylated polyamines determination in human urine samples, by using the highly selective **G/(Os-RP)-HRP-OPAO** biosensor, was proposed.

Keywords: *Amine oxidase, polyamine oxidase, amperometric reagentless biosensors, biogenic amines, human urine*

^a Lund University, Department of Analytical Chemistry, P.O. Box 124, SE-22100 Lund, Sweden

¹Present address: British School of Geneva, Avenue de Châtelaine 95A, CH-1219 Vernier, Geneva, SWITZERLAND

²Present address: Bioprocess Control Sweden AB, Scheelevägen 22, SE-22363 Lund, SWEDEN

³Present address: London Health Coaching, 52 Dulwich road, SE24 0PA London, UNITED KINGDOM

^b Babeş-Bolyai University, Faculty of Chemistry and Chemical Engineering, 11 Arany Janos str., RO-400028, Cluj-Napoca, Romania

^c Palacký University Olomouc, Centre of the Region Haná for Biotechnological and Agricultural Research, Šlechtitelů 27, CZ-78371, Olomouc, CZECH REPUBLIC

*Corresponding author: cpopescu@chem.ubbcluj.ro

INTRODUCTION

Biogenic amines (**BA**) are organic bases present in a wide range of food products and living organisms deriving mainly from microbial decarboxylation of amino acids or from amination and transamination of aldehydes and ketones [1]. Histamine (**Hist**), putrescine (**Put**), cadaverine (**Cad**), tyramine (**Tyra**), tryptamine (**Trypt**), phenylethylamine (**PEA**) and agmatine (**Agm**) are among the most important BA in food. Polyamines like spermine (**Spm**) and spermidine (**Spd**) are found only in small quantities in food like legumes and meat, but they take part in growth and development of cells [2, 3]. However, it has been demonstrated that high amounts of **Spm** and **Spd** in blood and urine are reliable markers for cancer therapy monitoring [4].

Oxidation of **BA** can be catalyzed by different types of amine oxidases (**AOs**). **AOs** are widely spread in bacteria, fungi, higher plants and animals [5]. Copper-containing **AOs** catalyze the oxidative deamination of **BA**, generating the corresponding aldehyde, ammonia and hydrogen peroxide [6, 7]. The reaction of flavin-containing polyamine oxidases (**PAOs**) results in the production of an aminoaldehyde (alternatively, typically in plants, they may form 1,3-propanediamine, **1,3-pn**) and hydrogen peroxide, but not in ammonia [7, 8]. Plant **PAOs** show very restricted substrate specificity, oxidizing only **Spm** and **Spd** including their *N*-acetyl derivatives [4, 5].

The determination of **BA** by enzymatic analysis using **AOs** and **PAOs** was previously studied. For example, the use of **PAOs** immobilized in reactors [9, 10] or cross-linked with glutaraldehyde onto electrochemical biosensors [11] as well as electrochemical enzyme probes based on oxygen electrodes and **AOs** [12] have been reported in the literature.

AOs-based amperometric biosensors for biogenic amines detection were formerly developed, both in single [13-16] and coupled enzyme-based designs (with peroxidase) [16, 17-20]. The single **AO**-based biosensors required high applied potentials (>200 mV vs. Ag/AgCl), which can lead to high background currents and interfering signals when complex matrices are analyzed. At the same time, the bienzyme electrodes, operated at lower applied potentials (-50 or 0 mV vs. Ag/AgCl) allowed a considerably reduction of the matrix interferences. However, such devices have a major drawback because they are not able to discriminate between different **BA** due to the low selectivity of the detecting **AO** used.

Various chromatographic techniques are frequently applied for separation of biogenic amines. Among these techniques HPLC [21-23], thin layer chromatography [24] or electrophoresis [25] are the most frequently used. Thin layer chromatography is simple and inexpensive but requires extensive analysis time and the obtained results are only semi-quantitative.

Capillary electrophoresis has been a popular tool for **BA** separation, but since the **BA** could not be detected directly in a sensitive manner [25], HPLC became a better alternative.

In a previous work [26], a new analytical system based on coupling a weak cation exchange column with an **AO**-based amperometric biosensor for determination of biogenic amines, with application in food analysis, was described.

Here we report on the construction and assembling of a highly specific and sensitive amperometric biosensor for polyamines incorporating polyamine oxidase from oat seedlings (**OPAO**), denoted **G/(Os-RP)-HRP-OPAO**, and its potential application in biomedical analysis. At the same time, the extended use of a previously reported amperometric biosensor [26], based on amine oxidase from grass pea (**GPAO**) (denoted **G/(Os-RP)-HRP-GPAO**) is discussed. A comparison between the two amperometric biosensors has been performed under similar experimental conditions.

Thus, both **OPAO** and **GPAO** were cross-linked to horseradish peroxidase (**HRP**) and an Os-based redox polymer (**Os-RP**) by using the poly(ethylenglycol) diglycidyl ether and were immobilized onto the surface of solid graphite (**G**). The detection of **BA** has been carried out amperometrically, by monitoring the H_2O_2 generated by the enzymatic reaction. At first, both biosensors, operated at a low applied potential (-50 mV vs. Ag/AgCl, $KCl_{0.1\ M}$), were integrated in a single line flow injection (**FI**) setup. Further, the amperometric detection was coupled with a cation-exchange column and the method was optimized for the separation and quantification of ten BA (**Tyra**; **Put**; **Cad**; **Hist**; **cystamine**, i.e. **Cyst**; **PEA**; **Agm**; **Trypt**; **Spm** and **Spd**) from a synthetic mixture. Finally, preliminary experiments were carried out by using **G/(Os-RP)-HRP-OPAO** biosensor to estimate the content of **Spd** and **Spm** in sample of human urine.

RESULTS AND DISCUSSION

A bienzymatic approach, based on **GPAO** or **OPAO** in combination with **HRP**, was considered for biosensors development. The biosensor design involved the immobilization of both enzymes (*i.e.*, the oxidase and the peroxidase) on solid graphite, and the detection was carried out by mediated electron-transfer using an Osmium-based redox polymer (**Os-RP**). The detection principle of the resulting biosensors is schematically presented in Figure 1. Due to the presence of **Os-RP** and to the low applied potential (-50 mV vs. Ag/AgCl, $KCl_{0.1\ M}$), this approach confers simultaneously a high sensitivity and an excellent selectivity to the amperometric measurements.

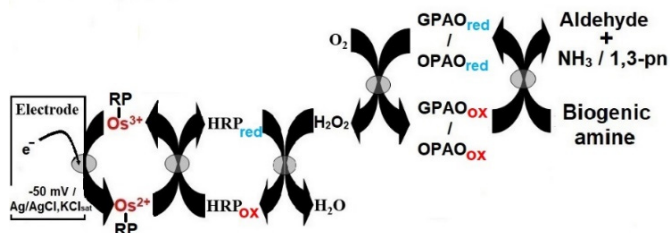


Figure 1. Detection principle of biogenic amines at **G/(Os-RP)-HRP-GPAO** and **G/(Os-RP)-HRP-OPAO** reagentless amperometric biosensors.

Individual calibration curves for ten BA (**Tyra**, **Put**, **Cad**, **Hist**, **PEA**, **Cyst**, **Agm**, **Spd**, **Trypt** and **Spm**) were recorded at both developed biosensors, **G/(Os-RP)-HRP-GPAO** and **G/(Os-RP)-HRP-OPAO**, in a single line FI setup (Figure 2).

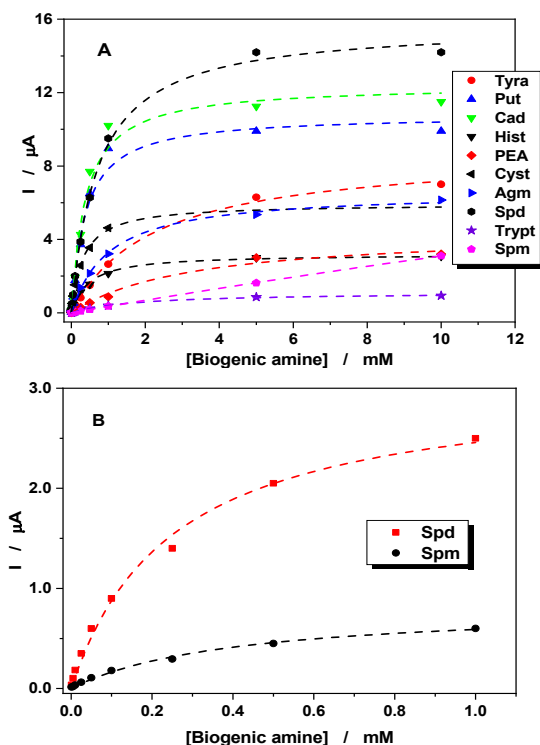


Figure 2. Calibration curves for different biogenic amines obtained at **G/(Os-RP)-HRP-GPAO (A)** and **G/(Os-RP)-HRP-OPAO (B)** biosensors, by using FI measurements.

Experimental conditions: supporting electrolyte, 0.1 M phosphate buffer (pH 7.2); applied potential, -50 mV vs. Ag/AgCl, KCl_{0.1M}; flow rate, 0.5 mL/min; injection loop, 100 μL; dispersion coefficient of the FI setup, 2.

The **G/(Os-RP)-HRP-GPAO** biosensor responded to all tested amines (Figure 2A), whereas **G/(Os-RP)-HRP-OPAO** biosensor could only detect Spm and Spd (Figure 2B), proving that **GPAO** is an enzyme with a much broader selectivity than **OPAO**.

As expected, the calibrations curves recorded for all tested amines follow a Michaelis-Menten pattern. The main kinetic (K_M , Michaelis-Menten constant; I_{max} , maximum current intensity) and analytical parameters (linear range, sensitivity -estimated as the slope of the linear domain-, and detection limit), were calculated from the calibration curves shown in figure 2 and are summarized in Table 1. It can be stated that, under the specified **FI** conditions, the sensitivities observed at the **GPAO** based biosensor decrease in the following sequence:

(Spd \approx Cad \approx Cyst) > Put > Agm > Hist > Tyra > PEA > Trypt > Spm

It is worth noticing that, for both investigated enzymes, the highest sensitivities correspond to the lowest Michaelis-Menten constants (Table 1). This fact suggests that, for the actual biosensor design, a high substrate-enzyme affinity can be considered as the main factor determining the biosensor sensitivity.

Next, **G/(Os-RP)-HRP-GPAO** and **G/(Os-RP)-HRP-OPAO** biosensors were alternatively coupled to a single line **FI** setup incorporating a cation-exchange column. A synthetic mixture containing all investigated BA was injected in the chromatographic column and the biosensor signal was recorded. In this way, by using the cation-exchange chromatography the BA mixture was firstly separated in its components and, subsequently, each resulted individual BA was detected by the biosensor used as a chromatographic electrochemical detector (Figure 3).

When the **G/(Os-RP)-HRP-GPAO** biosensor was used as chromatographic detector, the chromatogram recorded for a mixture of ten BA (**Tyra, Put, Cad, Hist, PEA, Cyst, Agm, Spd, Trypt** and **Spm**) evidences a complete separation of the initial mixture (Figure 3A). Contrarily, the **G/(Os-RP)-HRP-OPAO** biosensor was able to detect only **Spd** and **Spm** (Figure 3B). The total time spent for analysis was ~ 53 min. The sudden decrease of the baseline occurring around the 35th minute is due to an increase of the carrier concentration from 16 to 24 mM.

Table 1. Kinetic and analytical parameters for BA detection recorded at **G/(Os-RP)-HRP-GPAO** and **G/(Os-RP)-HRP-OPAO** biosensors used in FI setup. For experimental conditions see Figure 2.

BA	K_M^* (mM)	I_{max}^* (μ A)	Linear range (μ M)	Sensitivity (μA/mM) R^2 / N^{**}	DL^{***} (μ M)
G/(Os-RP)-HRP-GPAO					
Tyra	2.2 \pm 0.2	8.8 \pm 0.2	5-1000	$\frac{2.64 \pm 0.08}{0.9928 / 9}$	2.7
Put	0.38 \pm 0.06	10.8 \pm 0.4	1-500	$\frac{13.1 \pm 0.4}{0.9929 / 8}$	0.5
Cad	0.38 \pm 0.06	12.4 \pm 0.5	1-500	$\frac{15.6 \pm 0.4}{0.9958 / 8}$	0.4
Hist	0.45 \pm 0.04	3.2 \pm 0.1	1-100	$\frac{7.3 \pm 0.3}{0.9939 / 6}$	0.8
PEA	3.2 \pm 0.6	4.5 \pm 0.3	1-500	$\frac{1.06 \pm 0.03}{0.9960 / 8}$	0.5
Cyst	0.31 \pm 0.02	5.9 \pm 0.2	1-100	$\frac{15.0 \pm 0.7}{0.9906 / 6}$	0.4
Agm	1.01 \pm 0.07	6.6 \pm 0.1	1-100	$\frac{8.27 \pm 0.04}{0.9998 / 6}$	0.7
Spd	0.71 \pm 0.04	15.7 \pm 0.3	1-250	$\frac{15.5 \pm 0.8}{0.9874 / 7}$	0.4
Trypt	1.8 \pm 0.1	1.12 \pm 0.02	25-1000	$\frac{0.39 \pm 0.02}{0.9884 / 9}$	15.4
Spm	79 \pm 8.0	28 \pm 2.0	25-10000	$\frac{0.310 \pm 0.003}{0.9993 / 11}$	19.4
G/(Os-RP)-HRP-OPAO					
Spd	0.25 \pm 0.03	3.1 \pm 0.1	1-50	$\frac{11.3 \pm 0.6}{0.9916 / 5}$	0.5
Spm	0.40 \pm 0.05	0.83 \pm 0.05	5-100	$\frac{1.68 \pm 0.06}{0.9940 / 6}$	3.6

* K_M and I_{max} were estimated from the Michaelis-Menten non-linear fitting of the calibration curves (Figures 2A and 2B)

**R, correlation coefficient; N, number of experimental points

***DL was estimated for a signal/noise ratio equal to 3.

DETERMINATION OF BIOGENIC AMINES BY USING AMPEROMETRIC BIOSENSORS
BASED ON GRASS PEA AMINE OXIDASE AND OAT POLYAMINE OXIDASE

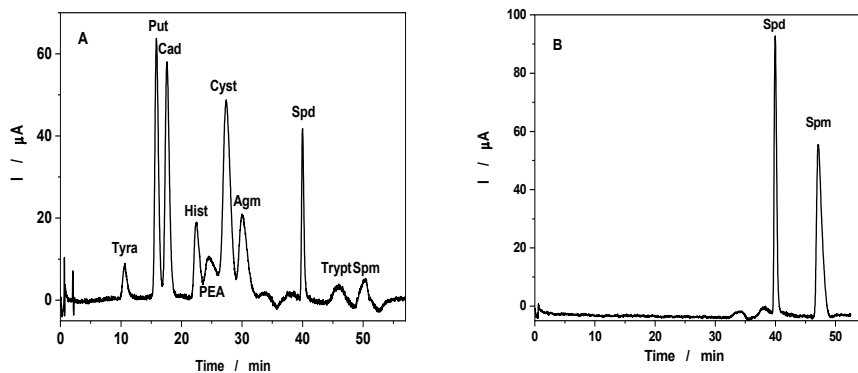


Figure 3. Chromatographic separation of a synthetic mixture of 10 biogenic amines by using **G/(Os-RP)-HRP-GPAO (A)** and **G/(Os-RP)-HRP-OPAO (B)** as amperometric detectors. Retention times: **(A): Tyra** (10.62 min), **Put** (15.83 min), **Cad** (17.58 min), **Hist** (22.45 min), **PEA** (24.51 min), **Cyst** (27.38 min), **Agm** (29.95 min), **Spd** (39.98 min), **Trypt** (46.22 min), and **Spm** (50.00 min); **(B): Spd** (39.95 min) and **Spm** (47.13 min). *Experimental conditions:* applied potential, -50 mV vs. Ag/AgCl, $\text{KCl}_{0.1\text{ M}}$; flow rate, 1.8 mL min^{-1} ; injection loop, 50 μL ; [**Put**], [**Cad**], [**Cyst**], and [**Spd**] were 100 μM ; [**Tyr**], [**Hist**] and [**Agm**] were 200 μM ; [**PEA**] was 500 μM ; [**Trypt**] and [**Spm**] were 1 mM; flow carrier, 12 mM **MSA**.

The electrochemical detection of biogenic amines, carried out after their separation by using high performance liquid chromatography, was found much more efficient than the ultraviolet detection [27, 28]. However, in these studies the separated amines were quantified by oxidation at unmodified electrodes poised at substantial positive potentials (+700 mV and +400 vs. Ag/AgCl, respectively). Aiming to show the efficiency of the developed biosensors, the amperometric responses observed for **Spd** at **G/(Os-RP)-HRP-GPAO** and **G/(OS-RP)-HRP-OPAO** were compared with those recorded at bare graphite electrodes, poised at two different applied potentials (Figure 4).

As it can clearly be seen from Figure 4, the bare graphite electrode, even poised at a relatively high positive potential (+550 mV vs. Ag/AgCl, $\text{KCl}_{0.1\text{ M}}$), is practically insensitive to the **Spd** presence. Contrarily, both biosensors are highly sensitive to **Spd**, **G/(Os-RP)-HRP-GPAO** being the most efficient. Moreover, due to the low applied potential, the **Spd** detection at both biosensors is practically without electrochemical interferences.

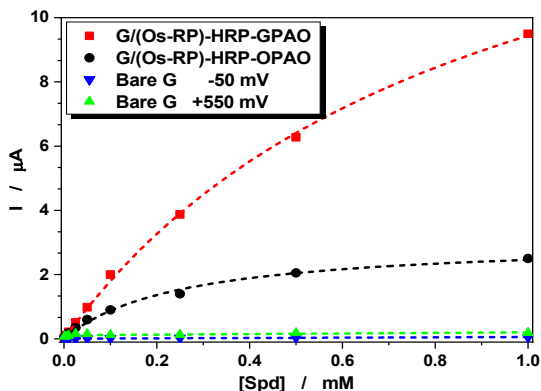


Figure 4. Spd amperometric detection at **G/(Os-RP)-HRP-GPAO**, **G/(Os-RP)-HRP-OPAO** biosensors and bare graphite electrodes (**G**) operated at two different applied potentials. *Experimental conditions:* supporting electrolyte, 0.1 M phosphate buffer containing 0.1 M KCl (pH 7.2); biosensors applied potential, -50 mV vs. Ag/AgCl, $\text{KCl}_{0.1\text{ M}}$; flow rate, 0.5 mL/min; injection loop, 100 μL ; dispersion coefficient of the FI setup, 2.

It is worth mentioning, that the response of the **G/(Os-RP)-HRP-OPAO** biosensor was examined for the acetylated **Spm** and **Spd** (**AcSpm** and **AcSpd**), since **Spm** and **Spd** are frequently found in these forms in real samples (Figure 5). The biosensor was found sensitive to both acetylated polyamines (**AcSpm**, $K_M = 136.5 \pm 33.8 \mu\text{M}$; $I_{\text{max}} = 67.2 \pm 5.9 \text{ nA}$; **AcSpd**, $K_M = 120.7 \pm 50.0 \mu\text{M}$; $I_{\text{max}} = 28.1 \pm 3.3 \text{ nA}$), but the signals were ~ 10 and ~ 100 times smaller than those corresponding to the unacetylated amines, respectively.

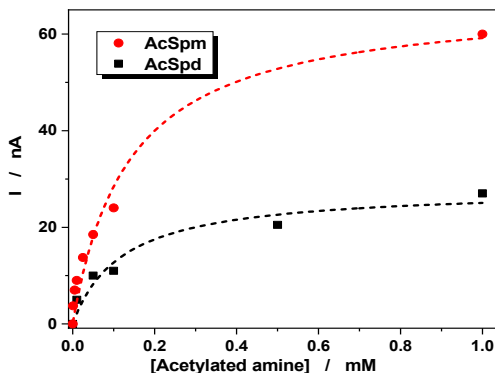


Figure 5. Calibration curves for **AcSpm** and **AcSpd** recorded at **G/(Os-RP)-HRP-OPAO** biosensor by using FI amperometric measurements. *Experimental conditions:* supporting electrolyte, 0.1 M phosphate buffer (pH 7.2); applied potential, -50 mV vs. Ag/AgCl, $\text{KCl}_{0.1\text{ M}}$; flow rate, 0.5 mL/min; injection loop, 100 μL ; dispersion coefficient of the FI setup, 2.

DETERMINATION OF BIOGENIC AMINES BY USING AMPEROMETRIC BIOSENSORS
BASED ON GRASS PEA AMINE OXIDASE AND OAT POLYAMINE OXIDASE

As a proof of concept, taking into account that the presence in human urine of high amounts of **Spm** and **Spd** and their N-acetylated forms are markers for a serious illness (e.g. cancer, osteoporosis, or hepatic cirrhosis) [9], some preliminary investigations using the **G/(Os-RP)-HRP-OPAO** biosensor were performed in order to estimate the polyamine content in real samples of human urine. Because polyamines exist in urine mainly in their conjugated form, an acid hydrolysis was carried out before the detection to ensure that all polyamines are present in their free form.

Due to the low concentrations of **Spm** and **Spd** that normally exist in the urine of healthy persons, they were not detected in fresh urine samples by using the **G/(Os-RP)-HRP-OPAO** amperometric biosensor coupled to a cation exchange column. However, the biosensor in contact with hydrolyzed samples of urine provided a signal ≈ 40 times higher than that corresponding to the non-hydrolyzed urine, indicating significant concentrations of acetylated polyamines (**AcSpm** and **AcSpd**). In order to facilitate the comparison, the estimated concentrations of **Spd** and **Spm** were expressed in mg/L urine and in mg/g creatinine, as well (Table 2). The obtained values were found similar to those reported in the literature [29], suggesting the suitability of the developed method for clinical assays.

Table 2. Spermine and spermidine concentrations in hydrolyzed human urine samples estimated by using the **G/(Os-RP)-HRP-OPAO** amperometric biosensor and **FI** measurements. For experimental conditions see Figure 5.

Biogenic amine	mM	mg/L urine	mg/g creatinine	Obs.
Spm	0.80 ± 0.06	162 ± 13	0.19 ± 0.001	Female (20 years)
Spd	1.20 ± 0.05	174 ± 7	0.20 ± 0.001	
Spm	1.00 ± 0.09	202 ± 19	0.24 ± 0.002	Male (23 years)
Spd	0.60 ± 0.05	87 ± 8	0.10 ± 0.001	

*The creatinine concentration in the urine samples was 0.12 g/dL

CONCLUSIONS

The chromatographic separation and electrochemical detection of ten BA (**Tyra**, **Put**, **Cad**, **Hist**, **PEA**, **Cyst**, **Agm**, **Spd**, **Trypt** and **Spm**) from a synthetic mixture were attempted in order to prove the full functionality of two amperometric biosensors, **G/(Os-RP)-HRP-GPAO** and **G/(Os-RP)-HRP-OPAO**, as electrochemical detectors for liquid chromatography. At the same time, the kinetic and analytical parameters of both biosensors were estimated by using the data shown in the calibration curves.

Irrespective of the BA nature, the **G/(Os-RP)-HRP-GPAO** biosensor showed a broad selectivity, a good linear response with low detection limits (from 0.4 μM for **Spd**, **Cad** and **Cyst**, to 20 μM for **Spm**) and upper limits of quantification ranging from 100 μM (**Hist**, **Cyst**, **Agm**) to 10 mM (**Spm**). Interestingly, the **G/(Os-RP)-HRP-OPAO** biosensor was found much more selective detecting only **Spm** and **Spd**.

Finally, the **G/(Os-RP)-HRP-OPAO** biosensor was used to estimate the polyamines content in human urine, after their hydrolysis with NaOH. Thus, an attempt for a simple and low-cost method for BA detection in biological fluids, suitable for clinical analysis was made.

EXPERIMENTAL SECTION

Reagents

Amine oxidase (EC 1.4.3.22) from grass pea (*Lathyrus sativus*) (**GPAO**) and polyamine oxidase (EC 1.5.3.14) from oat (*Avena sativa*) seedlings (**OPAO**) were isolated and purified according to previously published protocols [30, 31]. Horseradish peroxidase (EC 1.11.1.7) was purchased from Sigma Chem. Co. (St. Louis, MO, USA) as a lyophilized powder with an activity of 1100 U/mg solid. As described elsewhere [32], the osmium redox polymer (Os-RP) was prepared by complexing poly(1-vinyl imidazole) with $[\text{Os}(\text{4,4}'\text{-dimethylbipyridine})_2\text{Cl}]^{2+}$. Poly(ethyleneglycol) (400) diglycidyl ether (**PEGDGE**) from Polysciences (Warrington, PA, USA) was used for the cross-linking of the bienzyme mixtures, i.e. **GPAO-HRP** or **OPAO-HRP**, to **Os-RP**.

Histamine dihydrochloride (**Hist**), tyramine hydrochloride (**Tyra**), putrescine dihydrochloride (**Put**), cystamine dihydrochloride (**Cyst**), agmatine sulfate (**Agm**), spermine phosphate salt (**Spm**) and spermidine phosphate hexahydrate (**Spd**) were obtained from ICN Biochemicals Inc. (Aurora, OH, USA). Cadaverine dihydrochloride (**Cad**), N-acetylspermidine dihydrochloride (**AcSpd**) and N-acetylspermine trihydrochloride (**AcSpm**) were purchased from Sigma (St. Louis, MO, USA) whereas tryptamine hydrochloride (**Trypt**) and 2-phenylethylamine hydrochloride (**PEA**), were received from Fluka Chemie (Buchs, Switzerland). Methanesulfonic acid (>99 %) (**MSA**) was supplied by Sigma-Aldrich (Poole, UK) and hydrochloric acid (32%) by Merck (Darmstadt, Germany).

For flow injection (**FI**) measurements and chromatographic separation, standard solutions with concentrations ranging from 0.1 to 5000 μM were daily prepared by diluting the stock solutions of biogenic amines (10 mM in 0.1 M phosphate buffer) with 0.1 M phosphate buffer or aqueous solution of 12 mM **MSA**, respectively.

Disodium hydrogen phosphate dehydrate, potassium dihydrogen phosphate and sodium chloride purchased from Merck (Darmstadt, Germany) were utilized to prepare the 0.1 M phosphate buffer (pH 7.2), which was used as flow carrier in the **FI** setup or to neutralize the acidic effluent from the chromatographic column. Before usage, the buffer solution was filtered through a 0.45 μm filter type HA (Millipore, Molshem, France) and thoroughly degassed.

If not otherwise indicated, all solutions were prepared in purified water obtained from a Milli-Q system (Millipore, Bedford, MA, USA).

Equipment

A single line flow-injection (**FI**) system, consisting of a manual injection valve (Valco Instruments Co. Inc., Houston, TX, USA) with an injection loop of 100 μL , a peristaltic pump (Alitea AB, Stockholm, Sweden), a wall-jet electrochemical cell, a low current potentiostat (Zäta-Elektronik, Höör, Sweden) and a single channel chart recorder (Model BD 111, Kipp & Zonen, Delft, The Netherlands), was used to operate the amperometric biosensors. The "Peaksimple" software (SRI Instruments, Torrance, CA, USA) was employed for the data acquisition.

The tubing connecting the peristaltic pump to the flow-through electrochemical cell was made of teflon (0.5 mm i.d.). The enzyme-modified graphite electrode was the working electrode. An Ag/AgCl, $\text{KCl}_{0.1\text{M}}$ electrode and a Pt wire were used as reference electrode and counter electrode, respectively.

The chromatographic system consisted of a gradient HPLC pump (Varian, Varian Inc., USA), an injector with a loop of 50 μL , a weak acid cation exchange analytical column (IonPac CS-17, Dionex, Sunnyvale, CA, USA; 250 \times 4 mm; particle size 7 μM), and a pre-column IonPac (GC-17 Guard column, Dionex, Sunnyvale, CA, USA; 50 \times 4 mm; particle size 7 μM). The optimal gradient profile used was the following: from 0 to 30 min (8 mM **MSA**); from 32 to 34 min (16 mM **MSA**); from 36 to 44 min (24 mM **MSA**).

The biosensors, used as electrochemical detectors, were incorporated in the chromatographic system by coupling the effluent of the analytical column to the electrochemical cell, as described elsewhere [26]. In order to neutralize the acidic effluent before coming in contact with the amine oxidase based-biosensor, a post-column T-connection was used to mix the column eluate (0.9 mL min^{-1}) with a secondary flow containing phosphate buffer (0.9 mL min^{-1}).

Biosensor preparation

Prior to the modification, the rods of spectroscopic graphite (Ringsdorff-Werke GmbH, Bonn-Bad, Germany, type RW001, 3.05 mm diameter) were polished on a wet fine emery paper (Tufback, Durite P1200, Allar, Sterling Heights, MI).

In the case of **G/(Os-RP)-HRP-GPAO** electrode 5 μL of a mixture containing 2.5 mg/mL **GPAO**, 2.5 mg/mL **HRP**, 1 mg/mL **Os-RP**, and 1 mg/mL **PEGDGE** were placed on the top of a graphite electrode and left 1 day to dry at room temperature.

Similarly, in the case of **G/(Os-RP)-HRP-OPAO** electrode 5 μL of a mixture containing 2 mg/mL **OPAO**, 2 mg/mL **HRP**, 0.8 mg/mL **Os-RP**, and 0.8 mg/mL **PEGDGE** were deposited on the top of a graphite electrode and left 1 day to dry at room temperature.

Real samples preparation

The extraction of polyamines from urine was performed as previously described by Lipton et al. [33]: 1 mL of 10 M HCl was added to 1 mL of urine, pre-filtered through a 0.2 μm filter (Millipore) and then hydrolyzed with NaOH for 15 h at 110°C.

The hydrolyzed urine was evaporated to dryness on a Buchler rotary evaporator (Buchler Instruments Div., Searle Diagnostics Inc., Fort Lee, N. J.) and reconstituted in 1 mL of water. The same hydrolysis procedure was carried out for 1 mL of **AcSpm**, **AcSpd** and buffer (as control experiments).

ACKNOWLEDGEMENTS

L. A. gratefully acknowledges Romanian National Council of Research in Higher Education (CNCSIS) for financial support (research grant TD 267/2007-2008).

REFERENCES

1. M.H. Silla Santos, *Int. J. Food Microbiol.*, **1996**, 29, 213-231.
2. S. Bardocz, *Trends Food Sci. Technol.*, **1995**, 6, 341-346.
3. P. Kalac, P. Krausova, *Food Chem.*, **2005**, 90, 219-230.
4. L. Scarciglia, D. Compagnone, G. Federici, G. Palleschi, *Analisis*, **1998**, 26, 219-223.
5. M. Šebela, A. Radova, R. Angelini, P. Tavladoraki, I. Frébort, P. Pec, *Plant Sci.*, **2001**, 160, 197-207.
6. M.A. Medina, J.L. Urdiales, C. Rodríguez-Caso, F.J. Ramírez, F. Sánchez-Jiménez, *Crit. Rev. Biochem. Molec. Biol.*, **2003**, 38, 23-59.
7. A. Toninello, P. Pietrangeli, U. De Marchi, M. Salvi, B. Mondovi, *Biochim. Biophys. Acta*, **2006**, 1765, 1-13.

DETERMINATION OF BIOGENIC AMINES BY USING AMPEROMETRIC BIOSENSORS
BASED ON GRASS PEA AMINE OXIDASE AND OAT POLYAMINE OXIDASE

8. D.L. Morgan, *Biochem. Soc. Trans.*, **1985**, *13*, 322-326.
9. K. Hiramatsu, S. Kamei, M. Sugimoto, K. Kinoshita, K. Iwasaki, M. Kawakita, *J. Biochem.*, **1994**, *115*, 584-589.
10. N. Watanabe, *Biomed. Chromatogr.*, **1992**, *6*, 1-3.
11. M. Esti, G. Volpe, L. Massignan, D. Compagnone, E. La Notte, G. Palleschi, *J. Agric. Food Chem.*, **1998**, *46*, 4233-4237.
12. I. Karube, I. Satoh, Y. Araki, S. Suzuki, H. Yamada, *Enz. Microb. Technol.*, **1980**, *2*, 117-120.
13. R. Draisci, G. Volpe, L. Lucentini, A. Cecilia, R. Federico, G. Palleschi, *Food Chem.*, **1998**, *62*, 225-232.
14. R. Gasparini, M. Scarpa, M.L. Di Paolo, R. Stevanato, A. Rigo, *Bioelectrochem. Bioenerg.*, **1991**, *25*, 307-315.
15. M. Niculescu, T. Ruzgas, C. Nistor, I. Frébort, M. Šebela, P. Pec, E. Csoregi, *Anal. Chem.*, **2000**, *72*, 5988-5993.
16. S. Tombelli, M. Mascini, *Anal. Chim. Acta*, **1998**, *358*, 277-284.
17. R. Gasparini, M. Scarpa, F. Vianello, B. Mondovi, A. Rigo, *Anal. Chim. Acta*, **1994**, *294*, 299-304.
18. M. Niculescu, C. Nistor, I. Frébort, P. Pec, B. Mattiasson, E. Csoregi, *Anal. Chem.*, **2000**, *72*, 1591-1597.
19. M. Wimmerova, L. Macholan, *Biosens. Bioelectron.*, **1999**, *14*, 695-702.
20. T.J. Castilho, M.d.P.T. Sotomayor, L.T. Kubota, *J. Pharm. Biomed. Anal.*, **2005**, *37*, 785-791.
21. A. Onal, *Food Chem.*, **2007**, *103*, 1475-1486.
22. M.Y. Khuhawar, G.A. Qureshi, *J. Chromatogr. B*, **2001**, *764*, 385-407.
23. G. Taibi, M.R. Schiavo, M.C. Gueli, P. Calanni Rindina, R. Muratore, C.M.A. Nicotra, *J. Chromatogr. B*, **2000**, *745*, 431-437.
24. K.A. Khan, *Chromatogr.*, **2006**, *64*, 423-427.
25. S. Oguri, *J. Chromatogr. B*, **2000**, *747*, 1-19.
26. L. Muresan, R. Ronda Valera, I. Frébort, I.C. Popescu, E. Csoregi, M. Nistor, *Mikrochim. Acta*, **2008**, *163*, 219-225.
27. D. Bose, A. Durgbanshi, M.E. Capella-Peiro, M. Gil-Agusti, J. Esteve-Romero, S. Carda-Broch, *J. Pharm. Biomed. Analysis*, **2004**, *36*, 357-363.
28. C.A. Heidbreder, L. Lacroix, A.R. Atkins, A.J. Organ, S. Murray, A. West, A.J. Shah, *J. Neurosci. Methods*, **2001**, *112*, 135-144.
29. H. Inoue, K. Fukunaga, S. Munemura, Y. Tsuruta, *Anal. Biochem.*, **2005**, *339*, 191-197.
30. M. Šebela, L. Luhova, I. Frébort, H.G. Faulhammer, S. Hirota, L. Zajoncova, V. Stuzka, P. Pec, *Phytochem. Anal.*, **1998**, *9*, 211-222.
31. J. Stranska, M. Šebela, P. Tarkowski, P. Rehulka, J. Chmelik, I. Popa, P. Pec, *Biochim.*, **2007**, *89*, 135-144.
32. T.J. Ohara, R. Rajagopalan, A. Heller, *Anal. Chem.*, **1994**, *66*, 2451-2457.
33. A. Lipton, L.M. Sheehan, G.F. Kessler, *Cancer*, **1975**, *35*, 464-468.

IMPROVING THE CORROSION RESISTANCE OF MILD STEEL BY ZINC-GRAPHENE OXIDE COATINGS

NICOLETA COTOLAN^a, GRAZIELLA LIANA TURDEAN^a,
JULIETA DANIELA CHELARU^{a,*}

ABSTRACT. The main purpose of this work is to improve the corrosion resistance of steel substrates using the characterization of new composite zinc electrodeposits containing graphene oxides and reduced graphene oxide. The zinc-graphene based composite deposits were obtained by electrodeposition of an acidic electrolyte (pH = 5) at a current density of 20 mA/cm². Anionic surfactant (*i.e.*, sodium dodecyl sulfate) was used to obtain uniform and compact coating morphology. Also, the investigated deposits had in their structure the graphene oxides produced by graphite exfoliation and the results concerning corrosion behavior of the zinc electrodeposits (Zn/S235 and Zn-graphene/S235) were compared using the same experimental conditions. Microstructural characterization was carried out by SEM-EDS, whereas corrosion resistance was evaluated by EIS and polarization curves.

Keywords: *Graphene Oxide, Electrochemical Impedance Spectroscopy, Polarization Curves, Corrosion Resistance, Steel Corrosion*

INTRODUCTION

Steel is one of the most widely used materials in the industry and it is a subject of corrosion in industrial environments. The corrosion of steel has a great impact on economics thus, it is imperative to protect it. Coatings are one of the most cost-effective and practical strategies to protect a steel surface against attack from an aggressive species. Zinc is widely used as a sacrificial coating by providing a barrier in the traditional steel anticorrosion field and has an important role in protecting steel substrates. However, its lifespan is limited in aggressive environments, especially in humid conditions [1]. There

^a Babeş-Bolyai University, Faculty of Chemistry and Chemical Engineering, 11, Arany Janos St., RO-400028, Cluj-Napoca, Romania,

* Corresponding author: jdchelaru@chem.ubbcluj.ro

are several ways to improve the corrosion resistance of zinc-coated steel, varying from chromating the zinc surface to its coating with organic molecules and the incorporation of useful nanoparticles in the zinc coating [2].

Recently, research works have revealed that electrochemical methods are also powerful tools to prepare graphene materials through electrochemical exfoliation of graphite both in ionic liquids or aqueous solutions for ultra-capacitors [3]. From several past years' graphene has been at forefront of research because of its spectacular physics properties [4] and application potential arising from its unusual mechanical, thermal, optical, chemical, and electrical properties. Application of graphene for corrosion protection has been explored by various research groups due to its impermeability to ions and molecules [5].

Graphene oxide (GO) is one of the most commonly used materials for graphene-based applications. In the last decade, several synthesis routes have been proposed to prepare GO, such as: mechanical exfoliation [6], chemical vapor deposition [7], and thermal decomposition [8]. The most attractive property of GO is that it can be (partially) reduced to graphene-like sheets by removing the oxygen containing groups with the recovery of a conjugated structure [9].

Graphene (G), graphene oxide (GO) and reduced graphene oxide (rGO), has shown its potential use in anti-corrosion coating for metal substrates. Kirkland *et al.* [10] employed graphene as a corrosion protection barrier for nickel and copper. Singh *et al.* [11] reported the fabrication of a robust graphene-reinforced composite coating with excellent corrosion resistance by aqueous cathodic electrophoretic deposition. Ramezanzadeh *et al.* [12] developed a sol-gel based silane film filled with functionalized GO nanosheets to enhance the epoxy coating resistance against corrosion and cathodic delamination over the steel substrate [13].

In this context, the aim of the study was the preparation of zinc-graphene-based composite deposits and their characterization. The anticorrosion protective ability of the composite deposits in case of mild steel tested in an acidic solution was investigated by electrochemical methods (polarization measurements and electrochemical impedance spectroscopy).

RESULTS AND DISCUSSION

Microstructural characterization

The influence of graphene oxide on the composition and structure of zinc-graphene deposits were investigated by Scanning Electron Microscopy in conjunction with Energy Dispersive Spectroscopy (SEM-EDS) methods. Figure 1 shows the SEM images of Steel substrate (S235), Zn/S235,

Zn-rGO/S235 and Zn-GO/S235 deposits and Figure 2 shows EDS images for Zn-rGO/S235 and Zn-GO/S235 deposits. The images show a visual idea in which the formation of a protective film on the steel surface occurs to reduce the corrosion rate. It can be observed in the presented morpho-structural results that the surface morphology is different in all cases and a possible explanation could be the rearrangement of the zinc deposit microstructure in the presence of graphene materials.

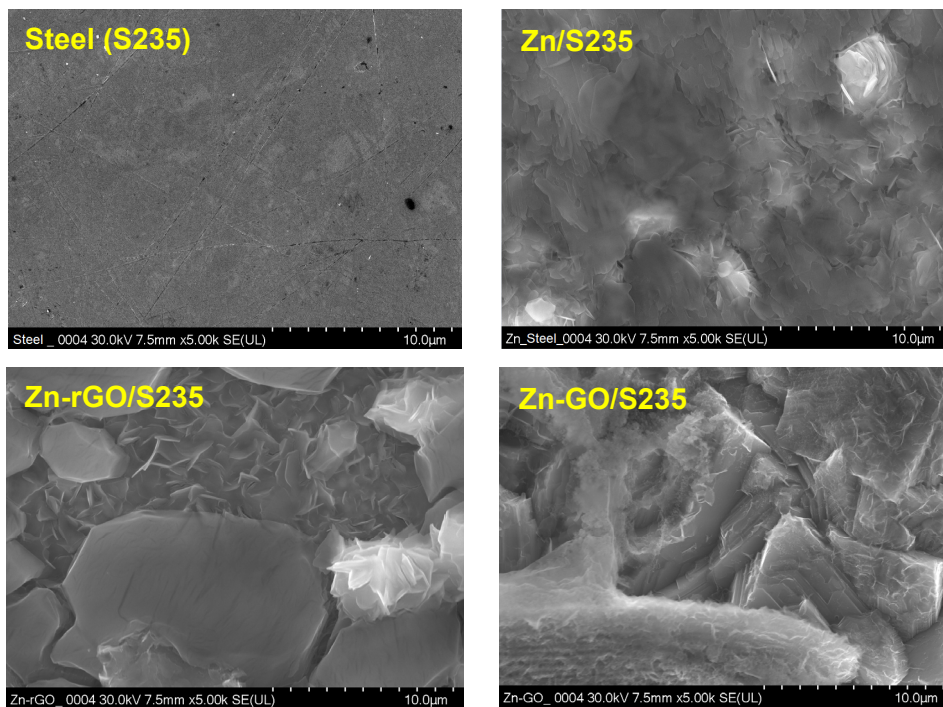


Figure 1. SEM micrographs of S235, Zn/S235, Zn-rGO/S235 and Zn-GO/S235.

Also, from the SEM micrographs can be observed a successful codeposition of GO in Zn matrix. The coatings: Zn-rGO/S235 and Zn-GO/S235 present inclusive and uniform deposits than Steel and Zn/S235 samples.

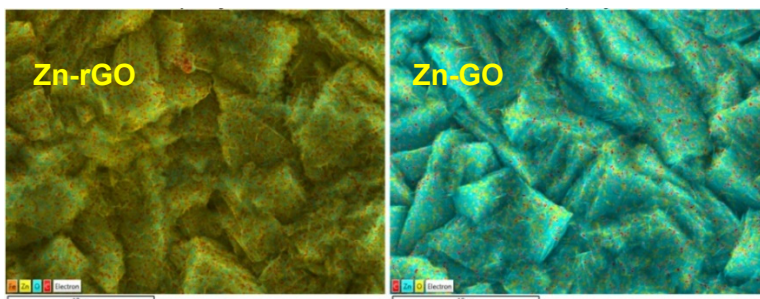


Figure 2. EDS quantitative X-ray microanalysis for Zn-rGO/S235 and Zn-GO/S235 deposits.

The elemental composition was determined by EDS investigation on the surface coating of the steel samples deposits. Analyzing the images from Figure 2 it can be observed a uniform distribution of the elements which makes up the deposit on the surface of the steel samples. As it can be seen from Table 1, the EDS analysis indicated in both cases that Zn has a large proportion but were also present O, C and Fe. The presence of the Fe in the substrate can be easily attributed to steel samples, while the presence of the O and C may be due to the process of coatings preparation. Since rGO was synthesized *via* the reduction of GO, the presence of oxygen was still noticeable, possibly due to the remaining oxygen functional groups in the air-dried Zn-rGO. It can be noticed a high percentage of Fe and O in the Zn-rGO deposit compare with the Zn-GO substrate. The occurrence of these elements may involve the formation of Fe oxides in the substrates. Based on the identification of the elements in the composite coatings (Zn-rGO and Zn-GO) deposited on the steel surface, rather it is expected a good corrosion protection if use Zn-GO.

Table 1. The weight percentage of the detected elements by the EDS on the samples surface region of the Zn-rGO and Zn-GO composite coatings (wt %)

Sample	Zn	O	C	Fe
Zn-rGO	57.29	22.78	2.50	17.43
Zn-GO	79.82	7.68	12.35	0.15

Corrosion tests of the coatings

Open circuit potential

The corrosion resistance of coatings was characterized by electro-chemical impedance spectroscopy and Tafel plots. In order to determine the corrosion behavior of mild steel (S235), in acidic media 3 wt.% NaCl, in the presence of Zn

and Zn/graphene based coatings, the experiments were started by recording the open circuit potential (OCP). The OCP was measured vs. Ag/AgCl/KCl_{sat} and become relatively constant after 1h. The OCP values were situated around -500 mV for steel samples and around -1 V for zinc deposited ones.

Electrochemical impedance spectroscopy

The EIS plots were recorded, immediately after open circuit potential (OCP), in order to investigate the corrosion protection efficiency of Zn, Zn-rGO, Zn-GO and Zn-2GO coatings. The results are presented in Figures 3 and 4. From the Nyquist plots, it can be observed that the impedance spectra are characterized by two time constants (or two capacitive loops). The impedance spectra were analyzed for all cases by fitting the experimental data with a $R_e(Q_{coat}(R_{coat}(Q_{dl}(R_{ct}))))$ equivalent electrical circuit (Figure 5). The equivalent electrical circuit from Figure 5 consists of:

- the $R_{ct} - Q_{dl}$ elements, exhibiting a loop at high frequencies, represents the charge transfer resistance R_{ct} and the constant phase element corresponding to the double layer capacity, Q_{dl} , at the coated steel | electrolyte interface.
- the $R_{coat} - Q_{coat}$ elements, exhibiting a loop at low frequencies, where R_{coat} represents the resistance of the corrosion products accumulated at the interface and Q_{coat} , the constant phase element corresponding to the capacity due to an oxidation-reduction process occurring into the coating layer
- R_e represents the electrolyte resistance between the reference electrode and the work electrodes surface,
- coefficients n_{dl} and n_{coat} represent the depressed feature of the capacitive loop in Nyquist diagram ($0 < n \leq 1$).

In order to understand the electrochemical process occurring at the work electrodes surface, the parameters for all samples were obtained by using the proposed equivalent electrical circuit. The quality of fitting procedure was evaluated by the chi squared (χ^2) values, which were of order 10^{-4} . The results are shown in Table 2.

Table 2. The electrochemical impedance parameters estimated by fitting the experimental impedance data from Figure 2.

Sample	R_e $k\Omega \cdot cm^2$	R_{coat}^a $k\Omega \cdot cm^2$	Q_{coat}		R_{ct}^a $k\Omega \cdot cm^2$	Q_{dl}		R_p $k\Omega \cdot cm^2$
			$Y_{0,coat}^b$ $\mu\Omega^{-1} \cdot cm^{-2} s^n$	n_{coat}^c		$Y_{0,dl}^b$ $m\Omega^{-1} \cdot cm^{-2} s^n$	n_{dl}^c	
Zn	0.012	0.072	128.20	0.62	0.174	9.16	0.81	0.250
Zn-rGO	0.011	0.176	49.41	0.69	0.239	9.14	0.64	0.398
Zn-GO	0.013	0.194	40.12	0.80	0.284	12.54	0.76	0.478
Zn-2GO	0.012	0.296	95.75	0.54	0.335	9.80	0.81	0.631

^aThe standard error for R_{coat} , R_{ct} values was between 1.05% - 5.18%;

^bThe standard error for Q_{coat} , Q_{dl} values was between 3.10%-4.31%;

^cThe standard error for n values was between 0.81% - 3.51%.

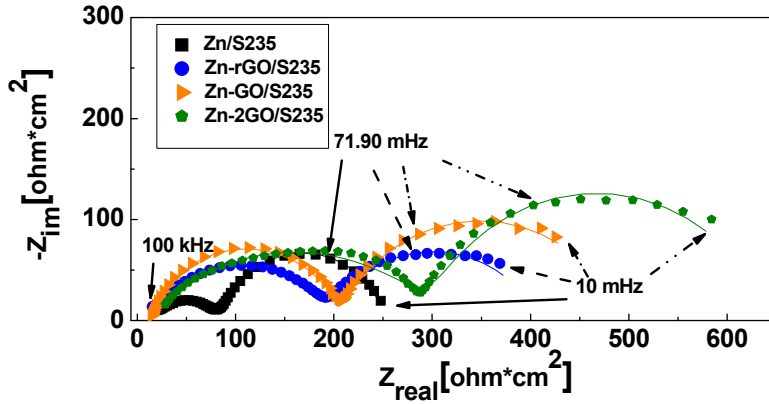


Figure 3. Nyquist impedance diagrams for the S235 electrodes coated with Zn, Zn-rGO, Zn-GO and Zn-2GO, immersed in 3 wt.% NaCl; the lines represent fitted data.

Based on the data from Table 2, it can be observed that the highest polarization resistance (obtained by the sum: $R_p = R_{ct} + R_{coat}$ [14]), which is an indicator of corrosion resistance, was obtained in the case of S235 coated with the Zn-2GO. Thus, increasing the quantity of GO in Zn coating favors the corrosion resistance of the S235. It can be presumed that the degree of inhibition depends on the amount of incorporated graphene, which also depends on the GO type.

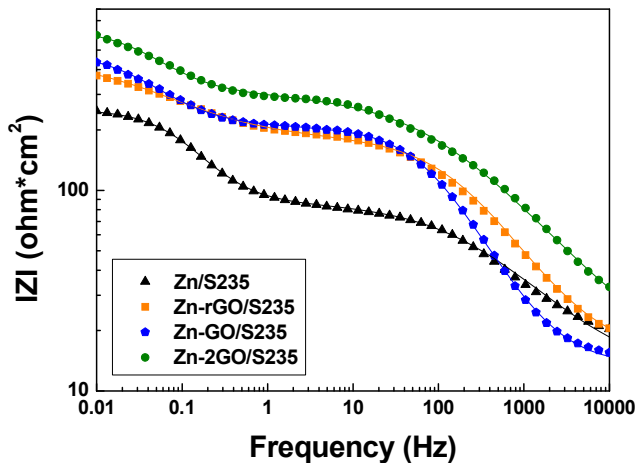


Figure 4. Bode plots for the steel electrodes coated with Zn, Zn-rGO, Zn-GO or Zn-2GO immersed in 3 wt.% NaCl; the lines represent fitted data.

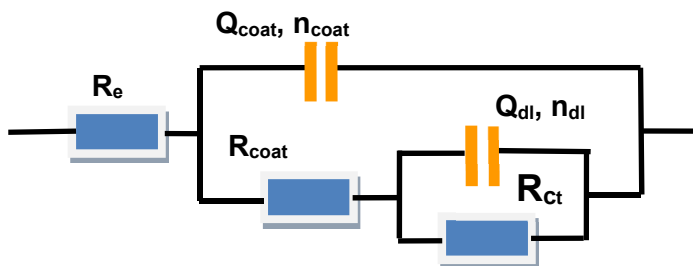


Figure 5. The equivalent electrical circuit used for fitting of the experimental results.

An increase of the absolute impedance at low frequencies region (10^2 mHz) in Bode plots (Figure 4) can be observed, in case of using oxide graphene coatings, suggested an improvement of the corrosion resistance.

Polarization measurements

In order to determine the corrosion current density (i_{corr}) and the corrosion potential (E_{corr}) were recorded the potentiodynamic polarization curves in the potential range of ± 200 mV vs. OCP (Figure 6). For all the coatings, the results obtained by Tafel interpretation of the polarization curves are presented in Table 3. Based on these results it can be seen that the value of i_{corr} decreased in all cases when used graphene oxide coatings, compared with Zn coated sample. This behavior can be due to the inclusion of the graphene oxide materials in the metallic deposit.

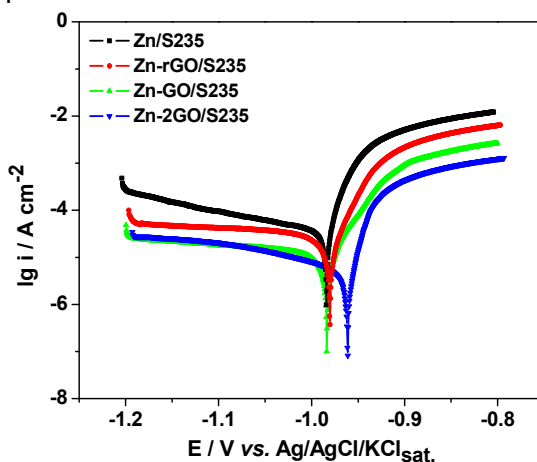


Figure 6. Tafel polarization curves recorded for steel coated with different type of Zn and Zn-GO-based protective deposits (see inset). Experimental conditions: current density, 20 mA/cm^2 ; deposition time, 20 minutes.

Table 3. The corrosion parameters, estimated by extrapolation of the Tafel curves of each sample

Sample	Zn	Zn-rGO	Zn-GO	Zn-2GO
Concentration of rGO/GO (mg/L)	-	50	50	100
E_{corr} (mV vs. Ag/AgCl/KCl sat)	- 996	- 983	- 986	- 963
I_{corr} (μ A)	64.71	26.91	11.74	6.35
Corrosion Rate (mm/year)	0.0751	0.03122	0.01362	0.00736

An important parameter for measuring the corrosion resistance is the corrosion rate. Based on Faraday's law, the corrosion rate (CR) can be calculated by the following equation [15]:

$$CR = \frac{K \cdot I_{corr} \cdot EW}{\rho \cdot A}$$

Where $K = 3272$ (mm / A·cm·year) is the corrosion rate constant

I_{corr} is corrosion current (A)

$EW = 27.9225$ g is equivalent weight of Fe

$\rho = 7.874$ g / cm³ is the density of Fe

$A = 0.5$ cm² is sample surface area.

The corrosion rate values are summarized in table 3. It can observe that the GO exhibited better corrosion protection property than Zn and Zn-rGO. In the case of using coating containing GO the protective effect increases after doubling its concentration. Thus, for 2GO, the value of CR decreases almost half compared with the value of CR in the case of GO. This behavior is in agreement with the results obtained from the EIS measurements.

CONCLUSIONS

In this paper, the corrosion resistance of two types of Zn/graphene based coatings on steel was examined. According to the electrochemical investigations, both coatings (Zn-rGO and Zn-GO) led to increasing the corrosion resistance of S235 steel compare with Zn coating. But a significant increase of the polarization resistance and decrease in the corrosion rate was observed for Zn-GO composite coating. Thus, the amount of GO material was raised and the obtained results have shown that the concentration gradient of GO material in zinc sulphate electrolyte has an important effect on the corrosion resistance. The corrosion rate for the Zn-GO composite coating has decreased by an order of magnitude, by doubling the amount of GO in coatings.

EXPERIMENTAL SECTION

Materials and solutions

The electrochemical cell contained three electrodes: working electrode (WE), reference electrode (RE), and counter electrode (CE). A steel (S235) disk electrode was the WE, $S = 0.5 \text{ cm}^2$. The Ag/AgCl/KCl_{sat} was used as RE and a Pt foil as CE. The S235 steel sample had the following composition: 0.22% C, 0.85% Mn, 0.055% P, 0.055% S and Fe balance. The surface of the S235 electrodes was examined by optical microscopy the results were reported previously [16]. WEs were cut from a steel bar and introduced in a Teflon cylinder; a copper rod was attached for ensuring electrical contact. Before using, the working electrode was wet polished on emery paper of different granulation (up to 2000 grade) and finally on felt with a suspension of alumina. After that, the electrode was ultrasonicated for 2 minutes, degreased with ethanol, and washed with distilled water in order to remove all the impurities from the surface and then dried at room temperature.

The acidic solution for corrosion measurements was the electrolyte with the following composition: 320 g/L ZnSO₄, 10 g/L NaCl, 30 g/L Na₂SO₄ and 0.05 g/L CH₃(CH₂)₁₁SO₄Na or sodium dodecyl sulfate (SDS) with pH = 5. All the reagents were obtained from Merck, Germany. All the coatings including pure Zn were electrodeposited using the same SDS concentration in order that corrosion behavior of the coatings can be studied as a function of GO content alone.

Two types of graphene materials were used for the zinc composites electrodeposition process: (i) water-ethanol graphene oxide GO suspension obtained by the method of protected sono-oxidative exfoliation of graphite (GO); (ii) commercial reduced graphene oxide (rGO), purchased from Graphenea, Spain. The preparation and characterization of GO material were described in detail by A. Pérez del Pino *et al.* [17].

Morpho-structural investigations

The Scanning Electron Microscopy (SEM) was performed using an Ultra High Resolution (UHR) SEM Hitachi 8230 system operated in high vacuum conditions. The instrument capabilities allow particular scanning options in order to show the distribution of components in relation to their chemical composition and topography of the studied surface. High resolution SEM images acquired at low landing voltage can be assessed without the destruction of the samples. The SEM accelerating voltage was 15kV in a vacuum of 10⁻⁵ mbar and secondary electrons images combined with Energy Dispersion Spectroscopy (EDS) analysis were used to investigate the morphological properties.

Electrochemical methods

The electrodeposition samples were obtained on a PC – controlled electrochemical analyzer PAR 2273 (Princeton Applied Research, USA).

The corrosion measurements were performed with a computer-controlled potentiostat AUTOLAB, PGSTAT302 N (Eco Chemie BV, Utrecht, Netherlands) and GPES/FRA program was used for data analysis. The open circuit potential for steel immersed in the corrosive solution was monitored for 1 hour. Electrochemical impedance spectroscopy (EIS) measurements were carried out at OCP, in the frequency range of 100 kHz-10 mHz at 10 points per decade with an AC voltage amplitude of ± 10 mV. Electrochemical impedance data were fitted using ZSimpWin 3.21 software. Immediately after the EIS measurement were recorded the polarization curves by scanning in a potential range of ± 200 mV vs. open circuit potential (for Tafel interpretation) with a scan rate of 0.166 mV/s. The testing temperature was $21 \text{ }^\circ\text{C} \pm 2 \text{ }^\circ\text{C}$.

ACKNOWLEDGMENTS

The authors would like to thank dr. Cosmin Cotet for the supply of graphene oxide material and dr. Lucian Barbu-Tudoran for SEM-EDS analysis.

REFERENCES

1. R. Jain; R. Pitchumani; *Surf. Coat. Tech.*, **2018**, *337*, 223-231.
2. C.T.J. Low; R.G.A. Wills; F.C. Walsh; *Surf. Coat. Tech.* **2006**, *201*, 371-383.
3. A. Ambrosi; M. Pumera; *Chem-Eur. J.*, **2016**, *22*, 153-159.
4. S. K. Choudhary; A. K. Gupta; *Solid State Commun.*, **2011**, *151*, 396-399.
5. M. Schriver; W. Regan; W.J. Gannett; A.M. Zaniwski; M.F. Crommie; A. Zettl; *ACS Nano*, **2013**, *7*, 5763-5768.
6. M. Yi; Z. Shen; *J. Mater Chem. A.*, **2015**, *3*, 11700-11715.
7. G. Allaedinia; E. Mahmoudia; P. Aminayib; S. Masrinda Tasirina; A. Wahab Mohammad; *Synth. Met.*, **2016**, *220*, 72-77.
8. X. Chen; D. Meng; B. Wang; B.W. Li; W. Li; C.W. Bielawski; R.S. Ruoff; *Carbon*, **2016**, *101*, 71-76.
9. A.B. López-Oyama; M.A. Domínguez-Crespo; A.M. Torres-Huerta; E. Onofre-Bustamante; R. Gámez-Corrales; N. Cayetano-Castro; *Diam. Relat. Mater.*, **2018**, *88*, 167-188.
10. N.T. Kirkland; T. Schiller; N. Medhekar; N. Birbilis; *Corros. Sci.*, **2012**, *56*, 1-4.
11. B.P. Singh; S. Nayak; K.K. Nanda; B.K. Jena; S. Bhattacharjee; L. Besra; *Carbon*, **2013**, *61*, 47-56.
12. B. Ramezanzadeh; A. Ahmadi; M. Mahdavian; *Corros. Sci.*, **2016**, *109*, 182-205.
13. J. Zhao; X. Xie; C. Zhang; *Corros. Sci.*, **2017**, *114*, 146-155.
14. X. Shen; J. Sheng; Q. Zhang; Q. Xu; D. Cheng; *J. Mater. Eng. Perform.*, **2018**, *27*, 3750-3761.
15. S. Ryu; Y.J. Kwon; Y. Kim; J. Uk Lee; *Mater. Chem. Phys.*, **2020**, *250*, 123039-123047.
16. J.D. Chelaru; D. Aylakov, L.M. Mureşan, *Studia UBB Chem.*, **2017**, *4*, 357-368.
17. A. Pérez del Pino; E. György; C. Cotet; L. Baia; C. Logofatu; *RSC Advances*, **2016**, *6*, 50034-50042.

SELECTIVE ELECTROEXTRACTION OF BASE METALS FROM LEACHING SOLUTIONS OBTAINED DURING THE RECYCLING OF WASTE PRINTED CIRCUIT BOARDS. I. INTENSIVE GALVANOSTATIC ELECTRODEPOSITION OF COPPER

MARIAN-IOSIF FRÎNCU^a, ENIKO COVACI^a,
SORIN-AUREL DORNEANU^{a,b,*}, PETRU ILEA^{a,b}

ABSTRACT. This article presents our results concerning the feasibility of selective electroextraction of copper from leaching solutions obtained during base metals recycling from waste printed circuit boards. The researches were focused on the intensive copper electrodeposition as a potential parallel paired process for the electrochemical regeneration of the leaching solutions. Preliminary tests, performed by cyclic voltammetry on 316 stainless steel disc electrode in synthetic solutions of CuBr_2 , SnBr_2 and PbBr_2 , indicate the possibility of selective electroextraction of Cu if the electrodeposition potentials of Sn and Pb are not exceeded. Therefore, selective and intensive Cu electrodeposition tests were accomplished in galvanostatic mode, in a real sample of leaching solution, using also 316 stainless steel sheets cathodes. The experimental results demonstrate that the selective electrodeposition of Cu is possible in a wide range of current densities, between 200 and 600 A/m^2 , if the concentration of Cu in solution of at least 12 g/L is maintained. Under these conditions, the purity of the obtained Cu deposits can attain 99.6%.

Keywords: *waste printed circuit boards, selective electroextraction, copper recovery, electrochemical parallel paired processes*

INTRODUCTION

As a result of the rapid growth of the world economy and improvement of living standards, the production rate of waste electrical and electronic equipment (WEEE) strongly increases [1], becoming two to three times higher

^a Babeş-Bolyai University, Faculty of Chemistry and Chemical Engineering, Department of Chemical Engineering, 11 Arany Janos Street, Cluj-Napoca, RO-400028, Romania

^b Babeş-Bolyai University, Interdisciplinary Research Institute on Bio Nano Sciences, 42 Treboniu Laurian Street, Cluj-Napoca, RO-400271, Romania

* Corresponding author: dorneanu@chem.ubbcluj.ro

than for other urban wastes [2]. In the past two decades, WEEE has become a worldwide major pollution problem [3] with estimated quantities of about 50 million tons in 2020 [4] and over 52.2 million tons in 2021 [5]. The global shift towards sustainable resource management and the continuous depletion of high-quality virgin ore resources increase the need to develop strategies for the cyclical use of metals found in WEEE, as well as for the safe disposal of residues after recovery of the desired materials [6,7]. The recycling of WEEE also represents a strategy to avoid environmental pollution, although landfilling is still a notorious way of disposing this solid waste in emerging countries [8]. The WEEE recycling process also offers a valuable source of raw materials for the electronics industry [9].

The printed circuit boards (PCBs) are the most used items in almost all electronic devices [10] and/or represent their core component [11]. Usually, PCBs contain thin layers of precious metals over the metal contacts [12], significant amounts of Cu [13], but also traces of highly toxic ones, like Pb and Cd [14].

Currently, various technologies have been developed for the metals recycling from waste printed circuit boards (WPCBs), such as physical-mechanical, pyrometallurgical, hydrometallurgical, bioleaching methods or combinations of these approaches [15]. The hydrometallurgical methods present many advantages over the pyrometallurgical ones, including lower energy consumption, reduced capital costs and low toxic gas emissions [16]. However, conventionally, hydrometallurgical processes consume large amounts of chemicals and generate large volumes of waste waters [17]. As an alternative to the traditional PCBs recycling methods mentioned before, the electrochemical recovery of metals from WPCBs gains more and more attention, due to the high environmental compatibility [18], high energy and economic efficiency [19], minimal involvement of auxiliary materials [20] and better recovery of valuable materials [21].

Starting from the very promising results of our previous researches [21-23], the present work aimed to check the feasibility of the copper selective electroextraction from the extremely complex solutions obtained during the recovery of base metals from WPCBs using the KBr/HBr/Br₂ leaching system. The studies were focused on the possibility to use the intensive (high rate) copper electrodeposition as a potential parallel paired process for the electrochemical regeneration of the leaching solutions which will be performed, obviously, in a divided reactor [21], simultaneously with the obtention of pure and easy valorisable Cu deposits. Before the galvanostatic experiments concerning the intensive Cu electrodeposition from the real leaching solution, preliminary tests were accomplished by cyclic voltammetry (CV) on a 316 stainless steel (SS) disc electrode in synthetic mono-component solutions of CuBr₂, SnBr₂

and PbBr_2 . CV results indicate that Cu can be electroextracted selectively if the electrodeposition potentials of Sn and Pb are not exceeded. Finally, the Cu deposits obtained by galvanostatic electrolysis were cleaned, dried, detached from the 316 SS sheet cathodes, mineralized with *aqua-regia*, and analysed by ICP-OES. The obtained results demonstrate that valuable and high purity Cu deposits (up to 99.6%) can be obtained using current densities between 200 and 600 A/m^2 and maintaining the Cu concentration in solution higher than 12 g/L.

RESULTS AND DISCUSSION

The results of the preliminary tests performed by CV on the 316 SS disc electrode of 3 mm diameter, in synthetic mono-component solutions of CuBr_2 , SnBr_2 and PbBr_2 , are presented in Figure 1.

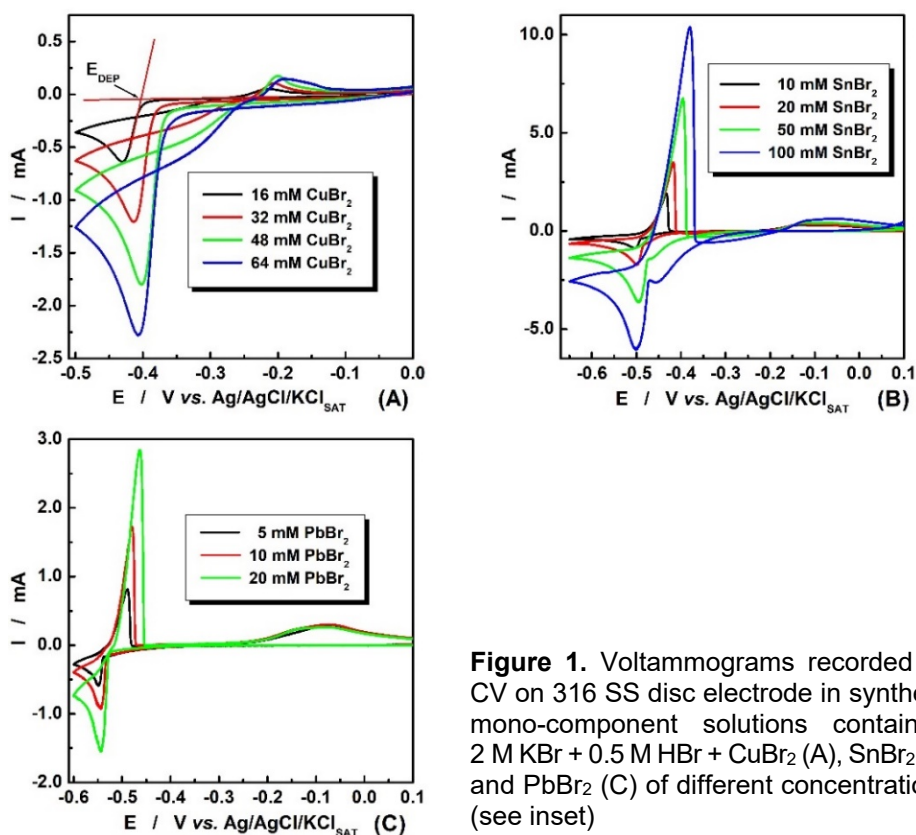


Figure 1. Voltammograms recorded by CV on 316 SS disc electrode in synthetic mono-component solutions containing 2 M KBr + 0.5 M HBr + CuBr_2 (A), SnBr_2 (B) and PbBr_2 (C) of different concentrations (see inset)

It is worth to note that the CV applied to study the process of metals electrodeposition/electrodissolution offers less accurate quantitative data, the peaks amplitude and position being strongly influenced by many factor like deposit morphology, electrode-deposit compatibility, vertex potential, etc. However, the CV remains a powerful tool for qualitative comparisons. Consequently, for a rigorous estimation of the Cu, Sn and Pb electrochemical behaviours, we decided to evaluate the electrodeposition potential, E_{DEP} , where the process start effectively. As exemplified in Figure 1.C, E_{DEP} corresponds to the intersection of the linear extrapolations associated with the Cu^{2+} to Cu^+ reduction process and the effective electrodeposition process. The evaluated E_{DEP} values are presented in Table 1.

Table 1. Evolution of E_{DEP} corresponding to the Cu^{2+} , Sn^{2+} and Pb^{2+} ions electrodeposition on 316 SS electrode from solutions containing different concentrations of CuBr_2 , SnBr_2 and PbBr_2 .

Cu		Sn		Pb	
[CuBr_2] (mM)	E_{DEP} (V/Ref.)	[SnBr_2] (mM)	E_{DEP} (V/Ref.)	[PbBr_2] (mM)	E_{DEP} (V/Ref.)
16	-0.407	10	-0.491	5	-0.541
32	-0.383	20	-0.485	10	-0.532
48	-0.366	50	-0.476	20	-0.526
64	-0.355	100	-0.472	-	-

As it can be seen from Figure 1 and Table 1, for all three studied ions, the modification of concentration values induces only minor changes of E_{DEP} in good agreement with the Nernst equation. Moreover, for the worst scenario, corresponding to the minimal Cu^{2+} concentration (16 mM \cong 1 g/L) and maximal concentration of Sn^{2+} (0.1 M \cong 10 g/L), substantial E_{DEP} gap, of ~ 70 mV, occurs for Cu and Sn. Similarly, for the highest Pb concentration (20 mM \cong 4 g/L), the E_{DEP} gap increase at ~ 120 mV. Considering these E_{DEP} gaps values and that, usually, the concentration of Cu, Sn and Pb ions in the spent leaching solutions vary between 300 and 600 mM, 50 and 90 mM, and 0.2 and 40 mM [23], respectively, we concluded that the selective electroextraction of Cu can be performed successfully on 316 SS electrodes if the operational parameters are rigorously controlled.

As stated before, the selective Cu electrodeposition tests from real leaching solutions were performed in galvanostatic mode, at current values (I_{WE}) imposed through the working electrode (WE) between -0.08 and -0.4 A, corresponding to current densities (i_{WE}) between 200 and 1000 A/m². Practically, using the experimental parameters indicated in Table 2, five distinct experiments were performed for similar quantities (Q) of electric charge (excepting the last

test), the corresponding Cu deposits being coded as D1 ÷ D5. In addition, in Table 2 are also presented the most important parameters evaluated from the experimental data: the current efficiency (C_{EF}), the specific energy consumption (W_s), the average values of the WE potential ($E_{WE, M}$) and of the oxidation/reduction potential (ORP_M). C_{EF} , W_s , $E_{WE, M}$ and ORP_M were evaluated using the main electrical parameters recorded during the experiments, presented in Figure 2, where E_{WE} , U_T , E_{CE} , pH and ORP represent the instant values of the WE potential, voltage at the terminals of the electrochemical cell, the counter electrode (CE) potential, pH and of the oxidation/reduction potential, respectively.

Table 2. The experimental parameters for the selective electrodeposition of Cu from a real leaching solution and the main evaluated parameters

Deposit	i_{WE} (A)	t (min)	i_{WE} A/m ²	Q (A*h)	C_{EF} (%)	W_s (kWh/kg)	$E_{WE, M}$ V/Ref	ORP_M V/Ref
D1	-0.40	127	1000	0.847	50.5	0.389	-0.363	0.047
D2	-0.32	158	800	0.843	54.6	0.292	-0.346	0.031
D3	-0.24	211	600	0.844	92.8	0.133	-0.343	0.020
D4	-0.16	316	400	0.843	90.8	0.105	-0.311	0.018
D5	-0.08	316	200	0.421	89.0	0.086	-0.287	0.032

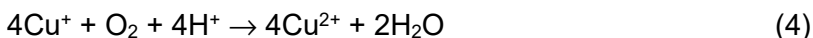
As can it be seen in Table 2, the current efficiency varies between 50.5 and 92.8%, considering that the Cu electrodeposition process occurs predominantly mono-electronic, described by the reaction:



Unfortunately, in parallel with this main process, a series of secondary processes take place, described by the reactions:



The intensity of the processes described by the equations (2) and (3) depends on the Cu^{2+} ion concentration and, especially, on the ratio between the Cu^{2+} and Cu^+ ion concentrations, which significantly influence the solution specific ORP value. From another point of view, it is important to note that, during the break between experiments and, especially, during them (when the solution is stirred), the Cu^+ ions are permanently oxidized to the Cu^{2+} ions due to the presence of atmospheric oxygen, according to the reaction:



This parasitic process is confirmed by the evolution of ORP throughout all experiments, which starts permanently, as illustrated in Figure 2, from a high value, and then decreases as Cu^{2+} ions get reduced to Cu^+ . The presence of the atmospheric oxygen has a negative effect on the Cu electrodeposition process, increasing Cu^{2+} concentration and favouring the secondary processes described by equations (2) and (3).

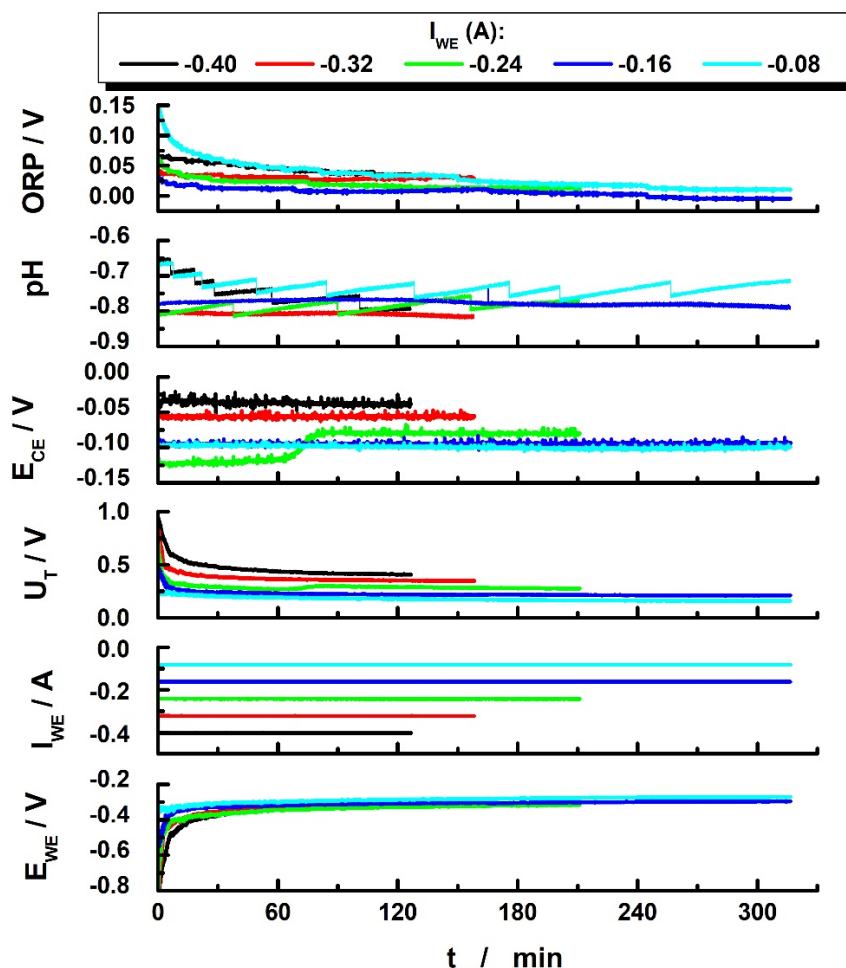


Figure 2. Evolution of the main electrical parameters during the experiments concerning the galvanostatic electrodeposition of Cu from the leaching solution

SELECTIVE ELECTROEXTRACTION OF BASE METALS FROM LEACHING SOLUTIONS OBTAINED DURING THE RECYCLING OF WASTE PRINTED CIRCUIT BOARDS

Inherently, as illustrated in Figure 3, the applied current density has a significant effect on the morphology, structure and appearance of the obtained deposits.

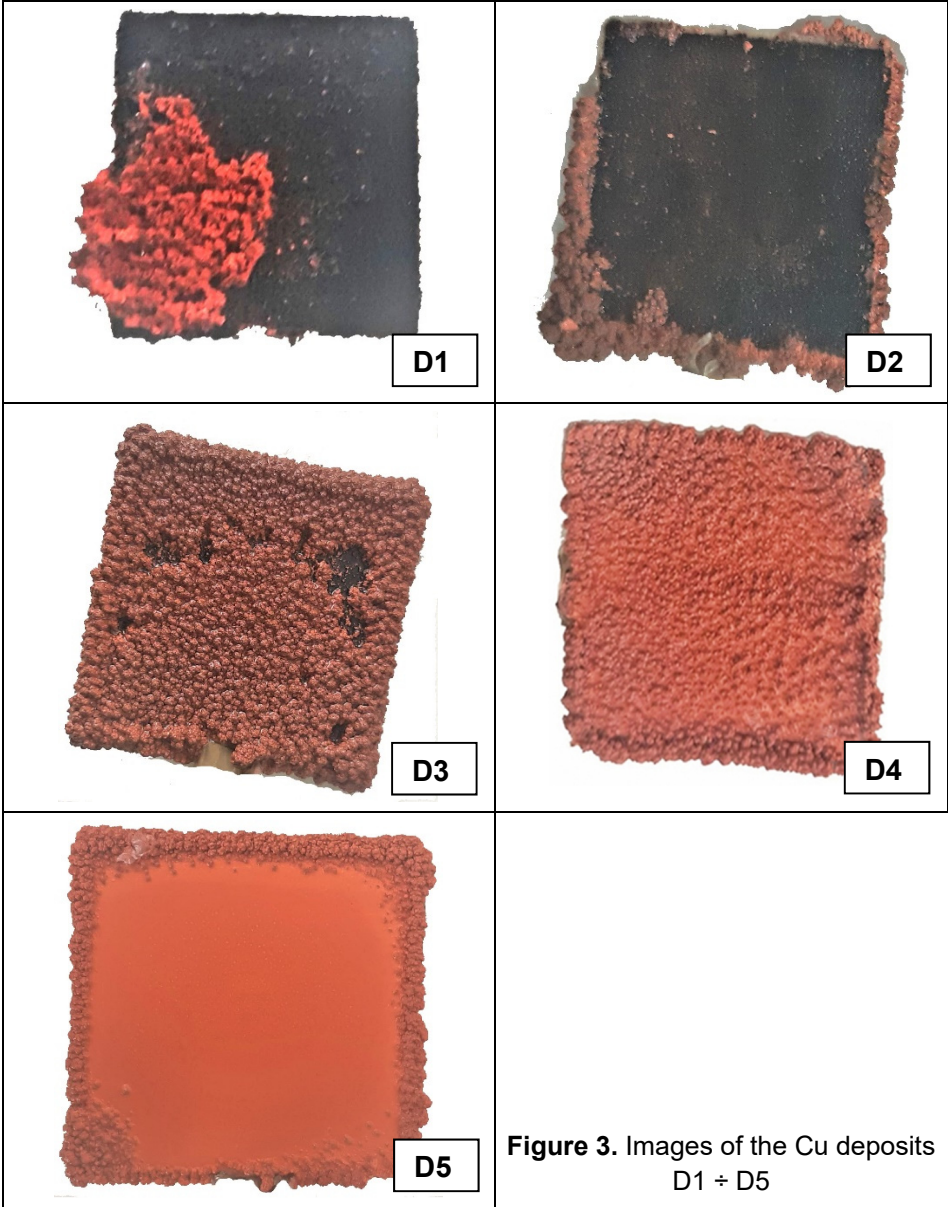


Figure 3. Images of the Cu deposits D1 ÷ D5

For an i_{WE} of 1000 A/m², the lowest C_{EF} and the highest W_S values were evaluated, simultaneously with the highest values for $E_{WE, M}$ and ORP_M , indicating clearly that the secondary processes (2) and (3) predominate during the experiment. Additionally, the resulting D1 covers only a small part of the cathode and has an accentuated dendritic structure, which induces high risk of detachment from the electrode surface.

For an i_{WE} of 800 A/m², the values of C_{EF} , W_S , $E_{WE, M}$ and ORP_M improve to a small extent, indicating a reduction in the ratio between Cu^{2+} and Cu^+ ion concentrations. In these conditions, it can be stated that the secondary processes (2) and (3) still predominate during the experiment. However, the aspect of the resulting D2 changes from an accentuated dendritic structure to a granular one. Also, in this case, D2 covers only a small part of the cathode.

At the i_{WE} of 600 A/m², the best value for C_{EF} (~ 93%), a much lower value for W_S , (0.133 kWh/kg) and acceptable values for $E_{WE, M}$ and ORP_M were obtained, indicating that, in this case, the predominant process becomes the mono-electronic electrodeposition of Cu. Under these conditions, D3 covers most of the cathode and has a predominantly granular structure, with a much-diminished edge effect.

For an i_{WE} of 400 A/m², the obtained results in terms of W_S , $E_{WE, M}$ and ORP_M are improved in comparison with D3. Unfortunately, the C_{EF} value presents a small decrease, suggesting that the rates of parasitic processes start to increase. In these conditions, D4 covers almost entirely the cathode surface and has a finer granular structure, but with a more evident edge effect than D3.

Finally, to avoid excessive experiment duration (more than 10.5 h), we decided to halve the Q value used for the i_{WE} of 200 A/m². In these conditions, the best value for W_S (0.086 kWh/kg) and an acceptable value for C_{EF} (89%) were obtained. This fact indicates that, although, in this case, the mono-electronic electrodeposition of Cu is the predominant process, the oxidation process with atmospheric oxygen is accentuated. As it can be seen in Figure 3, D5 completely covers the cathode with a smooth and compact film, but it has an accentuated edge effect.

In addition to the information concerning the C_{EF} , W_S , $E_{WE, M}$ and ORP_M , and those related to the deposits appearance, the establishment of optimal operating conditions must also take into account the purity of the obtained deposits. In this respect, the deposits were subjected to mineralization in *aqua regia*, and the concentrations of the metallic impurities were evaluated by ICP-OES. The results obtained from these analyses are summarized in Table 3 and represent the percentage concentration (w/w) relative to the mass of the deposits.

Table 3. Cu content and the percentage of the metallic impurities from the Cu deposits obtained by selective electrodeposition from real leaching solutions

Deposit	Cu (%)	Sn (%)	Pb (%)	Fe (%)	Ni (%)	Zn (%)	Ag (%)
D1	98.93	0.60	0.10	0.01	0.02	0.21	0.10
D2	99.40	0.21	0.05	0.01	0.01	0.21	0.08
D3	99.67	0.09	0.03	0.00	0.00	0.15	0.05
D4	99.67	0.06	0.03	0.01	0.00	0.19	0.04
D5	99.68	-	0.04	0.01	0.00	0.22	0.04

As it can be seen in Table 3, excepting the D1 case, for all other experiments, the purity of the obtained Cu deposits exceeds 99%, reaching 99.68% in the case of D5. The weaker results in case of D1 are justified by the fact that, at the beginning of the experiment, E_{WE} drops to values of -0.8 V/Ref, favouring the massive electrodeposition of impurities. Contrarily, at the lowest current density ($i_{WE} = 200 \text{ A/m}^2$), the concentration of impurities is minimal, but the electrodeposition rate becomes extremely low.

Corroborating the results presented in Figures 2 and 3, and Tables 2 and 3, it is obviously that the current density represents the key factor in the selective electroextraction of Cu. Practically, the increase of the current density induces more negative $E_{WE, M}$ values, increasing the risk of the other base metals co-deposition.

Based on these observations, we suppose that an improved selective electrodeposition can be achieved using a variable profile for the current density, starting from low values in order to cover the cathode surface with a layer of compact and pure Cu, and continuing with increasing current densities, up to 600 A/m^2 .

CONCLUSIONS

Based on the experimental results concerning the intensive electrodeposition of Cu on 316 SS electrodes from real solutions, we concluded that the selective Cu electroextraction can be successfully and efficiently used as the parallel paired process for the electrochemical regeneration of the leaching solutions based on the KBr/HBr/Br₂ system. High purity Cu deposits, up to 99.6%, can be obtained by maintaining the concentration of Cu ions in the leaching solution over 12 g/L and imposing cathodic current densities between 200 and 600 A/m^2 .

Increased purity of the deposits and better process efficiency can be achieved by using variable current profile, avoiding oxidation of the solution with atmospheric oxygen and increasing the thickness (mass) of the deposit.

EXPERIMENTAL SECTION

Chemicals

Reagents as: KBr, HBr, CuBr₂, SnBr₂, and PbBr₂ are purchased by Fluka and Sigma-Aldrich.

For the CV measurements, synthetic sample solutions are prepared by dissolving appropriate quantities of CuBr₂, SnBr₂, and PbBr₂ in 2 M KBr + 0.5 M HBr solution.

The real leaching solution was obtained by mixing equal samples from different solutions resulted by the leaching of the exposed metals from 10 PC motherboards in 2.2 L of 2 M KBr + 0.5 M HBr + 1 M Br₂ solutions [22]. The ORP of the resulting mixture (1 L) was lowered by placing it over 2 kg of WPCBs, after which the solution pH was adjusted to 0.1 by addition of HBr 47%. The concentrations of the main metallic ions in the solution were: 12 g/L Cu; 6.9 g/L Sn; 4.4 g/L Pb; 9 g/L Zn; 5.6 g/L Fe; 0.8 g/L Ni.

Experimental methods

Cyclic voltammetry was performed using a computer-controlled multi-channel potentiostat (DXC240, Datronix Computer, Romania). The electrochemical glass cell (50 mL) was equipped with a 316 SS disc ($\phi = 3$ mm) as WE, a Ag/AgCl/KCl_{sat} as reference electrode (Ref.) and a Pt wire ($\phi = 0.5$ mm, L = 10 cm) as CE. All the CV measurements were performed using a scan rate of 50 mV/s.

In order to preserve the electrolyte composition, the selective Cu electrodeposition experiments in galvanostatic mode (from real leaching solution) were performed in an undivided polypropylene electrochemical cell with a volume of 1 L, in which 400 mL of previous described real leaching solution was introduced. For the same reason, a 3 cm x 8 cm Cu plate with a thickness of 0.5 mm was used as CE (soluble anode). The cell was equipped with one 2 cm x 2 cm plate WE made from 316 SS sheet with a thickness of 0.2 mm, the face non-exposed to the CE being insulated. WE, CE and 2 reference electrodes of Ag/AgCl/KCl_{sat} type were connected to a computer controlled potentiostat (DXC236, Datronix Computer, Romania). Additionally, 2 laboratory multi-meters (Consort C863, Consort, Belgium) were used as galvanically insulated electrochemical interfaces with high input

impedance between the data acquisition board (NI6221, National Instruments, USA) and the pH and ORP sensors (SP10T and SO50X, respectively, both from Consort, Belgium). During the experiments, the electrolyte was stirred using a magnetic stirrer (FB 15001, Fischer Scientific). Before each test, the WE was polished using emery paper (1200 and 2000), washed with double-distilled water and dried under nitrogen jet. After each experiment, the SS electrode was removed from the electrochemical cell and the obtained Cu deposit was washed with 2 M KBr + 0.5 M HBr mixture (to avoid the precipitation of Cu, Sn and Pb ions), cleaned with double-distilled water and dried with pure acetone and pure nitrogen jet. Finally, the Cu deposits were detached from the SS cathode, weighed with an analytical balance, and mineralised with 28 mL of *aqua-regia*. The resulted solutions were analysed by ICP-OES method, using a SPECTRO CIROS CCD spectrometer (SPECTRO Analytical Instruments, Germany). The concentrations of the dissolved metallic ions from the leaching solutions were measured by flame atomic adsorption spectroscopy (FAAS), using an AVANTA-PM spectrometer (GBC, Australia).

ACKNOWLEDGMENTS

This work was supported by a grant of the Romanian Ministry of Research and Innovation, CCCDI-UEFISCDI, project number PN-III-P1-1.2-PCCDI-2017-0652 / 84PCCDI/2018, within PNCDI III.

REFERENCES

1. D. Zhang, Y. Cao, Y. Wang, G. Ding, *Resour. Conserv. Recycl.*, **2020**, *152*, 1-7.
2. S. Akbari, A. Ahmad, *Chem. Eng. Process.*, **2019**, *142*, 1-8.
3. Q. Tan, Q. Dong, L. Liu, Q. Song, Y. Liang, J. Li, *J. Clean. Prod.*, **2017**, *148*, 509-517.
4. R. Wang, Z. Zhu, S. Tan, J. Guo, Z. Xu, *J. Hazard. Mater.*, **2020**, *385*, 1-10.
5. H. Rau, A.R. Bisnar, J.P. Velasco, *Sustainability*, **2020**, *12(10)*, 4037, 1-21.
6. Z. Wu, W. Yuan, J. Li, X. Wang, L. Liu, J. Wang, *Front. Environ. Sci. Eng.*, **2017**, *11*, 8-21.
7. H. Wang, M. Han, S. Yang, Y. Chen, Q. Liu, S. Ke, *Environ. Int.*, **2011**, *37*, 80-85.
8. R.Z. Rebello, M.T.W.D. Carneiro Lima, L.H. Yamane, R.R. Siman, *Resour. Conserv. Recycl.*, **2020**, *153*, 1-7.
9. S. Ghosh, *Thin Solid Films*, **2019**, *669*, 641-658.
10. R.S. El-Nasr, S.M. Abdelbasir, A.H. Kamel, S.S.M. Hassan, *Sep. Purif. Technol.*, **2020**, *230*, 1-11.

11. X.N. Zhu, C.C. Nie, H. Zhang, X.J. Lyu, J. Qiu, L. Li, *J. Clean. Prod.*, **2020**, 248:119235, 1-8.
12. R.A. Mesquita, R.A.F. Silva, D. Majuste, *Process. Saf. Environ. Prot.*, **2018**, 120, 107-117.
13. T. Moyo, B.H Chirume, J. Petersen, *Resour. Conserv. Recycl.*, **2020**, 152, 1-7.
14. L. Leyssens, B. Vinck, C.V. Straeten, F. Wuyts, L. Maes, *Toxicology*, **2017**, 387, 43-56.
15. J. Hao, Y. Wang, Y. Wu, F. Guo, *Resour. Conserv. Recycl.*, **2020**, 157, 104787, 1-15.
16. A. Tuncuk, V. Stazi, A. Akcil, E.Y. Yazici, H. Deveci, *Miner. Eng.*, **2012**, 25, 28–37.
17. H. Li, J. Eksteen, E. Oraby, *Resour. Conserv. Recycl.*, **2018**, 139, 122-139.
18. S. Fogarasi, F. Imre-Lucaci, A. Egedy, Á. Imre-Lucaci, P. Ilea, *J. Waste Manag.*, **2015**, 40, 136-143.
19. L.A. Diaz, T.E. Lister, *J. Waste Manag.*, **2018**, 74, 384-392.
20. C. Cocchiara, S.A. Dorneanu, R. Inguanta, C. Sunseri, P. Ilea, *J. Clean. Prod.*, **2019**, 230, 170-179.
21. S.A. Dorneanu, *Studia UBB Chemia*, **2017**, LXII(3), 177-186.
22. S.A. Dorneanu, A.A. Avram, A.H. Marincaș, N. Cotolan, T. Frențiu, P. Ilea, *Studia UBB Chemia*, **2018**, LXIII(4), 147-158.
23. S.A. Dorneanu, E. Covaci, F. Imre-Lucaci, G. L. Turdean, *Studia UBB Chemia*, **2019**, LXIV(2), Tom II, 555-565.

COMPUTATIONAL IMAGE ANALYSIS AS AN ALTERNATIVE TOOL FOR THE EVALUATION OF CORROSION IN SALT SPRAY TEST

VITOR BONAMIGO MOREIRA^{a,b,*}, ALEX KRUMMENAUER^b,
JANE ZOPPAS FERREIRA^b, HUGO MARCELO VEIT^b,
ELAINE ARMELIN^{a,c} and ALVARO MENEGUZZI^{b,*}

ABSTRACT. The current standards for evaluating corrosion during salt spray tests rely on the visual analysis of the specimens, and this may be a limitation when higher resolution quantitative outputs are desired. In this work, computational image analysis was used to measure the area affected by corrosion during salt spray tests with aluminum alloy, copper, carbon steel and galvanized steel plates. The software ImageJ was used to select and measure the corroded areas differentiating the corrosion products from the metals uncorroded surfaces according to their different colors. With ten measurements for each selected exposure time, a 95 % confidence interval was calculated for each material and time of exposure, giving an indication of the precision of the estimated corroded area. These data were compared with a visual inspection carried out by an experienced technician. The results indicate that computational image analysis may be a powerful tool to obtain higher resolution in the results interpretation in comparison with the standard visual analysis.

Keywords: salt spray test, computational image analysis, corrosion assessment

INTRODUCTION

Although salt spray is extensively used as a comparative corrosion test, its outcome may be limited by the current standards. Corrosion evaluation

^a Departament d'Enginyeria Química, Universitat Politècnica de Catalunya, Campus Diagonal Besòs (EEBE), C/ Eduard Maristany, 10-14, Building I, 2nd floor, 08019, Barcelona, Spain

^b Programa de Pós-graduação em Engenharia de Minas, Metalúrgica e de Materiais (PPGE3M), Universidade Federal do Rio Grande do Sul (UFRGS), Av. Bento Gonçalves, 9500 – 91501-970, Porto Alegre, RS, Brazil.

^c Barcelona Research Center for Multiscale Science and Engineering, Universitat Politècnica de Catalunya, Campus Diagonal Besòs (EEBE), C/ Eduard Maristany, 10-14, Building I, basement floor, 08019, Barcelona, Spain.

* Corresponding authors: vitor.moreira@upc.edu and meneguzzi@ufrgs.br

standards, such as ASTM D610–08 [1], which uses visual examples as reference for comparison and subsequent rating of corrosion grades, are based on visual analysis. As such, they add some uncertainty to the results due to the adoption of subjective criteria and lowering the results resolution by limiting the outcome to an interval from 0 (zero) to 10, a discrete scale based on the percentage of area failed.

Computational image analysis may be an alternative to overcome this limitation by obtaining higher resolution data in order to improve the comparative investigation. One example was that reported by ASTM International with the standard D 7087-5a (2010) [2], where they reported a procedure for measuring rust creepage at scribe by an imaging technique. However, the withdrawal of this standard in 2019 showed that there are still challenges to be tackled in order to provide reliable methods for computational corrosion evaluation.

In a recent work, Denissen and Garcia [3] used iterative algorithms in the computational image analysis during electrochemical impedance spectroscopy tests in order to obtain complementary interpretation for such tests, showing the relevance of adequate assessment of the visible changes in the materials surface as an evidence of corrosive processes. Other authors [4–6] have already used image analysis for measuring corroded areas after corrosion tests. Although the successful use of those tools, there are no studies regarding the uncertainty of such analyses, from a statistical point of view, in salt spray tests.

Moreover, uncoated bare metal surfaces are not considered by the current corrosion evaluation standards. The inspection of the samples is usually limited by weight loss and corrosion analyses localized on the scribe of painted panels. Iribarren *et al.* [7] have demonstrated that dark and colored iron oxides and oxyhydroxides are associated with advanced carbon steel deterioration, due to their non-adherent properties and high permeability to ions. Therefore, the use of color evaluation not only allows to distinguish the uncorroded and corroded zones, but also indicates the severity of the corrosive process which the material has undergone.

Based on such examples, colors enable the use of image analysis tools to measure the fraction of the specimens' surface affected by corrosion.

In this work, salt spray tests were carried out with bare plates of four different metals: aluminum alloy, copper, carbon steel and galvanized steel. These specimens were evaluated periodically using ImageJ software (National Institutes of Health, Bethesda, Maryland, USA) in order to quantify the area affected by corrosion on each sample and perform the statistical analysis of the measurements. The observed results are represented in terms of failed area (%) versus the time of salt fog exposition, for each material. These plots were used to assess and to compare the 95 % confidence intervals (CI), of the means of different datasets [8].

For first time, the statistical reliability of the proposed technique, has been addressed. The main aim of such validation is to introduce a novel evaluation method in order to obtain high resolution results after conventional corrosion tests. The method can be extended to other destructive tests used for coatings and surface characterization, such as adhesion tests, blistering evaluation, and others.

RESULTS AND DISCUSSION

In this section the results obtained for each metal will be discussed as an independent analysis because the corrosion products are not the same for all samples. As expected, the tested metals demand a particular adjustment of parameters for correct selection of the corroded area because of the different visual aspects of the corrosion products.

Aluminum

Aluminum corrosion product is known to be white; therefore, it can be adequately identified by adjusting the brightness threshold. The interval plot of the measurements carried out in aluminum samples is depicted in Figure 1.

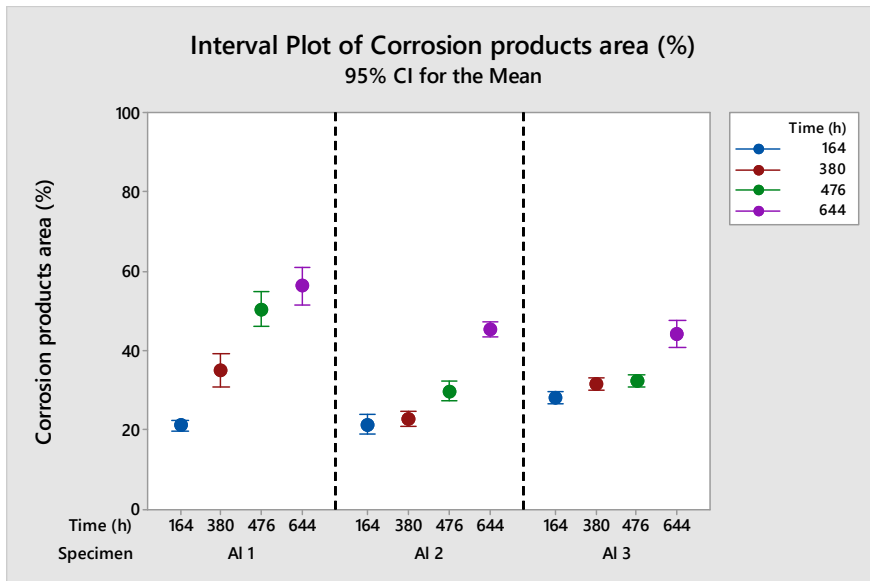


Figure 1. Interval plot of measurements performed in aluminum alloy samples using color threshold function on ImageJ. CI means the confidence interval of 95 % obtained by statistical analysis.

The visual aspect of white aluminum oxide formed changed throughout the test duration, being evidently enlarged over increasing salt fog exposition time, as can be seen in Figure 2.

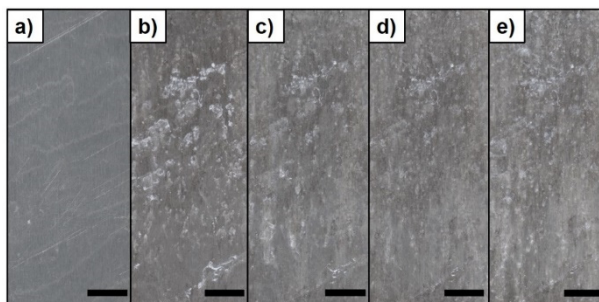


Figure 2. Aluminum sample (Al 1) during visual analysis a) before the test, b) after 164 h, c) 380 h, d) 476 h and e) 644 h. The bars correspond to 1 cm.

It is noticeable (Figure 2) that the corrosion products formed above the aluminum alloy surface, clearly delineated after 164 h of test, became less distinguishable assuming the aspect of the large stains with less brightness (light gray in color) in the following measurements. Therefore, the reduction of well-defined white oxides may be the reason why the data dispersion was increased for 380 h, 476 h and 644 h; resulting in broader confidence intervals. Those confidence intervals varied from 2.9 % for 164 h to 9.7 % for 644 h, for the sample Al 1; which are the lowest and the highest length of CI, respectively, for all measurements carried out in aluminum.

The comparison between the dispersion observed for Al 1 and Al 3 in the 380 h analysis confirms this hypothesis, once Al 3 still has well delineated corroded areas at this point, which does not occur with the sample Al 1. Comparison of both specimens is shown in the photograph images of Figure 3.

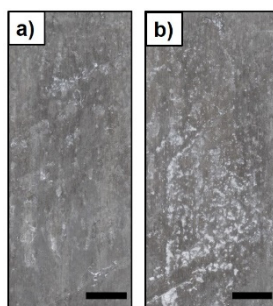


Figure 3. Visual aspect of the surface of: a) Al 1 and b) Al 3 specimens, after 380 h of exposure on salt spray.

Despite the difficulty imposed by the mentioned factor, the corroded areas are mostly statistically distinct and significant increases were observed for all samples during the test, as expected.

Figure 4 consists in a graphical comparison between the values measured using the ImageJ computer software and the values of corrosion grade, obtained with an adapted version of the standard ASTM D610 (described in the experimental section), for each aluminum sample.

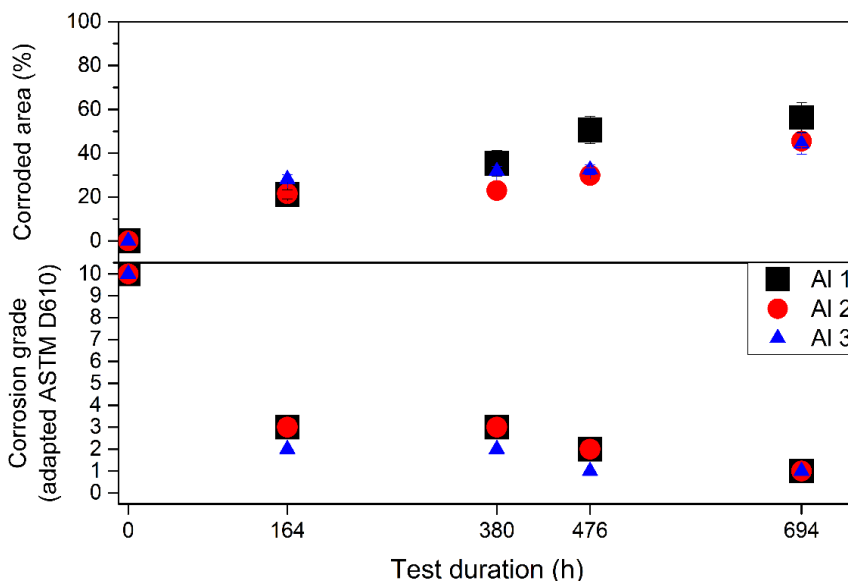


Figure 4. Comparison of the computational measure using the ImageJ software (above) and the corrosion grade obtained with the standard ASTM D610 (below) for aluminum specimens.

The corrosion grade measured for the aluminum specimens decreased from 3 to 2 at the first salt spray exposition (164 h), and then decreased more slowly until grade 1 at the end of the test. This sharp exponential curve decrease traduces in a less accurate measure for the samples with more corroded area, once the interval for the failed area does not allow differentiating a fine corrosion grade, in the ASTM D610 standard. On the other hand, the image analysis by adjusting the brightness for identifying the white aluminum oxides offers a linear ascending curve. This effect is noticeable during the test at 694 h, as the computational analysis provides distinct areas while the visual inspection, following the ASTM D610 criteria, results in the same corrosion grades for the three samples studied. Thus, the computational measure ensures a statistically relevant difference

of approximately 20 % in the corroded area of these specimens. This can be explained because the standard corrosion grades regard only corrosion up to 50 % in total area, so it was expected that for higher corroded areas the visual analysis could not provide adequate differentiation.

Copper

Considering the testing environment, the possible corrosion products from copper and their respective colors are: Cu_2O (red); CuO (black); $\text{Cu}(\text{OH})_2$ (blue); and, possibly, CuCl after the replacement of oxygen by chloride ions in Cu_2O composition, changing it to a yellow colored layer [9,10].

The scan images of one copper specimen (Cu 1) are depicted in Figure 5.

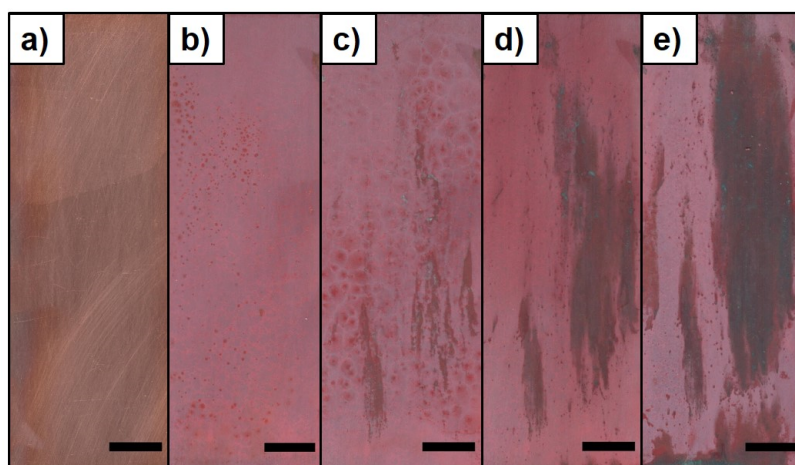


Figure 5. Copper sample (Cu 1) during visual analysis a) before the test, b) after 476 h, c) 716 h, d) 1052 h and e) 1388 h. The bars correspond to 1 cm.

In the first exposition time (476 h), remembering that either the salt fog spray exposition or the adjustments for the image analysis were not the same for each metal, the corrosion products were predominantly light red, and they were adequately selected by setting the saturation spectrum and allowing the establishment of the appropriate hues and brightness values. After 476 h, the predominant color of the corrosion products was a dark shade of red, possibly a mixture of CuO and Cu_2O , with some blue areas, possibly from $\text{Cu}(\text{OH})_2$. Those corrosion products are easily distinguished from the substrate by the control of the brightness values for all hue and saturation spectra. The interval plot for all measurements performed in copper samples is presented in Figure 6.

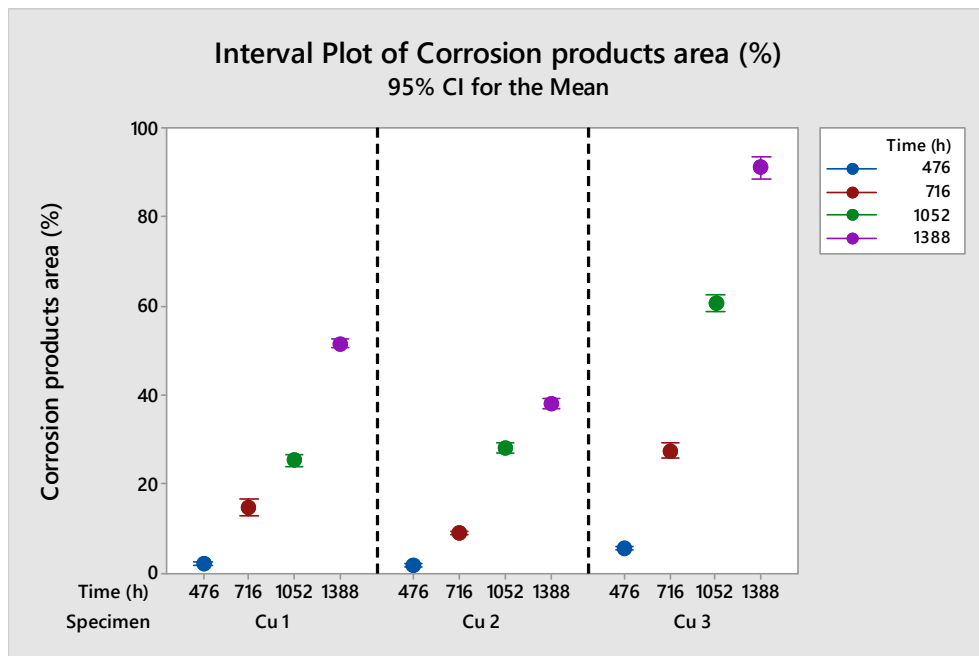


Figure 6. Interval plot of the measurements carried out in copper specimens using color threshold function on ImageJ. CI means the confidence interval of 95% obtained by statistical analysis.

The clear visual distinction of the corrosion products by color has influenced the data dispersion. The three analyzed specimens showed significant differences regarding the evolution of the corrosive process (Figure 5), but even with the observed differences all samples had a narrow data dispersion, indicating the reliability of our analysis method. The lowest length of CI for copper samples was observed for Cu 2 after 476 h, which was only 0.5 %; while the highest value was obtained for the sample Cu 3, 5.1 % length of CI. It is also noticeable that there are statistically significant differences for all of the points measured for each sample, indicating the expected evolution of the corroded area for all the specimens.

A graphical comparison between the computational image analysis and the visual inspection of copper corrosion products by using the adapted version of ASTM D610 is shown in Figure 7.

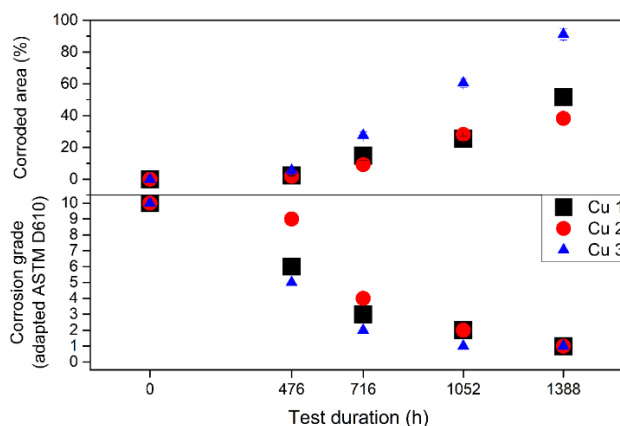


Figure 7. Comparison of the computational measure using the ImageJ software (above) and the corrosion grade obtained with the standard ASTM D610 (below) for copper specimens.

As observed previously in the aluminum specimens (Figure 4), the corrosion grade from the ASTM D610 fails again to differentiate samples with large corroded areas, while computational image analysis detects significant differences between the samples. One example of this evidence is the evolution of corrosion in sample Cu 3, which increased only one corrosion grade from 716 h to 1388 h after testing. Computational image analysis showed that, in the same time interval, this increase corresponds to an evolution of approximately 60 % more of copper oxide products respect to the total of the corroded area.

Carbon steel

The images used for the evaluation of one of the carbon steel samples (CS 1) throughout the test can be seen in Figure 8.

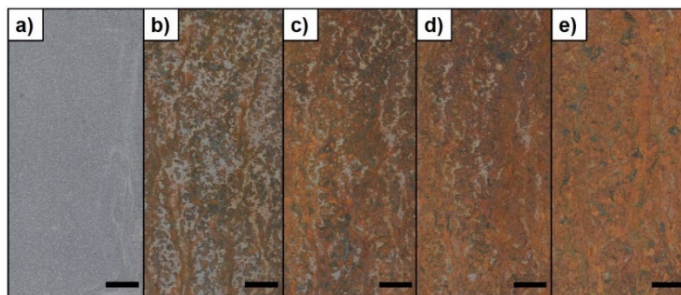


Figure 8. Carbon steel sample (CS 1) during visual analysis a) before the test, b) after 1 h, c) 2 h, d) 3 h and e) 5 h. The bars correspond to 1 cm.

For carbon steel samples the HSB color system adjustment fails for selecting the darker areas. Therefore, the RGB color system was chosen, and it offers a more efficient setting by limiting the green spectrum to a desired value and allowing the entire red and blue spectra to be selected, as observed experimentally. The interval plot of the performed measurements is shown in Figure 9.

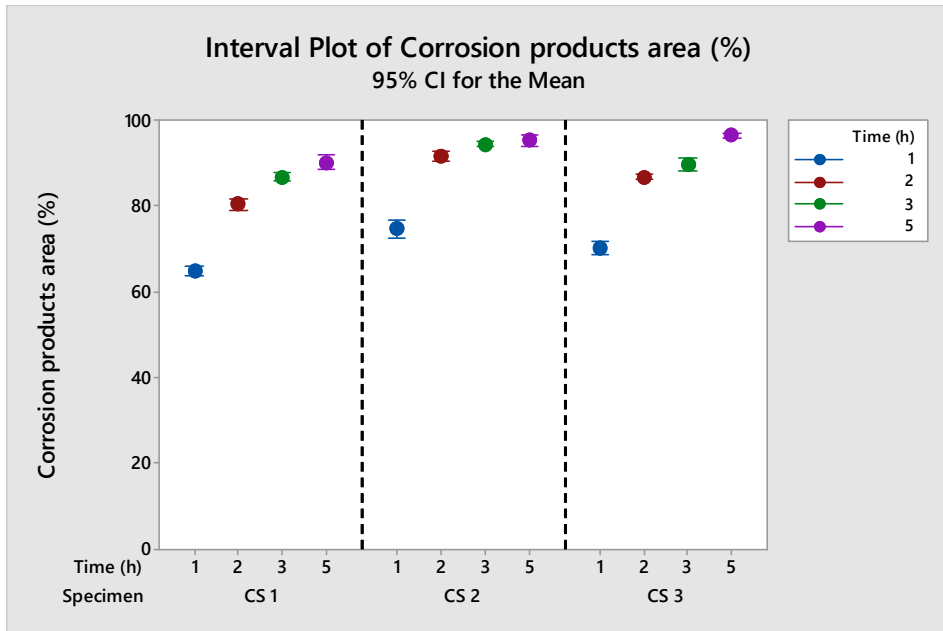


Figure 9. Interval plot of measurements performed in AISI 1020 steel samples using color threshold function on ImageJ. CI means the confidence interval of 95 % obtained by statistical analysis.

Carbon steel presents many corrosion products within a wide color range. For more details regarding the correlation among the oxides and oxyhydroxides products and specific colors, please, refer to the references [7, 11, 12]. The mean value of the corroded area (Figure 9) was higher than 60 % for all of the analyzed time intervals for all the specimens. These large areas did not lead to inconsistent data dispersion, with the lengths of CI being very low, between 1.1 % and 4.1 % for all samples. This range of lengths of CI is similar to that one observed for copper samples (with exception of Cu 3). As observed in copper analyses, the high contrast between the corrosion products and the bare metal substrate results in a narrow data dispersion once the visual distinction is facilitated.

The graphical comparison between the proposed technique and the visual analysis offered by ASTM D610 of carbon steel specimens is shown in Figure 10.

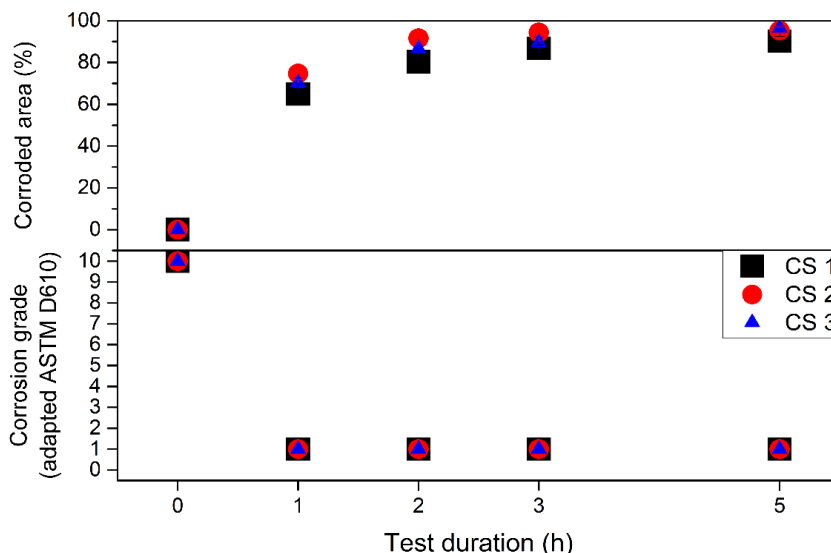


Figure 10. Comparison of the computational measure using the ImageJ software (above) and the corrosion grade obtained by with the standard ASTM D610 (below) for carbon steel specimens.

As can be seen in the Figure 10, the corrosion grade obtained with visual analysis (ASTM D610) resulted in no differentiation for large corroded areas, reaching the maximum rating number of 1 for any exposition time in salt spray test. By contrary, the corroded area measured with the computational image analysis indicated an exponential rise of the corroded area up to approximately 30 % from 1 h to 5 h of test. Altogether evidence that the computational software ImageJ can be used to achieve comparisons that are more accurate.

Galvanized steel

The corrosion products formed in galvanized steel are initially white, corresponding to ZnO molecules, and, after a severe corrosion of the zinc layer, red corrosion products are visible as a result of the underlying carbon steel corrosion process, as observed in Figure 11, which contains the analyzed images of a galvanized steel specimen (GS 1).

COMPUTATIONAL IMAGE ANALYSIS AS AN ALTERNATIVE TOOL FOR THE EVALUATION OF CORROSION IN SALT SPRAY TEST

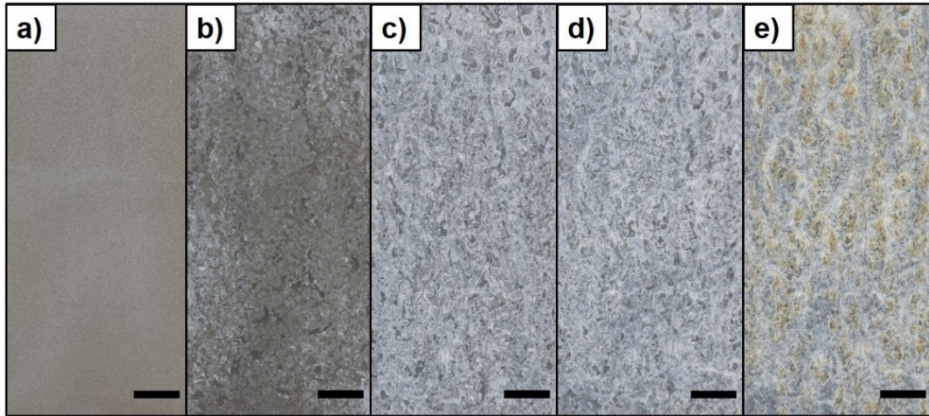


Figure 11. Galvanized steel sample (GS 1) during visual analysis a) before the test, b) after 2 h, c) 5 h, d) 10 h and e) 24 h. The bars correspond to 1 cm.

For the measurements carried out on galvanized steel specimens, the adjustment of the brightness was efficient for selecting the corroded area. The resulting interval plots are depicted in Figure 12.

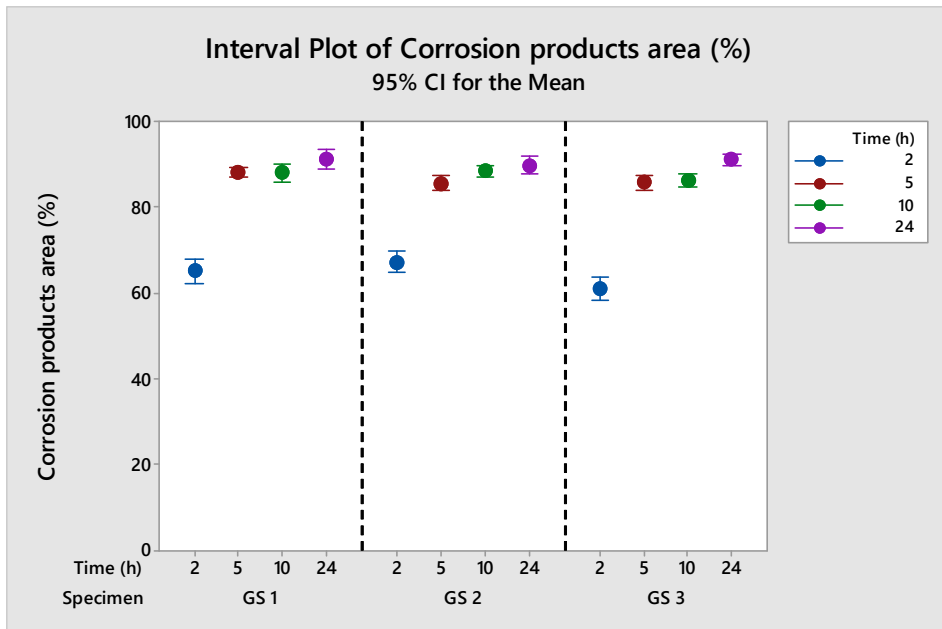


Figure 12. Interval plot of measurements performed in galvanized steel samples using color threshold function on ImageJ. CI means the confidence interval of 95 % obtained by statistical analysis.

Differently from that observed in aluminum, the white corrosion products on galvanized steel do not have a significant change regarding their visual aspect, *i.e.* the corroded areas on galvanized steel are more clearly delimited with the evolution of the corrosive process than in aluminum alloy. In other words, the specific corroded areas that are visible in the first analysis time remain well defined until the end of the test. This has resulted in a narrow data dispersion on larger testing times.

Although some of the measurements for 5 h, 10 h and 24 h in salt fog test are statistically equivalent, this is a result of a stabilization in the corrosion evolution on the tested specimens. Between 5 h and 24 h the CI length did not exceed 4.7 % for all samples, which indicates that even with large corroded areas the computational method may provide significant data. The lowest and the highest lengths of CI observed for galvanized steel were 2.3 % and 5.8 %, respectively.

Figure 13 shows the graphical comparison between both the image and the visual analyses, obtained from adapted ASTM 610, for galvanized steel specimens.

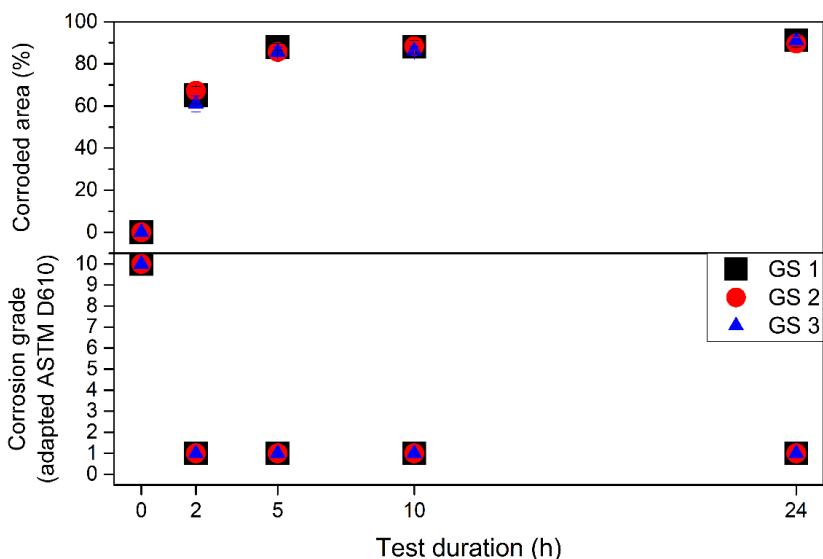


Figure 13. Comparison of the computational measure using the ImageJ software (above) and the corrosion grade obtained with the standard ASTM D610 (below) for galvanized steel specimens.

If we compare the Figures 8 and 10 (lower plots), it can be seen that there are no differences on the evaluation of the corroded area between carbon steel and galvanized steel, by using ASTM D610 visual inspection.

Nevertheless, the fast increase of corrosion areas from the first measurement (65 %, 2 h) towards the second time (88 %, 5 h) in the galvanized samples (Figure 13, upper plot) was discriminated by the computational image analysis. It corresponds to the elimination of the ZnO layer and the starting of under layer corrosion, which is more similar to that reported for the carbon steel (Figure 10, upper plot).

CONCLUSIONS

The use of a computational image analysis to measure corroded areas during salt spray test resulted in higher differentiation between specimens with statistically significant difference at 95 % confidence level for all the tested metals, if compared to the visual inspection suggested by ASTM D610 standard. Among the different metal compositions, a clear linear curve of corroded area over time was found to aluminum alloy and copper substrates, whereas the carbon steel and the galvanized steel showed an exponential increase of corrosion rate.

Thus, for first time, we have demonstrated a reliable and reproducible method for the evaluation of corrosion products by contrast, brightness, hue and saturation adjustment, after salt spray test, which will undoubtedly enrich the interpretation of the data obtained from such assays.

This technique may enable differentiation in the performance of materials that would not be measurable with the conventional evaluation methods, providing a quantitative character to such experiment, which is typically limited by the intrinsically qualitative aspect of simple visual analysis.

It must be mentioned that the proposed method is limited by the ability of acquiring representative two-dimensional images of the tested surfaces with no perspective. In this way, complex three-dimensional shapes inevitably introduce misleading inputs, as affected areas may appear smaller with increasing distance to the image foreground. Additional image processing or alternative image acquisition methods would be necessary to overcome this limitation.

The authors expect to set ground for further developments in the improvement of accelerated corrosion analysis, as the technique herein described can be applied to other tests, such as immersion or 100 % relative humidity tests. This can be also the initial step towards the development of automated corrosion evaluation by computational image analysis in accelerated corrosion tests. The new insights presented here can be extended to other destructive analyses, like those performed on coatings industry (pull-off test, blistering, rust creepage at scribe, and others).

EXPERIMENTAL SECTION

The metal plates used for this work were: aluminum (AA7075-T6; 80 mm × 40 mm × 3 mm), copper (UNS – C11000; 100 mm x 40 mm x 1 mm), carbon steel (AISI 1020; 100 mm × 50 mm × 1 mm) and galvanized steel (100 mm × 50 mm × 1 mm). Three specimens of each metal were tested. Individual specimens are referred to throughout this manuscript as: Al #, for aluminum alloy; Cu #, for copper; CS #, for carbon steel; GS #, for galvanized steel, being # a number from 1 to 3 that refers to the specimen tested.

Such metals were chosen due to the different surface contrast (by color) they present, as well as, due to the different contrast of their corrosion products. Aluminum provides a bright gray substrate with the formation of white corrosion products, which may not be easily distinguishable by visual analysis. Copper, as well as galvanized steel, may form more than one single corrosion product. Carbon steel, besides being one of the main structural materials for engineering applications, also form different corrosion products, with different colors. Therefore, its study is important for a broader application of the proposed technique.

All samples were degreased during 10 minutes at 70 °C with an industrial alkaline degreaser (Saloclean 667N – Klintex Insumos Industriais Ltda.) and subsequently washed with distilled water to eliminate the excess of degreaser agent.

Salt spray tests were carried out according to ASTM B117 [13]. Four analysis times were selected for each metal for the image analysis: 164 h, 380 h, 476 h and 644 h for aluminum; 476 h, 716 h, 1052 h and 1388 h for copper; 1 h, 2 h, 3 h and 5 h for carbon steel; 2 h, 5 h, 10 h and 24 h for galvanized steel; and 0 (before salt fog chamber conditioning). Such time intervals were defined individually for each material due to the differences in their reactivity, so that a wide range of corrosion levels would be measured.

For the computational image analysis, each specimen was scanned using an image scanner (HP Color LaserJet CM1312 MPF - Hewlett-Packard Company) as an important tool to eliminate the effect of picture perspective; which cannot be neglected if conventional photographs are used.

For image analysis, the “Color threshold” function was used. The desired area was selected and was measured by setting the adequate parameters in hue, saturation and brightness (HSB color system), after eliminating the edges and holes of the specimens and evaluating the visible corrosion products. Specifically, for carbon steel specimens, the Red, Green and Blue (RGB) color system was more adequate for selecting the correct areas. This measurement was repeated ten times for each sample and time, adjusting

COMPUTATIONAL IMAGE ANALYSIS AS AN ALTERNATIVE TOOL FOR THE EVALUATION OF CORROSION IN SALT SPRAY TEST

manually the parameters for each one of them in order to measure experimental error. These parameter adjustments were made for each repetition independently, without necessarily matching the previous measurements for the same specimen, allowing the evaluation of the experimental variability, shown graphically in the interval plots.

Figure 14 illustrates this procedure for one aluminum plate.

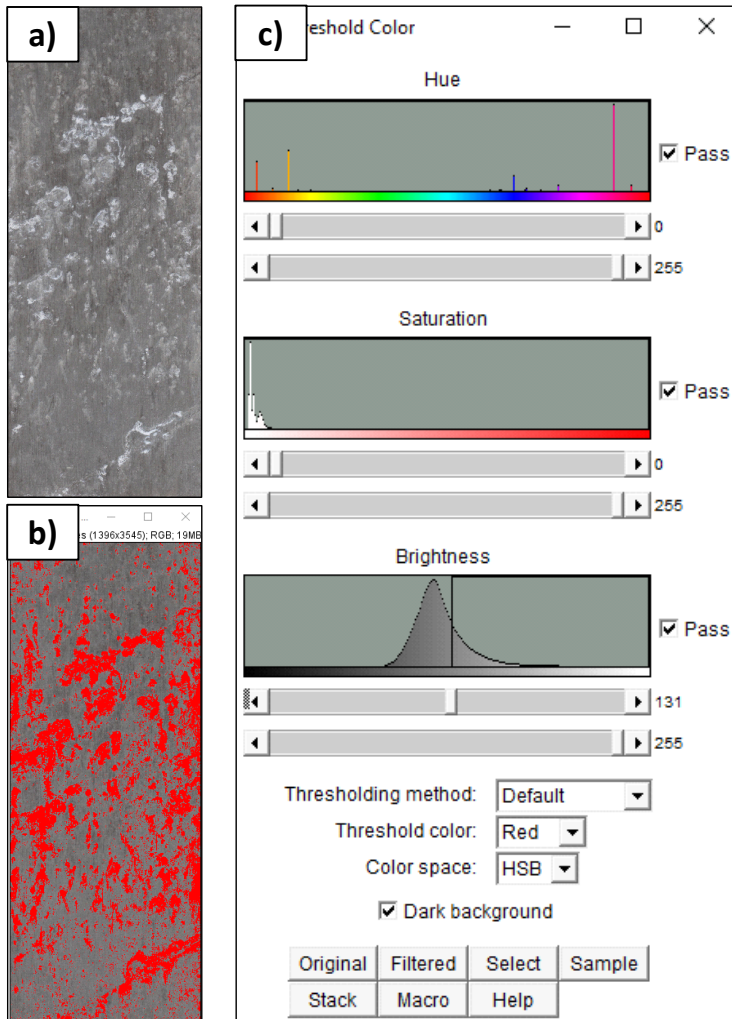


Figure 14. a) Aluminum sample with white corrosion products after salt spray test; b) ImageJ screen during color threshold adjustments for selecting the corroded area (in red); c) Parameters adjustments screen for color threshold in HSB color system.

The 95 % confidence interval (CI) were calculated using the software Minitab 17 (Minitab Inc., USA) by the statistical inference for small samples (less than 30 measurements) that uses the t distribution, also referred to as Student's t distribution. These CI are defined by the lower confidence limit (LCL) and the upper confidence limit (UCL), which are calculated using the Equations [1] and [2], respectively [14].

$$LCL = \bar{x} - t \cdot \frac{s}{\sqrt{n}} \quad [1]$$

$$UCL = \bar{x} + t \cdot \frac{s}{\sqrt{n}} \quad [2]$$

Where \bar{x} represents the sample mean, s stands for the sample standard deviation, n is the number of measurements and t is a factor depending on the degrees of freedom ($\nu = n - 1$) and the significance level (α). This way, being calculated for each sample at each time, the length of the CI is a measurement of the precision of the estimate value for the corroded area [14].

Each interval plot shows the results for a single material, with three analyzed samples and five different exposure times on the salt spray test. These plots were generated by the software Minitab 17. The whiskers show the lower and upper confidence limits, while the center marker indicates the mean value for the group [8].

With the lack of adequate standards for evaluating corrosion in uncoated bare metal samples, an adapted version of the ASTM D610 standard [1], which describes the practice for evaluating degree of rusting on painted steel surfaces by visual inspection, was used in order to compare to the computational image analysis proposed in the present study. The adaption of the standard was made comparing the test images of bare plates with the standard images for painted plates. Then, the corroded area was evaluated as if it was a paint failure area. Each specimen is then associated to a corresponding corrosion grade from 10 (0 % of corroded area) to 0 (zero, > 50 % of corroded area) in each evaluation time.

ACKNOWLEDGMENTS

Mr. Moreira acknowledges the fellowships received from the Conselho Nacional de Desenvolvimento Científico e Tecnológico – CNPq (grant 200890/2018-2 and project 405956/2016-9) and Coordenação de Aperfeiçoamento de Pessoal de Nível Superior – CAPES (grant 88881.188990/2018-01) for the PhD study and mobility. Mr. Krummenauer acknowledges CAPES (grant 88882.345832/2019-01) for the financial support.

REFERENCES

1. ASTM International; ASTM Stand., 2001, D610-01(Reapproved 2012), 1–6.
2. ASTM International; ASTM Stand., 2010, D7087-05a(Withdrawn 2019), 1–4.
3. P.J. Denissen; S.J. Garcia; *Electrochim. Acta*, 2019, 293, 514–524.
4. M. Rodošek; et al.; *Corros. Sci.*, 2017, 126(June), 55–68.
5. J.L. Daure; K.T. Voisey; P.H. Shipway; D.A. Stewart; *Surf. Coatings Technol.*, 2017, 324, 403–412.
6. X.-B. Chen; N. Birbilis; T.B. Abbott; *Corros. Sci.*, 2012, 55, 226–232.
7. J.I. Iribarren; F. Liesa; Á. Meneguzzi; C. Alemán; E. Armelin; *J. Cult. Herit.*, 2020, 42, 240–248.
8. W.P. Gardiner; *Statistical Analysis Methods for Chemists* Royal Society of Chemistry, Cambridge, 2007, doi:10.1039/9781847551924
9. A. Groysman; *Corrosion for Everybody* Springer Netherlands, Dordrecht, 2010, doi:10.1007/978-90-481-3477-9
10. S. Sathiyarayanan; M. Sahre; W. Kautek; *Corros. Sci.*, 1999, 41(10), 1899–1909.
11. R.A. Antunes; I. Costa; D.L. A. de Faria; *Mater. Res.*, 2003, 6(3), 403–408.
12. R.A. Antunes; R.U. Ichikawa; L.G. Martinez; I. Costa; *Int. J. Corros.*, 2014, 2014, 1–9.
13. ASTM International; ASTM Stand., 2019, B117-19, 1–11.
14. D.C. Montgomery; G.C. Runger; *Applied statistics and probability for engineers* Hoboken, USA, 2014, 6th editio Ed.

CHEMICALLY MODIFIED CHITOSAN COATINGS: WETTING AND ELECTROCHEMICAL STUDIES

PÉTER MÁRTON^a, EMŐKE ALBERT^a, NORBERT NAGY^b,
BORBÁLA TEGZE^a, GABRIELLA STEFÁNIA SZABÓ^{c*},
ZOLTÁN HÓRVÖLGYI^{a*}

ABSTRACT. Native chitosan coatings were prepared on glass and zinc substrates by dip-coating method. The native coatings were chemically modified: crosslinked with glutaraldehyde and sodium-tripolyphosphate and then silylated with dichlorodimethylsilane. The native layers prepared on zinc substrate were acylated with acetic anhydride and impregnated with indigo carmine (IC). Native coatings on different substrates showed different morphology and physical structure, which were explored by AFM studies. Examining the wetting properties of the coatings, it was found that the chemical modification can form a stable, hydrophobic (advancing contact angle of ca. 97°) and water repellent ($H_0 = 2^\circ$) layer on the glass substrate, while the same modifications reduce the hydrophobic nature and stability of the coating on zinc (contact angle decreases from ca. 100° to ca. 60°). Electrochemical studies of the coatings have shown that IC increases the corrosion protection (>90% inhibition efficiency) and reduces the permeability of the coating through ionic crosslinking, while acylation has the opposite effect and the acylated coating protection is worse than the native chitosan. The results can be used in the development of hydrophobic, water-repellent and temporary anti-corrosion coatings.

Keywords: *chitosan coating, contact angles, electrochemical measurements*

^a *Budapest University of Technology and Economics, Faculty of Chemical Technology and Biotechnology, Department of Physical Chemistry and Materials Science, Centre for Colloid Chemistry, H-1521 Budapest, Hungary*

^b *Institute for Technical Physics and Materials Science, Centre for Energy Research, H-1525 Budapest, Hungary*

^c *Babeş-Bolyai University, Faculty of Chemistry and Chemical Engineering, 11 Arany Janos str., RO-400028, Cluj-Napoca, Romania*

* *Corresponding authors: gszabo@chem.ubbcluj.ro, zhorvolgyi@mail.bme.hu*

INTRODUCTION

Glucosamine based biomaterials which can be frequently found in the nature are important synthesis materials for numerous products [1] [2]. Chitosan is a glucosamine based biopolymer produced from chitin [3], which is used in many industries due to its biocompatibility, biodegradability and antibacterial properties, such as food industry [4], medicine [5] and agriculture [6].

Chitosan can also be used in composite materials [7] and coatings to develop drug release systems that are very important in pharmacology. The permeability of chitosan coatings and its dependence on the layer thickness can be studied in bilayer systems [8]. The incubated molecule release kinetics is investigated from the chitosan-covered porous layer that is impregnated with the model molecule (usually an ionic dye). In this case, it is important to characterize the permeability of the chitosan coating, and one of the possible ways to do this is by determining its pseudo-porosity value from electrochemical studies, including polarization curves [9]. Due to the structure of chitosan, it can be regarded as a pseudo-porous layer through which the charged species of the electrolyte solution can reach the metal surface. Using the suitable equations, we can deduce the permeability from the rate of ion transport and the resistance of the coating.

Related to this, another area of application for chitosan is in corrosion protection [10]. Although unmodified native chitosan does not have a remarkable protective effect, it can provide effective protection when chemically modified or impregnated with various organic inhibitors. An example of such an inhibitor is indigo carmine (IC) [11], which is a natural dye and thus offers an eco-friendly alternative to more conventional corrosion inhibitors. The protective effect of these chitosan-based coatings were studied on various metallic surfaces, such as aluminum alloys [12], steel [13], zinc [14] and titanium [15]. Due to their low barrier properties, these types of chitosan-based films are often developed for less demanding applications, such as temporary protective layers. These types of coatings are capable of reducing the quantity of corrosion damage during shipment [16].

As was mentioned before, the chemical modification (e.g. impregnation with inhibitors) is a way to improve the protective effect of the coatings. If the hydrophobicity of the surface can be increased by some methods, the corrosion process can also be slowed down, as one of its primary causes is moisture. The production of hydrophobized chitosan has been reported in several articles, mainly silyl- [17] [18] or long-chain carboxylic acid derivatives [19] were used as reagents. Acylation of chitosan, which is basically a process in which chitin is produced, is also common [20] [21].

The aim of this paper is to investigate the effect of the mentioned chemical modifications on the wettability and pseudo-porosity (and related permeability) of chitosan coatings on various substrates. The purpose of the chemical modification with dichlorodimethylsilane (DCDMS) was to form a chitosan layer with hydrophobic and water-repellent properties. The change in the pseudo-porosity and corrosion protection of the coatings by reacting with acetic anhydride and impregnation with IC was also studied.

RESULTS AND DISCUSSION

Optical spectroscopy analysis of coatings deposited on glass substrates

The deposited layers on both substrates were transparent and completely covered the surface without any cracks or inhomogeneity. The analysis of the transmittance curves (see Fig. 1) for coatings on glass (Gls) substrates revealed layer thickness of 360 ± 10 nm and a refractive index of 1.54 ± 0.01 .

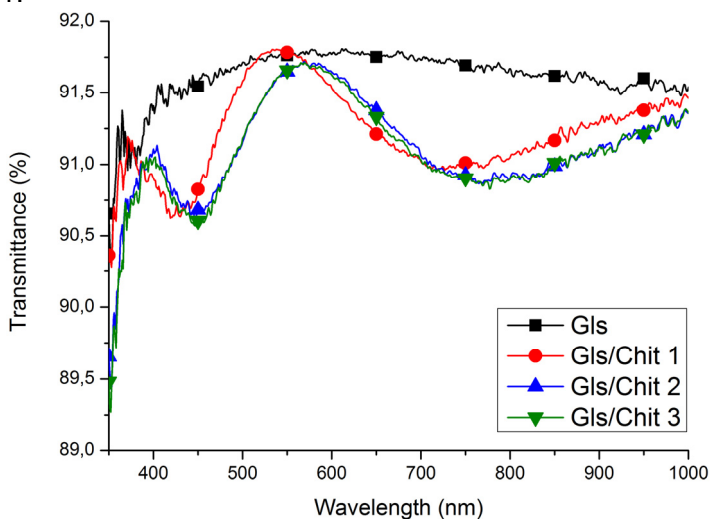


Figure 1. Transmittance spectra of the bare glass substrate and native coatings

AFM measurements

Fig. 2 shows the results of AFM measurements of the samples. The left image quartet shows the height (a) and phase image (b) of the bare glass substrate, and the height (c) and phase image (d) of the coated glass. The image quartet on the right is the same for the bare and coated zinc (Zn).

In the case of the bare glass substrate the surface irregularities are in the magnitude of 10 nm, while in the case of the much rougher Zn substrate there are height differences of 100 nm. The latter observation can be explained by the fact that the last step in the preparation of the metal substrates was polishing with 0.3 μm Al_2O_3 powder. It can be seen, that the surface properties of the substrates also influenced the morphology of the prepared coatings: the roughness of the chitosan layer formed on the Zn surface is an order of magnitude larger. In addition, a finer structure also appears in the coatings on Zn, which is presumably not due to the roughness of the substrate but a result of the chitosan's own structure.

Studying the phase images of the samples, it can be observed that in the case of the film prepared on glass substrate, the surface is smooth, but structurally inhomogeneous: the phase image shows brighter areas (islands with stronger physicochemical interactions, marked with black arrow) with a diameter of 1-2 μm . In contrast, the rougher surface on the Zn substrate has structural homogeneity. Presumably, the chitosan on the glass substrate separated into two domains with different surface properties before the gelation. A similar phenomenon was observed by Ye and Zao, who also reported in their paper the phase separation of a polymer layer [22]. It seems that the interactions between the molecules of the layer and the substrate greatly influence the structure and morphology of the final coatings.

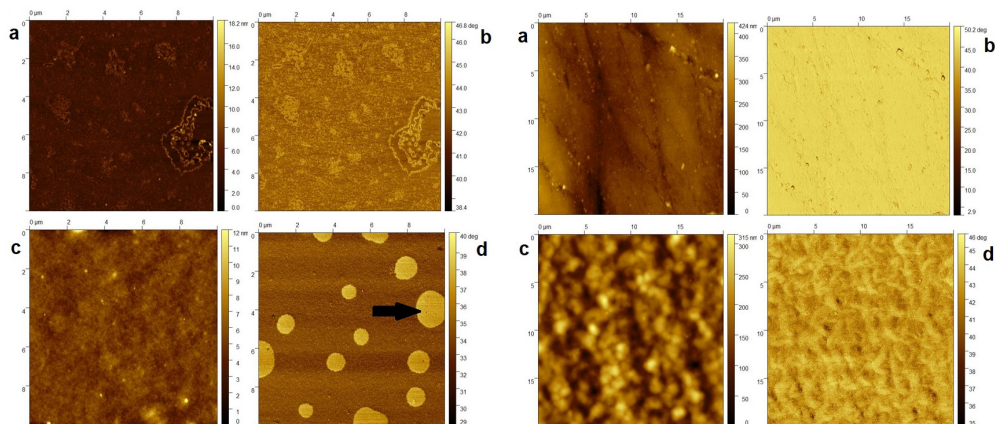


Figure 2. Results of AFM measurements: Height (a, c) and phase (b, d) images of bare (a, b) and coated (c, d) glass substrates (left) and the same for Zn substrates (right).

Wettability of the coatings

1. Native coatings

The values of the advancing and receding contact angles and the contact angle hysteresis measured on the different substrates for each measuring liquid are given in Table 1.

Table 1. Results of the wettability measurements of native coatings on both substrates (Θ_A : advancing contact angle, Θ_R : receding contact angle, H_θ : contact angle hysteresis)

Sample	Measuring liquid	Θ_A [°]	Θ_R [°]	H_θ [°]
Gls/Chit	Distilled water	71 ± 9	68 ± 9	4 ± 1
	0.2 g/L Na_2SO_4 solution	79 ± 1	57 ± 6	21 ± 5
Zn/Chit	0.2 g/L Na_2SO_4 solution	101 ± 8	74 ± 10	27 ± 8

For both cases significant contact angle hysteresis was found due to the chemical heterogeneity (21° , Gls/Chit) or the surface roughness (27° , Zn/Chit). Water contact angles, however, do not show significant hysteresis for samples Gls/Chit. Water is a better wetting agent than the aqueous salt solutions [23] and the quick penetration of water molecules into the layer can result in decreased surface microheterogeneity. However, it seems from the data, that this process manifests itself in a significant macroscopic heterogeneity demonstrated by a relatively high standard deviation of contact angle data (Table 1) and a significant deterioration of water contact angles on Gls/Chit during the investigated time period of 30 minutes (Fig. 3). Macroscopic heterogeneity was also observed with aqueous salt solutions for samples Zn/Chit but in that case the wetting stability of the chitosan layer was found to be much better (Fig. 3), which outlines the complexity of these processes.

In the case of Gls/Chit there is not much difference in the advancing contact angle values of the two measuring liquids, however, the value is below 90° in both cases, which indicates the hydrophilic nature of the surface. The contact angle hysteresis is low in the case of water, but much higher in the case of the Na_2SO_4 solution, so the surface has no water-repellent property. In the case of Zn/Chit, the advancing contact angle is well above 90° , but the hysteresis is also a high value, so the surface is hydrophobic, but does not show water-repellent effect.

The change in advancing contact angles over time is shown on Fig. 3. The results show that the contact angle on the coated Zn surface decreases very slowly below 90°, so it can be considered as a hydrophobic layer that is stable in time. However, in the case of the coated glass substrate the stability of the coating is poor, the contact angle decreases significantly over time.

The contact angle data help to interpret information obtained from the analysis of the AFM images (see Fig. 2). Knowing the measured contact angles on each surface, we can assume, that that the phase which produced a larger phase shift on the AFM images belongs to a more nonpolar structure, and on the Zn surface only that structure was formed. However, on the glass substrate a heterogeneous surface was formed (Fig. 2c) with smaller nonpolar domains (producing the same phase shift) surrounded by an area of presumably more polar character (producing a different, lower phase shift). These two phases together determine the wetting properties of the coating formed on glass. Knowing the value of the advancing contact angle of the Na₂SO₄ solution measured on the nonpolar surface (Zn/Chit), we can apply the Cassie-Baxter wetting model to determine the value of the advancing contact angle of the Na₂SO₄ solution on the polar phase formed on the glass substrate. The essence of the model is that on a heterogeneous surface consisting of areas with different wettability, the measurable contact angle can be calculated by a linear combination of the contact angles of each type of area [24].

$$\cos \theta_{obs} = f \cdot \cos \theta_1 + (1 - f) \cdot \cos \theta_2 \quad (1)$$

where θ_{obs} is the value of the observed contact angle (79°), θ_1 (101°) and θ_2 are the contact angles characterizing the nonpolar and polar domains of the surface, and f is the percentile area ratio of the nonpolar domains. This f parameter can be determined from the AFM phase images: 12%. The resulting contact angle value (θ_2) for the polar part of the surface is 76°. This is not a big difference from the measurable value but the presence of the nonpolar domains can cause significant contact angle hysteresis as was mentioned above.

Thus, it can be seen that coatings of the same material prepared with the same technique on the various surfaces show greatly different wettability behavior. This may be explained by the different chemical and physical nature of the Zn and glass substrates which can influence the structure (surface polarity) and morphology of the deposited layers.

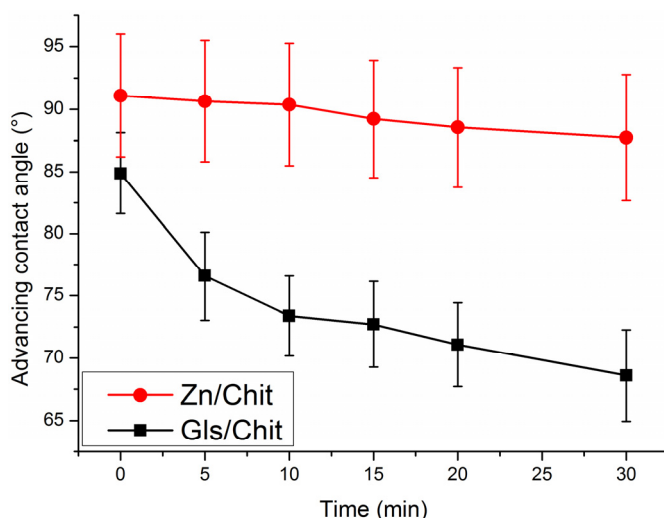


Figure 3. Change in advancing contact angle values over time for coatings on both substrates (In the case of glass substrates, the measurement was performed with distilled water, in the case of Zn substrates with 0.2 g/L Na_2SO_4 solution).

2. Silylated coatings

Preliminary investigations for the modified chitosan layers deposited on glass substrates

Fig. 4 shows the water droplet shapes and relating advancing contact angles on silylated chitosan coatings on glass substrates, measured 3, 5, 10, 20 and 40 seconds after the drop formation. For the native coating (Fig. 4a), the contact angles reach a relatively constant value (ca. 75°) after 10 s (also see Table 1). For the sample silylated without crosslinking (Fig. 4b), the contact angle initially exceeds 90° , but rapidly decreases below the value measured on the native coating. The same is observed for the coating crosslinked with pentasodium-tripolyphosphate (TPP), then silylated (Fig. 4c), but the decrease is smaller. However, the sample crosslinked with glutaraldehyde (GDA), then silylated (Fig. 4d) keeps a contact angle above 90° in the investigated 5-minute time range.

For interpreting the above observations, it should be taken into consideration that the silylation reaction with DCDMS produces HCl, which diffuses into the layer. When the droplet is placed onto the surface, in the aqueous medium the acid can protonate the free amino groups of chitosan forming a much more polar (i.e. hydrophilic) coating. In addition, the diffusion of the hydrophilic parts of the polymer chains to the surface become faster in

the aqueous medium (Fig. 4b). The crosslinkers, however, react with the amino groups of chitosan: TPP forms ionic bonds between the protonated amino groups in aqueous solution, and GDA is covalently bound to the nitrogen atoms. In both cases, the basicity of the amino groups decreases significantly, and the HCl is no longer able to protonate them, so that the contact angle does not decrease to the previously seen extent (Fig. 4c and d). In addition, crosslinking reduces the mobility of the polymer chains upon contact with the aqueous phase, therefore the hydrophobic silyl groups can stay on the surface while maintaining their effect. The results show that the covalently crosslinking agent (GDA) is better than the other one: temporal stability was only experienced for the case of GDA crosslinking (Fig. 4d).

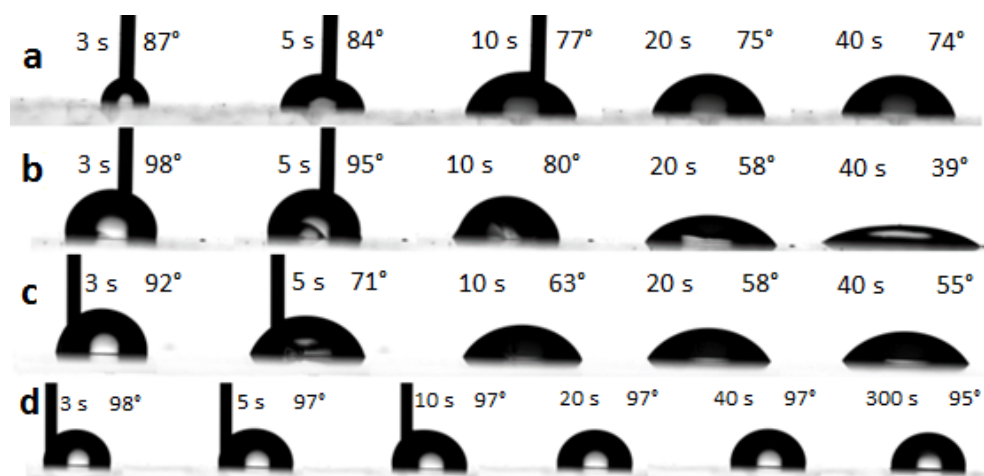


Figure 4. Water droplets on different surfaces: advancing contact angles at the indicated time after droplet formation (a: native chitosan, b: chitosan, silylated with DCDMS, c: chitosan, cross-linked with TPP, silylated with DCDMS d: chitosan, cross-linked with GDA, silylated with DCDMS)

Comparative investigation of the wetting properties of modified chitosan layers deposited on glass and Zn substrates

The advancing and receding water and Na₂SO₄ solution contact angles measured for the GDA-crosslinked and DCDMS-modified samples on glass (Gls/Chit-GDA-Silyl) and Zn substrates (Zn/Chit-GDA-Silyl) are shown in Table 2. All samples were silylated in the vapour phase of the n-hexane solution of DCDMS. Comparing the data in Tables 1 and 2, it can be observed that in the case of Gls/Chit-GDA-Silyl, the silylation improved the water-repellent

properties of the coating: the water contact angle is above 90° and the value of the hysteresis is very small, which means that the surface is hydrophobic and water-repellent. The water contact angles show a relatively good stability in the investigated time range (Fig. 5a). It is important to note, however, that the samples lose their advantageous properties by soaking them for 10 minutes in water: the value of the water contact angles decrease below the values measured on the native chitosan. However, the silylation improved the wettability of the chitosan layer on the Zn substrate compared to the wettability of the native chitosan layer, and the wetting stability also deteriorated (Fig. 5b). Interestingly, by increasing the time of silylation the resulting water contact angles will be even smaller (Fig. 5b).

The different behaviour of chitosan coatings on the glass and Zn substrates during the cross-linking and silylation processes can be attributed to the different polarity of the pertinent native coatings. During the cross-linking process the hydrophilicity of the native coatings on glass can further increase due to the chemisorption of GDA [8]. Furthermore, as this process is carried out in aqueous phase, the reorientation of the polymer segments is facilitated and this results in the increase of the surface concentration of hydroxyl groups. The efficiency of the silylation can be attributed to the latter process. The reorientation process is presumably hindered for coatings on Zn substrates due to the hydrophobic character of the surface. Water molecules cannot penetrate the outside of the layer fast enough and so the mobility of the polymer segments is lower. Hence, in this case the surface polarity increase can only happen due to chemisorption of GDA.

Table 2. Wettability results of coatings cross-linked with GDA and silylated with DCDMS under various conditions (*after 10 min swelling in distilled water and drying) (Θ_A : advancing contact angle, Θ_R : receding contact angle, H_Θ : contact angle hysteresis)

Sample	Silylation time	Θ_A [°]	Θ_R [°]	H_Θ [°]
Gls/Chit-GDA-Silyl	30 min	97 ± 1	95 ± 3	2 ± 2
		$48 \pm 2^*$	$31 \pm 8^*$	$16 \pm 6^*$
Zn/Chit-GDA-Silyl	5 min	77 ± 15	57 ± 24	20 ± 13
	10 min	64 ± 10	47 ± 13	23 ± 5

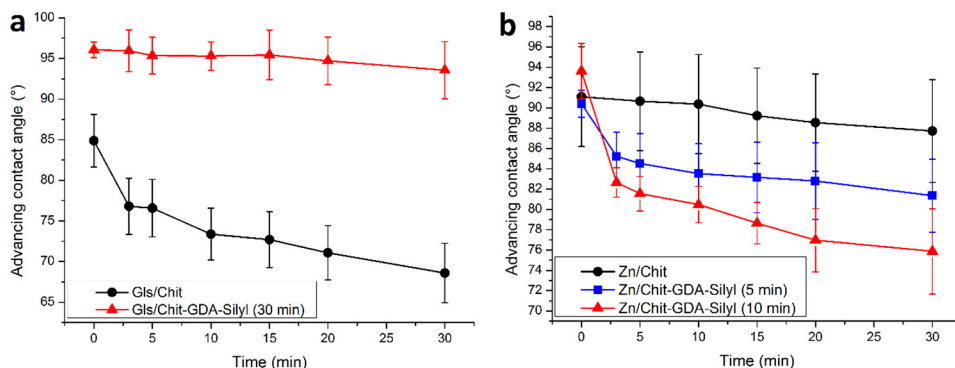


Figure 5. Advancing contact angle values measured in time for chemically modified (cross-linked with GDA and silylated with DCDMS) coatings on glass (a) and Zn (b) substrates. (In the case of glass substrates, the measurement was performed with distilled water, in the case of Zn substrates with 0.2 g/L Na₂SO₄ solution).

Electrochemical measurements of the coatings

The linear and semi-logarithmic polarization curves for the investigated samples are represented in Fig. 6.

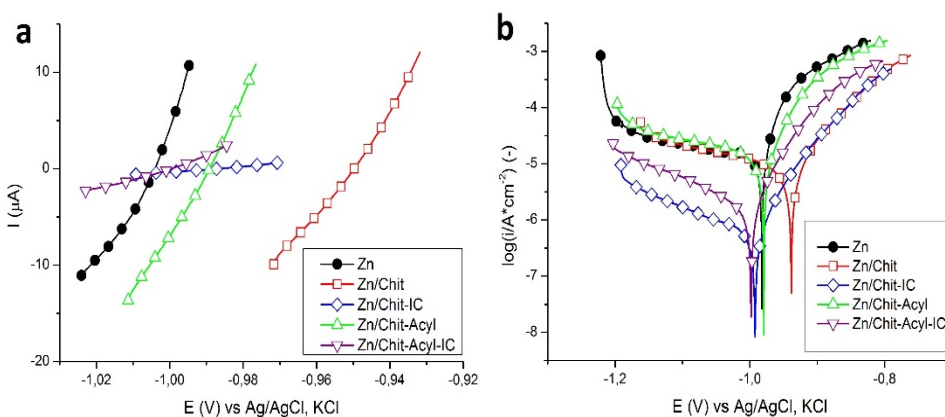


Figure 6. Linear (a) and semi-logarithmic (b) polarization curves for the bare Zn and the coated samples

In the Table 3. are introduced the OCP, the slopes of the fitted straight lines to the linear polarization curves and the calculated polarization resistance R_p . This is the inverse value of the straight line's slope, that was fitted to the linear portion of the curves. Further characteristics of the layers

like pseudo-porosity (P) can be calculated from the obtained data, using the following formula, assuming that the layer is electrochemically inert at low overpotentials [25]:

$$P = \frac{R_{ps}}{R_p} \cdot 10^{-\left(\frac{|\Delta E_{corr}|}{b_a}\right)} \cdot 100 (\%) \quad (2)$$

The R_{ps} and R_p represent the polarization resistance of the bare Zn substrate and the coated Zn, respectively, while ΔE_{corr} symbolizes the difference between the potential of the coated and uncoated samples, and b_a is the anodic Tafel coefficient of the bare substrate.

Table 3. The polarization resistance R_p : determined from the linear polarization curves recorded for the bare Zn and the coated samples. B represents the slope of the fitted line, R^2 the coefficient of determination, N the number of the points, OCP the open circuit potential and P the pseudo-porosity

Sample	R^2 [-]	N [-]	$10^4 \cdot B$ [1/ Ω]	R_p [Ω]	P [%]	OCP [V]
Zn	0.999	25	7.31	1368	-	-0.987
Zn/Chit	0.999	27	4.67	2141	44	-0.944
Zn/Chit-IC	0.999	33	0.28	35714	4	-0.977
Zn/Chit-Acyl	0.999	27	6.56	1524	88	-0.973
Zn/Chit-Acyl-IC	0.998	23	1.63	6135	19	-0.999

If the value of the polarization resistance is high, the coating has a good anti-corrosion property. Vice versa if it is low, protective property of the coating is poor. As one can see from Table 3, the highest corrosion resistance R_p is attributed to the Chit-IC layer, indicating the best anti-corrosion effect. The corrosion current densities are proportional to the corrosion rate, which means that this value is low in the case of a good protective coating. In Table 4 the lowest value is attributed to the Chit-IC coating, this has the best anticorrosion property, which is in a very good agreement with the R_p obtained for this layer from the linear polarization.

The low porosity of the Chit-IC coating is correlated with a relatively denser texture.

Table 4. Polarization parameters obtained by Tafel interpretation of the semi-logarithmic polarization curves: i_{corr} : corrosion current density, E_{corr} corrosion potential, b_a and b_c anodic and cathodic Tafel coefficients. IE represent the inhibition efficiency

Sample	i_{corr} [$\mu\text{A}/\text{cm}^2$]	E_{corr} [V]	b_a [V/dec]	b_c [V/dec]	IE [%]
Zn	8.945	-0.982	0.272	0.029	-
Zn/Chit	5.667	-0.939	0.144	0.057	36.6
Zn/Chit-IC	0.388	-0.992	0.040	0.105	95.7
Zn/Chit-Acyl	7.064	-0.979	0.036	0.097	21.0
Zn/Chit-Acyl-IC	0.688	-0.999	0.067	0.209	92.3

For the calculation of the inhibition efficiency (IE) formula (3) is used:

$$IE = \frac{i_{corr}^s - i_{corr}}{i_{corr}^s} \cdot 100 \quad (3)$$

where i_{corr}^s and i_{corr} are the corrosion current densities of the Zn substrate and the coated sample, respectively. From the IE value calculated for the native chitosan (Chit) coating, 36,6%, it can be deduced that the native chitosan layer has a very poor anti-corrosion effect. In the case of IC impregnated chitosan coating (Chit-IC) the corrosion current density decreased with one order of magnitude while the IE increase significantly (95,7%). This means that this kind of coating has a good anti-corrosion property. The acylation of both the native Chit and Chit-IC causes the decay of the anti-corrosion properties, namely the increase of the corrosion current density and the decrease of the IE. Although in the case of the acylated, impregnated chitosan coating (Chit-Acyl-IC) the i_{corr} is better than in the case of native chitosan, still the Chit-IC has the best IE.

Considering also the calculated pseudo-porosity values from Table 3, one can say that this kind of difference in behavior is due to the permeability of the thin layers. It can be seen, that the Chit-IC has the smallest porosity and for this reason has the best anti-corrosion property. The increasing order of the porosity in case of the other coatings is Chit-Acyl-IC, Chit and at last the Chit-Acyl with a very high value (88%).

The explanation of this phenomenon lays in the structure of the coatings. The IC molecules contain negatively charged groups and can cross-link the chitosan, forming ionic bonds with the protonated amino groups. The layer formed in this way has a reduced permeability. By acylation, the number

of the amino groups that can be protonated is significantly reduced, subsequently the extent of the crosslinked portions are reduced too and the permeability against the corrosive environment is increased. In this way the anti-corrosion properties of the coating are diminished. It can be assumed, that as a consequence of the acylation H bonds also cannot be formed between the amino groups. This could be the reason why the acylated coating protection is worse than even that of the native chitosan. The sterical effect of the acyl-groups can also be the cause of weaker structure formation. The acylating reaction conditions can induce the damage of the materials.

CONCLUSIONS

Wetting and electrochemical properties of chemically modified chitosan coatings prepared on glass and zinc substrates were investigated. The purpose of the research was to develop a water-repellent and corrosion protective polymer layer.

Wettability studies of native coatings have shown that the chitosan layer prepared on glass substrate is hydrophilic and unstable in time, while on the zinc substrate a highly hydrophobic and stable in time but non-water-repellent coating is formed under the same conditions. AFM analysis of the layers detected surfaces with different morphologies and signs of phase separation of chitosan on the glass substrate.

Examination of the wettability of the silylated coatings revealed that of the systems studied, only the samples crosslinked with GDA and then chemically modified with DCDMS provided a surface with satisfactory properties. In this way, a coating with hydrophobic and water-repellent properties, which is very stable in time, has been produced on a glass substrate, however, on zinc substrates the silylation greatly deteriorates the properties of the originally hydrophobic layer.

Electrochemical studies have shown that among the chemical modification methods studied, impregnation with IC improves the anti-corrosion effect of chitosan coatings which is explained by the cross-linking effect of IC. The acylation, however, greatly diminished the corrosion protection by increasing the pseudo-porosity of the coatings.

EXPERIMENTAL SECTION

MilliQ water (Millipore Simplicity 185, Resistance: 18,2 MΩcm); sulfuric acid (Carlo Erba, 96%, f. a.); isopropanol (Reanal Labor, 99,7%, f. a.); acetic acid (Lachner, 99,8% f. a.); chitosan (Sigma-Aldrich, Medium molecular weight, Viscosity: 598 cP); glutaraldehyde (Reanal Labor, 25%, purum);

pentasodium-tripolyphosphate-pentahydrate (Sigma-Aldrich, $\geq 98\%$, purum); dichlorodimethylsilane (Reanal Labor, $\geq 99\%$, f. a.); n-hexane (Merck, 95%, f. a.); indigo carmine (Reanal Labor, f. a.); acetic anhydride (Reanal, f. a.); methanol (Molar Chemicals Kft.).

The coatings were prepared on glass microscope slides (Menzel-Gläser) and zinc plates (Bronzker Bt.) with a dip coater made by Plósz Engineering Ltd.

Coatings preparation

The glass substrates were cleaned using aqueous detergent solution, 10% (w/w) sulfuric acid, isopropanol and MilliQ water. The Zn substrates were polished with emery paper (P1200, P2000, and P3000) and Al_2O_3 powder (particle size: 0,3 μm). Then they were washed with isopropanol and MilliQ water and ultrasonicated for 10 min to remove any powder residue. Before the dip-coating, 0.1 M HCl solution was used to clean the surface of any remaining zinc-oxide.

The dip-coating was performed with a withdrawal speed of 5 cm/min from 1% (w/w) chitosan solution. The chitosan was dissolved in 1% (v/v) acetic acid solution, stirred for 24 hours, then centrifuged (30 min, 4000 rpm) to remove any insoluble chitosan residue due to imperfect deacetylation. The prepared coatings were dried overnight at room temperature.

Chemical modification of the coatings

Some samples were chemically modified by acylation and/or impregnation with IC. Other samples were modified by cross-linking agents and/or silylation.

The acylation of the coatings was carried out in 10% (v/v) methanol-based acetic anhydride solution for 60 min. Afterwards, the samples were washed with methanol and dried at room temperature.

The impregnation was performed using the dip-coater: the samples were immersed in 0.01 M IC solution with 10 cm/min immersion speed, kept in the solution for 15 min, then withdrawn with 10 cm/min.

Two different cross-linking agents (covalent, ionic) were tried. The coatings on glass substrates were covalently cross-linked in 5% (w/w) aqueous glutaraldehyde solution for 5 min, while the coatings on Zn substrates were cross-linked in 1% (w/w) glutaraldehyde solution for 30 min, because the more concentrated solution damaged the coating on Zn. The ionic cross-linking by pentasodium-tripolyphosphate took place in a 3% (w/w) aqueous solution for 10 min. Then the samples were washed with distilled water and dried at room temperature.

For the silylation reaction the samples were kept in a desiccator. The silylating agent was an n-hexane solution of dichlorodimethylsilane. For the samples on glass 10% (w/w) solution and a reaction time of 30 min were used; while for the samples on Zn 5% (w/w) n-hexane solution with reaction times of 5 and 10 min were used. Afterwards, the samples were kept at room temperature in air for 10 min to remove any left-over reagent.

Transmittance measurements

The layer thickness and refractive index values of the coatings on glass substrates were determined by a thin-layer optical model [26] fitted to the transmittance spectra. The transmittance was measured using an Analytik Jena Specord 200 UV-Vis spectrophotometer in the 350-900 nm wavelength range with 1 nm resolution and a measurement speed of 10 nm/s.

AFM measurements

To explore surface properties, the samples were measured with an AIST-NT SmartSPM 1000 AFM device in tapping mode with a PPP-NCHR-20 needle made by NanoSensors (nominal radius of the needle <20 nm). In the range of 10×10 and 20×20 μm a height and phase image of the surfaces were recorded.

Wettability measurements

Contact angle measurements were performed on the native and on the silylated coatings deposited on glass and Zn substrates to get information about the effect of chemical modification on the surface polarity. The measurements were carried out with 0.2 g/L aqueous Na₂SO₄ solution, which was also used as electrolyte during electrochemical investigations. MilliQ water was also used for the characterization of coatings deposited on glass substrates. Wettability was studied by a Drop Shape Analysis System (DSA30, Krüss GmbH). Advancing contact angles were measured by the sessile drop method by the drop-build up technique at 25 °C and 90% humidity within the first minute after the droplet formation (20 μl). Then receding contact angles were also measured after removing ca. half the volume of the droplet. Contact angle hysteresis was determined as the difference of the advancing and receding angles. In certain cases, the advancing contact angles of 20 μl droplets were studied during a 30-minute time interval in order to characterize the stability of coatings. On some selected samples the contact angle values were determined after they were soaked in distilled water for 10 min and then dried.

Electrochemical measurements

The corrosion resistance of the coatings was investigated in an undivided electrochemical cell containing three electrodes, connected to the Metrohm Autolab PGSTAT 301N potentiostat. The coated Zn samples were used as working electrode, with a 2 cm² active surface area, while the Platinum wire and the Ag/AgCl, KCl (saturated) were the counter and the reference electrode, respectively. The aggressive environment consisted of a Na₂SO₄ solution with 0.2 g/L concentration. All measurements were carried out at room temperature.

First, for each sample the open circuit potential (OCP) was determined, and every measurement lasted for 60 min. The potentiodynamic polarization was performed in a potential range of OCP±20 mV and OCP±200 mV vs Ag/AgCl, KCl(saturated) electrode and the obtained curves were recorded with 0.166 mV/s rate. By Tafel interpretation of the semi-logarithmic polarization curves, namely by fitting straight lines to the anodic and cathodic branches, kinetic parameters (corrosion current densities, corrosion potentials, Tafel coefficients) were determined.

ACKNOWLEDGMENTS

The research reported in this paper was supported by the BME Nanotechnology and Materials Science TKP2020 IE grant of NKFIH Hungary (BME IE-NAT TKP2020). The research work has been accomplished in the framework of the "BME R+D+I project", supported by the grant TÁMOP 4.2.1/B-09/1/KMR-2010–0002. NRDI TNN-123631, NRDI K-128266, and NRDI FK-128901 grants are acknowledged. Emőke Albert's research work was supported by the European Union and the State of Hungary, co-financed by the European Social Fund in the framework of TÁMOP-4.2.4.A/2–11/1–2012–0001 "National Excellence Program"

REFERENCES

1. Z. Sebestyén, E. Jakab, A. Domán, P. Bokrossy, I. Bertóti, J. Madarász, K. László, *J. Therm. Anal. Calorim.* **2020**, 1-8.
2. B. Duan, Y. Huang, A. Lu, L. Zhang, *Prog. Polym. Sci.* **2018**, *82*, 1–33.
3. S. Kumari, S.H. Kumar Annamareddy, S. Abanti, P. Kumar Rath, *Int. J. Biol. Macromol.* **2017**, *104* 1697–1705.

4. S. Tripathi, G.K. Mehrotra, P.K. Dutta, *Int. J. Biol. Macromol.* **2009**, *45*, 372–376.
5. T. Dai, M. Tanaka, Y.Y. Huang, M.R. Hamblin, *Expert Rev. Anti. Infect. Ther.* **2011**, *9* 857–879.
6. P.L. Kashyap, X. Xiang, P. Heiden, *Int. J. Biol. Macromol.* **2015**, *77*, 36–51
7. T. V. Podust, T. V. Kulik, B.B. Palyanytsya, V.M. Gun'Ko, A. Tóth, L. Mikhalovska, A. Menyhárd, K. László, *Appl. Surf. Sci.* **2014**, *320*, 563–569.
8. M. Dabóczy, E. Albert, E. Agócs, M. Kabai-Faix, Z. Hórvölgyi, *Carbohydr. Polym.* **2016**, *136*, 137–145.
9. C. Liu, Q. Bi, A. Leyland, A. Matthews, *Corros. Sci.* **2003**, *45*, 1257–1273
10. M.L. Zheludkevich, J. Tedim, C.S.R. Freire, S.C.M. Fernandes, S. Kallip, A. Lisenkov, A. Gandini, M.G.S. Ferreira, *J. Mater. Chem.* **2011**, *21*, 4805–4812.
11. Á.F. Szőke, G.S. Szabó, Z. Hórvölgyi, E. Albert, L. Gaina, L.M. Muresan, *Carbohydr. Polym.* **2019**, *215*, 63–72.
12. O. Lundvall, M. Gulppi, M.A. Paez, E. Gonzalez, J.H. Zagal, J. Pavez, G.E. Thompson, *Surf. Coatings Technol.* **2007**, *201* 5973–5978.
13. S.A. Moren, M.J. Banera, T. Alonso-Garcia, C.A. Gervasi, M. V. Mirifico, *Cellulose*, **2013**, *20* 2529–2545.
14. Á.F. Szőke; G. Szabó; Z. Simó; Z. Hórvölgyi; E. Albert; A.G. Végh; L. Zimányi; L.M. Muresan; *Eur. Polym. J.*, **2019**, *118*, 205–212.
15. J. Redepenning; G. Venkataraman; J. Chen; N. Stafford; *J. Biomed. Mater. Res. - Part A.*, **2003**, *66*, 411–416.
16. J. Carneiro; J. Tedim; S.C.M. Fernandes; C.S.R. Freire; A. Gandini; M.G.S. Ferreira; M.L. Zheludkevich; *ECS Electrochem. Lett.*, **2013**, *2*, C19.
17. K. Kurita, M. Hirakawa, S. Kikuchi, H. Yamanaka, J. Yang, *Carbohydr. Polym.* **2004**, *56*, 333–337.
18. A. Tiwari, *J. Inorg. Organomet. Polym. Mater.* **2009**, *19*, 361–366.
19. S. Höhne, R. Frenzel, A. Heppe, F. Simon, *Biomacromolecules*. **2007**, *8*, 2051–2058.
20. J. Xu, S.P. McCarthy, R.A. Gross, D.L. Kaplan, *Macromolecules*. **1996**, *29*, 3436–3440.
21. K.Y. Lee, W.S. Ha, W.H. Park, *Biomaterials*. **1995**, *16*, 1211–1216.
22. Z. Ye, X. Zhao, *J. Microsc.* **2010**, *238*, 27–35.
23. Z. Hórvölgyi, M. Máté, M. Zrínyi, *Colloids Surfaces A Physicochem. Eng. Asp.* **1994**, *84*, 207–216.
24. E. Bormashenko, *Colloids Surfaces A Physicochem. Eng. Asp.* **2008**, *324*, 47–50.
25. B. Matthes, E. Broszeit, J. Aromaa, H. Ronkainen, S.P. Hannula, A. Leyland, A. Matthews, *Surf. Coatings Technol.* **1991**, *49*, 489–495.
26. E. Hild, A. Deák, L. Naszályi, Ö. Sepsi, N. Ábrahám, Z. Hórvölgyi, *J. Opt. A Pure Appl. Opt.* **2007**, *9*, 920–930.

ESTIMATION OF THE USEFULNESS OF GLASSY CARBON ELECTRODE IN NON-AQUEOUS SOLVENTS POLARIZED TO HIGHER ANODIC POTENTIALS

LÁSZLÓ KISS^{a,b*}, SÁNDOR KUNSÁGI-MÁTÉ^c

ABSTRACT. In this paper suitability of glassy carbon electrode in numerous non-aqueous solvents used widely in electrochemistry (methanol, acetone, dichloromethane, nitrobenzene, nitromethane, 1-butanol, dimethyl sulfoxide, dimethyl formamide, tetrahydrofuran) was studied by changing the potential of preanodisation. The potential range studied in viewpoint of preanodisation effect was between 1 and 3 V. At higher potentials, glassy carbon electrode deactivated in many solvents which was clearly demonstrated using the aqueous solution of a redox probe 1,4-dihydroxybenzene. Due to the low permittivity some solvents (ethyl acetate, chloroform) were investigated using a preanodisation at 3 V because of the significant ohmic drop and the surface state also changed. Results highlight the importance of this limitation caused by polarizing above 2 V and it must be considered when glassy carbon electrode is selected for the investigations carried out in these conditions.

Keywords: *Glassy carbon; Preanodisation; Permittivity; Deactivation; Non-aqueous solvents*

INTRODUCTION

During electrochemical studies of selected compounds in solution phase reproducibility of their voltammetric peak associated with each individual cycle helps to decide if it fouls the electrode or not. Usually when the voltammetric peaks decline continuously or rapidly the conclusion is that a fouling process takes place. In certain conditions both the electrode material

^a *University of Pécs, Department of General and Physical Chemistry, Ifjúság street 6, H-7624 Pécs, Hungary*

^b *János Szentágothai Research Center, Ifjúság útja 20, Pécs H-7624, Hungary*

^c *University of Pécs, Department of Organic and Pharmacological Chemistry, Honvéd street 1, Pécs H-7624, Hungary*

* *Corresponding author: kissl@gamma.ttk.pte.hu*

and solvent may affect the reproducibility of measurements. Recently, we found that electrochemical behavior of *N,N'*-diphenylguanidine can be very different depending on the solvent used [1]. In the electrochemical studies, many solvents are used which can provide an appropriate medium for the investigation of selected material or process. Many solvents prone to oxidation or reduction according to their chemical nature and estimation of usefulness of electrodes prepared from different materials is an essential information. Glassy carbon electrode has various properties which can affect its behavior in different electrolyte media during its use in electrochemistry. Usually, the surface of the glassy carbon electrode is covered by phenolic hydroxy groups and quinone moieties being capable for chemical modifications. The disturbance of certain components might cause undesired changes in the surface state. Contrarily, the modified glassy carbon surface in special conditions has advantageous properties which gained wide application in electroanalytical chemistry. The number of surface functional groups can be multiplied by several activation procedures which has been used for several decades to alter the surface properties favourable in improvement for analytical properties. There are recent developments also for activation of glassy carbon electrode [2-10].

In our earlier investigations glassy carbon electrode was studied in two solvents. Acetonitrile proved unreliable by polarizing this electrode to potentials higher than 2 V vs. Ag wire which was highlighted by investigating phenols [11]. In acetonitrile on platinum electrode at very high potentials a remarkable decrease of currents showed formation of products blocking the surface [12]. In the same conditions electrooxidation of some para-substituted phenols was studied on platinum electrode and reproducible voltammograms could be obtained. Therefore, platinum electrode is appropriate as standard if we want to exclude everything apart from the electropolymerization of the substrate indicated by the decline of the voltammetric peaks. In another work mesityl oxide was studied and it fouled strongly the surface of glassy carbon electrode since it could be electropolymerized [13]. Mesityl oxide showed also that the choice of electrode might strongly influence the structure and sometimes composition of polyphenol films. Electrooxidation of mesityl oxide also itself resulted in surface deactivation of glassy carbon electrode.

In this work, a large number of non-aqueous solvents were tested in conditions when polarization of glassy carbon electrode to higher anodic potentials is applied. The electrooxidation of several organic materials generates radicals which can be bound to the surface functional groups presenting on the surface of this type of electrode. Investigations focused on how these conditions affect the measurement of an appropriate redox probe considering the modified electrode's surface state.

RESULTS AND DISCUSSION

In order to assess the effect of preanodisation in the different solvents on the reliability of glassy carbon electrode in giving reproducible current signals the anodic potential was changed between 1 and 3 V in 0.5 V increments with duration of 10 s in their solutions containing 0.1 M tetrabutylammonium perchlorate (TBAP) supporting electrolyte. With the pretreated electrode in this way cyclic voltammograms were recorded between 0 and 1 V in the aqueous solution of 10 mM 1,4-dihydroxybenzene. This compound gives reproducible current signals on the commonly used electrodes while it oxidizes to *p*-benzoquinone in a $2e^-/2H^+$ reaction. The ratios of peak current measured with the pretreated electrode and of peak current measured with the bare electrode were used for the evaluation. Data were collected for each solvents and at the different anodic pretreatment potentials. The electrode surface was renewed before all pretreatments according to the procedure described in the Experimental section. The normalized peak currents are displayed in Fig. 1. The figure is divided into two (a and b) parts to see more clearly the effect of the numerous solvents.

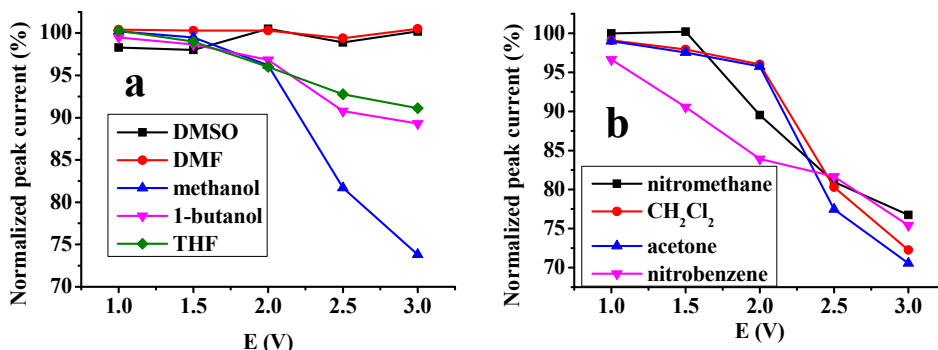


Figure 1. Normalized peak currents for aqueous solution of 10 mM 1,4-dihydroxybenzene after 10 s preanodisation at potentials ranging from 1 to 3 V in the different solvents (supporting electrolyte 0.1 M pH=7 phosphate buffer, scan rate 0.1 V/s)

Dimethyl sulfoxide (DMSO) and dimethyl formamide (DMF) are susceptible to oxidation compared with the other solvents. Due to this fact their use is limited to mildly anodic potentials as they start to react below 2 V by using the commonly used electrodes [14]. Therefore, application of these solvents at high potentials has low interest. Despite of their usefulness in these conditions the effect of pretreatment potential was investigated up to 3

V. Peak currents after the anodic pretreatments were identical to the value with subtle differences measured with the untreated electrode showing that glassy carbon surface does not change during the polarisation.

Alcohols can also serve as solvent especially the ones having larger molecular weight as their background currents are low according to our earlier findings obtained by investigation of phenol in solutions prepared with alcohol solvents [15]. Methanol produces significant currents above 1.5 V and therefore the electrochemical investigation of compounds seems very limited in this solvent. Moreover, glassy carbon surface deactivated remarkably by increasing the pretreatment potential. Increasing the molecular weight of alcohols, they start to oxidize at more and more positive potentials mainly due to the decrease of their dielectric constant. 1-butanol has broader potential window for experiments partly due to the lower dielectric constant. This property therefore resulted in lower current flows during the preanodisation steps compared to that measured in methanol. The normalized peak currents indicate electrode deactivation which however is smaller than in case of methanol. In presence of trace amount of water alcohols undergo predominantly oxidative dehydrogenation and the electrooxidation of produced aldehydes leads to the undesired surface modification which is faster in methanol.

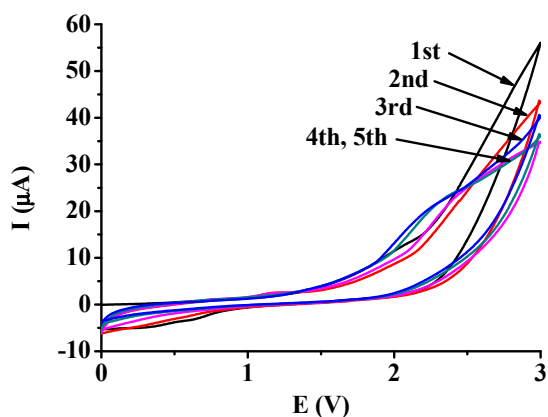


Figure 2. Voltammetric scans in nitrobenzene with glassy carbon electrode (supporting electrolyte 0.1 M TBAP, scan rate 0.1 V/s)

Nitrocompounds are not widespread in studying redox active compounds except for nitrobenzene which is used sometimes in electrochemistry. One of the possible reasons is its high toxicity. On the other hand, it has many advantages like high dielectric constant ($\epsilon=35.6$ [16]), inertness towards oxidation at moderate anodic potentials, therefore the wide potential window

ESTIMATION OF THE USEFULNESS OF GLASSY CARBON ELECTRODE IN NON-AQUEOUS SOLVENTS POLARIZED TO HIGHER ANODIC POTENTIALS

in the anodic part offers wide applicability of this solvent. Additional limitations come from the lower solubility of a large number of analytes. The data show that glassy carbon electrode strongly passivates increasing the pretreatment potential in both nitrobenzene and in nitromethane. Fig. 2 displays additional curves of further cyclic voltammetric experiments conducted in nitrobenzene. It clearly shows also the deactivation process during the repeated voltammetric cycles. For making the fouling process deeper the potential of glassy carbon electrode was kept at 3 V for 60 s in nitrobenzene. According to the expectations peak current of 1,4-dihydroxybenzene in its aqueous solution was reduced to 45.78 %. For comparison the curves are displayed in Fig. 3. Interestingly, the anodic peak potential for oxidation of the redox probe was significantly smaller and cathodic potential shifted significantly to the positive direction suggesting some electrocatalytic behaviour of pretreated electrode but tortuosity effect is very significant seen from the drastically reduced peak currents. Therefore, the highly increased mass transport resistance leads to diminished analytical signals. The cathodic peak current was significantly higher indicating that the deposited layer has binding sites being favourable for adsorption of *p*-benzoquinone which is the oxidation product of the redox probe. Nitromethane contains a methyl group being able to oxidize at appropriately high potentials followed by the formation of a nitromethyl radical. They may interact with the surface hydroxy groups of glassy carbon so they can be bound covalently to the surface. The rate of surface coverage increases in the presence of these groups by increasing the pretreatment potential and then, a large number of redox active molecules can not reach the electrode surface.

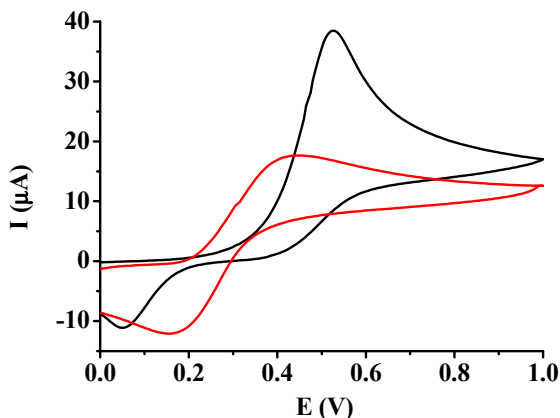


Figure 3. Voltammetric curves of 10 mM 1,4-dihydroxybenzene with bare glassy carbon (black curve) and with the same preanodized electrode in nitrobenzene at 3 V (red curve) (supporting electrolyte 0.1 M pH=7 phosphate buffer, scan rate 0.1 V/s)

Acetone is not used widely as solvent in electrochemistry in contrast to its potential window which might be exploited as its oxidation starts around 2 V and the favourable permittivity allows relatively small ohmic potential drop. Its high volatility is very disadvantageous by the majority of applications in electrochemistry. Anodic polarization causes surface alteration as this solvent oxidizes on its methyl groups and the formed radicals can couple with each other forming oligomers and also can bound to the surface hydroxy groups but the latter process is responsible for the electrode destroying.

Tetrahydrofuran (THF) is also a very volatile liquid, moreover has a very low permittivity, therefore insufficient for the dissolving of salts. Moreover, the ohmic drop is significant so these properties make it unpopular as solvent for electrochemists. It is used widely as aprotic solvent and co-solvent in characterization of chemical processes mainly with spectroscopic methods. The results obtained with preanodisation in tetrahydrofuran show that use of glassy carbon would be limited also to the lower potentials.

Dichloromethane has a broad interest in the electrochemical investigations therefore effect of anodic potential during pretreatment in it might provide worthy information. The peak currents of redox probe indicate a remarkable decrease by increasing the pretreatment potential. The reason for that might be the oxidative cleavage of C-H bonds and the subsequent radical formation can result chlorocarbons through their recombination and bound to the surface. The latter process enhances the surface resistivity therefore charge transfer reactions become inhibited.

There are low permittivity solvents used rarely as solvents in electrochemistry like ethyl acetate and chloroform only in combination with microelectrodes [17,18]. Therefore, it seems difficult to access their usefulness in their own liquid phase due to the very high degree of ionic association of supporting electrolyte. In case of these two solvents 60 s polarization was carried out at a constant potential 3 V. Then the voltammograms recorded respectively in the aqueous solution of model compound were used for the estimation of surface deactivation. In ethyl acetate the peak current declined to 63.6 % and in chloroform 64.2 % and showed that the polarisation to 3 V can lead to visible changes.

CONCLUSION

Numerous non-aqueous solvents were examined according to their different effects on the electrochemical behavior measured by cyclic voltammetry. It was found that they deactivate the surface of glassy carbon electrode and the limitations are revealed in cases when this electrode is selected for the

corresponding investigations. Nitrobenzene provided surprising findings as new layers can be prepared based on it giving alternatives for future investigations of modified electrodes. On the other hand, the investigation of other carbon based electrodes would be interesting regarding the effect of anodic pretreatment.

EXPERIMENTAL

For the electrochemical investigations analytical grade solvents were used. The supporting electrolyte was tetrabutylammonium perchlorate in the non-aqueous solvents and in aqueous solvents pH=7 phosphate buffer was used. The used non-aqueous solvents had low moisture content. In all electrochemical experiments the working electrode was a glassy carbon disc sealed in polyetheretherketone (1 mm in diameter) and a Pt wire served as counter electrode. Saturated calomel electrode was used as reference in aqueous solutions. The equipment used for the electrochemical experiments was a potentiostat (Dropsens, Spain).

The surface of glassy carbon electrode was sanded off with 4000 grit emery paper and then polished with 1 and 0.05 μm alumina slurry on a polishing cloth. Finally, it was thoroughly washed with twice deionized water. To minimize the introduction of water into the electrochemical cell the electrodes were thoroughly rinsed with dry acetone and allowed to dry completely.

ACKNOWLEDGEMENTS

Financial support of the GINOP 2.3.2-15-2016-00022 grant is highly appreciated.

REFERENCES

1. L. Kiss, F. Kovács, S. Kunsági-Máté, *Periodica Polytechnica Chemical Engineering*, <https://doi.org/10.3311/Ppch.14959>.
2. A.M. Abdel-Aziz, H.H. Hassan, I.H.A. Badr, *Analytical Chemistry*, **2020**, *92*, 7947.
3. A. Dekanski, J. Stevanovic, R. Stevanovic, B.Z. Nikolic, V.M. Jovanovic, *Carbon*, **2001**, *39*, 1195.
4. B. Farajmand, M.A. Kamyabi, F.Y. Sorkhani, H.S. Jam, H. Bahrami, *Journal of Electroanalytical Chemistry*, **2020**, *861*, DOI: 10.1016/j.jelechem.2020.113966.

5. Y.W. Li, J. Zhou, J. Song, X.S. Liang, Z.P. Zhang, D. Men, D.B. Wang, X.E. Zhang, *Biosensors & Bioelectronics*, **2019**, *144*, DOI: 10.1016/j.bios.2019.111534.
6. L.Y. Wang, Y. Wang, Q.F. Zhuang, *Journal of Electroanalytical Chemistry*, **2019**, *851*, DOI: 10.1016/j.jelechem.2019.113446.
7. T. Bystron, E. Sramkova, F. Dvorak, K. Bouzek, *Electrochimica Acta*, **2019**, *299*, 963.
8. S. Berto, L. Carena, F. Valmacco, C. Barolo, E. Conca, D. Vione, R. Buscaino, M. Fiorito, C. Bussi, O. Abollino, M. Malandrino, *Electrochimica Acta*, **2018**, *284*, 279.
9. X.B. Hu, W.H. Zheng, R.F. Zhang, *Journal of Solid State Electrochemistry*, **2016**, *20*, DOI: 10.1007/s10008-016-3302-8.
10. E. Chiavazza, S. Berto, A. Giacomino, M. Malandrino, C. Barolo, E. Prenesti, D. Vione, O. Abollino, *Electrochimica Acta*, **2016**, *192*, 139.
11. L. Kiss, S. Kunsági-Máté, *Periodica Polytechnica Chemical Engineering*, <https://doi.org/10.3311/Ppch.14311>.
12. J. Cassidy, S.B. Khoo, S. Pons, M. Fleischmann, *Journal of Physical Chemistry*, **1985**, *89*, 3933.
13. L. Kiss, F. Kovács, H. Li, A. Kiss, S. Kunsági-Máté, *Chemical Physics Letters*, **2020**, *754*.
14. L. Kiss, D. Bősz, F. Kovács, H. Li, G. Nagy, S. Kunsági-Máté, *Polymer Bulletin*, **2019**, *76*, 5849.
15. L. Kiss, D. Bősz, F. Kovács, H. Li, S. Kunsági-Máté, *Polymer Bulletin*, **2019**, *76*, 215.
16. David R. Lide, *Handbook of Chemistry and Physics*, 76th Edition **1995-1996**, Chapter 6, p. 170.
17. M.A. Hernández-Olmos, L. Agüí, P. Yáñez-Sedeno, J.M. Pingarrón, *Electrochimica Acta*, **2000**, *46*, 289.
18. L. Agüí, J.E. López-Guzmán, A. González-Cortés, P. Yáñez-Sedeno, J.M. Pingarrón, *Analytica Chimica Acta*, **1999**, *385*, 241.

Na⁺ - NH₄⁺ CATION EXCHANGE STUDY ON TREATED ZEOLITIC VOLCANIC TUFF IN FIXED BED COLUMN

S. ANDRADA MĂICĂNEANU^{a,*} and HOREA BEDELEAN^b

ABSTRACT. In this work Na⁺ - NH₄⁺ cation exchange process was studied on various samples of treated zeolitic volcanic tuff (ZVT). Irrespective of the treatment applied (washing, NaCl, acid, thermal), the Na⁺ concentration evolution closely mirrors the NH₄⁺ concentration evolution indicating that Na⁺ - NH₄⁺ is the main ion exchange process that takes place. Cation exchange capacities (CEC) between 5.42 and 33.8 mg NH₄⁺/g were obtained suggesting that not all treatments improved the ZVT's abilities to remove ammonium from wastewater. Changes in flow rate, Na⁺ concentration, NH₄⁺ concentration, ZVT amount, and ZVT grain size have all influenced the CEC in the considered system.

Keywords: *zeolitic volcanic tuff, clinoptilolite, ammonium, ion exchange, column, wastewater*

INTRODUCTION

Zeolitic volcanic tuff are materials containing different types of natural occurring zeolites in various amounts. Natural zeolites are low cost materials and are widespread around the world. American, Australian, Brazilian, Chilean, Chinese, Iranian, Serbian, Turkish, and Ukrainian natural zeolites are among the most studied ones.

Zeolites are porous hydrated aluminosilicates of alkali or alkaline earth metals. They have a three-dimensional crystalline lattice, consisting of SiO₄ and AlO₄ tetrahedra linked by shared oxygen atoms. The zeolite framework contains linked cages, cavities, and channels. The presence of Al³⁺ in the zeolite structure introduces a negative charge that is balanced by mono- and divalent cations, such as Na⁺, K⁺, Ca²⁺, or Mg²⁺. These cations loosely bound in the zeolite framework are called exchangeable cations. The

^a *Madia Department of Chemistry, Indiana University of Pennsylvania, Indiana, PA 15705, USA*

^b *Department of Geology, Babes-Bolyai University, 1 M. Kogălniceanu st., 400048, Cluj-Napoca, Romania*

*Corresponding author: Sanda.Maicaneanu@iup.edu

exchangeable cations along with their coordinated water molecules are located on specific sites in the zeolite structure. Consequently, zeolites present specific properties: hydration reversibility, ion exchange ability, and adsorption-desorption capacity [1-6]. Clinoptilolite, member of the heulandite group (HEU) is one of the most abundant natural zeolite minerals tested widely in various applications [2,5].

Nitrogen is an essential nutrient, but when present in high concentration contribute to accelerated eutrophication of surface waters, dissolved oxygen depletion, and fish toxicity [4,7]. Ammonium is one of the forms of inorganic nitrogen that is a common water pollutant, usually present in industrial, municipal, and agricultural wastewater. Several processes are available to remove ammonium ions from wastewaters, such as biological processes, air stripping, breakpoint chlorination, chemical precipitation, adsorption, and ion exchange [1,3,4]. Zeolites' ion exchange ability, their high availability, low cost, and ease of application makes them ideal materials for ammonium removal from wastewater [4,7,8].

A survey of the last 10 years literature shows that ammonium removal from wastewater using zeolites remains a subject of great interest. Ammonium removal using Chinese zeolite [9,10], Iranian zeolite [11,12], high purity Serbian zeolite ion exchange combined with nitrogen release for microalgae cultivation [13], Australian zeolite [14], Cuban zeolite ion exchange coupled with bioregeneration by nitrification [15], Slovakian zeolite usage with recovery as liquid fertilizers [16], American and Japanese zeolites [17], and synthetic zeolite [18] were all studied over the last decade.

In the desire to increase natural zeolites' cation exchange capacity, several studies attempted the usage of treated zeolites for ammonium removal from wastewater. Therefore, Chinese clinoptilolite treated with NaCl and mixed with Na₂SiO₃ and powdered activated carbon was used successfully to remove ammonium from drinking water [19], Yemeni natural zeolite treated with NaCl solution of different concentrations at various temperatures showed improved removal efficiency [20], Chinese zeolite modified with MgO showed an increase of removal efficiency up to 97.6% [21], hydrated aluminum oxide modified Slovakian zeolite was used to simultaneously remove phosphate and ammonium [22], Chinese zeolite modified with potassium permanganate did not show an improvement in ammonium removal efficiency [23], NaOH modified zeolite showed a slight decrease on ammonium adsorption [24], highly concentrated NaCl, HCl, and NaOH treated clinoptilolite exhibited various outcomes depending on the initial concentration of ammonium solution [25], while a Chinese zeolite modified with 3.0 M NaNO₃ and calcined at 500°C, proved to be with 39.88% more efficient than the untreated sample [26].

The purpose of this work was to study the Na⁺ - NH₄⁺ cation exchange process in the zeolitic (clinoptilolitic) volcanic tuff (ZVT) – ammonium aqueous solution system and to examine the influence of various treatments applied to the zeolite sample over its cation exchange capacity (CEC) in a downflow mode operated column. The impact of flow rate, Na⁺ concentration, NH₄⁺ concentration, ZVT amount, and ZVT grain size over the CEC were also considered.

RESULTS AND DISCUSSION

Zeolitic volcanic tuff characterization

The zeolitic volcanic tuff (vitric tuff) sample used in this work was collected from a deposit located in the north-western part of the Transylvanian Depression (Măcișaș) that is included in the Dej Formation of Badenian age [27]. The bulk chemical analysis showed the acid character of the tuff with SiO₂ about 64%. The loss of ignition value indicates that more than 60% of the crystallized fractions of the tuff is formed by zeolites [3].

In Figure 1 a typical XRD diffractogram of the Măcișaș zeolitic tuff (**M-s**) is presented together with the diffractograms of samples treated with NaCl (**M-Na-22**, **M-Na-100**), HCl (**M-H2-22**), and thermally treated (**M-250**, **M-500**, **M-750**). The X-ray diffraction patterns show an almost similar mineralogical composition, with the clinoptilolite as the main mineralogical phase and small amount of quartz and albite. The appearance of the diffraction line of the **M-750** sample is slightly different from the others. Even if the mineral phases are approximately the same, the diffraction shows the presence of an amorphous phase, identified by a slightly vaulted shape of the diffraction line broad centered at $2\theta = 20-25^\circ$. The peaks characteristic to the component minerals have a lower intensity, compared to other diffractions. All this suggests that at a temperature of 750°C, the structure of clinoptilolite begins to collapse after heating for 4 hours resulting in an amorphous phase [28]. The remaining peaks, after the clinoptilolite pattern had disappeared, belong to the minerals quartz and feldspar and possibly to the untransformed clinoptilolite (remnants).

FTIR spectra of the treated ZVT samples, for which the highest and lowest cation exchange capacity were calculated, are presented in Figure 2. The specific zeolite bands were identified as follows: 453 cm⁻¹ (medium) O-T-O tetrahedral angular deformation; 608 cm⁻¹ (medium) external vibrations of

T-O tetrahedral units coupled in rings; 669, 721, 790 cm^{-1} (weak) external T-O tetrahedral symmetric stretching; 1060 cm^{-1} (strong) external T-O tetrahedral asymmetric stretching; 1206 cm^{-1} (weak) internal T-O tetrahedral asymmetric stretching; 1636 cm^{-1} (weak) H-O-H angular deformation; 3448 cm^{-1} (medium) O-H stretching [3,29,30]. Additionally, the FTIR spectra of the treated samples displayed similar appearance, Figure 2, with specific features. Relative intensities of the specific bands decreased drastically, especially in case of **M-750** sample indicating structural changes in the ZVT structure. For the previous mentioned sample, the weak band at 1206 cm^{-1} almost disappeared, while for **M-H2-22**, the same band turned into a shoulder. OH/water bands in **M-750** became very weak and broad as expected for a sample treated at high temperature. 1060 cm^{-1} band position changes were recorded for **M-Na-100**, **M-H2-22**, **M-250**, and **M-750** to 1054, 1070, 1058, and 1073 cm^{-1} respectively.

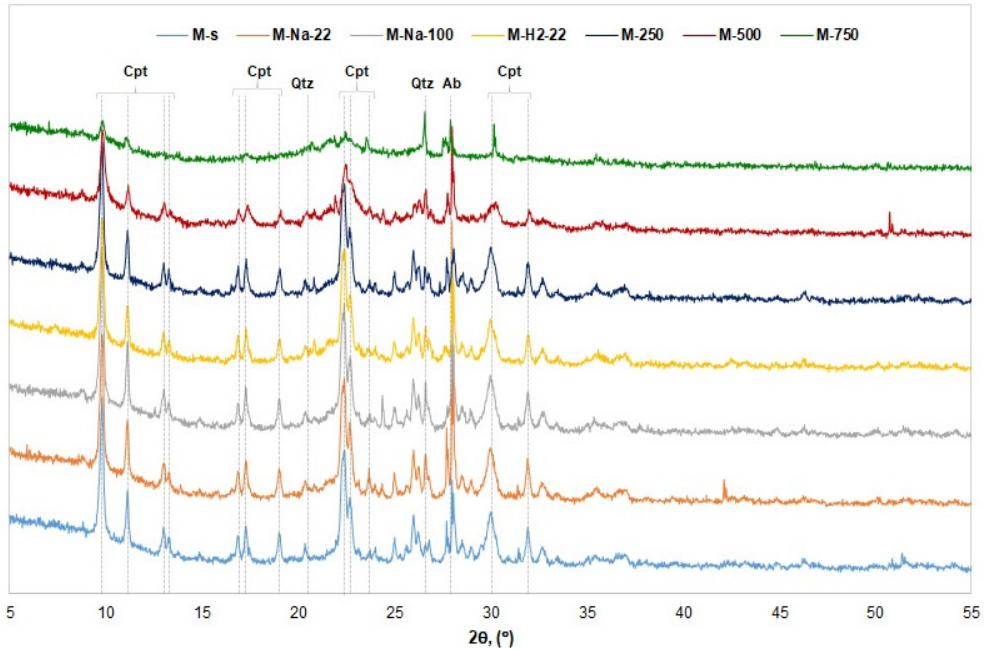


Figure 1. Powder X-ray diffractograms of some of the ZVT treated samples. Cpt - clinoptilolite, Qtz - quartz, Ab - albite.

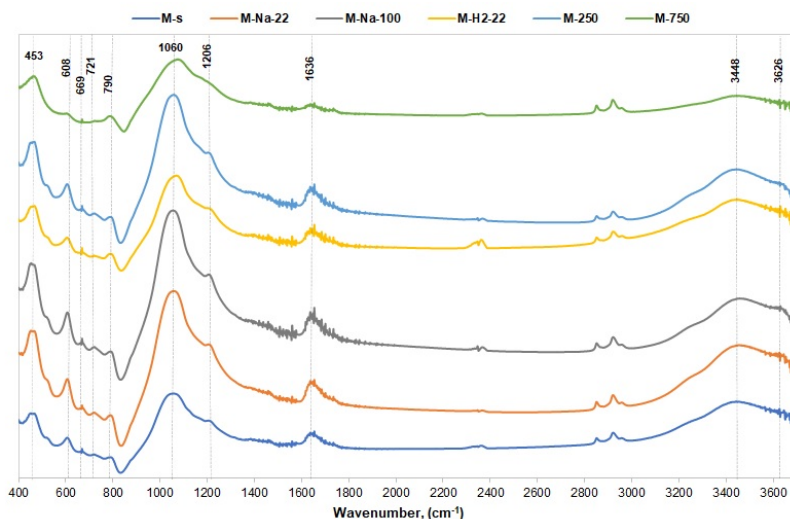


Figure 2. FTIR spectra of some of the ZVT treated samples.

Cation exchange results

As shown in Figure 3 (left), ZVT treatment plays an important role in the ammonium ion exchange process – *Experiment (1)*. CEC increased when the zeolite was treated with NaCl, the maximum value of 33.8 mg NH₄⁺/g being reached for the treatment realized at 100°C with 1 M NaCl solution. The acid treatment led to a decrease of CEC, the lowest value being determined for the treatment realized with 1 M H₂SO₄. As for the thermal treatment, CEC decreased abruptly with the increase of the temperature from 200 to 750°C. X-ray diffractograms and FTIR spectra showed that the ZVT structure underwent deterioration, especially during the 750°C treatment, therefore the CEC dropped to a minimum of 5.42 mg NH₄⁺/g. In terms of concentrations evolution, Figure 3 (right), presented as a comparison between the treatments that gave the best and the worst results, it can be seen that the breakthrough point is at about 25 minutes for **M-750** and about 75 min for **M-Na-100**. The slope of the breakthrough curve is very steep in case of **M-750** indicating the early ZVT sample exhaustion. After the first step of the process (25 min and 100 mL effluent collected), the Na⁺ concentration was determined to be 59.84 and 108.8 mg Na⁺/L for **M-750** and **M-Na-100** respectively, showing that the availability of exchangeable sodium ions in the thermal treated deteriorated ZVT structure is very low. Na⁺ concentration evolution mirrors closely the NH₄⁺ concentration evolution as presented in Figure 3 (right).

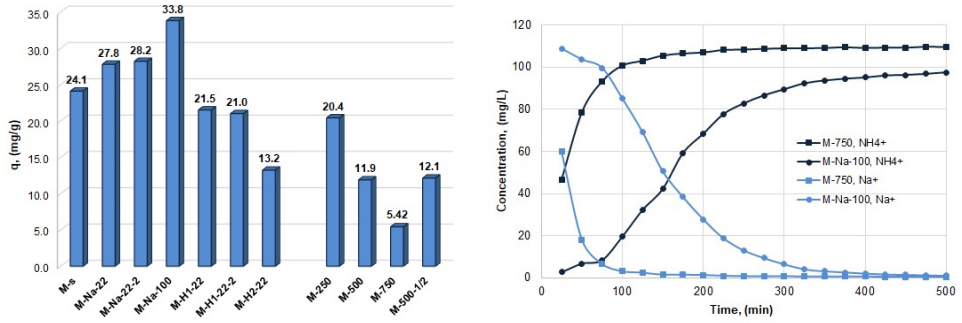


Figure 3. ZVT treatment influence over the ammonium CEC (left) and NH_4^+ and Na^+ concentrations evolution for **M-Na-100** and **M-750** (right); Experiment (1).

M-Na-100 ZVT sample was next used to test the influence of the flow rate over the ion exchange process – *Experiment (2)*. As the flow rate increased from 4 to 32 mL/min, the CEC decreased with about 30% from 33.8 to 23.3 mg NH_4^+ /g respectively, Figure 4 (left). Breakthrough curves, presented as a comparison between the lowest and the highest flow rate, Figure 4 (right), exhibited a steeper slope and an early breakthrough point in case of 32 mL/min flow rate, which indicates a premature exhaustion of the ZVT sample when operated in these conditions. Following the sodium ions concentration, we observed that after the first step (100 mL effluent collected) about the same amount of ions was exchanged, while as the process further evolves the amount of Na^+ exchanged each step decreased for the 32 mL/min experiment indicating that diffusion limitations hinder the exchange process. Operating the column at a high flow rate leads to an underuse of the internal surface area of the ZVT ion exchanger.

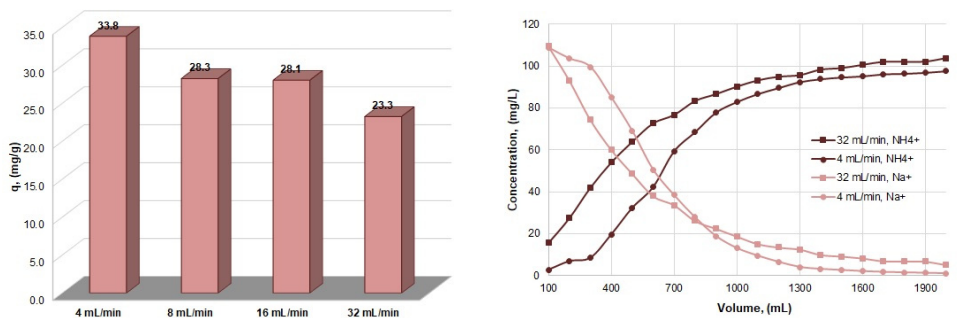


Figure 4. Ammonium CEC as a function of flow rate (left) and NH_4^+ and Na^+ concentrations evolution for **M-Na-100** (right); Experiment (2).

The influence of competitive sodium ions present in the ammonium solution – *Experiment (3)* – was also studied, using the **M-Na-100** sample. As depicted in Figure 5 (left), CEC slowly decreases from 28.3 to 22.6 mg NH₄⁺/g as sodium ions concentration increases from 0 to 100 mg Na⁺/L. As concentration increases further, up to 200 mg Na⁺/L, no significant influence was observed. Breakthrough curves show similar profiles with a more gentler slope, Figure 5 (right), when 100 mg Na⁺/L sodium ions were added indicating that the diffusion of Na⁺ from the ZVT structure is limited by the increased amount of Na⁺ in solution, therefore decreasing the rate of the ion exchange process.

Experiment (4) was conducted on the **M-Na-22** sample varying the amount of NH₄⁺ present in solution. As presented in Figure 6 (left) the CEC increased with an increase in ammonium ions concentration, indicating the ability of ZVT sample to retain high amounts of ions. CEC increased from 17.4 to 31.1 mg NH₄⁺/g as ammonium concentration in solution increased from 25 to 200 mg NH₄⁺/L. The slope of the breakthrough curves became steeper when the NH₄⁺ concentration increased, as presented in Figure 6 (right) for two concentrations. Sodium ions were not detected in solution after 425 min or 1700 mL eluent solution collected when the initial ammonium concentration was 200 mg NH₄⁺/L suggesting the depletion of the exchangeable ions in the ZVT structure, which led to a cease of the ion exchange process.

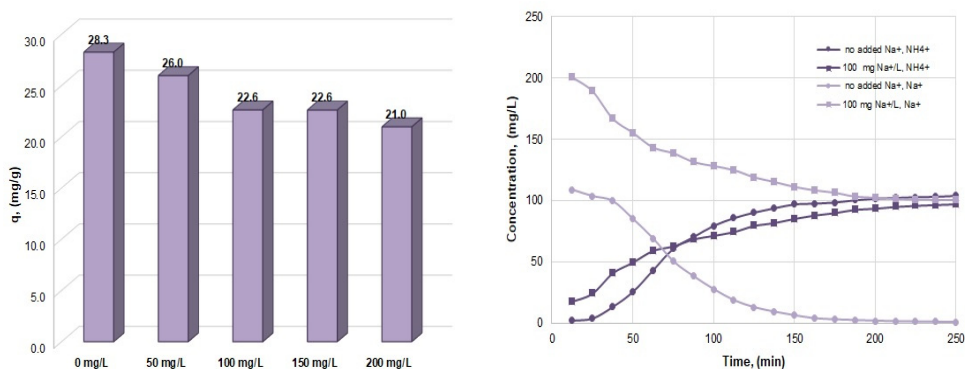


Figure 5. The influence of Na⁺ presence over the ammonium CEC (left) and NH₄⁺ and Na⁺ concentrations evolution for **M-Na-100**; Experiment (3).

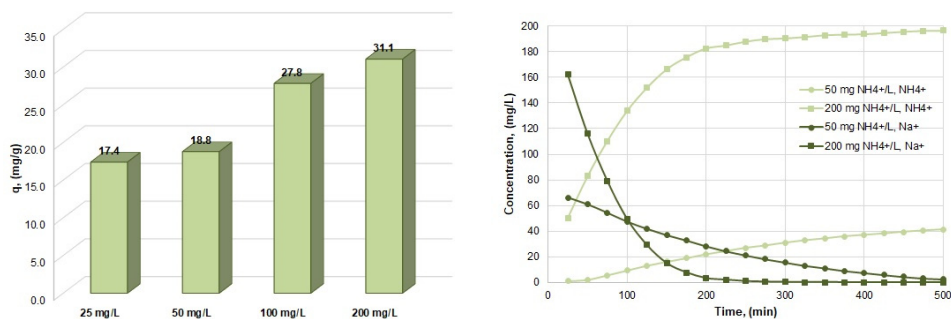


Figure 6. CEC as a function of the initial ammonium concentration (left) and NH_4^+ and Na^+ concentrations evolution for **M-Na-22** (right); Experiment (4).

For the final experiment, ZVT related parameters, amount and grain size were considered to study the Na^+ - NH_4^+ cation exchange process – *Experiment (5)*. As expected, the CEC decreased with an increase in the ZVT amount since for the same initial ammonium concentration a greater surface area is available, Figure 7 (left). With an increase in the grain size, CEC also decreased due to a decrease of the intraparticle diffusion rate, as most likely internal diffusion becomes rate limiting step, from 27.8 to 18.3 mg NH_4^+ /g for 0.2-0.4 and 1.25-1.60 mm respectively. Breakthrough curves reflect this behavior, a gentler slope was recorded for the biggest particles used (1.25-1.60 mm). Sodium ions concentration evolution follows the same trend indicating that the amount of Na^+ exchanged decreased as the grain size increased.

CONCLUSIONS

The results obtained in the present study indicated that the only treatment applied to the ZVT that actually increased CEC is the NaCl treatment, the best results being obtained on the treatment realized at 100°C with a 1 M NaCl solution. As this treatment will generate supplementary costs with the heating agent and reflux equipment that have to be used, the closest alternative is carrying out the treatment process at room temperature, which also gives very good results in terms of CEC. Na^+ concentration evolution closely mirrors NH_4^+ concentration evolution for all experiments. The completion of the Na^+ - NH_4^+ cation exchange process was recorded only when the highest concentration of ammonium was tested (200 mg NH_4^+ /L).

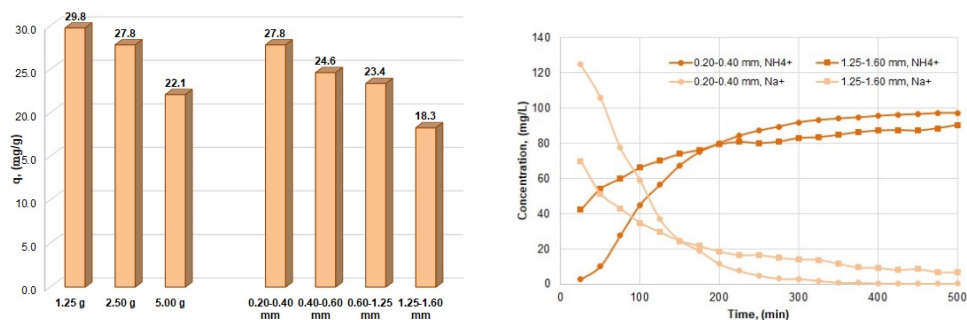


Figure 7. Influence of **M-Na-22** amount and grain size over the ammonium CEC (left) and NH₄⁺ and Na⁺ concentrations evolution for two grain sizes (right); Experiment (5).

EXPERIMENTAL

Zeolitic volcanic tuff

A sample of zeolitic volcanic tuff (ZVT) collected from Măciçaș (M) deposit (Cluj County, Transylvania, Romania) was used throughout this work. Raw ZVT was subjected to several treatments as follows:

(1) **grinding** followed by **size separation** to obtain the 0.20-0.40, 0.40-0.60, 0.60-1.00, 1.00-1.25, and 1.25-1.60 mm fractions;

(2) **washing** with distilled water and drying at 100±5°C for 24 h; samples of various grain size labeled **M-s** were obtained; these samples were further used to perform the subsequent treatments;

(3) **NaCl treatment** was realized using 1 M and 2 M NaCl solutions at room temperature, **M-Na-22** and **M-Na-22-2**, and under reflux at 100±5°C for 2 h, **M-Na-100**; a solid : liquid ratio of 1:10 and a stirring rate of 250 rpm were used; samples were washed with distilled water until no chlorine ions were identified in solution (AgNO₃ 0.01 M) and dried at 100±5°C for 24 h;

(4) **acid treatment** was realized using 1 M and 2 M HCl solutions, **M-H1-22** and **M-H1-22-2**, and 1 M H₂SO₄, **M-H2-22**, at room temperature for 2 h; a solid : liquid ratio of 1:10 and a stirring rate of 250 rpm were used; samples were washed with distilled water until no chlorine ions were identified in solution (AgNO₃ 0.01 M) and dried at 100±5°C for 24 h;

(5) **thermal treatment** was realized in a furnace at 250, 500, and 750°C for 4 hours, **M-250**, **M-500**, **M-750**, and 500°C for 2 h, **M-500-1/2**.

NaCl, HCl (36% w/w), H₂SO₄ (98% w/w), AgNO₃ used were of analytical purity (Merck, Germany).

ZVT characterization

XRD analyses of ZVT samples were performed using a D8 ADVANCE Bruker diffractometer, CuK α anticathode. The diffractograms were recorded from 5° to 60°, 2 θ degree. The analytic conditions were 40 kV, 40 mA, and a step of 0.02 degrees/min.

FTIR analyses were performed on dried samples prepared by encapsulating 1.2 mg of finely grounded particles in 300 mg of KBr. Infrared spectra were obtained using a JASCO 615 FTIR spectrometer 400-4000 cm⁻¹ (resolution, 2 cm⁻¹).

Ion exchange experiments

Ammonium removal experiments were conducted in a 20 mm diameter (450 mm length) column equipped with a glass frit in down flow mode. Glass wool fibers (layer of about 1.0 mm thickness) were set on the frit before the ZVT was added to avoid pores blockage. The liquid level in the column and the flow rate were maintained constant using a peristaltic pump and the column's stopcock.

NH₄Cl and NaCl of analytical purity (Merck, Germany), and distilled water were used to prepare stock solutions of 1000 mg/L. Solutions in 25-200 mg NH₄⁺/L range and 50-200 mg Na⁺/L were further prepared.

Ion exchange experiments were conducted as follows:

Experiment (1) – ZVT treatment – all prepared samples, 0.20-0.40 mm and 2.5 g, were tested using a 100 mg NH₄⁺/L solution and a flow rate of 4 mL/min (no sodium added);

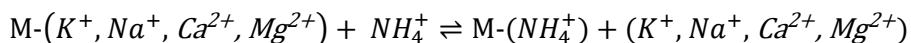
Experiment (2) – flow rate – **M-Na-100** sample, 0.20-0.40 mm and 2.5 g, was tested using a 100 mg NH₄⁺/L solution and a flow rate in the 4-32 mL/min range (no sodium added);

Experiment (3) – sodium ions presence in solution – **M-Na-100** sample, 0.20-0.40 mm and 2.5 g, was tested using a 100 mg NH₄⁺/L solution, a flow rate of 8 mL/min, and sodium ions concentration in the 50-200 mg/L range;

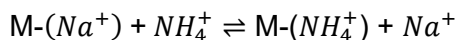
Experiment (4) – ammonium ion concentration – **M-Na-22** sample, 0.20-0.40 mm and 2.5 g, was tested using a flow rate of 4 mL/min and ammonium ion concentrations ranging from 25 to 250 mg/L (no sodium added);

Experiment (5) – zeolite amount and grain size – **M-Na-22** sample of all grain sizes, as listed in the previous section, were tested using a flow rate of 4 mL/min and a 100 mg NH₄⁺/L solution, while the 0.20-0.40 mm **M-Na-22** sample was also tested using 1.25, 2.50, and 5.00 g in the same conditions.

The general cation exchange reaction taking place in the considered system is:



while for the samples treated with NaCl, is expected that the prevailing reaction is:



Ammonium and sodium ions concentrations were determined using an ion chromatograph, Metrohm 761 Compact IC (Switzerland), equipped with a Metrosep C2-250 cation column ($t_{R,sodium} = 7.6$ min; $t_{R,ammonium} = 8.7$ min). Eluent composition for the above-mentioned column is 4.0 mmol/L tartaric acid and 0.75 mmol/L dipicolinic acid prepared in ultrapure degassed water and filtrated through 0.45 μ m cellulose filtrating disks using a vacuum filtering system. Ammonium and sodium ions concentration in solution was determined at the outflow of the column every 100 mL, up to 2000 mL for all experiments. Prior to the injection in the chromatograph, samples were filtrated using 0.45 μ m cellulose syringe filters.

Tartaric acid, dipicolinic acid of analytical purity (Merck, Germany), sodium standard solution (NaNO₃ in HNO₃, 1000 mg/L), ammonium standard solution (NH₄Cl in H₂O, 1000 mg/L) CentiPUR® Milipore Sigma, and ultrapure water were used.

An additional initial test in which beside Na⁺ and NH₄⁺, concentrations of Li⁺, K⁺, Ca²⁺, and Mg²⁺ were determined using the method described above (initial concentration of 100 mg NH₄⁺/L, **M-Na-22**) was performed. Lithium, potassium, and magnesium ions were not identified in any of the effluent samples collected, while calcium ions were determined to be about 7.8% of the initial ammonium concentration. Therefore, for the main experiments only Na⁺ and NH₄⁺ concentrations monitoring was considered.

The effectiveness of the ion exchange process was evaluated using the evolution of NH₄⁺ and Na⁺ concentrations in time and the operating exchange capacity, CEC, q (mg NH₄⁺/g), calculated using the following equation:

$$q_t = \left[\frac{(C_i - C_t)}{m} \cdot \frac{V}{1000} \right] + q_{t-1}$$

where, q_t and q_{t-1} are the ammonium operating cation exchange capacities at times t and $t-1$, respectively, in (mg/g); C_i and C_t are the ammonium concentrations, initial and time t , respectively, in (mg/L); m is the amount of ZVT sample in (g); V is the sample volume, in (L).

REFERENCES

1. A. Hedstrom; *J. Environ. Eng.*, **2001**, *127*, 673-681.
2. F. Cakicioglu-Ozkan; S. Ulku; *Microporous Mesoporous Mater.*, **2005**, *77*, 47-53.
3. A. Maicaneanu; H. Bedelean; S. Burca; M. Stanca; *Sep. Sci. Technol.*, **2011**, *46*, 1621-1630.

4. M. Turan; *Nanosci. Nanotechnol.*, **2015**, 477–504.
5. K. Stocker; M. Ellersdorfer; M. Lehner; J.G. Raith; *BHM*, **2017**, 162, 142-147.
6. P.J. Reeve; H.J. Fallowfield; *J. Environ. Manage.*, **2018**, 205, 253-261.
7. J. Huang; N.R. Kankanamge; C. Chow; D.T. Welsh; T. Li; P.R. Teasdale; *J. Environ. Sci.*, **2018**, 63, 174-197.
8. Z. Ghasemi; I. Sourinejad; H. Kazemian; S. Rohan; *Rev. Aquacult.*, **2018**, 10, 75-95.
9. H. Huang; X. Xiao; B. Yan; L. Yang; *J. Hazard. Mater.*, **2010**, 175, 247–252.
10. H. Huang; L. Yang; Q. Xue; J. Liu, L. Hou; L. Ding; *J. Environ. Manage.*, **2015**, 160, 333-341.
11. R. Malekian; J. Abedi-Koupai; S.S. Eslamian; S.F. Mousavi; K.C. Abbaspour; M. Afyuni; *Appl. Clay Sci.*, **2011**, 51, 323–329.
12. F. Mazloomi; M. Jalali; *J. Environ. Chem. Eng.*, **2016**, 4, 240-249.
13. G. Markou; D. Vandamme; K. Muylaert; *Bioresour. Technol.*, 2014, 155, 373-378.
14. G.J. Millar; A. Winnett; T. Thompson; S.J. Couperthwaite; *J. Water Process Eng.*, **2016**, 9, 47-57.
15. T.H. Martins; T.S.O. Souza; E. Foresti; *J. Environ. Chem. Eng.*, **2017**, 5, 63-68.
16. I. Sancho; E. Licon; C. Valderrama; N. de Arespacochaga; S. López-Palau; J.L. Cortina; *Sci. Total Environ.*, **2017**, 584-585, 244-251.
17. H-F. Chen; Y-J. Lin; B-H. Chen; I. Yoshiyuki; S. Y-H. Liou; R-T. Huang; *Minerals*, **2018**, 8, 499.
18. W. He; H. Gong; K. Fang; F. Peng; K. Wang; *J. Environ. Sci.*, **2019**, 85, 177-188.
19. M. Li; X. Zhu; F. Zhu; G. Ren; G. Cao; L. Song; *Desalination*, **2011**, 271, 295-300.
20. A. Alshameri; A. Ibrahim; A.M. Assabri; X. Lei; H. Wang; C. Yan; *Powder Technol.*, **2014**, 258, 20-31.
21. J. Guo; *Desalin. Water Treat.*, **2016**, 57, 5452-5463.
22. D. Guaya; C. Valderrama; A. Farran; C. Armijos; J.L. Cortina; *Chem. Eng. J.*, **2015**, 271, 204-213.
23. H. Guo; X.Y. Zhang; J.L. Liu; *Chem. Eng. Trans.*, **2016**, 55, 163-168.
24. Y. He; H. Lin; Y. Dong; Q. Liu; L. Wang; *Chemosphere*, **2016**, 164, 387395.
25. K. Stocker; M. Ellersdorfer; M. Lehner; A. Lechleitner; J. Lubensky; J.G. Raith; *Microporous Mesoporous Mater.*, **2019**, 288, 109553.
26. H. Fua; Y. Lia; Z. Yua; J. Shena; J. Lia; M. Zhanga; T. Dinga; L. Xua; S.S. Leeb; *J. Hazard. Mater.*, **2020**, 393, 122481.
27. F. Mumpton; *Am. Mineral.*, **1960**, 45, 351–369.
28. R. Plesa Chicinas; H. Bedeleian; A. Maicaneanu; *Stud. Univ. Babeş-Bolyai. Chem.*, **2016**, 61, 243-254.
29. G. Rodriguez-Fuentes; A. R. Ruiz-Salvador; M. Picazo; G. Quintana; M. Delgado; *Microporous Mesoporous Mater.*, **1998**, 20, 269-281.
30. M. Mozgawa; *J. Mol. Struct.*, **2000**, 555, 299-304.

COMPREHENSIVE ASSESSMENT OF ANTIOXIDANT AND CHELATING CAPACITY OF SOME BIOGENIC AMINES AND RELATED DRUGS

ALEXANDRINA GUIDEA^a, AUGUSTIN C. MOT^a,
COSTEL SÂRBU^{a*}

ABSTRACT. The radical scavenging, reducing power and metal-chelating capacity of some biogenic amines and related sympathomimetic drugs were clarified using various *in vitro* antioxidant assays as DPPH (1, 1-diphenyl-2-picryl-hydrazyl), ABTS (2,2'-azino-bis (3-ethylbenzthiazoline-6-sulfonic acid), SORS (superoxide anion (O₂⁻) radical-scavenging), nitric oxide (NO) radical scavenging, FRAP (ferric reducing antioxidant power), CUPRAC (cupric reducing antioxidant capacity) and CHROMAC (chromium reducing antioxidant capacity), including also FIC (ferrous ion-chelating capacity). The highest radical scavenging values in the case of DPPH test, for example, were obtained for methyl dopa (93.14%), isoprenaline (92.92%) adrenalone (90.76%) and dopamine (90.51%). The highest reduction power, according to FRAP test, presented the same compounds: adrenalone (96.02%) methyl dopa (95.97%), dopamine (94.67%) and isoprenaline (93.72%), except metaraminol (5.79%). Concerning the chelating capacity, adrenalone (66.35%), metaraminol (55.31%), metaproterenol (49.58%) and terbutaline (45.64%) showed the higher chelating capacity. The lowest value, in this case, was obtained for methyl dopa (0.28%). According to the results obtained in the present study, the investigated drugs showed an effective *in vitro* antioxidant and radical scavenging ability and metal-chelating capacity. In addition, applying hierarchical cluster analysis (HCA), principal component analysis (PCA) and the sum of ranking differences (SRD) similarities and differences of investigated compounds and considered assays were clearly proved.

Keywords: Antioxidant and chelating capacity, biogenic amines, sympathomimetic drugs, chemometrics

^a Faculty of Chemistry and Chemical Engineering, Department of Chemistry, Babeş-Bolyai University, 400028, Cluj-Napoca, Romania

* Corresponding author: csarbu@chem.ubbcluj.ro; Tel: (+40-264-59383)

INTRODUCTION

An antioxidant is a chemical that prevents the oxidation of other chemicals. According to *Halliwell* and *Gutteridge* [1, 2] an antioxidant is „any substance that delays, prevent or removes oxidative damage to a target molecule”. They protect the key cell components by neutralizing the damaging effects of free radicals, which are natural byproducts of cell metabolism. The free radicals attack the nearest stable molecules, stealing their electrons. When the attacked molecule loses its electrons, it becomes a free radical itself, beginning a chain reaction, finally resulting in the deterioration of a living cell. To protect the cells from the damage caused by oxidants, the organisms have evolved several antioxidant defense mechanisms for the rapid and efficient removal of reactive oxygen species (ROS) or reactive nitrogen species (RNS) from the intracellular environment [3,4]. In normal circumstances, there is a balance between antioxidants and oxidants. When the equilibrium between oxidants and antioxidants defense systems is imbalanced in favor of the oxidants, the condition is known as oxidative stress. Oxidative stress results in the damage of biopolymers including nucleic acids, proteins, polyunsaturated fatty acids and carbohydrates leading to a variety of human diseases like Alzheimer’s disease, Parkinson’s disease, atherosclerosis, cancer, arthritis, immunological incompetence and neurodegenerative disorders [5].

Biogenic Amines (BAs) are known to occur in all living organisms (microorganisms, plants, and animals). BAs are the basic nitrogenous compounds with aliphatic, (putrescine, cadaverine, spermine, spermidine), aromatic (tyramine, phenylethylamine), or heterocyclic (histamine, tryptamine) structure. The biogenic amines derived from amino acid tyrosine are called catecholamines because they contain a catechol or 3,4-dihydroxyphenyl group. In the human body, the most abundant catecholamines are epinephrine (adrenaline), norepinephrine (noradrenaline) and dopamine. Catecholamines are hormones released by the sympathetic nervous and adrenal medulla in response to a range of stresses to regulate the host physiological functions in living systems [6-10]. As it is also demonstrated, catecholamines are able to act as antioxidants or prooxidants depending on various factors such as concentration, pH, the test system used for investigation (*in vitro* and *in vivo*) or possible interaction with other antioxidants, different substrates or with transition metal ions [11-13]. The high antioxidant potential of catecholamine drugs is attributed to the fact that the semiquinone radical derived from H-atom donation of catechol can be stabilized by an intramolecular hydrogen bond and the electron-donating properties of the *ortho*-OH [11-15].

Since ROS and RNS are implicated in the pathogenesis of many chronic diseases, as has been shortly mentioned above, finding natural and synthetic antioxidants to combat ROS and RNS has attracted much attention [16-19].

Among the therapeutics with promising antioxidant activity, adrenergic drugs (agonists and antagonists - blockers) are of a large interest because they are considered the future medication for new improvements in different therapies [17, 20]. The beneficial effects shown by some adrenergic compounds in neuroprotection and in experimental models of Parkinson's disease, for example, has already been associated with their antioxidant properties and the current studies are oriented on the potential future use of these drugs in the treatment of various diseases as osteoporosis, cancer and malaria. Considering all these aspects, a better knowledge of the antioxidant profile of redox-active drugs will involve different investigations for increasing bioavailability, safety, and efficiency of future improved therapeutics.

In vitro antioxidant activity assays show extreme diversity concerning the distinct oxidation step, the measurement of the outcome and the mode of expressing the antioxidant activity results [21]. In the above considerations, the radical scavenging ability and reducing power capacity of some biogenic amines and related sympathomimetic drugs were investigated using various *in vitro* antioxidant assays including DPPH (1, 1-diphenyl-2-picryl-hydrazyl), ABTS (2,2'-azino-bis (3-ethylbenzthiazoline-6-sulfonic acid), SORS (superoxide anion (O_2^-) radical-scavenging assay), nitric oxide (NO) radical scavenging assay, FRAP (ferric reducing antioxidant power), CUPRAC (cupric reducing antioxidant capacity) and CHROMAC (chromium reducing antioxidant capacity), including also FIC (ferrous ion-chelating capacity) [22-25]. The results obtained allow a relevant comparison of the investigated compounds concerning their radical scavenging, reducing power and ion-chelating capacity and an objective comparison of the antioxidant assays applying various chemometric methods.

RESULTS AND DISCUSSION

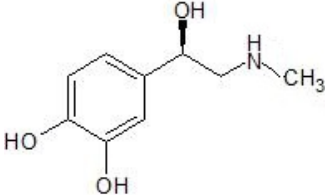
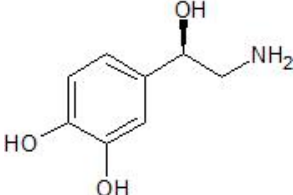
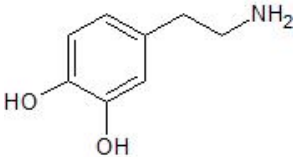
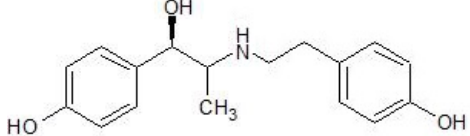
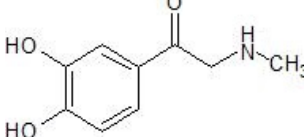
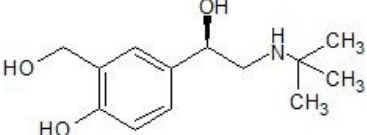
According to previous study [24], some important compounds (as biogenic amines and their related drugs) involved in usual metabolic processes proved to have effective *in vitro* radical scavenging activity based on DPPH assay. For a comprehensive evaluation of their radical activity profiles, the usage of several methods with different mechanisms, kinetics and oxidant species combined with chemometric methods was proposed and evaluated.

The results (mean \pm standard deviation) obtained in this study for the investigated compounds presented in Table 1 are shown in Table 2 and Figure 1a-b and Figure 2.

It can be easily observed from the box and whiskers plot that when a robust confidence interval is considered (Figure 1a) the outliers and extremes

values are not highlighted, and the distributions appear more or less asymmetric. When the classical confidence interval for mean is considered ($p = 0.95$) some outliers and few extremes values are highlighted (Figure 1b).

Table 1. Name, chemical structure and pharmacological activity of investigated compounds

No	Name	Structure	Activity
1	Adrenaline		Bronchodilator, adrenergic
2	Noradrenaline		Adrenergic
3	Dopamine		Adrenergic
4	Ritodrine		Adrenergic
5	Adrenalone		Hemostatic
6	Albuterol		Adrenergic

COMPREHENSIVE ASSESSMENT OF ANTIOXIDANT AND CHELATING CAPACITY
OF SOME BIOGENIC AMINES AND RELATED DRUGS

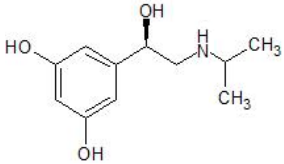
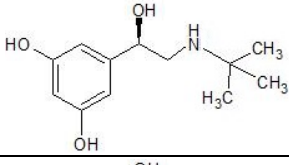
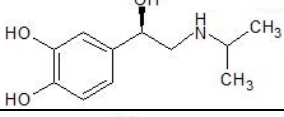
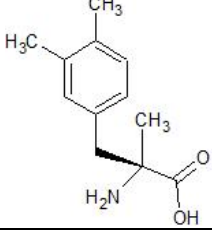
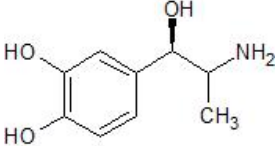
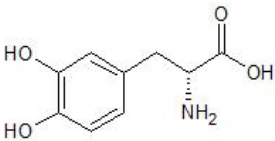
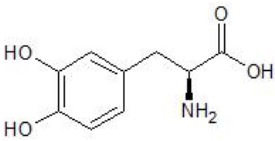
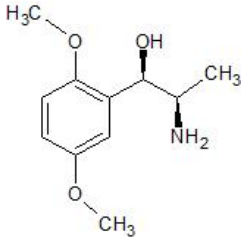
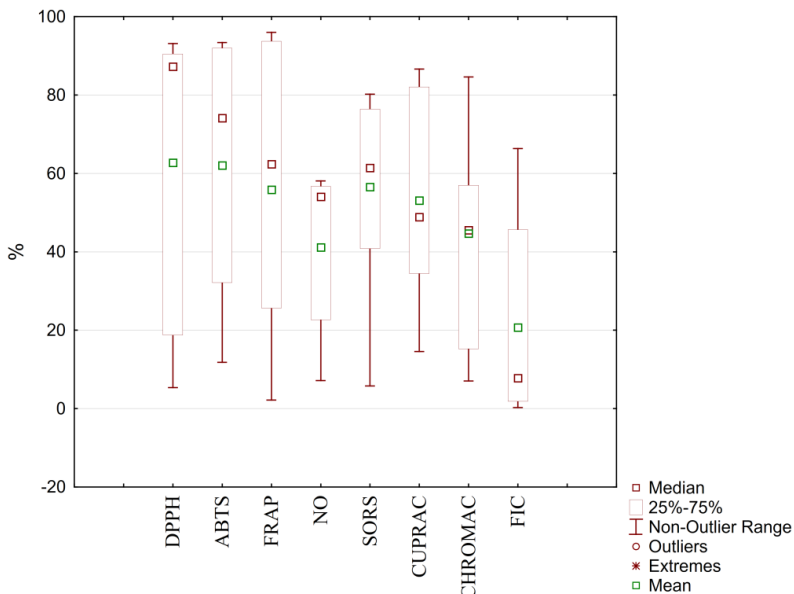
7	Metaproterenol		Bronchodilator
8	Terbutaline		Bronchodilator
9	Isoprenaline		Adrenergic
10	Methyldopa		Antihypertensive
11	Metaraminol		Antihypotensive
12	D-dopa		-
13	L-dopa		Antiparkinsonian
14	Methoxamine		Antihypotensive

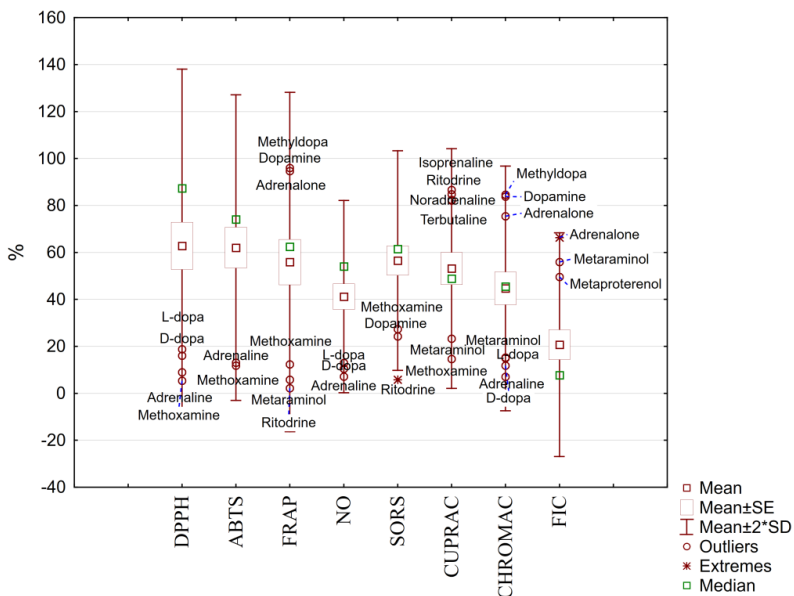
Table 2. The results (mean \pm standard deviation) obtained for all assays applied in this study

Name	DPPH %	ABTS %	FRAP %	NO %	SORS %	CUPRAC %	CHROMAC %	FIC %
Adrenaline	8.96 \pm 5.82	11.82 \pm 3.73	55.65 \pm 0.29	7.15 \pm 3.27	56.44 \pm 7.10	73.24 \pm 4.32	7.04 \pm 2.30	1.88 \pm 0.01
Noradrenaline	85.66 \pm 2.87	91.96 \pm 1.44	90.13 \pm 0.97	53.58 \pm 2.28	58.88 \pm 6.21	82.37 \pm 1.89	40.17 \pm 6.84	7.64 \pm 2.08
Dopamine	90.51 \pm 0.59	93.15 \pm 0.17	94.67 \pm 0.00	57.52 \pm 0.62	24.25 \pm 4.08	37.27 \pm 0.46	83.83 \pm 0.53	7.93 \pm 0.94
Ritodrine	23.17 \pm 6.43	89.43 \pm 1.73	2.18 \pm 1.09	23.27 \pm 0.65	5.78 \pm 3.75	84.78 \pm 0.67	38.31 \pm 5.15	4.95 \pm 0.45
Adrenalone	90.76 \pm 0.49	45.19 \pm 1.34	96.02 \pm 0.01	55.15 \pm 2.50	72.47 \pm 0.59	35.69 \pm 0.18	75.41 \pm 0.71	66.35 \pm 0.68
Albuterol	85.53 \pm 0.85	60.96 \pm 1.00	36.29 \pm 2.08	51.76 \pm 0.77	59.67 \pm 0.81	60.51 \pm 3.46	54.83 \pm 1.22	10.83 \pm 2.51
Metaproterenol	88.9 \pm 0.65	87.34 \pm 4.67	31.77 \pm 5.29	54.87 \pm 0.07	78.15 \pm 1.68	62.87 \pm 6.19	57.00 \pm 2.99	49.58 \pm 0.22
Terbutaline	89.29 \pm 0.11	90.43 \pm 1.39	25.66 \pm 5.04	58.08 \pm 0.43	78.07 \pm 0.32	82.11 \pm 3.23	54.42 \pm 3.46	45.64 \pm 2.97
Isoprenaline	92.92 \pm 0.07	93.39 \pm 0.25	93.72 \pm 0.40	56.72 \pm 0.80	76.43 \pm 3.47	86.62 \pm 0.32	50.92 \pm 2.73	31.85 \pm 6.79
Methyldopa	93.14 \pm 0.10	93.06 \pm 0.28	95.97 \pm 0.18	54.59 \pm 1.08	40.83 \pm 5.12	31.04 \pm 2.86	84.59 \pm 0.51	0.28 \pm 0.11
Metaraminol	90.05 \pm 0.02	32.14 \pm 10.53	5.79 \pm 2.19	57.52 \pm 0.06	80.21 \pm 0.08	23.26 \pm 1.54	15.29 \pm 3.84	55.91 \pm 4.98
D-dopa	16.01 \pm 3.99	30.62 \pm 8.85	69.13 \pm 0.56	10.51 \pm 2.37	63.2 \pm 5.91	34.46 \pm 0.43	11.81 \pm 8.44	1.76 \pm 1.34
L-dopa	18.76 \pm 5.55	36.09 \pm 0.72	73.29 \pm 2.40	12.95 \pm 0.25	70.34 \pm 6.20	34.96 \pm 0.43	14.98 \pm 8.31	1.82 \pm 0.91
Methoxamine	5.35 \pm 1.20	13.01 \pm 0.32	12.34 \pm 4.12	22.69 \pm 1.23	27.37 \pm 0.72	14.6 \pm 9.93	37.12 \pm 6.10	3.45 \pm 1.33
Quercetin	90.00 \pm 1.01		93.80 \pm 0.05	87.34 \pm 1.63	90.45 \pm 0.78	87.38 \pm 0.59	77.70 \pm 0.77	
Trolox		93.42 \pm 0.09						
EDTA								97.12 \pm 0.01

COMPREHENSIVE ASSESSMENT OF ANTIOXIDANT AND CHELATING CAPACITY OF SOME BIOGENIC AMINES AND RELATED DRUGS



(a)



(b)

Figure 1. Box and whiskers plot: robust confidence interval (a), classical confidence interval for mean (b)

By a carefully examination of the heat map (based on the intensity of colors) in Figure 2 it is interesting to remark that majority of adrenergic drugs have a highest antioxidant activity, except for Methoxamine, D-dopa and L-dopa. In the case of catecholamines, the obtained results for noradrenaline are much more similar to dopamine and adrenergic drugs, but they are quite different from adrenaline.

Radical scavenging ability of biogenic amines and their related drugs was estimated using four methods that implies two synthetic radicals (DPPH and ABTS) and two free radicals that play as a stress signalling molecules under certain physiological and pathological conditions (O_2^- and NO). Based on obtained results, the samples were grouped into three well defined classes: the group with the highest values for the majority of assays – metaproterenol, terbutaline, isoprenaline and noradrenaline; the group with at least three very high values – adrenalone, albuterol, metaraminol, dopamine, L-dopa, D-dopa and methylidopa and one group with the smallest values – adrenaline, ritodrine and methoxamine. By a comparative evaluation, the catecholamine related drugs (metaproterenol, terbutaline, isoprenaline) are more active than quercetin, in a good concordance with the results reported in the previous study [24] using only the DPPH method.

Considering now the results obtained by reducing antioxidant power assays also we can find some groups with very close values: noradrenaline and isoprenaline; dopamine, adrenalone, methylidopa; albuterol, metaproterenol, terbutaline; L-dopa and D-dopa; metaraminol, methoxamine with the smallest values for all these assays. Adrenaline and ritodrine appear again quite different. The highest reduction power, according to FRAP test, presented the same compounds as above: adrenalone (96.02%) methylidopa (95.97%), dopamine (94.67%) and isoprenaline (93.72%), except metaraminol (5.79%).

Metal chelating capacity of the studied compounds shows a low Fe^{2+} -chelating ability, except for adrenalone (66.35%), metaraminol (55.31%), metaproterenol (49.58%) and terbutaline (45.64%) which showed the higher chelating capacity. The lowest value, in this case, was obtained for methylidopa (0.28%).

These results are very well supported by the graphical representation heat map (Figure 2) in combination with the two dendrograms (obtained applying the HCA method, using the complete method as linkage procedure and Euclidean distance as a measure of similarity in both cases), where the similarity and differences amongst the investigated compounds and the assays can be observed simultaneously.

COMPREHENSIVE ASSESSMENT OF ANTIOXIDANT AND CHELATING CAPACITY OF SOME BIOGENIC AMINES AND RELATED DRUGS

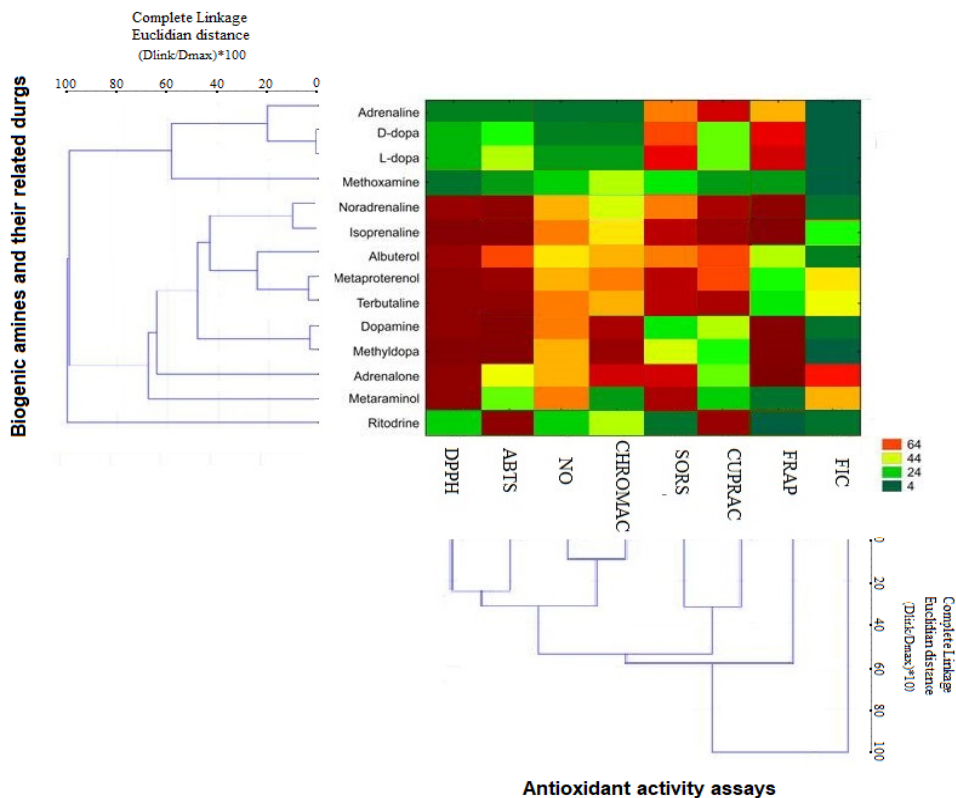


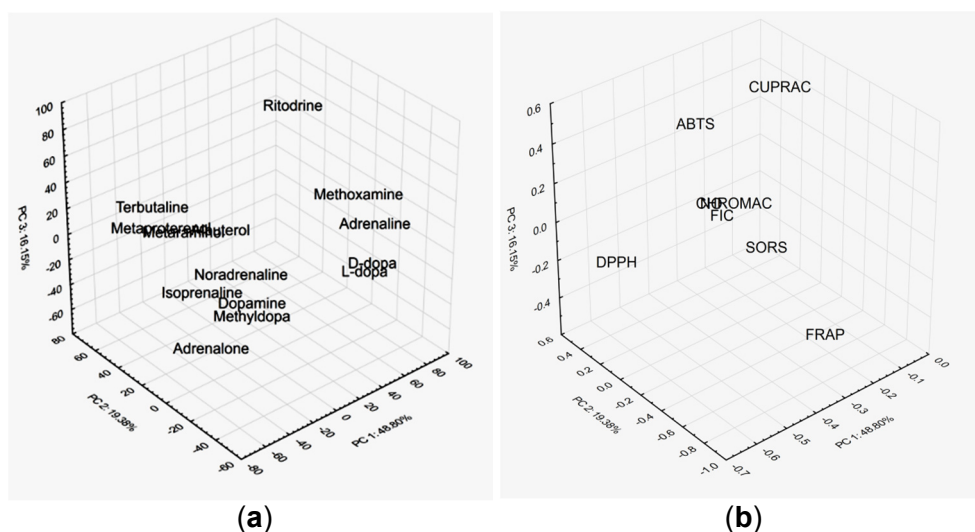
Figure 2. The heat map corresponding to all investigated compounds and all assays coupled with hierarchical cluster analysis

The results obtained from principal component analysis (PCA) using the raw data matrix (14 samples and 8 assays) indicate a significant reduction in the number of variables, in good agreement with the correlations shown in Table 3. The first three components explain 84.33% of the total variation, the first two components explaining 68.18% from total variance, and the first one only 48.80%. However, the 2D representation of the scores corresponding to the first two components (2D) or the first three components (3D) indicates a satisfactory separation of compounds according to their similarity (Figure 3a).

Also, the variables (assays) grouping in the space described by the loadings corresponding to the first three principal components confirms once more the similarity and differences established by correlation matrix and hierarchical cluster analysis (Figure 3b).

Table 3. Correlation matrix obtained for all assays and compounds

Variable	Marked correlations are significant at $p < .05000$							
	DPPH	ABTS	FRAP	NO	SORS	CUPRAC	CHROMAC	FIC
DPPH	1.000	0.664	0.302	0.975	0.380	0.160	0.691	0.586
ABTS		1.000	0.251	0.657	-0.115	0.537	0.666	0.099
FRAP			1.000	0.183	0.136	-0.023	0.396	-0.135
NO				1.000	0.283	0.124	0.719	0.601
SORS					1.000	0.078	-0.197	0.626
CUPRAC						1.000	-0.014	0.027
CHROMAC							1.000	0.224
FIC								1.000

**Figure 3.** 3-D score scatterplot of investigated compounds (a) and 3-D loading scatterplot corresponding to all assays used in this study (b)

According to SRD, the best method to express antioxidant activity of investigated biogenic amines and their related drugs is DPPH because it is the method closest to the “average antioxidant and chelating capacity” (the methods appearing on the left side of the Gaussian curve are most similar to the “average antioxidant activity”); thus, the performance of the presented methods should be representative of the final antioxidant behaviour of

investigated compounds ranks), while the FRAP method is the most different. The results are well illustrated in Figure 4. We have also to remark the high similarity of the assays clustering with the dendrogram obtained applying HCA.

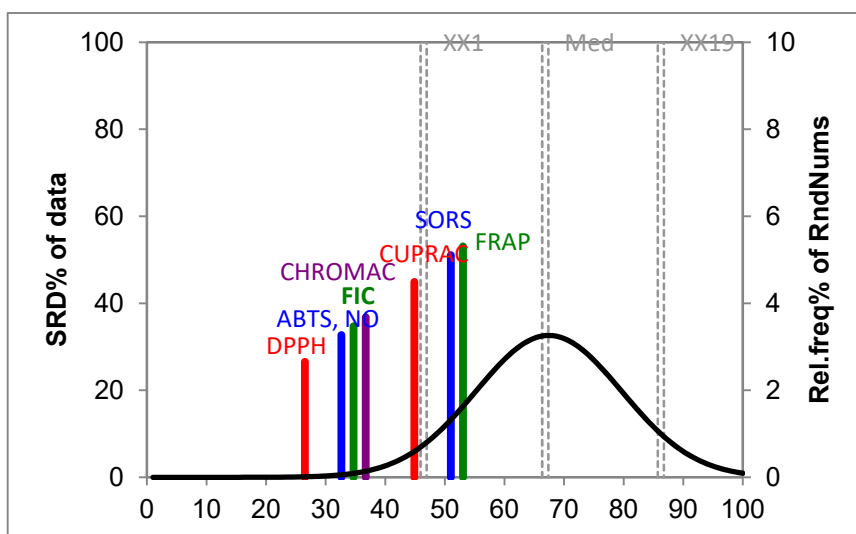


Figure 4. Evaluation of the eight assays using the sum of ranking differences. Average was used as a golden standard. Scaled SRD values are plotted on the x-axis and left y-axis, the right y-axis shows the relative frequencies (black curve). Parameters of the Gaussian fit: $m = 67$ $s = 10.3$ Probability levels 5% (XX1), Median (Med), and 95% (XX19) are also given.

CONCLUSIONS

In this study, applying several *in vitro* methods including mostly radical scavenging (DPPH, ABTS, SORS, NO) and reducing power (FRAP, CUPRAC, CHROMAC) assays, the high radical scavenging and reducing power capacity of some biogenic amines and related drugs were clearly demonstrated. In addition, the majority of the investigated drugs had shown a moderate ferrous chelating capacity. Moreover, applying hierarchical cluster analysis (HCA), principal component analysis (PCA) and the sum of ranking differences (SRD), similarities and differences of investigated compounds and considered assays were clearly proved.

EXPERIMENTAL SECTION

Chemicals and samples preparation

The biogenic amines investigated in this study include adrenaline, noradrenaline, dopamine, and related drugs: methyl dopa, L-dopa, D-dopa, metaraminol, ritodrine, adrenalone, albuterol, metaproterenol, terbutaline, isoprenaline, and methoxamine of analytical grade obtained from Merck and Sigma (Sigma-Aldrich GmbH, Sternheim, Germany). All other reagents were either of analytical grade or of the highest quality available.

The stock solutions of all compounds, including positive controls (quercetin and trolox) were prepared in absolute ethanol (96%) at concentration 1mM. EDTA solution was prepared in water at concentration 1mM. For those related drugs that were poorly soluble in ethanol (adrenaline, D-dopa), stoichiometric hydrochloric acid was added. The final concentration of investigated compounds (300 μ L) was: 1.67 μ M for DPPH, ABTS, SORS, FRAP, CUPRAC, FIC assays; 20 μ M for NO assay and 16.67 μ M for CHROMAC assay. The same concentrations are for reference antioxidant solutions.

Radical scavenging assays

The DPPH test was carried out according to the method described by Blois [26] with slight modifications. Briefly, 295 μ L of 0.15 mM DPPH^{*} prepared in absolute ethanol was added to 5 μ L of samples in 96 well cuvettes. The mixture was shaken and incubated for 30 min, in dark, at room temperature. Then, the absorbance was recorded at 517 nm, using a microplate reader (Tecan Spark™ 10M, Männedorf, Switzerland). All determinations were performed in duplicate. Ethanol and quercetin were used as a negative and positive control, respectively.

The ABTS cation radical scavenging capacity was determined according to the method developed by Re et al. [27]. The ABTS^{•+} cation radical was generated by adding ABTS stock solution (7mM) into potassium persulfate solution (2,45 mM), and the mixture was incubated in dark for 16 h at room temperature. The generated ABTS^{•+} cation radical was diluted with phosphate buffer (10 mM, pH 7.4) to an absorbance of 0.70 ± 0.02 at 734 nm. After that, 5 μ L of each sample was added to 295 μ L of diluted ABTS^{•+} solution in 96 well cuvettes. The mixture was kept in the dark for 10 min and detected at 734 nm, using a microplate reader. Ethanol and Trolox were used as a negative and positive control, respectively. All determinations were performed in duplicate.

The SORS of all considered samples has been investigated using the method described by Li and co-workers [28]. Briefly, 5 μL of the sample solution was mixed with 200 μL of 2-amino-2-hydroxymethyl-propane-1,3-diol (Tris-HCl) buffer (20 mM, pH 8) in 96 well cuvettes. Then proper aliquots from followed solution were added: 30 μL of 1.8 mM nicotinamide adenine dinucleotide (NADH), 30 μL of 3.6 mM nitro blue tetrazolium (NBT) and 40 μL 1.34 mM phenazine methosulfate (PMS). The mixture was left to react for 5 min at 25 $^{\circ}\text{C}$, following the detection at 560 nm for each sample by means of a microplate reader. Ethanol and quercetin were used as a negative and positive control, respectively. All determinations were performed in duplicate.

The NO scavenging capacity was determined according to the method described by Streejayan and Rao [29]. Griess reagent was freshly prepared as a mixture of equal volumes of sulfanilic acid solution with α -naphthylamine solution. For the preparation of sulfanilic acid solution 0.3 g of sulfanilic acid was dissolved in 10 mL glacial acetic acid and 5 mL distilled water by heating on a water bath. After cooling, 10 mL of 10% (m/V) sodium chloride was added, and the solution was diluted to 50 mL with distilled water. The α -naphthylamine solution was prepared by dissolving 0.015 g of α -naphthylamine hydrochloride in 5 mL hot water. After cooling, 10 mL glacial acetic acid was added, and the resulted solution was diluted to 50 mL with distilled water. A volume of 90 μL of 15 mM sodium nitroprusside in 7.4 pH phosphate buffered was mixed with 60 μL of the sample in 96 well cuvettes and incubated at 25 $^{\circ}\text{C}$ for 120 min. Then, 150 μL of freshly prepared Griess reagent was added and left to react for 25 min. The detection was carried out at 540 nm using a microplate reader. Ethanol and quercetin were used as a negative and positive control, respectively. All determinations were performed in duplicate.

Reducing antioxidant power

The FRAP of the samples was determined using the method developed by Benzie and Strain [30]. In brief, the FRAP reagent was freshly prepared by mixing acetate buffer (300 mM, pH 3.6), a solution of 10 mM 2,4,6-tripyridyltriazine (TPTZ) in 40 mM HCl, and 20 mM FeCl_3 at 25:1:1 (v/v/v). A volume of 295 μL of FRAP reagent and 5 μL of sample solution were added in 96 well cuvettes and mixed thoroughly. The absorbance was taken at 593 nm after incubation for 30 min with a microplate reader. Ethanol and quercetin were used as a negative and positive control, respectively. All determinations were performed in duplicate.

The CUPRAC was determined using the method proposed by Apak *et al.* [31]. For this method, a solution consisting of 2 mM neocuproine, 1 mM $\text{CuSO}_4 \cdot 5\text{H}_2\text{O}$ and 1 M ammonium acetate was prepared and incubated for 5 min for the bis(neocuproine) copper (II) complex to be formed. An aliquot

of 200 μL of this solution was mixed with 95 μL ultrapure water and a 5 μL of sample and placed in 96 well cuvettes. The absorbance was taken at 450 nm with a microplate reader. Ethanol and quercetin were used as a negative and positive control, respectively. All determinations were performed in duplicate.

The CHROMAC assay followed the method applied by Işık and co-workers [32]. With respect to this, 200 μL of 100 mg/L $\text{K}_2\text{Cr}_2\text{O}_7$ dissolved in a 50 mM phosphate buffer pH 2.8 was mixed with 50 μL of sample and incubated for 5 min in a 96 wells cuvette. Afterward, 50 μL of 0.5 mM 1,5-diphenylcarbazide was added and the absorbance was taken with a microplate reader at 540 nm. Ethanol and quercetin were used as a negative and positive control, respectively. All determinations were performed in duplicate.

The ability of biogenic amines and related drugs to chelate metal ions has been studied using the method developed by Dinis *et al.* [33]. Firstly, 5 μL of samples were mixed with 200 μL water and 40 μL 0.375 mM Mohr's Salt ($(\text{NH}_4)_2\text{Fe}(\text{SO}_4)_2 \cdot 6\text{H}_2\text{O}$) in 96 well cuvettes. The reaction mixture was incubated at room temperature for 5 minutes. After this, an aliquot of 40 μL of 3.75 mM ferrozine solution was added to the mixture and homogenized and the absorbance was recorded at 546 by means of a microplate reader. Ethanol and ethylenediaminetetraacetic acid (EDTA) were used as a negative and positive control, respectively. All determinations were performed in duplicate.

The antioxidant and chelating capacity were expressed in % and were calculated using formula (1) for determination that implies color consumption and formula (2) for assays that involve color formation (FRAP, CUPRAC and CHROMAC):

$$(\%) = \frac{A_{\text{negative control}} - A_{\text{sample}}}{A_{\text{negative control}}} \times 100 \quad (1)$$

$$(\%) = \frac{A_{\text{sample}} - A_{\text{negative control}}}{A_{\text{positive control}}} \times 100 \quad (2)$$

Chemometrics

Cluster analysis allows meaningful generalizations to be made about large quantities of data by recognizing among them a few basic patterns. It plays a key role in searching for structures in data. Each of these structures is called cluster or class. A class is a group of individuals (samples) which resemble each other more strongly, in terms of properties, than they resemble members of other classes. Generally, two types of algorithm are distinguished, these being hierarchical and non-hierarchical or relocation clustering. Both methods require the calculation of a (dis)similarity matrix. This (dis)similarity

which is really a measure of the proximity of the pair of objects (points) in the p -dimensional characteristic space, defined by the p properties measured for each individual, is usually expressed in terms of either the Euclidean or the Mahalanobis distance between the two points. Two approaches are known to hierarchical clustering, these being agglomerative and divisive procedures. An agglomerative hierarchical clustering approach places each object in its own cluster and gradually merges these atomic clusters into larger and larger clusters until all objects are in a single cluster. Divisive hierarchical clustering reverses the process by starting with all objects in one cluster and subdividing it into smaller ones until, finally, each object is again in a cluster of its own. The number of clusters to be generated can be specified in advance, or it may be optimized by the algorithm itself according to certain criteria.

Cluster imaging applied also in this study is a modification of cluster analysis. Whereas cluster analysis is useful for grouping samples or variables, in cluster imaging (also called two-way joining), samples and variables are clustering simultaneously. A two-way hierarchical cluster analysis with visual pairs of data sets is accomplished. This approach can provide extensive information and details on data structure and variability when both samples and variables are suspected to contribute simultaneously to the uncovering of meaningful patterns of clusters [33].

Principal component analysis (PCA) is a favorite tool in chemometrics for data compression and information extraction. PCA finds linear combinations of the original measurement variables that describe the significant variations in the data. PCA is reducing the dimensionality of the original dataset by explaining the correlation amongst many variables in terms of a smaller number of underlying factors (principal components or PCs) without losing much information. The PCs are a very useful tool for examining the relationships between objects (samples), looking for groups and trends, sorting out outliers. The PCA and CA are unsupervised techniques which offer useful information about samples, but sometimes when the similarities are very prominent, they are not enough for a highly sustained conclusion [35].

All the graphs and classical chemometric methods namely HCA and PCA were performed using Statistica 8.0 (StatSoft, Inc. 1984–2007, Tulsa, USA).

The sum of ranking differences (SRD) compares methods not based on raw data but based on ranks. This chemometric method corresponds to the principle of parsimony and provides an easy tool to evaluate the methods: the smaller the sum, the better the method. The ranking differences are calculated based on the “average antioxidant activity” rank [36, 37]. The sum of ranking differences (SRD) method was applied, using the instructions provided in <http://aki.ttk.mta.hu/srd/>. The detailed description of the method can be found in the original publication of *Károly Héberger* [37].

REFERENCES

1. B. Halliwell; J.M.K. Gutteridge; *Free Radicals in Biologie and Medicine*, 4th ed., Oxford University Press, Oxford, **2007**.
2. J.M.K. Gutteridge; B. Halliwell; *Biochem. Biophys. Res. Commun.*, **2010**, *393*, 561-564.
3. D.L. Gilbert; C.A. Colton; *Reactive Oxygen Species in Biological Systems: An Interdisciplinary Approach*. Kluwer Academic Publishers, New York, **2002**.
4. E. Cadenas; L. Packer; *Handbook of Antioxidants*. 2nd ed., Marcel Dekker, Inc., **2010**.
5. L. Saso; O. Firuzi; *Curr. Drug Targets*, **2014**, *15*, 1-23.
6. H.E. Himwich; W.A. Himwich; *Biogenic Amines*, Elsevier, Amsterdam, **1964**.
7. D.S. Goldstein, R. McCarty; T. Nagatsu; T. Mabeshima; *Catecholamine Research: From Molecular Insights to Clinical Medicine*, Kluwer Academic Publisher, New York, **2002**.
8. S. Shioda; I. Homma; N. Kato; *Transmitters and Modulators in Health and Disease*, Springer, Tokyo, **2009**.
9. M.A. Medina; J.L. Urdiales; C. Rodríguez-Caso; F.J. Ramírez; F. Sánchez-Jiménez; *Crit. Rev. Biochem. Mol. Biol.*, **2003**, *38*, 23-59.
10. B.J. Mans; J.M.C. Ribeiro; J.F. Andersen; *J. Biol. Chem.*, **2008**, *283*, 18721-18733.
11. T. Miura; S. Muraoka; T. Ogiso; *Biochem. Pharmacol.*, **1998**, *55*, 2001-2006.
12. I. Gülçin; *Chem. Biol. Int.*, **2009**, *179*, 71-80.
13. T. Kawashima, K. Ohkubo, S. Fukuzumi, *J. Phys. Chem. B*, **2010**, *114*, 675-680.
14. H.Y. Zhang; *Quant. Struct-Act. Relat.*, **2000**, *19*, 50-53.
15. H.Y. Zhang; Y.M. Sun; X. L. Wang; *Chem. Eur. J.*, **2003**, *9*, 502-508.
16. H.Y. Zhang; *Curr. Comput-Aided Drug. Des.*, **2005**, *1*, 257-273.
17. Y. Da-Peng; J. Hong-Fang; T. Guang-Yan; R. Wei; Z. Hong-Yu; *Molecules*, **2007**, *12*, 878-884.
18. F. Shahidi; *Natural Antioxidants: Chemistry, Health Effects, and Applications*, AOCS Press, **1997**.
19. C.E. Thomas; *Handbook of Synthetic Antioxidants*, Marcel Dekker, Inc., New York, **1997**.
20. *Comprehensive Medicinal Chemistry, Release 2004.1*; MDL Information Systems Inc., San Leandro, CA, **2004**.
21. K. Robards; P.D. Prenzler; G. Tucker; P. Swatsitang; W. Glover; *Food Chem.*, **1999**, *66*, 401-436.
22. R. Apak; E. Capanoglu; F. Shahidi; Editors, *Measurement of Antioxidant Activity & Capacity: Recent Trends and Applications*, 1st ed., John Wiley & Sons Ltd., Chichester, **2018**.
23. C. Sârbu, D. Casoni; *Cent. Eur. J. Chem.*, **2013**, *11*, 679-688.
24. D. Casoni; C. Sârbu; *Spectrochim. Acta A*, **2014**, *118*, 343-348.

COMPREHENSIVE ASSESSMENT OF ANTIOXIDANT AND CHELATING CAPACITY
OF SOME BIOGENIC AMINES AND RELATED DRUGS

25. A. Guidea; C. Zăgrean-Tuza; A.C. Moț; C. Sârbu; *Spectrochim. Acta A*, **2020**, 233, 118158.
26. M.S. Blois; *Nature*, **1958**, 181, 1199–1200.
27. P. Re; N. Pellegrini; A. Proteggente; A. Pannala; M. Yang; C. Rice-Evans; *Free Radic. Biol. Med.*, **1999**, 26, 1231-1237.
28. X.L. Li; A.G. Zhou; Y. Han; Y. *Carbohydr. Polym.*, **2006**, 66, 34-42.
29. M.N.A. Rao; *J. Pharm. Pharmacol.* **1997**, 49, 105-107.
30. I.F. Benzie; J.J. Strain; *Anal. Biochem.*, **1996**, 239, 70-76.
31. R. Apak; K. Güçlü; B. Demirata; et al. *Molecules*, **2007**, 12, 1496-1547.
32. E. Işık; S. Şahin; C. Demir; *Talanta*, **2013**, 111, 119-124.
33. T.C.P. Dinis; V.M.C. Madeira; L.M. Almeida; *Arch. Biochem. Biophys.*, **1994**, 315, 161-169.
34. L. Wilkinson; M. Friendly; *Am. Stat.*, **2009**, 63, 179—184.
35. O. Horovitz; C. Sârbu; H.F. Pop; Clasificarea rațională a elementelor chimice, Editura Dacia, Cluj-Napoca, **2000**.
36. K. Héberger; *Trac. Trends Anal. Chem.*, **2010**, 29, 101–109.
37. K. Héberger; K. Kollár-Hunek; *J. Chemom.*, **2011**, 25, 151–158.

INVESTIGATION, SIMULATION AND COMPARISON OF VARIOUS ROUTES FOR BIOETHANOL PRODUCTION

LETITIA PETRESCU^{a*}, ANA-MARIA POSA^a

ABSTRACT. Bioethanol has proven its value as an alternative fuel to gasoline, in fact, more as an adding than a competitor. Bioethanol has attracted a lot of interest due to its biodegradable nature, low cost, low toxicity and safety. The present work is focused on process modelling and simulation of bioethanol production using biomass and / or CO₂ and H₂ as raw-materials. The first scenario investigated considers the biomass fermentation, the second scenario considers the thermo-catalytic hydrogenation of CO₂ while the combination of the previously methods was assumed in the third scenario. The main advantages of these routes are the reduction of greenhouse gas emissions and the production of one valuable chemical, bioethanol. A productivity of 30,000 tones/year of bioethanol is set for all three cases. Purities, higher than 90% for the main product, are obtained. The technical comparison of the three scenarios leads to the conclusion that the best option to obtain bioethanol is from cellulosic biomass. In this first case, the energy consumption is 0.08 kW / kg bioethanol and the carbon dioxide emissions are 0.96 kg CO₂ / kg bioethanol being much lower than in the other two considered cases.

Keywords: *Bioethanol production, process modelling and simulation, technical comparison*

INTRODUCTION

Renewable energy has gained great importance nowadays, given the problem of environmental concerns and the increased demand for energy. Bioethanol is one of these renewable energy types, which became more and more attractive in the recent years. Bioethanol production and its use as an alternative fuel have a long story, being hard to explore when humans exactly started this production from the solid feed-stock. Compared to the conventional

^a *Department of Chemical Engineering, Babeş-Bolyai University, Faculty of Chemistry and Chemical Engineering, 11 Arany Janos str., RO-400028, Cluj-Napoca, Romania.*

* *Corresponding author: letitiapetrescu@chem.ubbcluj.ro*

fuels (e.g. gasoline), ethanol is able to reduce emissions of particulate matter, toxic chemicals, and greenhouse gasses when it is used in cars engines [1]. The most important characteristic of ethanol, which makes it suitable as a fuel for Otto and diesel engines, is its high octane number [2]. Using bioethanol on a large scale will minimize evaporative emissions, minimizing its impact on the greenhouse gas effect by up to 61% compared to gasoline [3, 4]. Beside a higher octane number it also presents a broader flammability limits, higher flame speeds and higher heats of vaporization than gasoline, thus, allowing for higher compression ratio, shorter burn times and leaner burn engines [5]. Obtaining bioethanol by fermentation can reduce the carbon dioxide emissions because the biomass used in its production is considered to be carbon neutral. Its cycle, from crops to CO₂ usage, is presented in Figure 1.

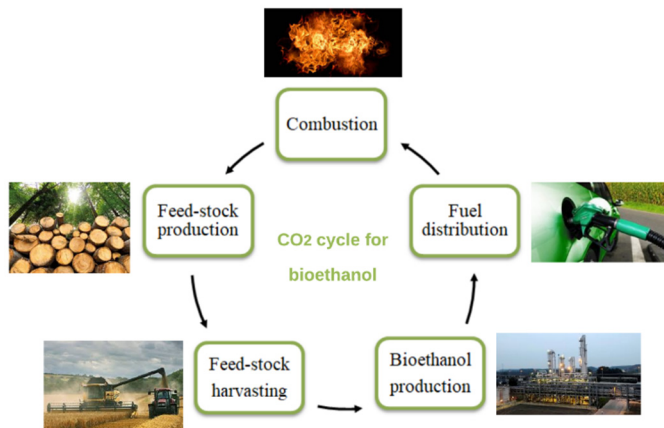


Figure 1. Bioethanol cycle

Balat and co-authors presents also some disadvantages of bioethanol such as: its corrosiveness, low flame luminosity and miscibility with water [5].

There are two types of ethanol industrially produced: synthetic ethanol and fermentation ethanol. Synthetic ethanol is obtained artificially from petrochemical raw-materials, generally by the hydration reaction of ethylene. To achieve a high-quality alcoholic product, the synthesis is performed based on the reaction between ethylene and water, ethylene being produced in refineries. For instance, about 85% of ethanol produced in the United States comes from a fermentation process, but the remaining amount comes from the catalytic hydration in the gas phase of ethylene [6]. Fermentation ethanol or bioethanol can be produced from biomass materials containing sugars, starches or cellulose. The fermentation step is necessary

to convert the sugar into ethanol. It will be followed by a more or less advanced distillation step to separate the alcohol from the water. According to European Renewable Ethanol the main raw-materials used for bioethanol production in Europe are: corn with 43%, wheat with 26%, sugars with 21% followed by other cereals (e.g. 6%) and ligno-cellulosic raw-materials (e.g. wood chips with 4%) [7]. The raw-materials for cellulosic biomass is widely available, it can grow on poor quality marginal land with less water and fertilizer and does not compete with food crops. Cellulosic biomass can be obtained from a variety of sources such as agricultural residues (i.e. corn stover, sugar cane, etc.), agricultural raw-materials grown as energy crops (i.e. switch grass, etc.), forest residues (i.e. fallen branches, leaves, sawdust, etc.), municipal solid waste (i.e. paper and cardboard products) and industrial waste (i.e. sludge for manufacturing paper) [8]. The technology for converting various types of biomass into ethanol is constantly improving and also competes with gasoline production, in terms of costs. Cellulose biomass must be very well prepared to produce fermentable sugars, to obtain as much ethanol as possible [9]. Instead of chemical synthesis, the fermentation process of simple sugars, mostly glucose, will be used to produce ethanol from biomass, especially waste biomass.

Biomass conversion methods to various products are represented in Figure 2. There are three main routes for the production of biofuels from biomass, one involving thermochemical processing, the second one involving biochemical processing and the last one involving physical processing [10].

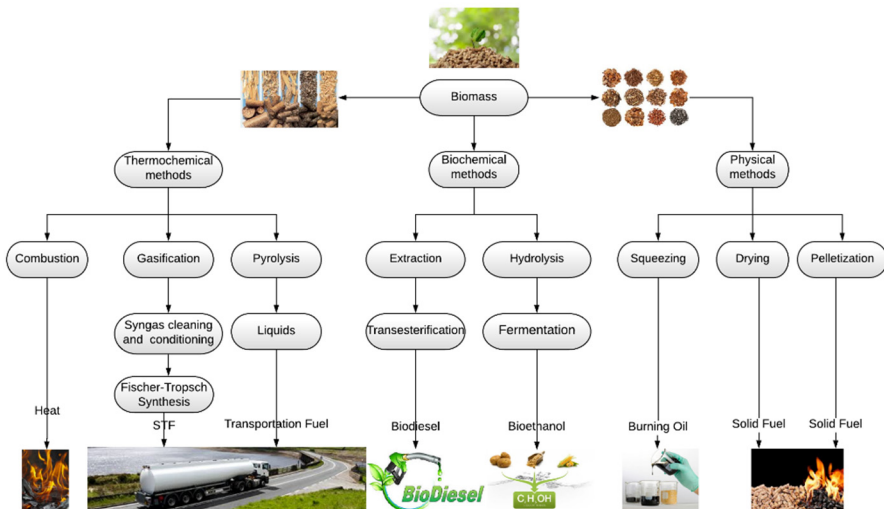


Figure 2. Biomass conversion routes

“Thermo” processing defines the conversion of biomass into a range of products, by thermal decay and chemical reformation, and essentially involves heating biomass in the presence of different oxygen concentrations. Thermal processes are sufficient in terms of energy because the energy required to heat the biomass up to the requested temperatures can be supplied by the partial or total oxidation of carbon from the biomass, reactions that are usually very exothermic [11].

Biochemical conversion of cellulose into ethanol occurs in three stages, pre-treatment, hydrolysis and fermentation. In general, the purpose of pre-treatment is to weaken the structure of the plant cell wall and to improve the access of hydrolytic enzymes to sugar polymers. The raw-material is subjected to mechanics or thermochemical treatment to make the carbohydrate polymers necessary for hydrolysis. Cellulose and hemicellulose must be separated from the lignin, this being possible either by physical and chemical and / or biological pre-treatment. No physical substances are involved in physical pre-treatment. The addition of dilute acid and high-pressure steam, so-called acid-catalysed steam explosion, can improve the enzymatic hydrolysis of cellulose. If pre-treatment takes place chemically, some concentrated or dilute acids will be added to the raw-material. However, concentrated acids are toxic, corrosive, and must be recovered after the process. Therefore, dilute acid hydrolysis has been used instead of many applications, having a high reaction rate and efficient hydrolysis of cellulose [12, 13]. This step is followed by hydrolysis. Water molecules react with the bonds in the structure of cellulose and hemicellulose and degrade them in sugar units such as glucose, xylose, etc. Mineral acids (i.e. sulphuric, hydrochloric, and nitric acid) are used for this process in concentrations between 0.5 and 1.5% [14]. Hydrolysis is usually performed at 100 - 240°C and lasts 2 - 10 minutes. The production of fermentable sugars by acid hydrolysis is between 75 - 90%. Hydrolysis can also be enzymatic. In enzymatic hydrolysis, the structure of cellulose is converted into glucose by enzymes. The biomass must first be treated with a short, diluted step of acid hydrolysis, in which the cellulose structure is disturbed and the hemicellulose decomposes into fermentable sugars. The cellulose is then broken down into cellobiose, which in turn is broken down into glucose. Optimal enzyme activity and optimal reaction conditions such as temperature (e.g. 45 - 50°C) and pH (e.g. 4.8) will increase the ethanol yield. The best method to produce ethanol from biomass is the application of enzymatic hydrolysis [15]. When the sugars have been released, fermentation takes place. The anaerobic bacteria used at this stage to convert sugars (both glucose and xylose) into ethanol is *Zymomonas mobilis*. During the fermentation process, it is important to separate the ethanol produced from the initial liquid, as many microorganisms may not survive the high concentration of ethanol. It is also necessary to separate the solid residue (including lignin) from the liquid mixture. From the remaining liquid containing ethanol, water, and other compounds, the desired product can be separated by distillation [15].

INVESTIGATION, SIMULATION AND COMPARISON OF VARIOUS ROUTES
FOR BIOETHANOL PRODUCTION

The present paper aims to model, simulate and compare, in the ChemCAD 7 software, different technologies for bioethanol production. Cellulosic biomass for the first process respectively carbon dioxide and hydrogen for the second process, and a combination of biomass, carbon dioxide and hydrogen for the third case are proposed as raw-materials for the technologies under investigation. The productivity of the bioethanol plant was set to 3681 kg/h, the equivalent of 30,000 tons/year.

RESULTS AND DISCUSSION

The case studies investigated in the present work are:

Case 1: Bioethanol from biomass production;

Case 2: Bioethanol from CO₂ and H₂;

Case 3: Bioethanol from biomass coupled with bioethanol from CO₂ and H₂.

A schematic representation of the cases under study is illustrated in Figure 3, Figure 4 and Figure 5 under the EXPERIMENTAL SECTION.

Main input and output streams from process modelling and simulation of bioethanol production from biomass (**Case 1**) are centralized in Table 1 and Table 2.

Table 1. Main inputs for bioethanol production from biomass (**Case 1**)

Parameters	Unit of measure	Streams			
		Feed-stock	Acid feed	Enzyme feed	Inoculum feed
Pressure	atm	1	4	1	1
Temperature	°C	45	745	20	41
Vapour fraction	-	-	1	-	-
Liquid fraction	-	1	-	1	1
Component mass flow-rate					
Water	kg/h	6,284.33	13,719.50	873.38	4,730.80
Sulphuric acid		-	402.13	-	-
Cellulose		4,353.38	-	-	-
Hemicellulose		3,200.88	-	-	-
Lignin		2,094.73	-	-	-
Acetate		340.00	-	-	-
Enzyme		-	-	79.31	-
Z. mobilis		-	-	-	26.95
DAP		-	-	-	18.99
CSL		-	-	-	151.78
Total flow-rate		kg/h	16,273.32	14,121.63	952.69

DAP - Di-ammonium Phosphate; CSL - Corn Step Liquor

Table 2. Main outputs for bioethanol production from biomass (**Case 1**)

Parameters	Unit of measure	Streams			
		Output from reactor 3	Wastewater	Bioethanol	CO ₂ stream
Pressure	atm	1	1	1.91	4.76
Temperature	°C	41	101.93	90.97	60
Vapour fraction	-	-	1	-	1
Liquid fraction	-	1	0	1	-
Component mass flow-rate					
Water	kg/h	2,2637.80	4,457.93	303.65	63.38
CO ₂		3,490.86	-	-	3,490.86
O ₂		31.78	-	0.01	31.78
Sulphuric acid		402.13	-	-	-
Glucose		105.14	-	-	-
Xylose		255.72	-	-	-
Cellulose		191.41	-	-	-
Hemicellulose		80.02	-	-	-
Lignin		2,094.73	-	-	-
Furfural		64.15	52.25	0.04	-
Cellobiose		50.51	-	-	-
Glycerol		29.01	-	-	-
Succinic acid		75.66	-	-	-
Acetic acid		374.45	81.22	-	-
Lactic acid		15.87	-	-	-
Xylitol		156.86	-	-	-
Bioethanol	3,683.70	-	3,681.50	2.04	
Total flow-rate	kg/h	33,739.80	4,591.40	3,985.20	3,588.06

As noticed from Table 1, the quantity of biomass introduced into the system is 16,273.32 kg/h. In addition to the biomass raw-material, water, catalyst, steam, enzyme, and inoculum flows are also added. The outputs of the system, which include the desired amount of bioethanol (e.g. 3,681.5 kg/h), are reported in Table 2. All by-products will be recycled into the system, except for water, which is sent to the wastewater treatment plant, and CO₂. Table 3 presents the validation of the proposed model.

Table 3. Model validation for bioethanol production process (**Case 1**)

Stream name	Outputs stream (simulation)	Literature [16]
	Bioethanol output	Bioethanol output
Components flows	ton/h	ton/h
Water	34.10	34.21
CO ₂	25.00	25.00
Bioethanol	26.36	22.75
Total mass flow	85.46	82.01

From the ChemCAD simulation performed during this study it can be concluded that starting from a quantity of 114.34 tons/h of cellulosic biomass, a quantity of 26.36 tons/h of bioethanol (with 92.38% purity) was obtained. Data from the literature indicate a flow rate of 22.75 tons/h bioethanol, 99% purity. Calculating the error between the data obtained in the simulation and those in the literature, an error of less than 3% is obtained, which allows us to state that there is a very good concordance between the two data sets. After the model was validated, it was updated to the desired bioethanol production capacity (e.g. 3.68 tons/h).

The inputs and output streams for bioethanol production from CO₂ and H₂ (**Case 2**) are summarized in Table 4.

Table 4. Main inputs & outputs for bioethanol production from CO₂ & H₂ (**Case 2**)

Parameters	Unit of measure	Streams			
		CO ₂	H ₂	Bioethanol	Waste water
Pressure	atm	24.67	24.67	0.19	0.98
Temperature	°C	50	50	39.59	46.25
Vapour fraction	-	1	1	-	-
Liquid fraction	-	-	-	1	1
Component mass flow-rate					
CO ₂	kg/h	18,369.29	-	23.78	10.56
H ₂		-	2,510.71	0.21	0.16
CO		-	-	0	0.71
Dimethyl ether		-	-	110.13	0
Methanol		-	-	33.32	133.45
Ethanol		-	-	3,681.91	192.68
Water		-	-	77.84	8,154.48
Total flow-rate	kg/h	18,369.29	2,510.71	3,927.19	8,492.04

The quantity of the raw-material introduced into the system (i.e. CO₂ and H₂) is 20,880 kg/h. The outputs of the plant, which include the desired amount of bioethanol (e.g. 3,681.9 kg/h), are also reported in Table 4. Model validation is summarized in Table 5.

Table 5. Model validation for bioethanol production process (**Case 2**)

Stream name	Outputs stream (simulation)	Literature [17]
	Bioethanol output	Bioethanol output
Components flows	ton/h	ton/h
Methanol	0	0
Water	0	0
Bioethanol	2.50	2.51
Total mass flow	2.50	2.51

In the first step, after building the model this was compared with a literature model. The simulation results show that starting from a quantity of 20.88 tons/h of CO₂ and H₂, a quantity of 2.50 tons/h of ethanol is obtained, with 99.80% purity. Literature data indicate a flow rate of 2.51 tons/h ethanol, with 100% purity. Calculating the error between the data obtained in the simulation and those in the literature, an error of less than 3% is obtained, which allows us to state that there is a very good concordance between the two data sets. After the model was validated it was updated to the desired ethanol flow-rate (e.g. 3.68 tons/h), rescaling all the inputs streams.

Case 3 represents a combination of the first two cases. The CO₂ generated within **Case 1** combined with H₂ from water electrolysis, electricity for water electrolysis being generated using renewable sources (i.e. biomass, wind, photovoltaic) leads to additional bioethanol. Therefore, using a smaller amount of biomass, more exactly 13,879.51 kg/h a quantity of 3,140.50 kg/h bioethanol and 2,976.02 kg/h CO₂ will be generated. The CO₂ captured together combined with a H₂ stream, will generate an additional amount of bioethanol, more precisely 541.50 kg/h. The total amount of bioethanol generated within the combined technologies case will be about 3682 kg/h.

A comparison of the three cases analysed in the present research study is presented in Table 6.

Table 6. Comparison of the three cases of bioethanol production

Case no.	Case 1	Case 2	Case 3
Raw materials	Biomass	CO ₂ + H ₂	Biomass & (CO ₂ + H ₂)
Mass flow-rate [kg/h]	16,273.32	20,880.00	17,262.50
Main product	Bioethanol		
Molar-flow-rate [kmol/h]	79.91	79.92	79.92
Mass flow-rate [kg/h]	3,681.50	4,681,91	3,682.00
Ethanol Purity [%]	92.38	94.00	93.00
Energy consumption [kW / kg ethanol]	0.08	1.97	0.36
CO ₂ emissions [kg CO ₂ /kg ethanol]	0.95	3.36	1.30
Equipments no.	15	42	57

The simulation for the third case, called **Case 3**, indicates that starting from a quantity of 17.26 tons/h of biomass and CO₂ and H₂, a quantity of 3.68 tons/h of ethanol is obtained, with 93% purity. Comparing all three cases investigated, as seen in the above mentioned table, the goal of obtaining the same amount of main product is achieved. It results that the best process to obtain bioethanol is from biomass. The first case, **Case 1**, determines purity higher than 90% of the main product, lower energy consumption and lower carbon dioxide emissions than in the other two cases studied.

According to the scientific literature [17], the cost of ethanol production from corn stover is about 0.56 euro/l while the ethanol production from CO₂ is around 1.33 euro/l. Even if the ethanol production price from corn stover is expected to rise in the near future more effort should be paid by the CO₂ utilization route in order to be competitive with the bio-based routes. The technical, environmental as well as economic aspects stress once more the benefits of obtaining bioethanol from corn stover.

CONCLUSIONS

The present work aimed at modelling and simulation of three production plants of 30,000 tons/year of bioethanol, starting from different raw-materials. Bioethanol production from cellulosic biomass (i.e. corn stover) was compared to bioethanol production obtained from thermo-catalytic hydrogenation of CO₂ and with a third method consisting of a combination of the above

mentioned two cases. The three processes were modelled and simulated in the ChemCAD software program version 7.1.5. The obtained models were validated using data from the scientific literature, observing a good correlation between the simulated data sets and those presented by the scientific literature, the error between them being less than 3%. After models validation they have been adapted to the desired productivity. The desired purity of the final product was over 90%. In the case of the bioethanol production from biomass, a purity of 92.38% bioethanol was obtained; in the case of the thermo-catalytic hydrogenation process of carbon dioxide a purity of 94% was obtained, while in the third case the purity was 93.00%. In addition, for comparison of the three cases, beside the purity of the main product, other parameters such as specific energy consumption or CO₂ emissions should be considered. Therefore, as can be deduced from the previous data, the amount of energy required for the operation of the plant in the first case is 0.08 kW / kg ethanol. The second case has an energy requirement of 1.97 kW / kg ethanol and the third case of 0.36 kW / kg ethanol. The lowest CO₂ emissions are registered in the first case. The value is 0.29 times lower than the value obtained in the second case and 0.74 times lower than the value obtained in the third case. Having all the necessary data for a comparison between the three cases, it results that the best method to obtain bioethanol is represented by **Case 1**, by using a biomass raw-material of 16.27 tons/h.

EXPERIMENTAL SECTION

GENERAL PRESENTATION

In the present study, the raw-material used in the production of bioethanol is represented by the residues left on the field after the corn harvest. The main compounds of this biomass are cellulose, hemicellulose, and lignin. As mentioned above, there are three pathways to obtain bioethanol: biochemical, thermochemical and physical. The biochemical pathway was used in this study, which is based on the presence of microorganisms and enzymes. The flow-sheet of the bioethanol production process is presented in Figure 3.

INVESTIGATION, SIMULATION AND COMPARISON OF VARIOUS ROUTES
FOR BIOETHANOL PRODUCTION

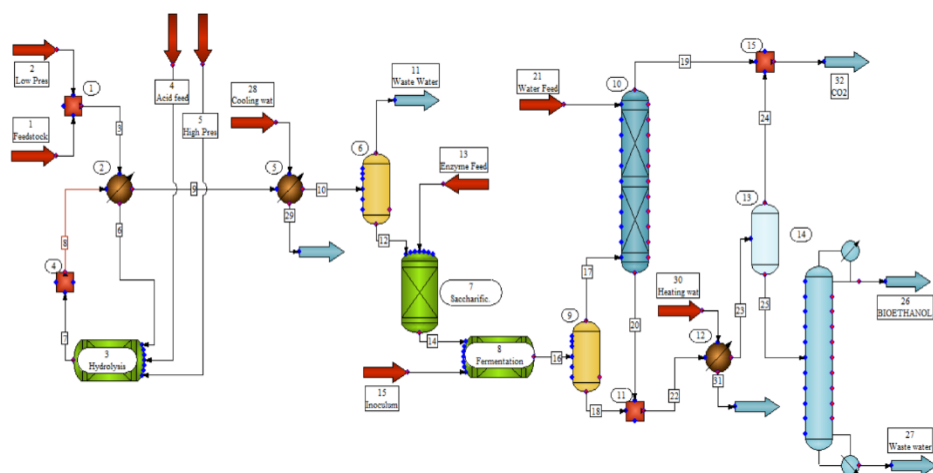


Figure 3. Process flow diagram for bioethanol production from biomass

The production capacity of the plant is approximately 3,681 kg/h bioethanol (equivalent to an annual production of 30,000 tons/year). Sulphuric acid is used as catalyst in this process. The purity of the ethanol obtained is 92.38% (by weight). The mixture of raw-material (Stream 1) and the low-pressure steam (Stream 2) is sent to a heat exchanger (Unit 2). It uses as a heating agent the heat given off by the reaction products, raising the flow temperature from 96.64°C to 100°C. The slightly impure stream together with the acid stream (Stream 4) and the high-pressure steam (Stream 5) are transferred to a reactor (Unit 3). The steam characteristics are 268°C and 13 atm. In the equilibrium reactor, the hydrolysis of the cellulosic raw-material takes place, in which most of the hemicellulose is converted to xylose. The reactor is considered to be adiabatic. The remaining cellulose and hemicellulose and all lignin will remain unconverted through the hydrolysis process. Because the conversion is done by fermenting sugars, the process cannot convert non-carbohydrate components from biomass (such as lignin and proteins). The gaseous flow leaves the reactor at 217.17°C and 12.1 atm. Stream 9 reaches a heat exchanger that uses water as a cooling agent, decreasing the flow temperature from 217.17°C to 190°C. A separator (Unit 6) is present between the hydrolysis reactor and the saccharification reactor (Unit 7). The separator is an isentropic flash working at 1 atm. It is operated at atmospheric pressure to evacuate part of the water and some by-products. The liquid (Stream 12) leaving the separator together with a stream of enzymes is sent to a second reactor (Unit 7). The saccharification reactor converts cellulose and cellobiose into sugars, such as glucose. The reactor works isothermally at 65°C. The stream leaving the second reactor (Stream 14) and the inlet

stream containing the fermentative bacteria (Stream 15) are mixed in a third reactor. Thus, the fermentation process of the formed sugars takes place in the equilibrium reactor (Unit 8). A second flash (Unit 9) is used after the fermentation reactor to separate the condensable (most of the CO₂). This gas-liquid separator works at 1 atm and 41°C. A scrubber with 4 stages (Unit 10) is used to separate the ethanol and the water contained in the gas stream (Stream 17) coming from the flash separator (Unit 9). A flow-rate of 5,026.68 kg/h water (Stream 21) with a temperature of 26°C and a pressure of 1 atm is fed on the first stage, while the gas flow (Stream 17) with a temperature of 41°C and a pressure of 1 atm enters on the last stage; At the top of the column is recovered most of the CO₂ (Stream 19) in the form of vapours. The liquid flow at the bottom of the distillation column (Stream 20) and the liquid at the bottom of the separator (Stream 18) are mixed; the mixed stream is preheated from 41°C to 100°C, using a heat exchanger (Unit 12). Another flash is used to separate all the carbon dioxide in the form of vapours (Stream 24). The impure ethanol (Stream 25) is directed to a distillation column (Unit 14). This unit has 34 plates, the feed stage being stage number 5. This column separates the ethanol as distillate. The specifications used for this column are: distillate component (i.e. ethanol) recovery 99.99%, bottom component (i.e. water) recovery 98.90%. All the CO₂ recovered together with a stream of hydrogen produced by the process of electrolysis of water can be used to produce ethanol again. Finally, all the water flows leaving the process are mixed and sent to a waste-water treatment plant. ChemCAD process simulator (version 7) was used to simulate the above described process using the NRTL thermodynamic package. The reactions taking place in the biomass conversion to ethanol are reported in Table 7.

Table 7. Main reactions considered in bioethanol production from biomass

Reaction section	Reaction	Fractional conversion used in ChemCAD
Hydrolysis	$Cellulose + H_2O \rightarrow Glucose$	0.007
	$Cellulose + 0.5H_2O \rightarrow 0.5\ Cellobiose$	0.007
	$Hemicellulose + H_2O \rightarrow Xylose$	0.925
	$Hemicellulose \rightarrow Furfural + H_2O$	0.05
	$Acetate \rightarrow Acetic\ acid$	1
Saccharification	$Cellulose + H_2O \rightarrow Glucose$	0.94
	$Cellulose + 0.5H_2O \rightarrow 0.5\ Cellobiose$	0.012
	$Cellobiose + H_2O \rightarrow 2Glucose$	1

INVESTIGATION, SIMULATION AND COMPARISON OF VARIOUS ROUTES
FOR BIOETHANOL PRODUCTION

Reaction section	Reaction	Fractional conversion used in ChemCAD
Fermentation	$Glucose \rightarrow 2 CH_3CH_2OH + 2 CO_2$	0.95
	$3 Xylose \rightarrow 5 CH_3CH_2OH + 5 CO_2$	0.85
	$Glucose + H_2O \rightarrow 2 Glycerol + O_2$	0.004
	$Glucose + 2CO_2 \rightarrow 2 Succinic acid + O_2$	0.006
	$Glucose \rightarrow 3 Acetic acid$	0.015
	$Glucose \rightarrow 2 Lactic acid$	0.002
	$3 Xylose + 5 H_2O \rightarrow 5 Glycerol + 2.5 O_2$	0.003
	$Xylose + H_2O \rightarrow Xylitol + 0.5 O_2$	0.046
	$3 Xylose + 5 CO_2 \rightarrow 5 Succinic acid + 2.5 O_2$	0.009
	$2 Xylose \rightarrow 5 Acetic acid$	0.014
	$3 Xylose \rightarrow 5 Lactic acid$	0.002

A comparison with other renewable process for ethanol production is described in this section as we can see in Figure 4 and Figure 5. The comparison method refers to ethanol production by thermo-catalytic hydrogenation of carbon dioxide.

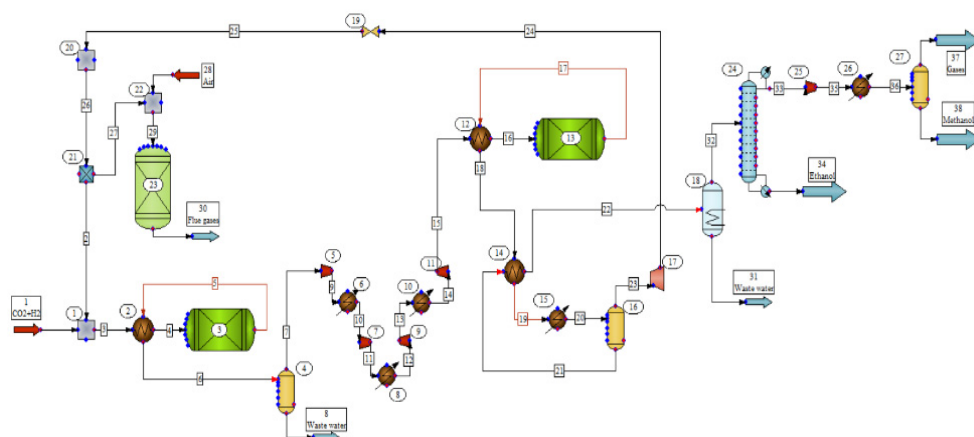


Figure 4. Process flow diagram for bioethanol production from CO₂ and H₂

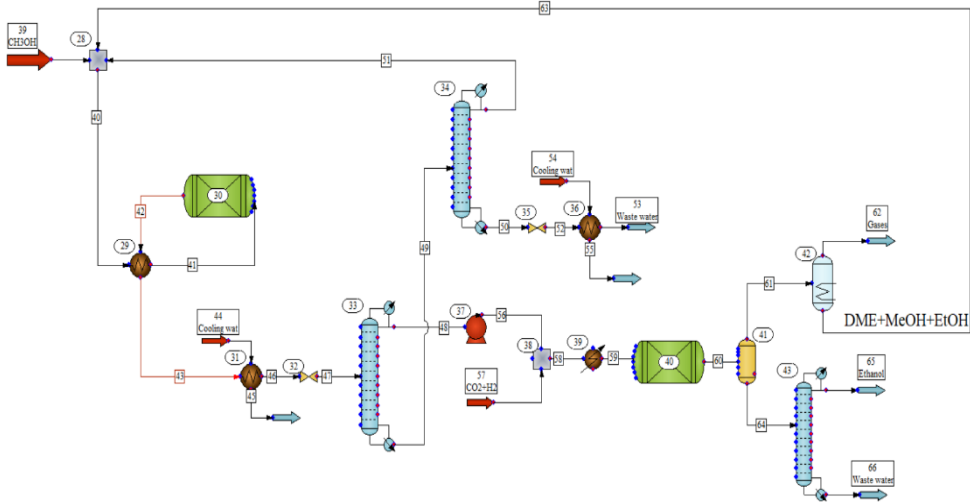


Figure 5. Process flow diagram for bioethanol production from methanol

The reaction mechanism consists of:

- hydrogenation of carbon dioxide to carbon monoxide and water (reverse Water Gas Shift (WGS) reaction)
(R1): $CO_2 + H_2 \leftrightarrow CO + H_2O$ and
- syngas conversion to ethanol and water
(R2): $2CO + 4H_2 \leftrightarrow C_2H_5OH + H_2O$.

After the WGS reactor, the resulting water is removed from the system and the remaining gas is introduced into alcohol synthesis reactor, in which the methanol is recycled, the following reactions taking place.

- (R3): syngas conversion to methanol $CO + 2H_2 \leftrightarrow CH_3OH$,
- (R4): methanol hydrogenation with ethanol and water formation $CH_3OH + CO + H_2 \leftrightarrow C_2H_5OH + H_2O$, and
- (R5): ethanol hydrogenation with propanol and water formation (side reaction) $C_2H_5OH + CO + 2H_2 \leftrightarrow C_3H_7OH + H_2O$.

This route was also modelled using ChemCAD process simulator (version 7). The production capacity of the plant is 3681 kg/hour of ethanol, the desired purity of the ethanol being higher than 90% by weight. The PSRK and Mixed Model packages were used for the enthalpies. The raw-materials introduced in the system are: carbon dioxide, 18,369.29 kg/h, with a pressure of 24.6 atm and a temperature of 50°C and hydrogen, 2,510.72 kg/h, with a

pressure of 24.6 atm and a temperature of 50°C. The CO₂ and H₂ mixture is sent to a heat exchanger that uses as heating agent the heat given off by the reaction products, raising the flow temperature from 37.48°C to 487.8°C. The stream is introduced into a reactor operated at 560°C and 24.6 atm. The reactor is considered to work isothermal, the reactions, (R1) and (R2) occurring in series. The raw-materials conversion is 62%. The reaction products leave the reactor at 560°C, but using a cooler, the stream temperature is decreased to 112°C. The products are sent to a phase separator, in this case, a gas-liquid separator, operating at a 30°C and 15.8 atm. The resulting vapours suffer a compression process. 85% efficiency was considered for the compressors the pressure being increased from 19.7 atm to 78.9 atm. Four compressors with four intercooling heat exchangers are used. The pressure was increased with 20 bars after each compression step. This mixture is heated, raising the temperature from 114.56°C to 200.94°C. The stream is furthermore introduced into another reactor operated isothermally at 300°C and 78.9 atm. A conversion of 85% is achieved in this unit. The reaction products are introduced into a heat exchanger, the temperature decreasing to 211.9°C. The gas-liquid separation occurs at 50°C and 98.6 atm in a flash unit. The resulting vapours, at the top of the separator, are compressed until they reach a pressure of 78.9 atm. The compressor is an adiabatic compressor having an efficiency of 80%. The vapour stream is mixed with the input stream of the process. A percentage of 77.25% of this stream is recycled back to the process, while the remaining stream, along with an air stream, is introduced into a Gibbs reactor operated at 1000°C and 19.7 atm. The remaining liquid is sent to a distillation column with 20 plates, the feed stage being stage 10; the separation of ethanol from methanol takes place in this column. The distillate temperature was considered 26.5°C, ethanol component mole fraction being 0.997. Part of the methanol is recycled, being mixed with the streams at the entrance to the process while the other part is directed to the dimethyl ether (DME) production process, which will generate additional ethanol. Thus, slightly impure methanol is mixed with a recycled stream containing more than 95% ethanol, methanol, and water. The mixture reaches a heat exchanger that uses as heating agent the heat released by the reaction products, raising the flow temperature from 100°C to 250°C. The stream is introduced in a reactor operated at 280°C and 14.5 atm, the methanol conversion being 80%. Reaction products and unreacted ethanol are cooled from 113°C to 89°C in a heat exchanger using cooling water. The cooling flow pressure (i.e. 14.5 atm) is reduced using a valve up to 7.3 atm. The mixture is furthermore introduced in a distillation column with 24 stages, the feed stage being stage number 13; the separation of DME as distillate takes place in a proportion of 80%. The specifications used for this column are: reflux ratio 0.36, bottom product temperature 153°C. Un-separated DME, methanol, ethanol and water from the bottom of the column are sent to a second

distillation column, having 28 stages, the input feed being on stage 15. The separation of waste-water from the mixture takes place here, the mixture being recycled and mixed with the input methanol stream. The specifications used for this column are: distillate temperature 75°C, 99.99% water in the bottom stream. The separated DME stream from the first column is mixed with a stream containing CO₂ and H₂, then preheated to 180°C, using a heat exchanger. The stream is sent to a reactor operated at 180°C. A DME conversion of 72% was assumed here. The slightly formed ethanol will be separated from the vapor stream thus formed, and the rest of the mixture is recycled, mixing with the methanol flow at the beginning of the process. Impure ethanol is fed to a distillation column having 20 stages, the input stream being fed on stage 10, where the separation of ethanol as distillate takes place. Finally, all the waste-water streams leaving the process are mixed and sent to the waste-water treatment plant.

REFERENCES

1. G. Whitten. Air Quality and Ethanol in Gasoline, Smog Reyes, December, **2004**.
2. M. Arshadi, H. Grundberg H. Biochemical production of bioethanol. *Handbook of Biofuels Production*, **2011**, 199 – 220.
3. Renewable Fuels Association, <http://www.ethanolrfa.org> (Accessed in June 2020).
4. Natural Resources Defense Council, *Unlocking the Promise of Ethanol*, February **2006**.
5. M. Balat, H. Balat, C. Öz. *Progr. Energ. Combust. Sci.*, **2008**, 551 – 73.
6. H.J. Arpe, K. Weissmermel K. *Industrial Organic Chemistry*, **2010**, Vol.8, 393.
7. <https://epure.org> (Accessed in February 2020).
8. U.S. Department of Energy, Energy Efficiency and Renewable Energy (EERE) Biomass Program, *Feedstock Types*, **2012**.
9. P.C. Badger. *Ethanol from cellulose: A general review*, **2002**, 17 – 21.
10. V.S. Sikarwara, M. Zhaoa, P.S. Fennelld, N. Shahd, J.A. Edward. *Progr. Energ. Combust. Sci.*, **2017**, 189 – 248.
11. S. Clarke, F, Preto, *Biomass densification for energy production*, Ontario Ministry of Agriculture and Food factsheet, 2011 (Accessed March 2020).
12. S. Brethauer, M. H. Studer. *Int. J. Chem.*, **2015**, 572 – 581.
13. C.E. Wyman C.E. Handbook on bioethanol. Production and utilization. Washington, DC, **1996**.
14. D. Pimentel, T.W. Patzek T.W. *Nat. Resour. Res.*, **2005**, 65 – 70.
15. M. Arshadi, H. Grundberg. *Processes and Technologies. Biochemical production of bioethanol*, Handbook of Biofuels Production, **2011**.
16. http://www.bioethanol.prosim.net/E10_BioethanolPlant.pdf (Accessed in March 2020).
17. K. Atsonios, K.D. Panopoulos, E. Kakaras. *Int. J. Hydrog. Energ.*, **2016**, 792 – 80.

THE INFLUENCE OF GEOGRAPHIC LOCATION AND ENZYME-ASSISTED EXTRACTION ON ESSENTIAL OILS COMPOSITION OF *THYMUS SERPYLLUM* GROWING WILD IN TRANSYLVANIA

IOANA GOJA^a, ADELINA ULICI^a, MONICA CULEA^b,
VASILE MUNTEANU^c, PAULA PODEA^a

ABSTRACT. A comparative study concerning the influence of geographic location and also the influence of enzyme-assisted extraction on the essential oils isolated from Transylvanian wild *Thymus serpyllum* was achieved. The collected *Thymus serpyllum* plants, from three different regions from Transilvania, were hydrodistilled to yield essential oils. The influence of enzymatic assisted extraction on the essential oils isolated from *Thymus serpyllum* was evaluated. All analyzed plants proved to belong to carvacrol chemotype class. The major constituents of wild *Thymus serpyllum* from these three regions were carvacrol (26.58%-47.62%), p-cymene (8.61%-18.97%), methylcarvacrol (8.81%-13.35%), thymol (1.6%-11.07%), gamma-terpinene (2.09%-7.55%), beta-bysabolene (3.42%-5.18%), caryophyllene (3.17%-4.83%). Using the enzymatic treatment, the percentage in composition of some components was modified and proved to have an improvement on antioxidant and antimicrobial properties. All studied essential oils exhibited considerable antioxidant and antimicrobial activity.

Keywords: *Thymus serpyllum* essential oils, enzyme assisted extraction, antioxidant activity, antimicrobial activity, GC/MS

^a Babes-Bolyai University, Faculty of Chemistry and Chemical Engineering, Kogalniceanu str. No. 1, RO-400084 Cluj-Napoca, Romania

^b Babes-Bolyai University, Faculty of Physics, Kogalniceanu str. No. 1, RO-400084 Cluj-Napoca, Romania

^c Babes-Bolyai University, Faculty of Biology and Geology, Kogalniceanu str. No. 1, RO-400084 Cluj-Napoca, Romania

* Corresponding author: mpaula@chem.ubbcluj.ro

INTRODUCTION

Thymus serpyllum L., also known as wild thyme, belongs to the Lamiaceae plant family. *Thymus serpyllum* is growing spontaneous in extended regions of northern and central Europe and at high altitude in Mediterranean areas¹.

Based on several studies *Thymus serpyllum* essential oil are an excellent source of bioactive compounds with powerful antioxidant, strong antibacterial and antifungal activity, anti-inflammatory, antitumor, and cytotoxic properties^{1,2,3}.

A highly variation in *Thymus serpyllum* essential oil compounds proportion was observed due to the origin, environmental condition oil also with plant stage of development and metabolism⁴. The essential oils isolated from *Thymus* genus plants, are characterized by a chemical polymorphism. Depending on source and geographical location several chemotypes (geraniol, germacrene D, citral, linalool, (E) caryophyllene, α -terpinyl acetate, carvacrol, and thymol) has been considered¹. Growing spontaneous, *Thymus serpyllum* could also been characterized by a variety of chemotypes, even within on growing area⁵.

Due to great variability in *Thymus serpyllum* essential oil composition, the evaluation of *Thymus serpyllum* grown wild in different regions is of high interest. Climatic conditions and the applied extraction technique, can influence both the qualitative composition and contents of the individual components of the isolated essential oils and consequently the bioactive properties like antioxidant and antimicrobial activity. Enzyme-assisted extraction technique is emerging as an alternative and eco-friendly approach to extract volatile oils. The biotechnological application of enzymes is not currently exploited to its maximum potential. Hydrolytic enzymes can interact with cell walls, break down their structural integrity and facilitate the release of intracellular contents from plant materials⁶. In this way, enzymes will ease the extraction and higher yields in essential oils will be obtained. Also, using this enzymatic treatment, the flavours profile can be easily modified, in sense that the percentage in composition of some components can be enhanced and also as a result of these different bioactive properties can appear. Enzymatic treatment in essential oil obtained from some spices as fenugreek, garlic, cumin, celery, pepper, mustard, chilli and citrus peel has been reported^{7,8,9,10,11,12,13}. Also results about the enzymatic influence on *Thymus capitatus* and *Rosmarinus officinalis* leaves were reported¹⁴.

In order to establish the impact of geographic location on the composition of the volatile oils, we propose a comparison study on isolated essential oils from *Thymus serpyllum* plants, collected from three different

geographic areas of Transylvania, Romania. Our purpose is to investigate the isolated essential oils chemical components and to compare them in terms of antioxidant and antimicrobial activities. Also, the influence of an enzymatic the effects of enzymatic pre-treatment on the yields, chemical composition and biological properties of *Thymus serpyllum* essential oil will be evaluated.

RESULTS AND DISCUSSION

The goal of this work was to obtain a comparative study concerning the influence of the growth regions and also the influence of enzymatic assistant extraction on the essential oils isolated from *Thymus serpyllum*. The collected *Thymus serpyllum* plants were from three different regions from Transilvania. Chemical composition, the antioxidant and antimicrobial activities of isolated essential oils were determined and compared. The influence of enzymatic assistant extraction on the essential oils isolated from *Thymus serpyllum* was investigated. The essential oil from plants collected from Nasaud area was extracted using classic Clevenger method and comparative the plant was treated with an enzymatic prepartate with a cellulosic and pectolytic activity followed by Clevenger hydrodistillation.

The *Thymus serpyllum* volatile oils obtained were light-yellow in color with herbaceous odor. Identification of chemical components in isolated essential oils by GC/MS was investigated.

The essential oils yields and the chemical composition of the essential oil analyzed by GC–MS

The yields of the obtained essential oils are provided in Table 1. Comparing the obtained essential oils from selected *Thymus serpyllum* plants, the highest yield was obtained for essential oil obtained from Nasaud area (0.50 ± 0.1 (%v/w)), followed by Tamasesti area (0.41 ± 0.1 (%v/w)). The lowest essential oils yield was obtained in case of Mociu area (0.34 ± 0.1 (%v/w)). The obtained essential oil yields are comparable, not such a big difference was observed. In case of the plant enzymatic treatment a yield improvement was observed with 12 % (0.56 ± 0.1 (%v/w)). The effect of enzymes treatment on the essential oil yield was not so high, but differences in composition were observed.

There are some reports on chemical composition and yields of the essential oils from *Thymus serpyllum* and from these studies we can conclude that chemical composition and yields are consider to be highly affected of

factors like climatic conditions, geographic growth region, stage of plant maturity and even the altitude of the growth region^{1,4,5}. Our results were similar with literature reported yields. The reported *Thymus serpyllum* essential oils yields, originated from different countries is between 0.07% to 0.6%⁵ and even higher 0.1 to 1%¹⁵. For *Thymus serpyllum* grown in Northern Kazakhstan, the essential oils yields were between 0.4- 1.4%¹⁶.

Table 1. Essential oils yields.

Yield(%v/w)	<i>Thymus serpyllum</i>
0.38±0.05	Mociu area
0.41±0.05	Tamasesti area
0.50±0.05	Nasaud area
0.56±0.05	Nasaud area enzymatically treated

The main components of the essential oils obtained from *Thymus serpyllum* plants are presented in Table 2. Identification of the constituents was based on comparison with mass fragmentation pattern and spectral comparison using NIST and Wiley mass spectra libraries of standards.

Totally 70 components were identified in the analysed plants. The composition of the studied essential oils showed that the plants are related, but differences appear in compounds relative concentration. The major constituents of *Thymus serpyllum* growing in these three regions from Transylvania were carvacrol (26.58% - 47.62%), p-cymene (8.61%-18.97%), methylcarvacrol (8.81%-13.35%), thymol (1.6%-11.07%), gamma-terpinene (2.09%-7.55%), beta-bisabolene (3.42%-5.18%), caryophyllene (3.17%-4.83%). In all three analysed essential oils, carvacrol was the majority compound.

According to *Thymus serpyllum* research studies, there is high variability in chemical composition of studied essential oils. *Thymus serpyllum* essential oil has a variety of chemotypes. Carvacrol is considered the main component, conformable to PDR from Herbal Medicine¹, but a number of studies present thymol as the major constituent in *Thymus serpyllum* essential oils^{2,17}. Thymol is the isomer of carvacrol, so differences between their ratio can exist. European Pharmacopeia agreed that a total content of carvacrol and thymol should be around 40% or more¹. Even that carvacrol and thymol are considered the principal components, some studies show other main constituents, carvacrol and thymol being just minority constituents^{1,5,18,19,20}. In some essential oil obtained from *Thymus serpyllum* growing wild in Lithuania, carvacrol and thymol weren't identified, the major components were 1,8-cineole (16.3-19.0 %), myrcene (9.7-10.7 %), 3-caryophyllene (9.6-11.3%), germacrene D (5.9-8.0%)²¹. The significant variety in composition is

connected with plant stage of development and metabolism and also with climatic conditions and geographic position of the growth region. An example was given by content of *Thymus serpyllum* essential oil growing wild in Altai Mountains, in which compositional differences appear depending on the altitude²². Also *Thymus serpyllum* grown in Kumaon region of Western Himalaya was investigated, and seasonal variation in essential oil composition was found⁴.

Table 2. Chemical composition of the obtained essential oils analysed by GC-MS

Component	M	RT	<i>Thymus serpyllum</i> %			
			Mociu	Tamasesti	Nasaud	Nasaud enzymatic
thujene	136	7.58	-	-	0.47	-
alpha -pinene	136	7.76	0.59	0.29	1.13	-
trans- ocimene	136	7.83	-	0.39	-	-
carene	136	8.07	-	0.19	0.15	-
camphene	136	8.37	0.31	-	0.79	-
beta-myrcene	136	9.23	1.17	0.81	-	-
beta-pinene	136	9.52	0.21	0.58	0.71	-
1-octen-3-ol	130	9.98	3.3	1.7	1.26	1.0
delta-carene	128	10.18	-	-	0.19	-
cis ocimene	136	10.48	-	-	-	<0.1
alpha- terpinene	136	10.62	1.13	-	0.91	-
p-cymene	134	10.99	10.66	8.61	18.97	2.37
limonene	136	11.04	-	0.31	-	-
eucaliptol	136	11.11	-	-	-	0.4
sabinene	136	11.61	-	<0.1	<0.1	-
gamma-terpinene	136	12.07	7.55	2.09	3.95	0.52
beta ocimene	136	12.97	-	-	-	<0.1
terpinolene	136	13.03	-	0.09	0.14	-
linalool	136	13.59	1.64	2.6	0.78	2
terpineol	154	13.82	-	<0.1	0.14	<0.1
octyl-acetate	172	14.16	-	0.32	-	-
verbenol	152	14.3	-	0.1	-	<0.1
tujanol	152	14.58	<0.1	<0.1	0.09	0.14
camphor	152	15.49	0.12	0.09	0.14	0.25
citronellol	156	15.62	-	-	-	0.14
izomentona	154	15.75	-	0.17	<0.1	-
Borneol	154	16.36	3.1	2.27	1.8	0.8
4-terpineol	154	16.6	1.49	1.39	0.91	3.18
thujone	152	16.78	-	0.17	0.48	-

Table 2 (continued)						
Component	M	RT	Mociu	Tamasesti	Nasaud	Nasaud enzymatic
cuminol	150	16.94	-	-	0.25	<0.1
beta-fenchol	150	17.32	0.5	0.1	0.31	0.64
cis-carveol	152	17.35	-	<0.1	-	-
p-cymen-8-ol	150	17.5	0.6	-	-	0.29
carvomenthol	156	17.96	0.15	<0.1	-	-
trans-carveol	152	18.15	-	0.1	-	-
thymol methyl ether	164	18.23	4.15	3.78	3.34	3.74
methylcarvacrol	164	18.62	13.35	8.81	9.17	8.21
thymoquinone	164	19.18	0.46	<0.1	-	0.74
geraniol	154	19.24	-	0.09	1.58	1.95
piperitona	152	19.83	0.17	2.62	0.94	-
izopiperitona	152	19.9	-	0,28	-	-
cis-geraniol	154	20.08	-	-	-	<0.1
dihydroedulan	194	20.27	-	0.1	-	-
thymol	150	20.67	4.84	1.6	11.07	24.01
carvacrol	150	21.11	31.32	47.62	26.58	28.81
isoeugenol	164	21.83	-	-	-	0.11
terpinyl acetate	196	22.24	<0.1	0.11	0.39	0.52
eugenol	164	22.65	-	-	-	0.6
carvacryl acetat	192	22.87	-	<0.1	<0.1	-
copaene	204	23.08	-	1.3	0.09	0.13
geranyl acetate	198	23.18	-	-	0.15	0.27
beta-bourbonene	204	23.36	0.1	1.18	0.22	0.37
longifolene	204	24.04	-	-	-	0.15
caryophyllene	204	24.6	4.83	3.17	4.49	4.1
germacrene	204	24.87	0.09	0.12	0.15	0.23
aromadendrene	204	25.14	-	0.09	<0.1	0.12
farnesene	204	25.44	-	-	0.09	0.19
humulene	204	25.71	<0.1	<0.1	0.24	0.25
muurolene	204	26.29	<0.1	<0.1	0.26	0.53
cubebene	204	26.51	0.14	0.43	0.24	0.33
valencene	204	26.8	-	-	0.16	0.31
beta-bysabolene	204	27.33	5.18	3.42	4.31	5.62
gamma-cadinene	204	27.55	-	<0.1	0.18	0.35
delta-cadinene	204	27.65	-	-	0.28	0.52
trans-nerolidol	222	29.11	-	-	0.55	3.11
caryophyllene oxyde	220	30.28	2.49	1.98	1.63	2.21

In our study the highest concentration of carvacrol was found in Tamasesti sample (47.62%), but the concentration of thymol was little (1.6%). Similar composition was found for Mociu sample, but a little smaller carvacrol relative concentration (31.32%), and a higher thymol concentration (4.84%) also a relative high methyl-carvacrol concentration (13.35%). This kind of composition was encountered to other essential oil samples originated from Hungary²³, North-East Italy²⁴, some area in Pakistan²⁵ and also from other Romanian region²⁶. The *Thymus serpyllum* essential oil from Nasaud area, carvacrol (26.58%), thymol (11.07%), p-cymen (18.97%) is similar in composition with samples originated from central Dalmatia and Bosnia and Herzegovina²⁷, Northern Kazakhstan¹⁶ and some area in Iran²⁸.

Even if the enzyme assisted extraction didn't have a much influence on the yield of extraction, the chemical composition suffered some modifications. In the case of carvacrol, no significant quantity increase was observed, but in case of thymol the increase was really significant from 11.07% to 24.81%. An amount decreased was observed in case of p-cymen from 18.97% to 2.37%. p-Cymen, it is known as a biological precursor of carvacrol and thymol¹ so an enzymatic transformation could explain the increase with 100% the quantity of thymol. Actually, a decreasing in the amount of monoterpene hydrocarbons was observed from 28.76% to 3.96%, while the oxygenated monoterpenes grew in quantity from 58.27% to 77.01%. New compounds were identified in enzyme assisted extracted essential oil like eucalyptol (0.4%), eugenol (0,6%) and isoegenol (0.1%), while other, from monoterpene hydrocarbons class, weren't identified.

The volatile compounds classes percentages are provided in Table 3. Oxygenated monoterpenes were the predominant class in all studied oils.

Table 3. Compound classes classification in studied essential oils

Components	<i>Thymus serpyllum</i> %			
	Mociu	Tamasesti	Nasaud	Nasaud enzymatic
Monoterpene hydrocarbons	24.92	15.11	28.76	3.96
Oxygenated monoterpenes	62.01	72.44	58.27	77.01
Sesquiterpene hydrocarbons	10.49	9.88	10.77	13.2
Oxygenated sesquiterpenes	2.49	1.98	2.18	5.32

Antioxidant activity

Antioxidant activities of obtained *Thymus serpyllum* essential oils were investigated using DPPH scavenging method. DPPH percent scavenging activities of volatile oils were measured at different concentrations between 0.5 and 5 $\mu\text{l/ml}$. EC50% is a parameter used for quantification of antioxidant activity and is giving by the concentration of essential oil used for decreasing the initial DPPH concentration by 50%. A lower EC50% indicates a higher antioxidant activity. All tested essential oils presented a high antioxidant and free radical scavenging activities. The highest antioxidant activity was found for *Thymus serpyllum* essential oil originated in Nasaud (EC50% = 2.3 ± 0.2 $\mu\text{l/ml}$), but comparable activity was revealed in Tamasesti essential oil (EC50% = 2.8 ± 0.1 $\mu\text{l/ml}$). Mociu essential oil proved also a high antioxidant activity (EC50% = 3.4 ± 0.1 $\mu\text{l/ml}$). The enzymatic extraction demonstrated to have a beneficial effect on the antioxidant activity. The essential oil obtained after enzymatic treatment exhibited a really high antioxidant activity (EC50% = 0.6 ± 0.1 $\mu\text{l/ml}$). The high antioxidant activity could be explain due to the formation by enzymatic treatment of a high quantity of thymol and also of some quantity of eugenol with it is proved to have high antioxidant properties²⁹.

Also in literature the *Thymus serpyllum* essential oil was identified like a potent antioxidant. The *Thymus serpyllum* essential oil originated from Croatia proved to have a higher antioxidant activity (EC50% = 0.4 $\mu\text{g/ml}$)²⁷, while *Thymus serpyllum* essential oil originated from Greece had also a high activity (EC50% = 0.96 $\mu\text{g/ml}$)². The high antioxidant activity in *Thymus serpyllum* essential oil, should be correlated to the phenolic compounds (thymol and carvacrol)³⁰, but also to the large number of components which have a synergic effect¹.

Table 4. Antioxidant capacity parameters

<i>Thymus serpyllum</i>	EC50%($\mu\text{L/mL}$)
Mociu area	3.4 ± 0.1
Tamasesti area	2.8 ± 0.1
Nasaud area	2.3 ± 0.2
Nasaud area enzymatically treated	0.6 ± 0.1

Antimicrobial activity

The antimicrobial activity of the obtained essential oils was evaluated against a panel of six microorganisms using of agar disc diffusion method. The data expressed as diameter of growth inhibition zone (mm). The results are illustrated in Table 5. All samples of volatile oils exhibited a high antibacterial

and antifungal activity. The highest antibacterial activity was observed against gram positive bacteria *Staphylococcus aureus*, *Bacillus cereus*. Also *Thymus serpyllum* essential oils demonstrated a very high antifungal activity on *Candida albicans*. A high antimicrobial activity on gram-negative bacteria *E. Coli* and *Klebsiella pneumonia* was observed, while against other gram-negative bacteria *Pseudomonas aeruginosa*, the

Thymus serpyllum essential oils manifested a medium antibacterial activity. The standard used, amoxicillin, proved to be not effective on gram-negative bacteria *Klebsiella pneumonia* and *Pseudomonas aeruginosa*.

An improvement in antimicrobial activity of essential oil obtained using enzymatic assisted treatment was observed, which can be explained by the composition percentages modification.

The antimicrobial activity of our *Thymus serpyllum* essential oils is in agreement with other literature results^{2,31}. From literature the antimicrobial activity is assigned to the high concentration of carvacrol in essential oils^{32,33}, but also to the presence of thymol in a high proportions^{34,35}. Our study confirms the high antimicrobial activity of essential oils containing large percentages of phenolic compounds.

The high antimicrobial activity of *Thymus serpyllum* essential oils from plants growing wild in Transylvania make them an important source of new therapeutic and antimicrobial preparates.

Table 5. Antimicrobial activity of studied essential oils

Microbial species	Inhibition diameter (mm)				
	<i>Thymus serpyllum</i> essential oil				
	Mociu	Tamasesti	Nasaud	Nasaud enzymatic	Amoxicillin
<i>Staphylococcus aureus</i>	34±1	35±1	32±1	35±1	25±1
<i>Bacillus cereus</i>	24±1	27±1	25±1	30±1	12±1
<i>E. coli</i>	24±1	30±1	22±1	25±1	18±1
<i>Klebsiella pneumoniae</i>	16±1	20±1	14±1	20±1	0
<i>Pseudomonas aeruginosa</i>	7±1	11±1	7±1	8±1	0
<i>Candida albicans</i>	26±1	30±1	26±1	30±1	18±1

CONCLUSIONS

A comparative study for analysis of influence of the geographical location and also the influence of enzymatic assistant extraction on the essential oils isolated from *Thymus serpyllum* growing wild in Transylvania was achieved.

Analysing the composition of the essential oils of *Thymus serpyllum* plants collected from different geographic areas of Transylvania showed that the plants are related, belonging to carvacrol chemotype class, but differences appear in composition and also the relative concentration of major compounds. The variation in the amount of carvacrol and other components might be connected with climatic and meteorologic conditions also with plant stage of development and metabolism.

The influence of enzymatic assistant extraction on the essential oils was studied. A highly variation in essential oil compounds proportion was observed which induced a remarkable effect on the antioxidant and antimicrobial activities. Enzyme assisted extraction could be consider as an alternative procedure to improve the quality of the essential oils and also some specific enzymes treatment might be used to modulate a specific activity. However, more studies and others hydrolytic enzymes should be investigate.

All studied essential oils demonstrated very high antioxidant and, antimicrobial activity, proving that essential oils isolated from plants growing wild in Transylvania, could be a good, inexpensive, natural, indigenous sources for natural food additives, new pharmaceutical preparates and also natural additives in cosmetic industry.

EXPERIMENTAL SECTION

MATERIAL AND METHODS

The *Thymus serpyllum* plants were collected from Nasaud area (47°17'0"N 24°24'24"E) from Bistrita-Nasaud district, Tamasesti area (7°30'12"N 23°1 1'20"E) from Maramures district, and Mociu area from Cluj district, all regions in Transylvania, Romania. The collected plants were identified at Faculty of Biology and Geology from 'Babes-Bolyai' University, Cluj-Napoca. The entire plants were naturally dried and grounded. All reactive and standards were purchased from Merck (Darmstadt, Germany). For the enzymatic treatment, a mixture of pectolytic and cellulotic enzymes, commercial preparate named Rapidase(DSM Food), was used. Antioxidant activity was determined using a Varian Cary 50 Spectrophotometer in a kinetic mode.

GC–MS Apparatus

A Trace DSQ Thermo Finnigan quadrupole mass spectrometer coupled with a Trace GC was used. The Rtx-5MS capillary column, 30mx 0.25mm, 0.25µm film thickness was used in a temperature program from 50°C, 2 min, then 8°C /min to 250°C, with 30°C /min at 310°C (10min) for essential oils compounds analysis. Helium was used as carrier gas at a flow rate of 1 mL/min. 1µL of each sample was injected into the GC-MS using the split mode (10:1) using a TriPlus autosampler (Proanalysis, Bucharest, Romania). The mass spectrometer was operated in EI mode at 70 eV, emission current was 100µA and mass spectra mass range 50-500 a.m.u. Transfer line temperature was set at 250°C, injector at 250°C and ion source at 250°C.

Extraction Procedure for Essential Oils

50 g of dried plant were submitted to hydrodistillation in a Clevenger type apparatus for 4h. The collected essential oils were dried over anhydrous Na₂SO₄. For the GC-MS analysis samples were diluted 100µL/mL in absolute ethanol.

Enzymatic Assisted Treatment

For enzymatic assisted treatment, 50 g of dried plant was treated with solution of 0.2% enzymatic prepartate in water for 24h at 37°C. After the enzymatic treatment a Clevenger hydrodistillation was achieved to yield the essential oil.

Determination of Antioxidant Activity

For determination of antioxidant activity, DPPH antioxidant assay was used. Samples essential oils were used to decolorize an ethanolic solution of 40µM DPPH. The monitoring of DPPH reduction was followed at 517nm. The percentage of DPPH scavenging activity is expressed using following formula: $DPPH_{inhibition}\% = [(A_i - A_t) / A_i] \times 100$. For determination of effective concentration (EC₅₀), different concentration of essential oils 0.5, 1, 2, 3, 4, 5 µL/mL in absolute ethanol were used. The EC₅₀ was determined by plotting the DPPH_{inhibition}% against used extract concentration.

Determination of Antimicrobial Activity

In vitro antibacterial activity of the of the essential oils were tested using Agar Diffusion Test (ADT) with evaluation of inhibition zones (IZ). For testing the antibacterial activity of the obtained essential oils, two Gram-positive, three

Gram-negative bacteria and a fungus were used as follow: *Staphylococcus aureus* ATCC 6538P, *Bacillus cereus* ATCC 14579, *Escherichia coli* ATCC 10536, *Klebsiella pneumoniae* (isolated from human urine), *Pseudomonas aeruginosa* ATCC 27853, *Candida albicans*. Amoxicillin 25 µg/disc was used as standard antibiotic in order to control the sensitivity of the microorganisms. The incubation conditions used were 24 h at 37°C. 5 µl of each volatile oils of *Thymus serpyllum* were applied on the paper disc, then disc papers were placed in the inoculated plates. After 24 h of incubation at 37 degrees Celsius the diameter of growth inhibition zones were measured.

REFERENCES

1. S. Jarik, M. Mitrovic, P. Pavlovic, *Evidence-Based Complementary and Alternative Medicine*, **2015**, 1-10.
2. M. Nikolic, J. Glamoclija, I. Ferreira, R. Calhelha, Â. Fernandes, T. Markovic, D. Markovic, A. Giweli, M. Sokovic, *Industrial Crops and Products*, **2014**, 52, 183–190.
3. V. Vaiciulyte, R. Butkiene, K. Loziene, *Phytochemistry*, **2016**, 1-7.
4. R.S. Verma, R.K. Verma, A. Chauhan, A.K. Yadav, *Indian Journal of Pharmaceutical Sciences*, **2011**, 73 (1), 233-235.
5. A. Raal, U. Paaver, E. Arak, A. Orav, *Medicina (Kaunas)* **2004**, 40(8), 795-800.
6. M.K Bhat. *Biotechnology Advances*, **2000**, 18, 355–383.
7. I.S. Blank, D.H. Jaeger, B.D. Zurbruggen, *US patent US6013289*, **2000**.
8. H.B Sowbhagya, K.T. Purnima, P. Suma Florence, A.G. Appu Rao, P. Srinivas, *Food Chemistry*, 113(4), 1234–1238, 2009.
9. H.B. Sowbhagya, P. Srinivas, Kaul T. Purnima, N. Krishnamurthy, *Food Chemistry*, **2011**, 127, 1856–1861.
10. H.B. Sowbhagya, P. Srinivas, N. Krishnamurthy, *Food Chemistry*, **2010**, 120, 230–234.
11. S. Dobozi, A. Halasz, K.E. Kovacs, G. Szacks, *Applied Microbiology Biotechnology*, **1988**, 29(1), 39–43.
12. R.I. Santamaria, M.D. Duarte, E. Barzana, D. Fernando, F.M. Gama, M. Mota, *Journal of Agricultural and Food Chemistry*, **2000**, 48(7), 3063–3067.
13. M. Salgado-Roman, E. Botello-Alvarez, R. Rico-Martinez, H. Jimenez-Islas, M. Cardenas-Manriquez, J.L. Navarrete-Bolanos, *Journal of Agricultural and Food Chemistry*, **2008**, 56(21), 10012–10018.
14. K. Hosni, I. Hassen, H. Chaabane, M. Jemli, S. Dallali, H. Sebei, H. Casabianca, *Industrial Crops and Products*, **2013**, 47, 291-299.
15. W.C Evans, "Trease and Evans Pharmacognosy", 15th Ed. Edinburgh Saunders, **2000**.

16. V. Kirillov, T. Stikhareva, B. Mukanov, N. Chebotko, O. Ryazantsev, G. Atazhanova, S. Adekenov, *Journal of Essential Oil Bearing Plants*, **2016**, *19* (1), 212- 222.
17. A. Pruteanu, C. Popescu, V. Vladut, G. Gageanu, *Romanian Biotechnological Letters*, **2018**, *23*(5), 14013-14024.
18. U. Paaver, A. Orav, E. Arak, U. Maeorg, A. Raal, *Natural Product Research*, **2008**, *22*(2), 108–115.
19. B. Nikolić, M. Matović, K. Mladenović, M. Todosijević, J. Stanković, I. Dordević, P.D. Marin, V. Tešević, *Natural Product Communications*, **2019**, 1-3.
20. E. Osinska, Z. Weglarz, M. Angielczyk, *Proceeding XVIth EUCARPIA Genetic Resources*, **2002**, 253-256.
21. K Loziene, J Vaiciūniene, P R Venskutonis, *Planta Medica*, **1998**, *64*, 772-773.
22. Y.A. Banaeva, L.M. Pokrovsky, A.V. Tkachev, *Proceedings of the International Conference on Natural Product and Physiologically Active Substance*, **1998**, 6-7.
23. M. Oszagyan, B. Simandi, J. Sawinsky, A. Kery, *Journal of Essential Oil Research*, **1996**, *8*, 333-335.
24. C. Da Porto, D. Decorti, *Journal of Essential Oil Bearing Plants*, **2012**, *15*, 561-571.
25. A.I. Hussain, F. Anwar, S.A.S. Chatha, S. Latif, S.T.H. Sherazi, A. Ahmad, J. Worthington, S.D. Sarker, *Food Science and Technology*, **2013**, *50*, 185-192.
26. C. Rus, R.M. Sumalan, E. Alexa, D.M. Copolovici, G. Pop, D. Botau, *Plant Soil and Environment*, **2015**, *61*(7), 297–302.
27. T. Kulisic, A. Radonic M. Milos, *Italian Journal of Food Science*, **2005**, *17*(3), 315-324.
28. I. Rasooli, S.A. Mirmostafa, *Fitoterapia*, **2002**, *73*, 244-250.
29. G. Ilhami, *Journal of Medicinal Food*, **2011**, *14*, 975-985.
30. M. Hazzit, A. Baaliouamer, A.R. Verissimo, M.L. Faleiro, M.G. Miguel, *Food Chemistry*, **2009**, *116* (3), 714-721.
31. G. Kavita, K. Santosh, S. Reeta, *Journal of Pharmacy Research*, **2011**, *4*(3), 641–642.
32. N. Chorianopoulos, E. Kalpoutzakis, N. Aligiannis, S. Mitaku, G.J. Nychas, S. A. Haroutounian, *Journal of Agricultural and Food Chemistry*, **2004**, *52*(26), 8261–8267.
33. S. Bounatirou, S. Smiti, M.G. Miguel, *Food Chemistry*, **2007**, *105*(1), 146–155.
34. M. Sokovic, J. Glamocija, A. Ciric, *Drug Development and Industrial Pharmacy*, **2008**, *34*(12), 1388–1393.
35. M.D. Sokovic, J. Vukojevic, P.D. Marin, D.D. Brkic, V. Vajs, L.J.L.D. van Griensven, *Molecule*, **2009**, *14*(1), 238–249.

RADIOCARBON DATING OF THE HISTORIC LIVINGSTONE TREE AT CHIRAMBA, MOZAMBIQUE

ADRIAN PATRUT^{a,b,*}, ROXANA T. PATRUT^c, MICHAEL J. SLATER^d,
LASZLO RAKOSY^c, DANIEL A. LÖWY^e, KARL F. VON REDEN^f

ABSTRACT. The article reports the AMS (accelerator mass spectrometry) radiocarbon dating results of the Livingstone Tree, a large African baobab on the right bank of the Zambezi, near Chiramba, Mozambique. In 1858, David Livingstone, who discovered the baobab, carved his monogram on the walls of its inner cavity. In 1996, the historic baobab was uprooted when a cyclone struck the area. Several wood fragments were extracted from the remains of the toppled tree. Five samples which originate from these fragments were subsequently dated by radiocarbon. The oldest sample had a radiocarbon date of 1598 ± 17 BP, that corresponded in 1996 to a calibrated age of 1490 ± 35 calendar years. According to this value, the Livingstone Tree at Chiramba becomes one of the oldest known African baobabs, with an age of over 1500 years. The Livingstone Tree had a closed ring-shaped structure, that consisted of 4 fused stems around a false cavity and also 2 additional stems outside the ring.

Keywords: AMS radiocarbon dating, *Adansonia digitata*, tropical trees, age determination, closed ring-shaped structure, false cavity

^a Babeş-Bolyai University, Faculty of Chemistry and Chemical Engineering, 11 Arany Janos, RO-400028, Cluj-Napoca, Romania.

^b Babeş-Bolyai University, Raluca Ripan Institute for Research in Chemistry, 30 Fantanele, RO-400294 Cluj-Napoca, Romania.

^c Babeş-Bolyai University, Faculty of Biology and Geology, 44 Republicii, RO-400015, Cluj-Napoca, Romania.

^d Mozguide, 14 Kinross Road, Parkview, 2193 Johannesburg, South Africa.

^e VALOR HUNGARIAE, Dept. of Science and Innovation, 4 Nagysándor József, 1054 Budapest, Hungary.

^f NOSAMS Facility, Dept. of Geology & Geophysics, Woods Hole Oceanographic Institution, Woods Hole, MA 02543, U.S.A.

* Corresponding author: apatrut@gmail.com

INTRODUCTION

The iconic African baobab (*Adansonia digitata* L.) is the best known and the most widespread of the eight or nine species of the *Adansonia* genus. The African baobab is endemic to the tropical arid savanna of the African continent. Its distribution throughout the tropics also covers several African islands and different areas outside Africa, where it has been introduced [1-5].

In 2005, our international team started an extended research project in order to clarify several controversial aspects related to the architecture, growth and age of the African baobab [6-16] and of other *Adansonia* species [17-20]. This research is based on a new approach, which is not limited to fallen specimens, but allows to investigate and date live individuals, as well. Our original approach consists of AMS (accelerator mass spectrometry) radiocarbon dating of minute wood samples extracted from inner cavities, deep entrances in the trunk, fractured stems and from the outer part (exterior) of large baobabs [7, 12, 13].

According to research results, young baobabs, which usually start growing as single-stemmed trees, have the ability to produce new stems over time, developing structures of increasing complexity. Consequently, we focused on the investigation of superlative specimens, i.e., very large and potentially old baobabs. Our studies have identified a new type of architecture, which we named ring-shaped structure (RSS), that enables baobabs to reach large sizes and old ages. There are two subtypes of RSSs: the open RSS and the closed RSS. The most frequent is the closed RSS, in which the fused stems are disposed in a ring with a natural empty space inside, that we named false cavity. Certain specimens may also have additional stems outside the ring [10, 18]. The first noticeable characteristic of false cavities, unlike normal ones, is the presence of bark on the cavity walls. The second characteristic is the fact that, due to stem growth, false cavities close progressively over time, retaining eventually only a small opening toward the exterior. The oldest African baobabs were found to have ages up to 2,500 years. By this value, the African baobab is the longest-living angiosperm in the world.

On September 16, 1858, the Scottish explorer and missionary David Livingstone discovered on the right bank of the Zambezi, near Chiramba, Mozambique, a very large baobab. The baobab was found to be 72 feet in circumference, at about three feet from the ground. Livingstone described it as “a magnificent baobab hollowed out into a good-sized hut”. “It was hollow and had a wide high doorway to it. The space inside was 9 feet in diameter and about 25 feet high. A lot of bats clustered about the top of the roof and I noticed for the first time that this tree had bark inside as well as without” [21]. Livingstone carved his monogram on the bark of the inner cavity. In his honour, the baobab was named Livingstone Tree. It is also known as the baobab at Chiramba.

In 1958, the explorer and film-maker Quentin Keynes, who was a grand-grandson of Darwin, decided to retrace the 1858-1864 Zambezi Expedition of Livingstone. On this occasion, Keynes rediscovered, with the assistance of locals, the Livingstone Baobab. He measured and filmed the wide baobab, which was “easily distinguished from others along the way by a narrow slit in its trunk. The slit provided a doorway taller than a man, and all three of us were able to walk upright through it into the tree’s dark interior. Here we found a perfect natural shelter, which I estimated to be over 30 feet high and perhaps 30 feet around. Excitedly I peered around for initials... I turned to face the entrance way and there, a foot or so from the edge of the slit, was the mark that I immediately deciphered as the work of David Livingstone from the characteristically looped ‘D’ and ‘L’ of his signature” [22,23].

In 1965, C.L. Guy, a retired forester, measured the circumference of the baobab near Chiramba at the same three feet from the ground and found it to be 73.95 feet. By considering the growth rate over 107 years, Guy stated that the baobab could well be over 1,700 years old [24,25].

In 1982, Wickens mentioned in his first monograph on baobabs, that “some trees, such as the famous Livingstone Tree at Chiramba on the lower Zambezi River, must be over 2000 years old” [1]. For over 30 years, based on Wickens' monograph, many books and articles about baobabs mentioned the tree at Chiramba as the oldest baobab. Despite the fame of this tree, the number of explorers and researchers who have seen it must be extremely low.

The mighty baobab was uprooted and died in January 1996, when Cyclone Bonita made landfall in Mozambique, causing severe damage. Moreover, most researchers are still unaware even now, after a quarter of a century, that the baobab near Chiramba has died.

In certain cases, the wood samples, which we investigated by radiocarbon, originated from the remains of baobabs and/or stems that had toppled months or even years prior to sampling. This was the case of Grotboom, our first dated African baobab [6], of Dorslandboom and Glencoe, two very old baobabs [8,9], as well as of Panke, the oldest known baobab [13]. Here we present the radiocarbon dating results of several wood samples collected from the remains of the collapsed Livingstone Tree at Chiramba, two years after its demise.

RESULTS AND DISCUSSION

The Livingstone Tree and its area. The baobab was located 3 km NW of the Chiramba village, Chemba district, Sofala province, Mozambique. The local population belongs to the Makonde ethnic group. The GPS coordinates

of the depression where the baobab once stood are 16°52.724' S, 034°37.531' E and the elevation is 94 m. The distance from this location to the Zambezi is 440 m. The mean annual rainfall in the area is 715 mm and the mean annual temperature reaches 24 °C.

The baobab at Chiramba had a maximum height of 27 m, the circumference at breast height (cbh; at 1.30 m above ground level) was 22.25 m and the overall wood volume (stems and branches) was around 350 m³ (**Figure 1**).

According to photographs and the video recording of Keynes, the baobab at Chiramba had a closed ring-shaped structure, with a ring composed of 4 perfectly fused stems around a false cavity. The baobab also had 2 additional stems outside the ring. The slit, which represented the entrance to the cavity, was around 6 m high. The false cavity, with the shape of a bell and with the walls covered by bark, had a height of 9 m and the quasi-circular base was 9 m around.



Figure 1. A very rare photo that shows the beautiful Livingstone Tree near Chiramba. One can observe the central slit, which is the entrance to the cavity.

Wood samples. Several wood fragments, with the mass of several grams each, were collected as a souvenir from the partially decayed remains of the baobab. Five samples, which originate from these wood fragments, were labelled from C-1 to C-5.

AMS results and calibrated ages. Radiocarbon dates of the 5 samples are displayed in Table 1. The radiocarbon dates are expressed in ^{14}C yr BP (radiocarbon years before present, i.e., before the reference year 1950). Radiocarbon dates and errors were rounded to the nearest year.

Calibrated (cal) ages, expressed in calendar years CE (CE, i.e., common era), are also presented in Table 1. The 1σ probability distribution (68.2%) was selected to derive calibrated age ranges. For two samples (C-3, C-4), the 1σ distribution is consistent with one range of calendar years. For the other three samples (C-1, C-2, C-5), the 1σ distribution is consistent with two ranges of calendar years. In these cases, the confidence interval of one range is considerably greater than that of the other; therefore, it was selected as the cal CE range of the sample for the purpose of this discussion. For obtaining single calendar age values of samples, we derived a mean calendar age of each sample from the selected range (marked in bold). Sample ages represent the difference between the year 1996 CE, when the baobab died, and the mean value of the selected range, which represents the assigned year, with the corresponding error. Sample ages and errors were rounded to the nearest 5 yr. We used the same approach for selecting calibrated age ranges and single values for sample ages in our previous articles on AMS radiocarbon dating of large and old angiosperms, especially baobabs [6-20,26,27].

Table 1. Radiocarbon dating results and calibrated ages of samples that originate from the Livingstone Tree at Chiramba.

Sample code	Radiocarbon date [error] (^{14}C yr BP)	Cal CE range 1σ [confidence interval]	Assigned year [error] (cal CE)	Sample age ¹ [error] (cal CE)
C-1	1210 [± 16]	860-898 (41.5%) 930-960 (26.7%)	879 [± 19]	1115 [± 20]
C-2	964 [± 18]	1046-1087 (43.8%) 1132-1160 (24.4%)	1066 [± 20]	930 [± 20]
C-3	1092 [± 25]	990-1019 (68.2%)	1005 [± 15]	990 [± 15]
C-4	1598 [± 17]	468-542 (68.2%)	505 [± 37]	1490 [± 35]
C-5	875 [± 26]	1181-1230 (62.1%) 1252-1260 (6.11%)	1195 [± 25]	800 [± 25]

¹ in 1996.

Dating results of samples. Three samples (C-1, C-3, C-4) had radiocarbon dates over 1000 BP, namely 1210 ± 16 BP, 1092 ± 25 BP and 1598 ± 17 BP. These values correspond to calibrated ages of 1115 ± 20 , 990 ± 15 and 1490 ± 35 calendar yr. The other two samples (C-2, C-5) had lower radiocarbon dates, i.e., 964 ± 18 BP and 875 ± 26 BP, that correspond to calibrated ages of 930 ± 20 and 800 ± 25 cal yr.

Age of the Livingstone Tree at Chiramba. Taking into account the particular circumstances in which the samples were collected, their initial position in the living baobab is not known. Therefore, we can only state that the baobab at Chiramba must have been older than the age of the oldest dated sample, i.e., most likely older than 1500 years.

CONCLUSIONS

The research discloses the AMS radiocarbon dating results of samples which originate from the remains of the famous Livingstone Tree, a large and old African baobab near Chiramba, Mozambique, that died in 1996.

Five wood samples were subsequently processed and dated by AMS radiocarbon. Three samples were found to have ages greater than 1000 BP. The oldest dated sample had a radiocarbon date of 1598 ± 17 BP, that corresponded in 1996 to a calibrated age of 1490 ± 35 calendar years. According to dating results, one can state that the Livingstone tree at Chiramba was older than 1500 years. This value includes it among the oldest known African baobabs.

The baobab at Chiramba exhibited a closed ring-shaped structure, that consisted of 4 fused stems around a false cavity, and 2 additional stems outside the ring.

EXPERIMENTAL SECTION

Sample collection. Five small and partially decayed wood samples, which originate from the remains of the baobab, were processed and investigated by AMS radiocarbon dating.

Sample preparation. The standard acid-base-acid pretreatment method was used for removing soluble and mobile organic components [28]. The pretreated samples were combusted to CO_2 by using the closed tube combustion method [29]. Next, CO_2 was reduced to graphite on iron catalyst, under hydrogen atmosphere [30]. Finally, the resulting graphite samples were analyzed by AMS.

AMS measurements. AMS radiocarbon measurements were performed at the NOSAMS Facility of the Woods Hole Oceanographic Institution (Woods Hole, MA, U.S.A.) by using the Pelletron® Tandem 500 kV AMS system. The obtained fraction modern values, corrected for isotopic fractionation with the normalized $\delta^{13}\text{C}$ value of -25‰ , were ultimately converted to a radiocarbon date.

Calibration. Radiocarbon dates were calibrated and converted into calendar ages with the OxCal v4.3 for Windows [31], by using the SHCal13 atmospheric data set [32].

ACKNOWLEDGEMENTS

Authors would like to acknowledge George Perry, who collected in 1998 wood fragments from the remains of the baobab. The research was funded by the Romanian Ministry of National Education CNCS-UEFISCDI under grants PN-II-ID-PCE-2013-76 and PN-III-P4-ID-PCE-2016-0776, Nr. 90/2017.

REFERENCES

1. G.E. Wickens, *Kew Bull.*, **1982**, 37(2), 172-209.
2. G.E. Wickens, P. Lowe, "The Baobabs: Pachycauls of Africa, Madagascar and Australia", Springer, Dordrecht, **2008**, pp. 232-234, 256-257, 295-296.
3. D.A. Baum, *Ann. Mo. Bot. Gard.*, **1995**, 82, 440-471.
4. J.D. Pettigrew, L.K. Bell, A. Bhagwandin, E. Grinan, N. Jillani, J. Meyer, E. Wabuye, C.E. Vickers, *Taxon*, **2013**, 61, 1240-1250.
5. G.V. Cron, N. Karimi, K.L. Glennon, C.A. Udeh, E.T.F. Witkowski, S.M. Venter, A.E. Assobadjo, D.H. Mayne, D.A. Baum, *Taxon*, **2016**, 65, 1037-1049.
6. A. Patrut, K.F. von Reden, D.A. Lowy, A.H. Alberts, J.W. Pohlman, R. Wittmann, D. Gerlach, L. Xu, C.S. Mitchell, *Tree Physiol.*, **2007**, 27, 1569-1574.
7. A. Patrut, K.F. von Reden, R. Van Pelt, D.H. Mayne, D.A. Lowy, D. Margineanu, *Ann. Forest Sci.*, **2011**, 68, 93-103.
8. A. Patrut, K.F. von Reden, D.A. Lowy, D.H. Mayne, K.E. Elder, M.L. Roberts, A.P. McNichol, *Nucl. Instrum. Methods Phys. Res. Sect. B*, **2010**, 268, 910-913.
9. A. Patrut, K.F. von Reden, D.H. Mayne, D.A. Lowy, R.T. Patrut, *Nucl. Instrum. Methods Phys. Res. Sect. B*, **2013**, 294, 622-626.
10. A. Patrut, S. Woodborne, K.F. von Reden, G. Hall, M. Hofmeyr, D.A. Lowy, R.T. Patrut, *PLOS One*, **2015**, 10(1): e0117193.

11. A. Patrut, L. Rakosy, R.T. Patrut, I.A. Ratiu, E. Forizs, D.A. Lowy, D. Margineanu, K.F. von Reden, *Studia UBB Chemia*, **2016**, LXI, 4, 7-20.
12. A. Patrut, S. Woodborne, K.F. von Reden, G. Hall, R.T. Patrut, L. Rakosy, J-M. Leong Pock Tsy, D.A. Lowy, D. Margineanu, *Radiocarbon*, **2017**, 59(2), 435-448.
13. A. Patrut, S. Woodborne, R.T. Patrut, L. Rakosy, D.A. Lowy, G. Hall, K.F. von Reden, *Nat. Plants*, **2018**, 4(7), 423-426.
14. A. Patrut, R.T. Patrut, L. Rakosy, D.A. Lowy, D. Margineanu, K.F. von Reden, *Studia UBB Chemia*, **2019**, LXIV, 2 (II), 411-419.
15. A. Patrut, S. Woodborne, R.T. Patrut, G. Hall, L. Rakosy, C. Winterbach, K.F. von Reden, *Forests*, **2019**, 10, 983-993.
16. A. Patrut, A. Garg, S. Woodborne, R.T. Patrut, L. Rakosy, I.A. Ratiu, *PLOS One*, **2020**, 15(1): e0227352.
17. A. Patrut, K.F. von Reden, P. Danthu, J-M. Leong Pock Tsy, R.T. Patrut, D.A. Lowy, *PLOS One*, **2015**, 10(3): e0121170.
18. A. Patrut, K.F. von Reden, P. Danthu, J-M. Leong Pock-Tsy, L. Rakosy, R.T. Patrut, D.A. Lowy, D. Margineanu, *Nucl. Instrum. Methods Phys. Res. Sect. B*, **2015**, 361, 591-598.
19. A. Patrut, R.T. Patrut, P. Danthu, J.-M. Leong Pock-Tsy, L. Rakosy, D.A. Lowy, K.F. von Reden, *PLOS One*, **2016**, 11(1): e0146977.
20. R.T. Patrut, A. Patrut, J-M Leong Pock-Tsy, S. Woodborne, L. Rakosy, P. Danthu, I-A. Ratiu, J. Bodis, K.F. von Reden, *Studia UBB Chemia*, **2019**, LXIV, 4, 131-139.
21. C. Livingstone, D. Livingstone, "Narrative of an Expedition to the Zambezi and its Tributaries", **1865**, Murray, London.
22. R. Cashel, "The Baobab in fact and fable", **1995**, Cashel, Amanzimtoti, Natal.
23. Q. Keynes, "Dr. Livingstone, I presume! – A personal look at his Africa", **1960**, documentary film.
24. C.L. Guy, *Rhodesiana*, **1967**, 16, 17-26.
25. C.L. Guy, *Proc. Trans. Rhodesian Sci. Assoc.*, **1970**, 54(2), 68-84.
26. A. Patrut, R.T. Patrut, L. Rakosy, J. Bodis, D.A. Lowy, E. Forizs, K.F. von Reden, *Studia UBB Chemia*, **2016**, LXI, 4, 21-30.
27. A. Patrut, S. Garnaud, O. Ka, R.T. Patrut, T. Diagne, D.A. Lowy, E. Forizs, J. Bodis, K.F. von Reden, *Studia UBB Chemia*, **2017**, LXII, 1, 111-120.
28. I.U. Olsson, Radiometric Methods. In: B. Berglung, editor "Handbook of Holocene palaeoecology and palaeohydrology", Wiley, Chichester, **1986**, pp. 273-312.
29. Z. Sofer, *Anal. Chem.*, **1980**, 52(8), 1389-1391.
30. J.S. Vogel, J.R. Southon, D.E. Nelson, T.A. Brown, *Nucl. Instrum. Methods Phys. Res. Sect. B*, **1984**, 5, 289-293.
31. C. Bronk Ramsey, *Radiocarbon*, **2009**, 51, 337-360.
32. A.G. Hogg, Q. Hua, P.G. Blackwell, M. Niu, C.E. Buck, T.P. Guilderson, T.J. Heaton, J.G. Palmer, P.J. Reimer, R.W. Reimer, C.S.M. Turney, R.H. Zimmerman, *Radiocarbon*, **2013**, 55(4), 1889-1903.

SYNTHESIS AND CHARACTERIZATION OF NANOBIOTRICALCIUM SILICATE, AS A COMPONENT OF AN ENDODONTIC SEALER

LUCIA TIMIȘ^a, ALEXANDRA AVRAM^{b*}, MARIA GOREA^{b*},
LILIANA BIZO^b, SANDA CÎMPEAN^a, RADU SEPTIMIU CÂMPIAN^c

ABSTRACT. Endodontic sealers are designed to be used in conjunction with semi-rigid materials during endodontic treatment, in order to obtain a three dimensional obturation of the root canal. During the last years, tricalcium silicate (C₃S), due to its increased biocompatibility, and superior physicochemical properties, has been investigated as an important component of endodontic filling materials. For most materials available on the market the source of C₃S alongside C₂S is MTA (mineral trioxide aggregate), but obtaining C₃S through synthesis is considered to be a much better alternative due to its superior purity and controlled size of the particles. In this study C₃S was synthesized in nanosized particles, by sol-gel method, from TEOS and calcium nitrate tetrahydrate without or with mineralizer NaF. A study was conducted in order to analyze the obtained powder and the hydrated samples which were prepared by mixing the powder with water in a ratio of 0.4, and cured for 28 days. The dried gels were thermally treated at 1450 °C respectively at 1350 °C. XRPD and TEM revealed the main presence of nanosized tricalcium silicate besides dicalcium silicate and small quantities of calcium hydroxides at both of synthesis temperatures. The hydration compounds evidenced by XRPD were calcium silicate hydrate alongside calcium hydroxide and calcium carbonate. FTIR analysis evidenced the specific vibration bands for O-H and Si-O bounds in hydrated calcium silicates.

Keywords: endodontic sealer, calcium silicate

^a Iuliu Hațieganu University of Medicine and Pharmacy, Faculty of Dentistry, Department of Odontology, 33 Moșilor str., RO-400001, Cluj-Napoca, Romania

^b Babeș-Bolyai University, Faculty of Chemistry and Chemical Engineering, Department of Chemical Engineering, 11 Arany Janos str., RO-400028, Cluj-Napoca, Romania

^c Iuliu Hațieganu University of Medicine and Pharmacy, Faculty of Dentistry, Department of Oral Rehabilitation, 15 Victor Babeș str., RO-400012, Cluj-Napoca, Romania

* Corresponding author: mgorea@chem.ubbcluj.ro; aavram@chem.ubbcluj.ro

INTRODUCTION

Root canal obturation is the last phase of the endodontic treatment that will, if performed correctly, ensure the long-term success of the endodontic treatment [1]. The requirements for the ideal root canal filling material are multiple, and currently there is no such a material to fulfil all of them, even though there is a wide variety available on the market [2, 3].

In the last decades, as a progress in the field of nanotechnology new materials have been introduced in endodontics: bioceramic materials. Bioceramics are materials with increased biocompatibility such as alumina and zirconia, bioactive glass, glass ceramics, calcium silicates, calcium phosphates which can be biodegradable, bioinert or bioactive [4-6].

Tricalcium silicate (C_3S) is the main component of MTA (mineral trioxide aggregate), a cement with a similar composition with Portland cement, which has been successfully used in endodontic surgery and vital pulp therapy [7]. Lately C_3S was introduced as a main component of endodontic sealers, because of its outstanding biological and physicochemical properties.

Because endodontic obturation, will be in contact for a long period of time, with the periapical tissues, endodontic sealers which are genotoxic, mutagenic, carcinogenic will interfere with the periapical healing process. [8]. Compared to other materials, calcium silicate-based materials, due to their increased biocompatibility, do not induce an inflammatory response into periradicular tissues [9, 10].

Calcium silicate sealers exhibit excellent antibacterial properties better or at least similar to conventional sealers [2, 11, 12]. The lack of volumetric shrinkage upon setting, good adhesion to dentin, and lack of solubility makes them suitable for being placed in a moist environment [13]. Because of their hydrophilic properties, a certain amount of moisture is required to initiate the setting reaction, moisture that is provided by the dentine [14]. After the hydration process, a rigid matrix consisting of calcium silicate hydrates and calcium hydroxide is formed [15]. The calcium hydroxide released will exhibit antibacterial and anti-inflammatory properties and will induce bone mineralization [16, 17].

The bioactivity of calcium silicates was demonstrated in *in vitro* studies by the presence of a layer of calcium phosphates or even hydroxyapatite after soaking the samples in simulated body fluid (SBF) [18-20].

A large number of studies have been conducted in order to evaluate the properties of (tri)calcium silicates and the best method of their synthesis [21-25].

SYNTHESIS AND CHARACTERIZATION OF NANO BIOTRICALCIUM SILICATE, AS A COMPONENT OF AN ENDODONTIC SEALER

Most calcium silicate-based materials for endodontic use, which are available on the market, consist of MTA. In order to obtain a new material, more biocompatible, with better physicochemical properties, a lower setting time, and a controlled size of the particles, the synthesis of calcium silicates as a main component of endodontic sealers became a necessity.

The main purpose of this study was to synthesize bio nano tricalcium silicates (C_3S) from TEOS, $Si(OC_2H_5)_4$, (tetraethyl orthosilicate) and $Ca(NO_3)_2 \cdot 4H_2O$ (calcium nitrate tetrahydrate) without or with mineralizer NaF by a sol-gel method, and characterize them for obtaining the endodontic sealer.

RESULTS AND DISCUSSIONS

Thermal analysis

Main thermal effects

The thermal analysis curves (TG/DSC) for the gel without additive, dried at 250 °C, are displayed in Figure 1, and those for the mixture with NaF, dried at 120 °C, are shown in Figure 2. In both cases, a 10 °C /min heating rate up to 1400 °C was performed.

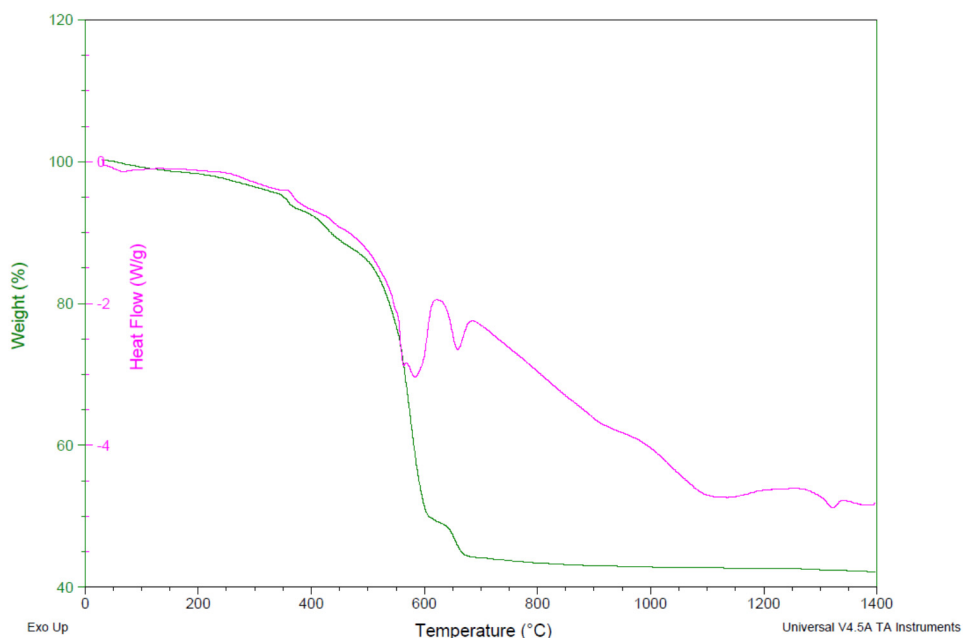


Figure 1. Thermal behaviour of dried gel (250 °C) without additive.

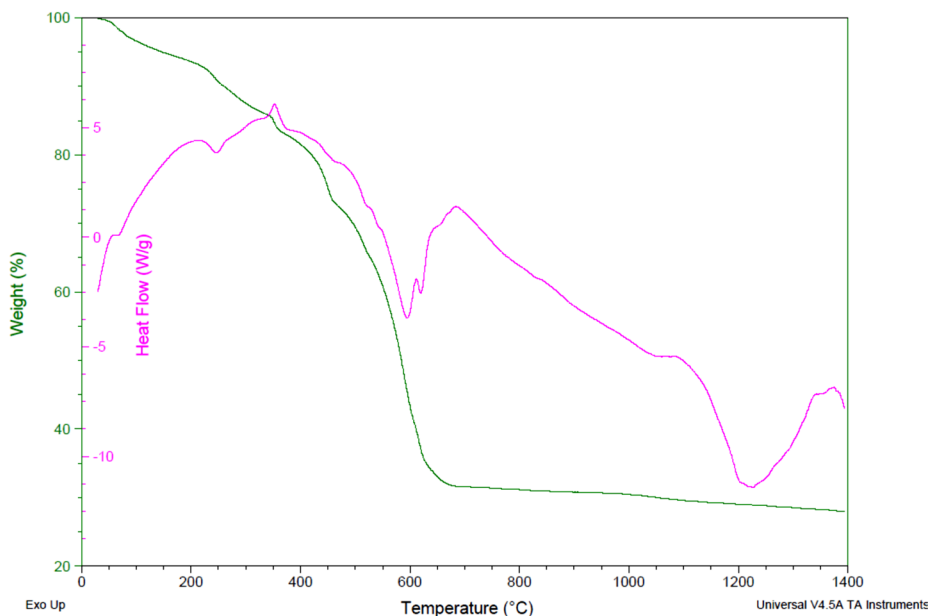


Figure 2. Thermal behaviour of dried gel (120 °C) with NaF.

At lower temperatures ($T < 200$ °C) endothermic effects can be noticed, as a result of the removal of adsorbed water in the sample. In the 200-750 °C temperature range pronounced endothermic effects are visible, due to the elimination of hydrated water and decomposition of calcium nitrate tetrahydrate ($\text{Ca}(\text{NO}_3)_2 \cdot 4\text{H}_2\text{O}$) and tetraethyl orthosilicate, $\text{Si}(\text{OC}_2\text{H}_5)_4$ (TEOS). The large exothermic peak that can be observed at about 1000 °C, corresponds to the crystallization of dicalcium silicates and the one at around the 1300 °C is attributed to the formation of tricalcium silicate.

The total weight loss for the sample without mineralizer, dried at 250 °C is 57.59 %, and for the sample with NaF dried at 120 °C is 72 %.

X-ray powder diffraction (XRPD) of synthesized powders

The XRPD patterns of synthesized calcium silicates at 1450 °C and 1350 °C are presented in Figure 3 a and b. The phase composition of the thermally treated powders, determined by XRPD, revealed the main presence of tricalcium silicate (C_3S), besides dicalcium silicate (C_2S) and calcium hydroxide $\text{Ca}(\text{OH})_2$, as a result of hydration of calcium oxide, CaO . The presence of dicalcium silicate and calcium hydroxide indicates an incomplete reaction between reactants, but their presence in endodontic sealer would not be harmful to human cells.

SYNTHESIS AND CHARACTERIZATION OF NANO BIOTRICALCIUM SILICATE,
AS A COMPONENT OF AN ENDODONTIC SEALER

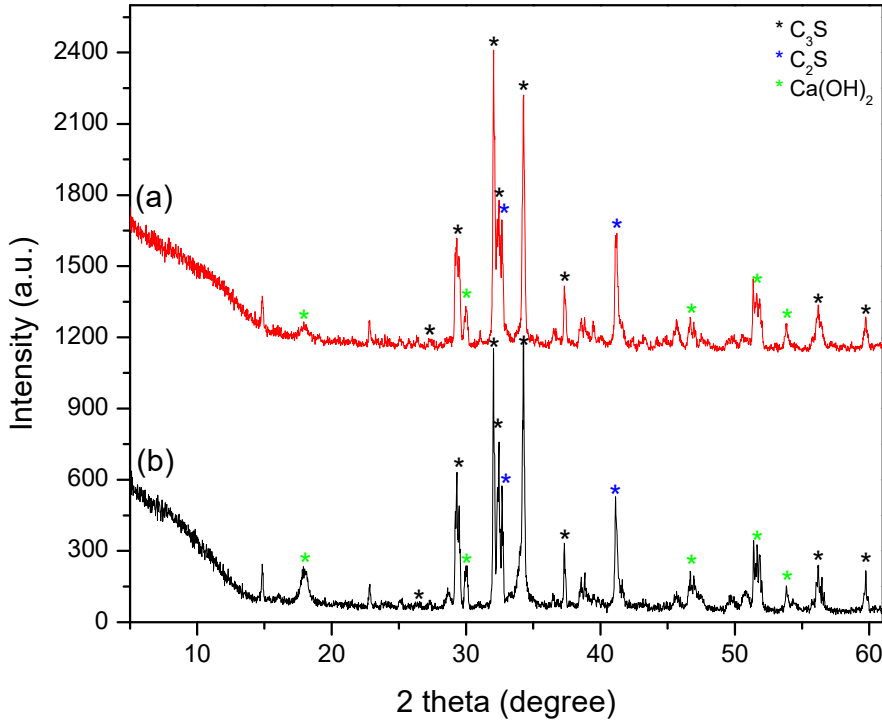


Figure 3. XRPD patterns for the (a) 1450 °C and (b) 1350 °C synthesized samples.

The crystallite sizes of tricalcium silicate were calculated from XRPD data using Scherrer formula. The average values for the C_3S obtained at 1450 °C, was 41.51 nm and those for C_3S with mineralizer obtained at 1350 °C was 54.78 nm.

Transmission electron microscopy (TEM)

TEM was used to illustrate the shape and morphology of mineral compounds. The presence of rhombohedral well-developed, nanometric-sized crystals of tricalcium silicate, besides of small quantities of hexagonal crystals of dicalcium silicate are illustrated in Figure 4.

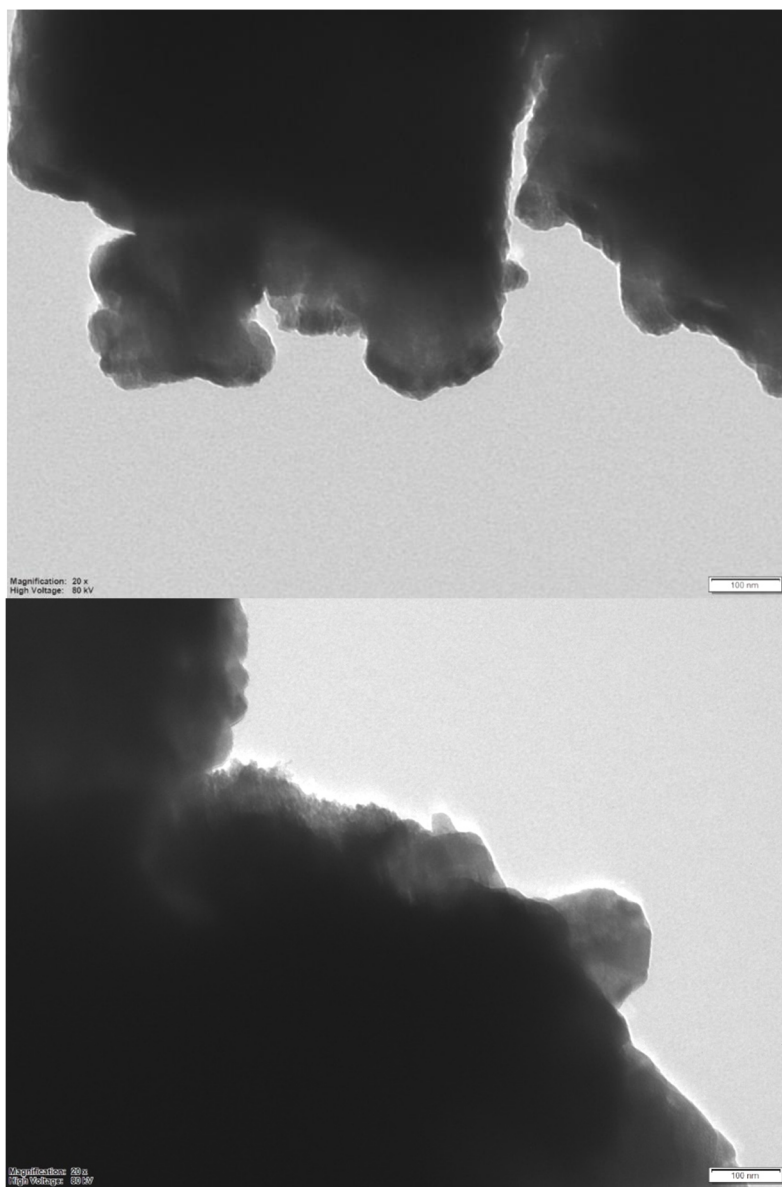


Figure 4. TEM image of tricalcium silicate powder synthesized at 1450 °C (up) and 1350 °C (down).

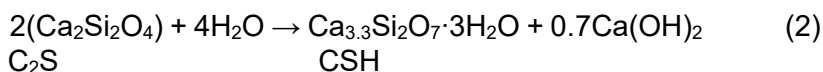
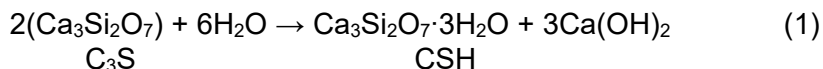
Figure 4 (up) presents the shape and sizes of the powder synthesised at 1450 °C and figure 4 (down) for the powder obtained at 1350 °C. No differences can be observed in the characteristics of the calcium silicates minerals. Both syntheses led to rhombohedral shapes and nanometric sizes for tricalcium silicates.

Hydration mechanism of calcium silicates

In order to facilitate the use of calcium silicates as endodontic sealers, they have to be mixed with aqueous solutions. This ensures hardening which comes due to the crystallization of calcium silicate hydrates.

Calcium silicates hydration determines protons fixation, so O^{2-} is changed into HO^- , SiO_4^{4-} in $H_nSiO_4^{(n-4)}$, Ca^{2+} ions in Ca^{2+} Aq. HO^- and Ca^{2+} ions migrate in solution and a calcium silicate hydrate (CSH) layer is formed on the calcium silicate surface. This layer is preponderantly constituted from $H_3SiO_4^-$ and $H_4Si_2O_7^{2-}$ ions.

The schematic reactions of tri- and dicalcium silicates are illustrated in Eq. 1 and 2.



During the hydration, the thickness of the calcium silicate hydrate (CSH) layer and the index of crystallinity are increased. The hydration process is slow depending on the diffusion rate of the ions inside the new formed layer and the ion change from solid to solution.

XRPD of hydrated calcium silicates

The XRPD patterns of synthesized samples at 1450 °C, after the hydration process, cured for 28 days in 90 % relative humidity at 22 °C, and 37 °C, are shown in Figure 5 a and b.

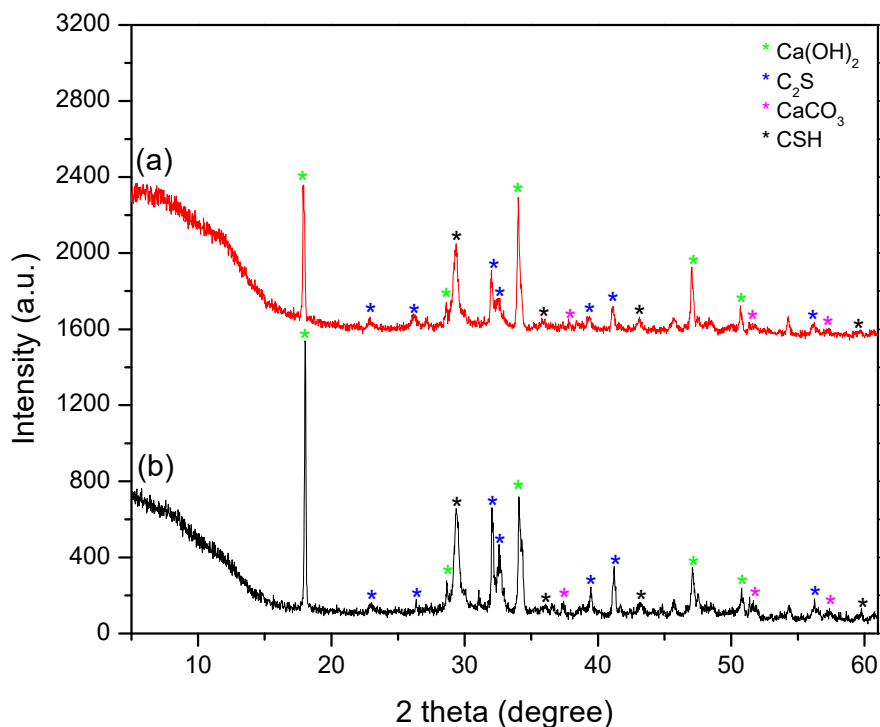


Figure 5. XRPD patterns for samples cured for 28 days at (a) 22 °C and (b) 37 °C.

The hydration compounds evidenced by XRPD are hydrated calcium silicate (CSH) alongside calcium hydroxide, calcium carbonate and dicalcium silicate (C_2S). The crystallinity index of CSH is low for both samples due to the short time of hydration, higher for the sample cured at 37 °C (Figure 4b). The calcium hydroxide is evidenced in the pattern as a hydration product of calcium silicates. The presence of CO_2 in the environment and its partial reaction with Ca(OH)_2 explains the presence of CaCO_3 crystals. As observed from Figure 5, C_2S is present in both samples. The presence of C_2S could be due to its long-time necessity for hydration or due to its high grain size.

The crystallite sizes of calcium silicates hydrates were calculated from XRPD data using Scherrer formula. The average values were 26.59 nm for samples cured at 22 °C and 22.39 nm for samples cured at 37 °C.

FTIR analysis for hydrated calcium silicates

The FTIR spectra for hydrated calcium silicates, after the hydration process, cured at 22 °C respectively at 37 °C for 28 days, are presented in Figure 6 a and b.

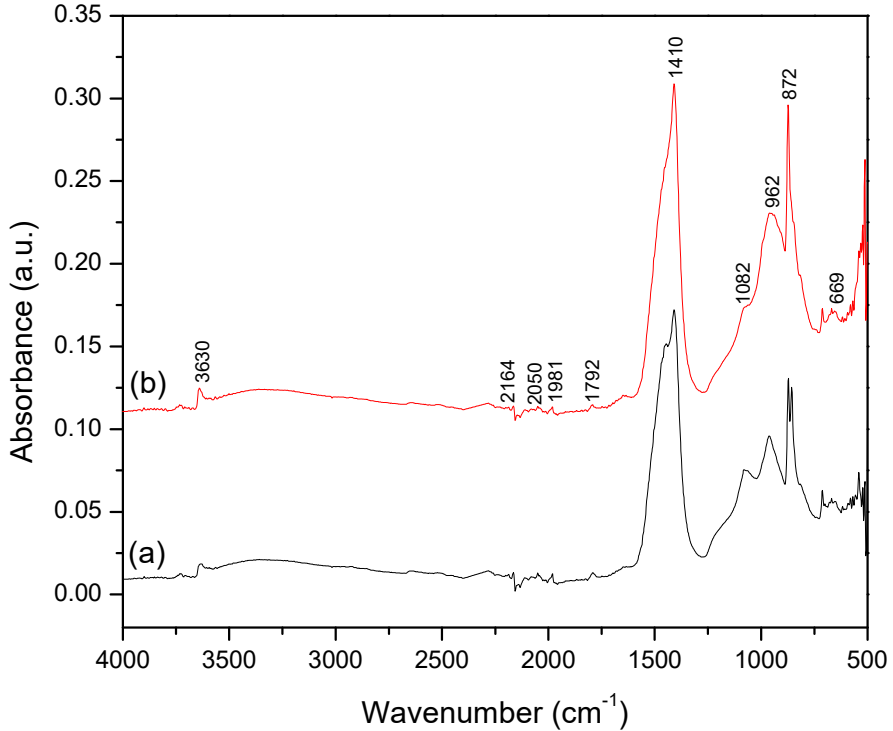


Figure 6. FTIR spectra for C_3S cements cured for 28 days at (a) 22 °C and (b) 37 °C, respectively.

Due to the hydration process two broad absorption bands around the 1400 -1600 cm^{-1} and 3400 – 3600 cm^{-1} are caused by the bending vibration of bound water incorporated in hydrated calcium silicates. The peak at 3630 cm^{-1} corresponds to $Ca(OH)_2$, which is formed during the hydrolysis of silicate phases

The specific vibration bands of Si-O bonds from SiO₄ groups for silicates can be evidenced. High spectral intensity bands are observed from ~900 cm⁻¹ to ~1000–1100 cm⁻¹, which suggests some rearrangements in the silica subsystem in the presence of water. These features reflect the dissolution of calcium silicates (C₃S, C₂S) and the polymerization of calcium silicate hydrate CSH. The small absorption band around 1081 cm⁻¹ could be attributed to both the vibration of the CO₃⁻ group in the newly formed carbonates and the stretching vibration of Si-O bound in calcium silicate hydrates.

CONCLUSIONS

Tricalcium silicate (C₃S), was successfully synthesized at 1450 °C respectively 1350 °C from TEOS and calcium nitrate tetrahydrate without and with mineraliser by a sol-gel method.

X-ray powder diffraction (XRPD) revealed the main presence of tricalcium silicates (C₃S), alongside dicalcium silicate (C₂S) and small quantities of calcium hydroxides Ca(OH)₂, at both synthesis temperatures. In samples cured for 28 days, the compounds evidenced by XRPD were calcium silicate hydrates (CSH), calcium hydroxide Ca(OH)₂ and calcium carbonate CaCO₃.

FTIR spectroscopy confirmed the presence of specific bands corresponding to the hydrated compounds in the solid. TEM images showed the well-developed nanocrystals of tri- and dicalcium silicates.

The data obtained revealed that the powder consists mainly of nano-sized tricalcium silicates, with a good hydration rate, making it suitable for endodontic use.

EXPERIMENTAL PART

Synthesis of tricalcium silicate

In order to synthesize tricalcium silicate (Ca₃SiO₅), calcium nitrate tetrahydrate (Ca(NO₃)₂·4H₂O, 99.5 % purity, Merck) and tetraethyl orthosilicate, (TEOS - C₈H₂₀O₄Si, Merck), were used as main raw materials. Ethanol (C₂H₅OH) and nitric acid (HNO₃) were used as pH regulators. In order to reach calcium silicate stoichiometry the molar ratio of CaO/SiO₂ was established at 3/1.

SYNTHESIS AND CHARACTERIZATION OF NANO BIOTRICALCIUM SILICATE,
AS A COMPONENT OF AN ENDODONTIC SEALER

The flowchart of steps involved in the tricalcium silicate synthesis is presented in Figure 7.

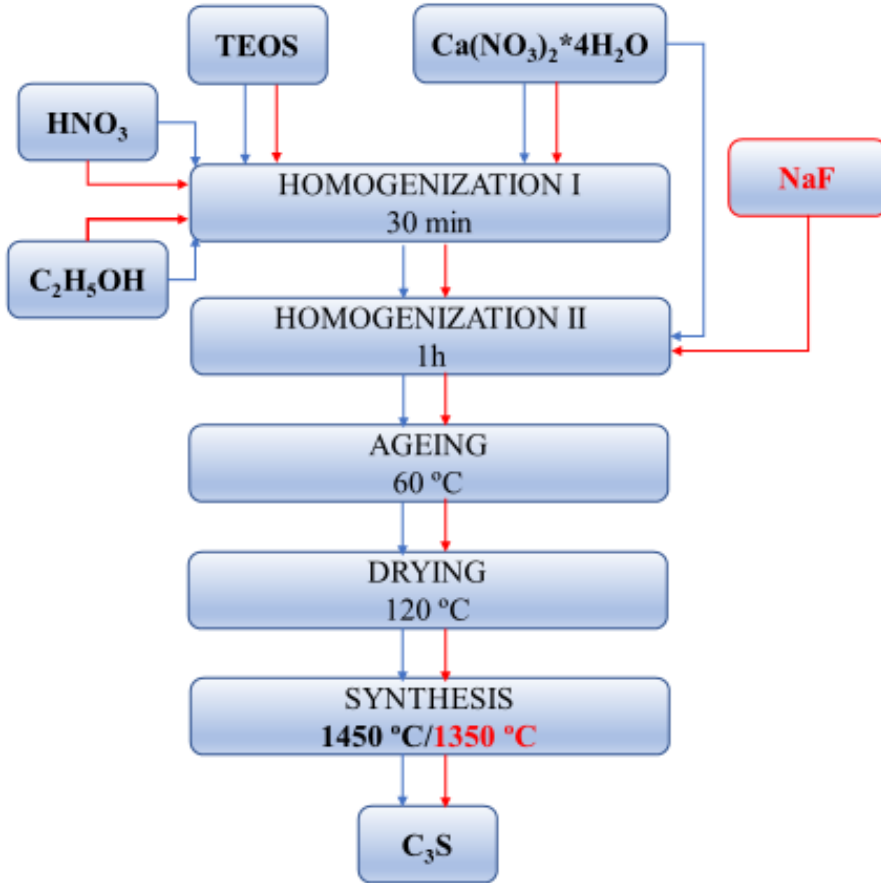


Figure 7. The synthesis flow chart of tricalcium silicate (C₃S).

The homogenized mixture of TEOS, calcium nitrate, ethanol, and nitric acid, was dried at 60 °C for gelation. The resulted gel was further dried at 120 °C and, afterwards, thermally treated at 1450 °C for 4 hours.

In the other mixture, in order to facilitate the reaction between compounds and to reduce the temperature of thermal treatment, an additive of NaF (1 %) was added in the homogenization step. After drying the obtained gel was thermally treated in two steps: at 600 °C for 6 hours and at 1350 °C for 30 minutes.

Characterization of C₃S powder

X-ray powder diffraction (XRPD)

The phase composition of C₃S powder was determined using a Bruker D8 Advance diffractometer, with Co, K α_1 = 1.79026 Å, operated at 35 kV and 40 mA. The pattern was collected for 2 θ range from 5° to 65°, with a step size of 0.02 °/ sec.

Transmission Electron Microscopy (TEM)

The size and shape of calcium silicate crystallites were investigated by TEM on HITHACHI H-7650 equipment.

Thermal analysis

The thermal behaviour of gels obtained by the sol-gel method, was studied by thermal analysis, conducted by the thermogravimetric (TG) and differential scanning calorimetry (DSC) using a TA Instruments DSC SDT Q600 thermogravimetric analyser.

Fourier transform infrared (FTIR) spectroscopy

The FTIR absorption spectra were recorded with a JASCO V-670 UV–Vis–NIR spectrophotometer.

REFERENCES

1. J. Branstetter; J.A. von Fraunhofer; *J. Endod.*, **1982**, 8(7), 312-316.
2. H.M. Zhou; Y. Shen; W. Zheng; L. Li, Y.F. Zheng, M. Haapasalo, *J. Endod.*, **2013**, 39(10), 1281-1286.
3. D. Orstavik, *Endodontic Topics*, **2005**, 12(1), 25-38.
4. S. Utneja; R.R. Nawal; S. Talwar; M. Verma; *Restor. Dent. Endod.*, **2015**, 40(1),1-13.
5. K. Koch; D. Brave, *Dentaltown*, **2009**, 39-43.
6. L. Bizo; K. Sabo; R. Barabas; G. Katona; L. Barbu-Tudoran; A. Berar; *Studia UBB Chemia*, LXV, 1, **2020**, 137-148.
7. N. Meschi, X. Li, G. Van Gorp, J. Camilleri, B. Van Meerbeek, P. Lambrechts, *Dent Mater.* 2019, 35(9), 1342-1350.
8. F.C. Martinho; S.E.A. Camargo; A.M.M. Fernandes; M.S. Campos; R.F. Prado; C.H.R. Camargo; M.C. Valera; *International Endodontic Journal*, **2018**, 51, 41-57.
9. D. Brave; A.A. Nasseh; K. Koch; *Roots*, **2013**, 4(4), 6-12.
10. E.J. Silva; P.M. Senna; G. De-Deus; A.A. Zaia; *Int. Endod. J.*, **2016**, 49(6), 574–580.
11. S. Jitaru; I. Hodisan; L. Timis; A. Lucian; M. Bud; *Clujul Med.*, **2016**, 89(4), 470-473.

SYNTHESIS AND CHARACTERIZATION OF NANO BIOTRICALCIUM SILICATE,
AS A COMPONENT OF AN ENDODONTIC SEALER

12. H. Zhang; Y. Shen; N.D. Ruse; M. Haapasalo; *J. Endod.*, **2009**, 35(7),1051–1055.
13. A. Avram; M. Gorea; R. Balint; L. Timiș; S. Jitaru; A. Mocanu; M. Tomoaia-Cotișel; *Studia UBB Chemia*, LXII, 4, Tom I, **2017**, 81-92.
14. G.C. Gritti; S.I.A. Cavalcante; E.M. Maia-Filho; J. Bauer; M.C. Bandéca; G. Gavini; C.N. Carvalho; *Braz. Oral Res.*, **2017**, 31, e76.
15. B. Darvell; R.C.T. Wu; *Dent. Mater.*, **2011**, 27, 407-422.
16. H.K. El-Hamid; H.H. Abo-Almaged; M.M. Radwan; *J. App. Pharm. Sci.*, **2017**, 7(10), 001- 008.
17. A. Koutroulis, S.A. Kuehne, P.R. Cooper, J. Camilleri, *Sci. Rep.*, **2019**; 9, 19019.
18. W. Zhao, J. Chang, *Mater. Lett.*, **2004**, 58, 2350-2353.
19. X. Liao, H. Zhu, G. Yin, Z. Huang, Y. Yao, X. Chen, *Bull. Mater. Sci.*, **2011**, 34, 1151–1155.
20. M.C. Jimenez-Sanchez; J.J. Segura Egea; A. Diaz-Cuenca; *J. Clin. Exp. Dent.* **2019**, 11(4), e322-326.
21. M. Wu; T. Wang; Y. Wang; F. Li; M. Zhou; X. Wu; *Mater. Lett.*, **2018**, 227, 187-190.
22. P. Torkittikul, A. Chaipanich, *Mater. Sci. Eng. C*, **2012**, 32, 282-289.
23. K.B. Wiltbank, S.A. Schwartz, W.G. Schindler, *J. Endod.*, **2007**, 33(10), 1235-1238.
24. L. Wang, X. Xie, C. Li, H. Liu, K. Zhang, Y. Zhou, X. Chang, H.H. K. Xu., *J. Dent.*, **60**, **2017**, 25-35.
25. L. Grech, B. Mallia, J. Camilleri, *Dent. Mater.*, 29, **2013**, 20-28.

A STRAIGHTFORWARD SYNTHESIS OF NOVEL 1,3,5-TRIAZINE-BASED MACROCYCLIC SCAFFOLDS

COSMIN V. CRIȘAN^a, NICULINA D. HĂDADE^a, ION GROSU^a,
ANDREEA P. CRIȘAN^{a*}, ANAMARIA TEREÇ^{a*}

ABSTRACT. The synthesis and structural investigation of a series of three macrocycles bearing 2,4,6-tris(*p*-phenylene)-1,3,5-triazine central units and oligoethyleneoxide bridges are reported. The approach implied the synthesis of non-symmetrical 1,3,5-triazines obtained *via* a cross-cyclotrimerization reaction, followed by a direct macrocyclization with the corresponding ditosylated oligoethyleneglycols. The obtained non-symmetrically C-substituted 1,3,5-triazines macrocycles were characterized by NMR spectroscopy and High-Resolution Mass Spectrometry (HRMS).

Keywords: *macrocycles, 1,3,5-triazine, cross-cyclotrimerization, oligoethylene bridges*

INTRODUCTION

The study of macrocyclic molecules has long been an underlying research area in supramolecular chemistry due to the interdisciplinary nature of the research work involved in investigating this type of molecules. Macrocycles are well known for their molecular recognition properties [1], but their applicability is far from being limited to this field. The versatility of macrocyclic molecules makes them suitable for a wider range of scientific interest and commercial applications such as materials science [2], catalysis [3], drug delivery systems [4]. Moreover, macrocyclic molecules have been employed as key components in the construction of non-symmetrical cryptands [5], a new class of cage molecules, which is beginning to spark an increased interest from the research community. As well, triazine-based macrocycles have been reported to be well suited as building blocks for covalent organic frameworks (COFs) [6].

^a Babeș-Bolyai University, Faculty of Chemistry and Chemical Engineering, Department of Chemistry and SOOMCC, Cluj-Napoca, 11 Arany Janos, 400028, Cluj-Napoca, Romania
*Corresponding authors: adiac@chem.ubbcluj.ro; asuciu@chem.ubbcluj.ro

The 1,3,5-triazine motif is an intensely studied building block in supramolecular chemistry, due to its ease of synthesis and availability, being investigated on a large scale in various research areas such as CO₂ capture/storage and separation [7], materials science [8] and other industrial applications (e.g. furniture industry) [9]. Additionally, triazine-based host molecules proved to be highly efficient in capturing one of the most harmful class of pollutants, namely the polycyclic aromatic hydrocarbons (PAHs) [10].

In our previous work [11], we reported and investigated several cryptands exhibiting 1,3,5-triazine or 2,4,6-triphenyl-1,3,5-triazine aromatic units and oligoethyleneoxide bridges which displayed a high affinity for alkali metal ions (particularly for Na⁺ and K⁺) and organic ammonium ions such as the dication of 1,5-naphthylenediamine.

Therefore, based on the versatility of the triazine scaffold and the prodigious applicability of macrocyclic molecules, we considered it of great interest to design and synthesize macrocycles exhibiting 1,3,5-triazine moieties and oligoethyleneglycol bridging units of various lengths, as presented in Figure 1.

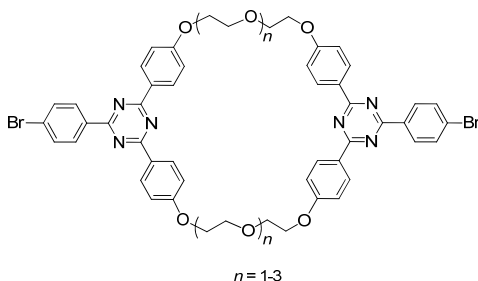


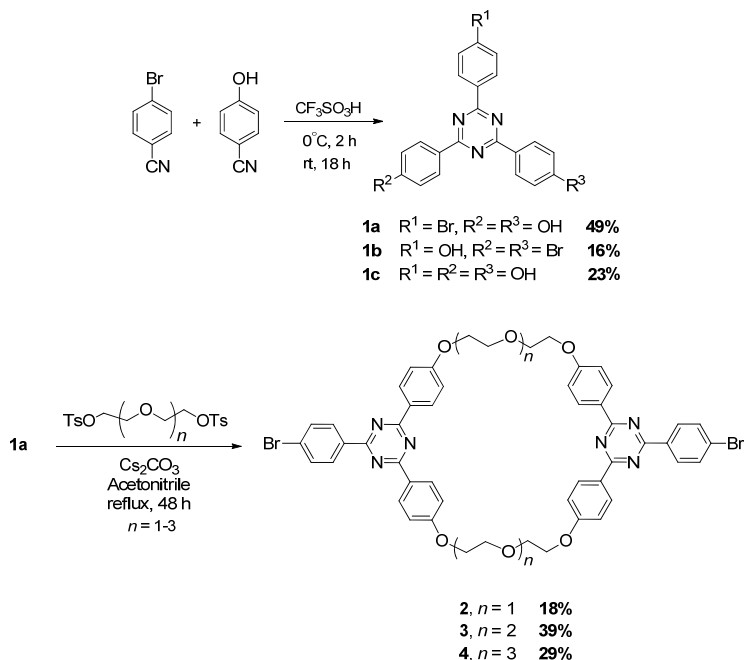
Figure 1. Target macrocycles with triazine units and oligoethyleneoxide bridges

RESULTS AND DISCUSSIONS

In order to access the target molecules, a two-step strategy was envisioned (Scheme 1). The key component in the construction of the macrocycles was the non-symmetrically C-2,4,6-trisubstituted 1,3,5-triazine unit **1a**, which provides a precise control of the size, as well as the functionality of the final targets. Thus, the synthetic approach implied the preliminary preparation of the compound bearing suitable functional groups, followed, in the second step, by a direct macrocyclization reaction with selected ditosylated oligoethyleneglycols.

Symmetrically C-substituted 1,3,5-triazine derivatives are conventionally obtained by the cyclotrimerization of nitriles [12]. For our non-symmetrically C-2,4,6-trisubstituted 1,3,5-triazine unit, we had a different strategy, i.e., by introducing 4-bromobenzonitrile alongside 4-hydroxybenzonitrile (in 1:2.5 molar

ratio) in a cross-cyclotrimerization process catalysed by triflic acid. As depicted in Scheme 1, a mixture of three differently C-substituted 1,3,5-triazines, **1a-c**, was obtained, the desired **1a** being predominant (values of partial conversions of starting nitriles based on the amount of material isolated by column chromatography are presented).



Scheme 1. Synthesis of 1,3,5-triazine-based macrocycles

The desired non-symmetrically substituted 1,3,5-triazine **1a** was used in the macrocyclization step. The target macrocycles **2-4** were thus obtained by directly reacting derivative **1a** with readily available [13] ditosylated mono-, di- and triethyleneglycols using Cs₂CO₃ as a template and proton scavenger. In such doing, the triazine derivative **1a** and the base, Cs₂CO₃, were dissolved in acetonitrile at high dilution and with slow addition of the solution containing the corresponding ditosylated glycol in order to favour the formation of the macrocycle over the oligomerization products. As shown in Scheme 1 and depending on the size ($n = 1-3$) of the oligoethyleneglycol, the above protocol afforded the desired macrocycles **2-4** with yields ranging from 18% to 39%. The highest yielding result was obtained when the ditosylated triethyleneglycol was used as bridging unit.

Formation of macrocycles **2–4** was confirmed by NMR and HRMS experiments. The NMR spectra of all three macrocycles exhibited only a unique pattern of resonances, proving the symmetrical nature of the structures. Thus, the common ^1H NMR pattern for this series of compounds (Figure 2) consisted of two AA'-XX' coupling patterns in the aromatic region, with a very slight upfield shift for each of the compound's aromatic signals as the oligoethyleneglycol bridge grew longer. Also, the difference in the size of the compounds is clearly demonstrated by the appearance of an additional signal located in the 3.5-4.5 ppm range for each extra ethylene group in the chain.

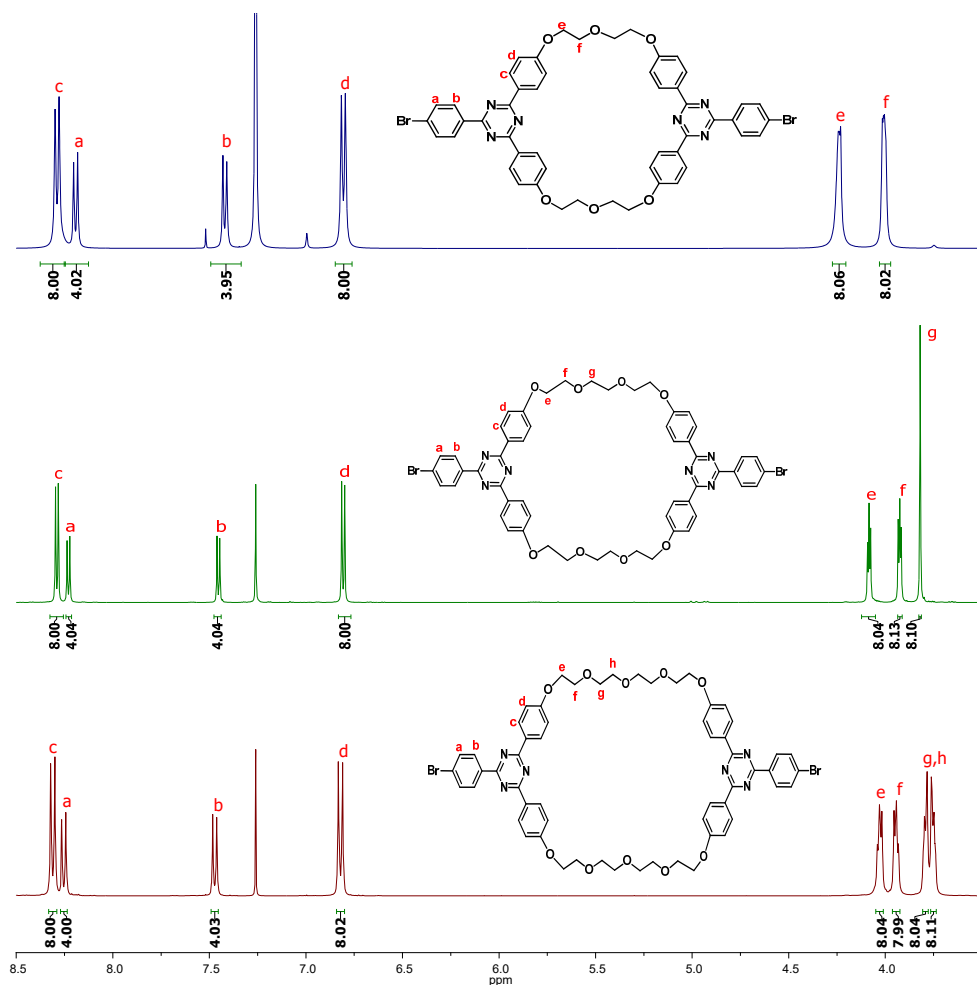


Figure 2. ^1H NMR (600 MHz, CDCl_3) stacked spectra of macrocyclic derivatives **2–4** having different oligoethyleneglycol bridges

Furthermore, the formation of the [2+2] product was confirmed by the HRMS spectra, which reveal in case of all three macrocycles the molecular peaks corresponding to the protonated species $[M+H]^+$ at $m/z = 981.1442$ for **2**, $m/z = 1069.1969$ for **3** and $m/z = 1557.2494$ for **4**, respectively. Additionally, as presented in Figure 3, the expected molecular peaks exhibit a typical isotopic pattern of a di-brominated chemical species.

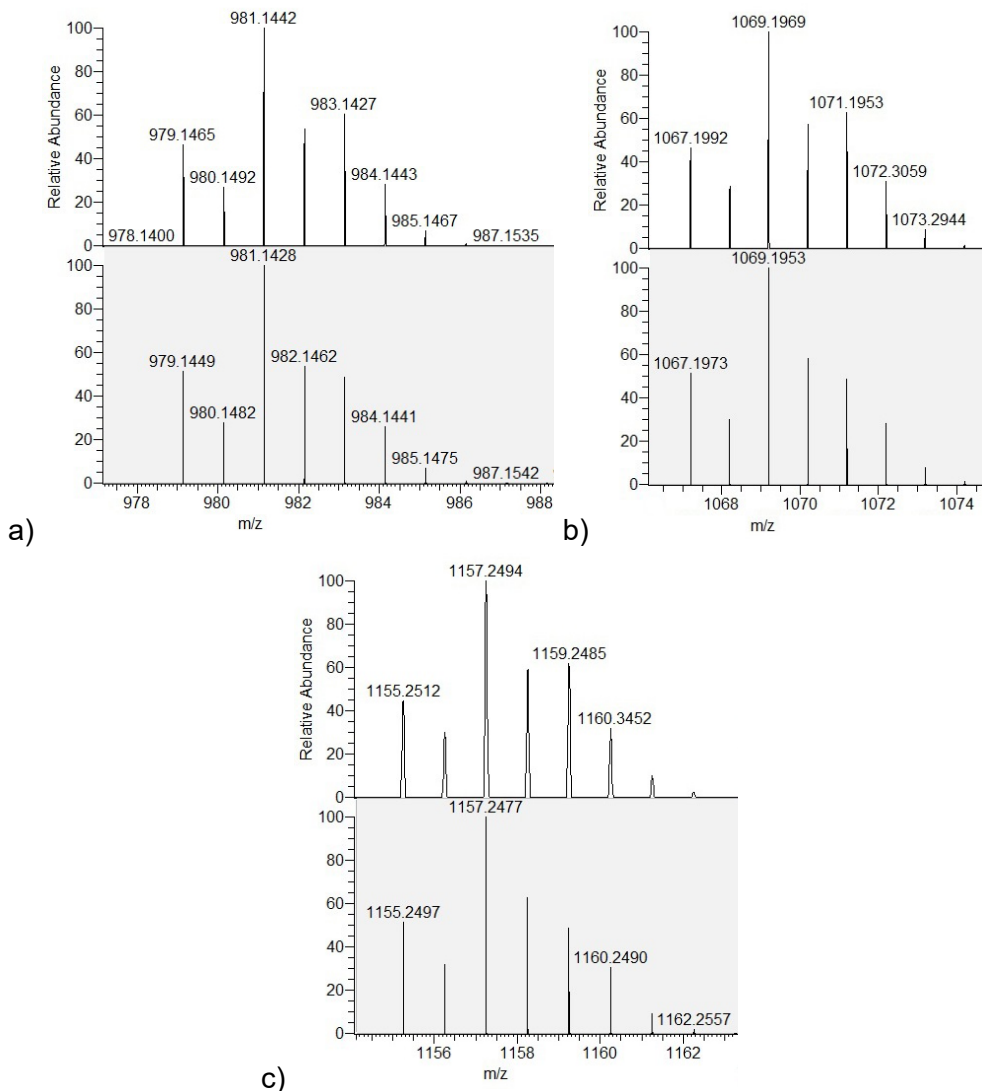


Figure 3. APCI(+)-HRMS spectra of macrocycles **2** (a), **3** (b) and **4** (c). Comparison of the experimental spectra (top) and simulated isotopic patterns (bottom).

CONCLUSIONS

In summary, a series of three novel 1,3,5-triazine-based macrocycles was synthesized and fully characterized. In order to access the target macrocycles, a novel non-symmetrical 2,4,6-C-trisubstituted-1,3,5-triazine derivative was obtained by adapting an efficient and innovative synthetic strategy. The straightforward procedure and the above findings prompt toward future design and synthesis of novel “intelligent organic molecules”.

EXPERIMENTAL SECTION

General data: NMR spectra were recorded at room temperature, in CDCl_3 or $\text{DMSO}-d_6$ as solvents, on instruments operating at 400 or 600 MHz for ^1H and 100 or 150 MHz for ^{13}C nuclei. Chemical shifts (δ) are reported in parts per million (ppm) using residual solvent peak as internal standard. High resolution mass spectra (HRMS) were recorded in positive mode, on a LTQ ORBITRAP XL spectrometer using external mass calibration. The ditosylated oligoethyleneglycols were obtained following a procedure described in the literature [13], while the other reagents were commercially available and were used without further purifications. Thin layer chromatography (TLC) was conducted on silica gel 60 F254 TLC plates. Solvents were dried and distilled under argon using standard procedures.

Procedure for the unsymmetrical cyclotrimerization providing compounds 1a-c (Scheme 1)

To ice-cooled (0°C) trifluoromethanesulfonic acid (0.300 mL, 0.510 g, 3.30 mmol), an anhydrous CHCl_3 solution (20 mL) containing 4-bromobenzonitrile (0.100 g, 0.55 mmol) and 4-hydroxybenzonitrile (0.164 g, 1.37 mmol) was added dropwise over 30 minutes. After additional stirring (18 h) at room temperature, water (50 mL) was added and the resulting precipitate was filtrated off, then washed with water to neutrality. The isolated dried solid was further separated by column chromatography on silica gel (eluent AcOEt/PE 1:1 v/v, Scheme 1) to provide compounds **1a** (0.110 g, 49% partial conversion of 4-bromobenzonitrile), **1b** (0.042 g, 16% partial conversion of 4-bromobenzonitrile) and **1c** (0.045 g, 23% partial conversion of 4-bromobenzonitrile).

2-(4-Bromophenyl)-4,6-bis(4-hydroxyphenyl)-1,3,5-triazine (1a). White solid; Mp.: 325°C with decomposition; $R_f = 0.65$ (AcOEt:PE 1:1 v/v). ^1H NMR (400 MHz, $\text{DMSO}-d_6$) δ_{H} (ppm): 10.36 (s, 2H), 8.60 (d, $^3J_{\text{H,H}} = 8.6$ Hz, 2H), 8.56 (d, $^3J_{\text{H,H}} = 8.8$ Hz, 4H), 7.83 (d, $^3J_{\text{H,H}} = 8.6$ Hz, 2H), 6.98 (d, $^3J_{\text{H,H}} = 8.8$ Hz, 4H). ^{13}C NMR (100 MHz, $\text{DMSO}-d_6$) δ_{C} (ppm): 170.5 (C=N), 169.5 (C=N),

162.1 (C=C, Ar), 135.1 (C=C, Ar), 131.9 (HC, Ar), 130.8 (HC, Ar), 130.4 (HC, Ar), 126.6 (C=C, Ar), 126.2 (C=C, Ar), 115.7 (HC, Ar). HRMS (APCI+): calculated for $C_{21}H_{15}BrN_3O_2$ $[M+H]^+$: 420.0342; found: 420.0332.

2-(4-Hydroxyphenyl)-4,6-bis(4-bromophenyl)-1,3,5-triazine (1b).

White solid; $R_f = 0.9$ (AcOEt:PE 1:1 v/v). 1H NMR (400 MHz, DMSO- d_6) δ_H (ppm): 10.44 (s, 1H), 8.62 (d, $^3J_{H,H} = 8.6$ Hz, 4H), 8.58 (d, $^3J_{H,H} = 8.8$ Hz, 2H), 7.84 (d, $^3J_{H,H} = 8.6$ Hz, 4H), 7.00 (d, $^3J_{H,H} = 8.8$ Hz, 2H). HRMS (APCI+): calculated for $C_{21}H_{14}Br_2N_3O$ $[M+H]^+$: 483.9478; found: 483.9465.

2,4,6-Tris(4-hydroxyphenyl)-1,3,5-triazine (1c). White solid; $R_f = 0.4$ (AcOEt:PE 1:1 v/v). 1H NMR (600 MHz, DMSO- d_6) δ_H (ppm): 10.28 (s, 3H), 8.55 (d, $^3J_{H,H} = 8.6$ Hz, 6H), 6.97 (d, $^3J_{H,H} = 8.6$ Hz, 6H). HRMS (APCI+): calculated for $C_{21}H_{16}N_3O_3$ $[M+H]^+$: 358.1186; found: 358.1178.

Procedure for the synthesis of triazine-based macrocycles 2–4

To a solution of **1a** (0.100 g, 0.238 mmol) in MeCN (100 mL), Cs_2CO_3 (0.390 g, 1.19 mmol) was added and the resulting mixture was heated to 80 °C. The corresponding ditosylated oligoethyleneglycol (0.238 mmol) solubilized in THF (5 mL) was added dropwise over 6 h and the mixture was stirred for another 48 h until the reactants were fully consumed (TLC monitoring). After cooling, the solvent was removed under vacuum and the resulting mass was solubilized in $CHCl_3$ (30 mL) and washed with water (40 mL). The aqueous phase was further extracted with $CHCl_3$ (3 x 25 mL), the combined organic layers were dried over $MgSO_4$ and the solvent removed under reduced pressure. The isolated crude product was further separated by column chromatography on silica gel (gradient of eluent: Toluene/AcOEt 10:1 v/v for **2**, Toluene/AcOEt 5:1 v/v for **3**, Toluene/AcOEt 3:1 v/v for **4**) to afford compounds **2** (0.042 g, 18% partial conversion of **1a**), **3** (0.100 g, 39% partial conversion of **1a**), **4** (0.080 g, 29% partial conversion of **1a**).

Macrocycle 2. White solid; Mp.: 193 °C; $R_f = 0.3$ (Toluene:AcOEt 10:1 v/v). 1H NMR (400 MHz, $CDCl_3$) δ_H (ppm): 8.29 (d, $^3J_{H,H} = 8.7$ Hz, 8H), 8.19 (d, $^3J_{H,H} = 8.4$ Hz, 4H), 7.42 (d, $^3J_{H,H} = 8.4$ Hz, 4H), 6.81 (d, $^3J_{H,H} = 8.7$ Hz, 8H), 4.24 (m, 8H), 4.00 (m, 8H). ^{13}C NMR (150 MHz, $CDCl_3$) δ_C (ppm): 170.3 (C=N, Ar), 169.7 (C=N, Ar), 161.9 (C=C), 135.3 (C=C), 131.6 (HC_{ar}), 130.5 (HC_{ar}), 130.0 (HC_{ar}), 128.7 (C=C), 127.0 (C=C), 114.6 (HC_{ar}), 69.9 (CH_2), 68.2 (CH_2). HRMS (APCI+): calculated for $C_{50}H_{41}Br_2N_6O_6$ $[M+H]^+$: 981.1428; found: 981.1442.

Macrocycle 3. White solid; Mp.: 179 °C; $R_f = 0.23$ (Toluene:AcOEt 1:1 v/v). ^1H NMR (600 MHz, CDCl_3) δ_{H} (ppm): 8.29 (d, $^3J_{\text{H,H}} = 8.7$ Hz, 8H), 8.23 (d, $^3J_{\text{H,H}} = 8.4$ Hz, 4H), 7.45 (d, $^3J_{\text{H,H}} = 8.4$ Hz, 4H), 6.81 (d, $^3J_{\text{H,H}} = 8.7$ Hz, 8H), 4.09 (m, 8H), 3.92 (m, 8H), 3.82 (s, 8H). ^{13}C NMR (150 MHz, CDCl_3) δ_{C} (ppm): 170.4 (C=N), 169.7 (C=N), 162.4 (C=C, Ar), 135.3 (C=C, Ar), 131.6 (HC, Ar), 130.6 (HC, Ar), 130.2 (HC, Ar), 128.6 (C=C, Ar), 127.0 (C=C, Ar), 114.2 (HC, Ar), 71.2 (CH_2), 69.8 (CH_2), 67.4 (CH_2). HRMS (APCI+): calculated for $\text{C}_{54}\text{H}_{49}\text{Br}_2\text{N}_6\text{O}_8$ $[\text{M}+\text{H}]^+$: 1069.1953; found: 1069.1969.

Macrocycle 4. White solid; Mp.: 163 °C; $R_f = 0.15$ (Toluene:AcOEt 3:1 v/v). ^1H NMR (400 MHz, CDCl_3) δ_{H} (ppm): 8.31 (d, $^3J_{\text{H,H}} = 8.8$ Hz, 8H), 8.25 (d, $^3J_{\text{H,H}} = 8.5$ Hz, 4H), 7.47 (d, $^3J_{\text{H,H}} = 8.5$ Hz, 4H), 6.82 (d, $^3J_{\text{H,H}} = 8.8$ Hz, 8H), 4.03 (m, 8H), 3.95 (m, 8H), 3.79 (m, 8H), 3.75 (m, 8H). ^{13}C NMR (150 MHz, CDCl_3) δ_{C} (ppm): 170.4 (C=N), 169.7 (C=N), 162.5 (C=C, Ar), 135.3 (C=C, Ar), 131.6 (HC, Ar), 130.7 (HC, Ar), 130.3 (HC, Ar), 128.6 (C=C, Ar), 127.1 (C=C, Ar), 114.2 (HC, Ar), 71.3 (CH_2), 70.8 (CH_2), 69.9 (CH_2), 67.7 (CH_2). HRMS (APCI+): calculated for $\text{C}_{58}\text{H}_{57}\text{Br}_2\text{N}_6\text{O}_{10}$ $[\text{M}+\text{H}]^+$: 1157.2477; found: 1157.2494.

ACKNOWLEDGMENTS

Financial support provided by Romanian National Authority for Scientific Research and Innovation, CNCS-UEFISCDI, Project number PN-II-ID-PCE-2012-4-0248, is gratefully acknowledged.

REFERENCES

- (a) Z. Liu; S.K.M. Nalluri; J.F. Stoddart; *Chem. Soc. Rev.*, **2017**, *46*, 2459-2478; (b) I. Medruț; R. Turdean; R. Gropeanu; F. Pop; L. Toupet; N.D. Hădade; E. Bogdan; I. Grosu; *Tetrahedron Lett.*, **2013**, *54*, 1107-1111.
- D. Shetty; J.K. Khedkar; K.M. Parkad; K. Kim; *Chem. Soc. Rev.*, **2015**, *44*, 8747-8761.
- Y. Liu; Y. Chen; H.-Y. Zhang; *Handbook of Macrocyclic Supramolecular Assembly*, Springer Nature Singapore Pte Ltd., **2019**.
- X. Ma; Y. Zhao; *Chem. Rev.*, **2015**, *115*, 7794-7839.
- (a) M. Zhang; X. Yan; F. Huang; Z. Niu; H.W. Gibson; *Chem. Commun.*, **2020**, *56*, 766-769; (b) M. Otte; M. Lutz; R.J.M. Klein Gebbink; *Eur. J. Org. Chem.*, **2017**, *12*, 1657-1661; (c) X. Ji; M. Zhang; X. Yan; J. Li F. Huang; *Chem. Commun.*, **2013**, *49*, 1178-1180; (d) P. Wei; H. Wang; K. Jie; F. Huang; *Chem. Commun.*, **2017**, *53*, 1688-1691.

6. (a) G. Wang; T. Zhoua; Y. Lei; *RSC Adv.*, **2020**, *10*, 11557-11564; (b) P. Bhanja; K. Bhunia; S.K. Das; D. Pradhan; Ry. Kimura; Y. Hijikata; S. Irle; A. Bhaumik; *Chem. Sus. Chem.*, **2017**, *10*, 921-929.
7. P. Puthiaraj; Y.-R. Lee; S. Zhanga; W.-S. Ahn; *J. Mater. Chem. A.*, **2016**, *4*, 16288-16311.
8. (a) G.J.A.A. Soler-Illia; O. Azzaroni; *Chem. Soc. Rev.*, **2011**, *40*, 1107-1150; (b) M.A. Mintzer; M.W. Grinstaff; *Chem. Soc. Rev.*, **2011**, *40*, 173-190; (c) Y. Gao; Y. Qu; T. Jiang; H. Zhang; N. He; B. Li; J. Wu; J.J. Hua; *Mat. Chem. C*, **2014**, *2*, 6353-6358; (d) A. Modak; M. Pramanik; S. Inagaki; A. Bhaumik; *J. Mat. Chem. A*, **2014**, *2*, 11642-11650; (e) P. Puthiaraj; K. Pitchumani; *Chem.-Eur. J.*, **2014**, *20*, 8761-8770; (f) J. Lim; M. A. Mintzer; L.M. Perez; E.E. Simanek; *Org. Lett.*, **2010**, *12*, 1148-1151; (g) V. Percec; M.R. Imam; M. Peterca; W.D. Cho; P.A. Heiney; *Isr. J. Chem.*, **2009**, *49*, 55-70.
9. (a) C.B. Verma; M.A. Quraishi; E.E. Ebenso; *Inter. J. Electrochem. Sci.*, **2014**, *9*, 5537; (b) L.-J. Shao; G.-Y. Xing; C.-Z. Qi; *Chem. Pap.*, **2014**, *68*, 983; (c) M. N.S. Rad; S. Behrouz; A. Movahedian; M.M. Doroodmand; Y. Ghasemi; S. Rasoul-Amini; A.-R.A. Gandomani; R. Rezaie; *Helv. Chim. Acta*, **2013**, *96*, 688.
10. (a) R.- F. Zhang; W.- J. Hu; Y.A. Liu; X.- L. Zhao; J.- S. Li; B. Jiang; K. Wen; *J. Org. Chem.*, **2016**, *81*, 5649-5654; (b) J. Samanta; R. Natrajan; *Org. Lett.*, **2016**, *18*, 3394-3397.
11. (a) C.V. Crişan; A. Terec; N.D. Hădade; I. Grosu; *Tetrahedron*, **2015**, *71*, 6888-6893; (b) F. Pop; C. Socaci; A. Terec; E. Condamine; R.A. Varga; C.I. Raţ; J. Roncali; I. Grosu; *Tetrahedron*, **2012**, *41*, 8581-8588; (c) A. Woiczehowski-Pop; D. Gligor; A. Bende; C. Varodi; E. Bogdan; A. Terec; I. Grosu; *Supramol. Chem.*, **2015**, *27*, 52-58; (d) C. Lar; A. Woiczehowski-Pop; A. Bende; I.G. Grosu; N. Miklasova; E. Bogdan; N.D. Hădade; A. Terec; I Grosu; *Beilstein J. Org. Chem.*, **2018**, *14*, 1370-1377.
12. (a) B.P. Dash; R. Satapathy; J.A. Maguire; N.S. Hosmane; *Organometallics*, **2010**, *29*, 5230-5235; (b) A. Woiczehowski-Pop; I.L. Dobra; G.D. Roiban; A. Terec; I. Grosu; *Synth. Commun.*, **2012**, *42*, 3579-3588; (c) F. Piron; C. Oprea; C. Cismaş; A Terec; J. Roncali; I. Grosu; *Synthesis*, **2010**, 1639-1644.
13. K.M. Bongers; R.J.B.H.N. van den Berg; L.H. Heitman; A.P.I. Jzerman; J. Oosterom; C.M. Timmers; H.S. Overkleefta; G.A. van der Marel; *Bioorg. Med. Chem.*, **2007**, *15*, 4841-4856.

THE CORRELATION BETWEEN REACTIVE OXYGEN SPECIES AND ANTIOXIDANTS

ALINA OANA RUSU (MOLDOVAN)^{a,b}, MARIA IULIANA GRUIA^{c*},
VIORICA LAZAR LORDEAN^d, DAN MIHU^b

ABSTRACT. Oxidative stress represents as an important factor in carcinogenesis and may play a role in initiation and progression of tumors. Oxidative stress is responsible for DNA damage, and includes a multitude of lesions, many of which are mutagenic and have multiple roles in cancer and aging. The aim of the study is to demonstrate that an antioxidant treatment administration before surgery can influence the breast cancer patients' immune response. Whole blood samples from 113 patients with breast cancer, admitted in the Surgery Department III of the Oncology Institute of Bucharest were collected and the blood serum was isolated, and then made determinations of malondialdehyde, ceruloplasmin, albumin thiols, and total antioxidants. What was shown in this study is that ROS can increase cell proliferation and genomic instability, which stimulates disease progression, and the tumor is an oxidative stress inducer that can influence the redox balance. The key of an effective compensatory body response to this imbalance, cannot be done without exogenous antioxidant support.

Keywords: ROS, breast cancer, oxidative stress mechanisms, antioxidants

INTRODUCTION

The interest in a more accurate understanding and deepening the underlying oxidative stress mechanisms and its implications in various

^a Department of Surgery III, "Prof. Dr. Alexandru Trestioreanu" Institute of Oncology, Bucharest, 252 Fundeni Road, Bucharest, Romania

^b Department of Obstetrics and Gynecology II, "Iuliu Hațieganu" University of Medicine and Pharmacy, 55-57 21 December 1989 Bulevard, Cluj-Napoca

^c Department of Biochemistry and Radiobiology, "Prof. Dr. Alexandru Trestioreanu" Institute of Oncology, 252 Fundeni Road, Bucharest, Romania

^d Department of Medicine II, "Vasile Goldis" University of General Medicine, 86 Liviu Rebreanu Street, Arad, Romania

* Corresponding author: gmariaiuliana@yahoo.com

neoplasms has become very high in the recent decades. To prevent cell damage by oxidative stress, the aerobic body cells have developed over time a series of extremely powerful anti-oxidant strategies.

Antioxidants are compounds with the ability to reduce ROS and are classified into endogenous and exogenous, enzymatic and non-enzymatic antioxidants.

Among the primary important endogenous antioxidants, we can mention the enzymatic ones (superoxide dismutase, catalase and glutathione peroxidase) or the non-enzymatic ones (vitamin E, C) while the exogenous ones are chemical compounds with polyphenolic structures, anthocyanins, etc. [1]

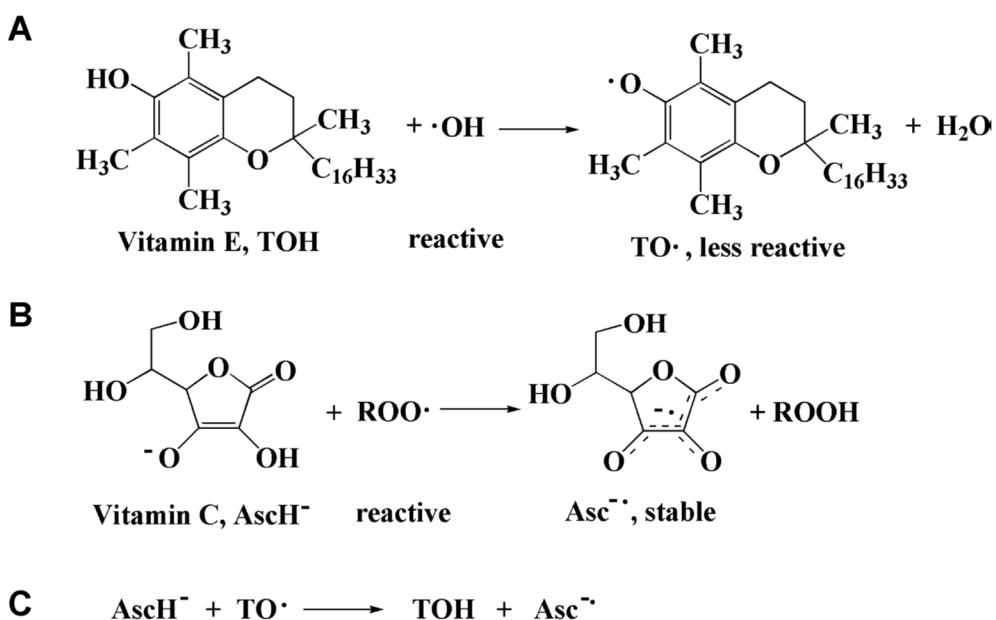


Figure 1. Direct reactions of vitamin E (TOH) with $\cdot\text{OH}$ (A) and vitamin C (AscH) with $\text{ROO}\cdot$ (B) and regeneration of vitamin E from vitamin C (C).

Antioxidants can be molecules that can neutralize free radicals by accepting or donating electrons to eliminate the unpaired state of the radical. Antioxidant molecules can directly react with reactive radicals and destroy them, while new free radicals can become less active, have a longer lifespan and be less dangerous than those radicals they have neutralized. They can be neutralized by other antioxidants or other mechanisms to end their radical status. Many antioxidants have aromatic ring structures and are able to

relocate unmatched electrons (Fig.1). Vitamin C (AscH) in the aqueous phase and vitamin E (TOH) in the lipid phase will react directly with or will neutralize the hydroxyl, alkoxyl and lipid peroxy ($\text{ROO}\cdot$) radicals and form H_2O , alcohol and lipid hydroperoxides.

Vitamin E itself becomes a phenyl radical, and vitamin C will become into a very stable radical (Asc \cdot), due to its delocalized structure (Fig. 1A and B). In addition, vitamin C can also neutralize the radical form of other antioxidants such as the glutathione radical and vitamin E radical and regenerate them (Fig. 1C). Vitamin C itself is easily regenerated into Asc \cdot with NADH or NADPH dependent reductase [2].

In case of increased oxidative stress, free radicals can cause cytotoxicity, inhibit cell proliferation and have an important role in inducing cell death by apoptosis or necrosis.

Medium or low oxidative stress can induce cellular mutations [3]. It is well known that in high concentrations, ROS have a destructive action at the cellular level, but in low concentrations they can act as signaling molecules.

Once reactive oxygen species are formed, they are rapidly broken down in by the cells' endogenous antioxidant systems.

Recent studies show that in the breast cancer microenvironment, oxidative stress causes mitochondrial dysfunction at the subcellular level. This is manifested by regulating several factors, such as nuclear respiratory factor 1 (NRF1), which increases in the tumor tissue due to the installed oxidative stress [4].

Reactive oxygen species (ROS) are produced by both enzymatic and non-enzymatic systems in eukaryotic cells and play important roles in the cells' physiology and pathophysiology. Although physiological concentrations are essential for cell survival, overproduction of ROS is detrimental in normal cells and is considered a key factor in the onset of several diseases, such as neurodegenerative diseases, cardiovascular disorders and cancer [5].

Increased production of reactive oxygen species has been shown in many cancers, but their involvement in carcinogenesis and tumor progression is not yet fully understood. High ROS levels are oncogenes, that can cause DNA damage, promote genetic instability and tumorigenesis, act as signaling molecules, cause tumor cell proliferation and survival. They also stimulate abnormal cell growth, invasion and metastasis, and produce resistance to apoptosis [6,7,8].

Reactive oxygen species interact with essential macromolecular structures, especially with nucleic acids, proteins and lipids. Because these structures are essential for the tumor metabolism, ROS interferes with the normal cell function [9].

The aim of the study is to demonstrate that an antioxidant treatment administration before surgery can influence the breast cancer patients' immune response.

RESULTS AND DISCUSSION

The patients' clinical condition was assessed by a complete clinical examination and the performance status was assessed using the ECOG scale.

At diagnosis, 72.6% of patients (82/113) presented a good performance status ECOG 0 (Fully active), 24.8% (28/113) with ECOG 1 (able to perform normal light or sedentary physical activities) and 2.6% (3/113) with ECOG 2 (mobile, apparently active, but unable to work over 50% of their physically active time) (Fig. 2).

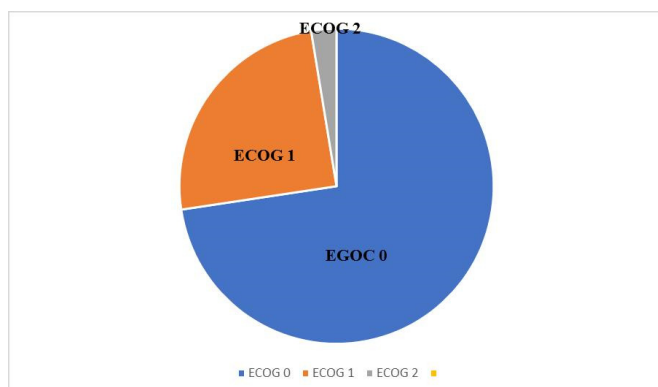


Figure 2. Representation of patients' performance status.

In the studied group, the staged distribution of the disease was heterogeneous: stage IIA - IIB and IIIA, with 80% invasive ductal carcinomas: solid tumors, imprecisely delimited, hard consistency, firm, because of the calcifications and desmoplastic reaction.

The remaining 20% patients presented lobular carcinomas with a discrete, firm form, a grey-white mass with irregular borders. The background stroma is densely fibrous and contains foci with periductal and perivascular elastosis, with or without peritumoral lymphocytic infiltrate.

The patients' elective surgical indication was radical mastectomy. All the patients received premedication and standardized anesthesia and were admitted to intensive care after surgery.

For the investigated group, the obtained average values of the oxidative stress parameters are presented in the table below. There is a statistically significant increase of all registered parameters compared to the normal value (Table 1). For each patient were taken four blood samples, in dynamic: 24 hours before surgery, at the time of the anesthetic administration, 24 hours after surgery and at 7 days after surgery.

Table 1. The average values of the oxidative stress parameters

	Malondialdehyde ($\mu\text{mol} / 100 \text{ ml}$ ser)	Cerulo- plasmin	Thiols	Antioxidants
Average	6.84	164.51	383.14	1.36
Standard median error	0.20	4.1	8.89	0.03
Median	6.35	169	325	1.34
Standard deviation	1.94	62.84	132.11	0.49
Minimum	3.16	65	183	0.06
Maximum	10.83	264,02	583.28	4.10
Normal value	0-4 $\mu\text{mol}/100 \text{ ml}$	80- 120 U.I	370 - 450 $\mu\text{mol}/\text{l}$	0.9-1.4 $\mu\text{mol}/\text{l}$

Regarding the dynamic evolution of the lipid peroxidation, it is found that the value of malondialdehyde decreased after the anesthetic-surgical time. The mean value recorded at the first administration was $8.95 \mu\text{mol} / 100 \text{ ml}$, much higher than the normal maximum value of $4 \mu\text{mol} / 100 \text{ ml}$ decreasing to $7.07 \mu\text{mol}/100$. All ceruloplasmins' values remained relatively constant, the initial value being 176.04 U.I., and at the end registering the value of 199.29 U.I. (Fig. 3).

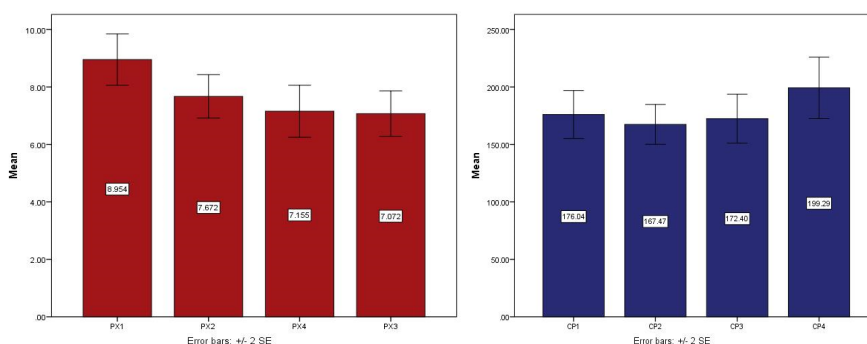


Figure 3. Evolution in dynamics of lipid peroxidation by determining the values of malondialdehyde and ceruloplasmin

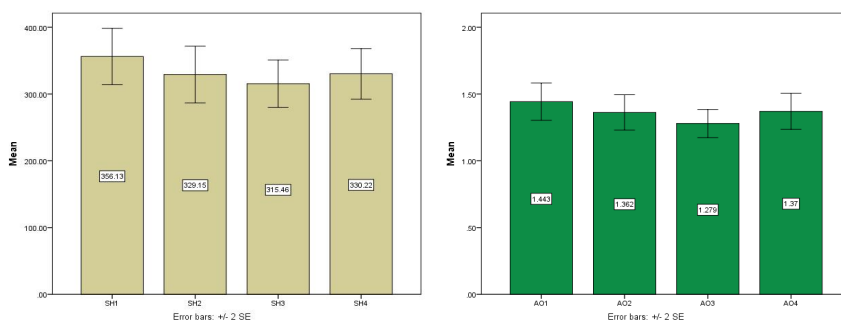


Figure 4. Dynamic evolution of albumin thiols and changes in dynamic of the average values of the total antioxidants

Albumin thiol values also decreased after the surgical treatment from 357.18 $\mu\text{mol} / \text{l}$ to 330.21 $\mu\text{mol} / \text{l}$.

The dynamics of antioxidants was similar with the thiols, so that the average value at the first determination was 1.44 $\mu\text{mol} / \text{l}$, and finally 1.37 $\mu\text{mol} / \text{l}$ (Fig. 4).

The presented data claim that the oxidative stress balance is more inclined in the favor of free oxygen radical excess production in the detriment of their uptake. The defense mechanisms represented by antioxidants can't compensate for the fact that the tumor is an inducer of oxidative stress (Fig. 5).

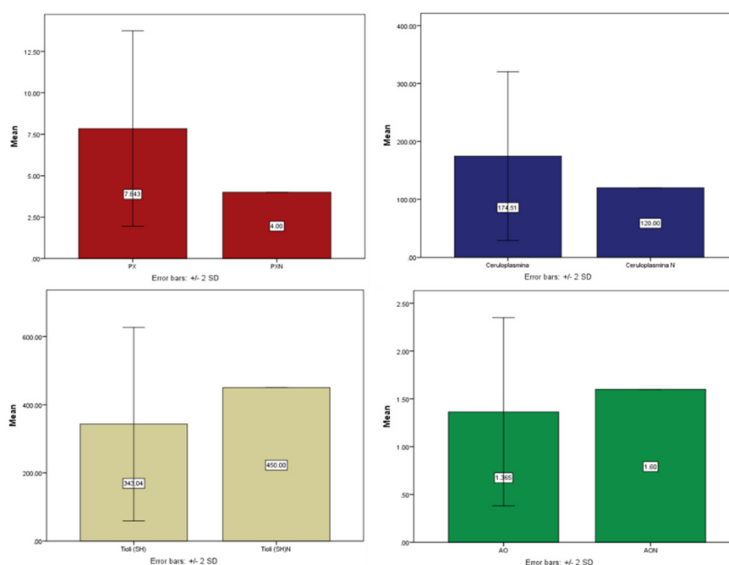


Figure 5. Average values of malondialdehyde, ceruloplasmin, thiols and antioxidants

THE CORRELATION BETWEEN REACTIVE OXYGEN SPECIES AND ANTIOXIDANTS

In our study group, it was found that there is a very strong correlation between lipid peroxidation values determined by measuring malondialdehyde and ceruloplasmin values ($r = 0.382$, $p < 0.0001$). There are statistically significant correlations between the values of ceruloplasmin and albumin thiols ($r = 0.260$, $p < 0.0001$) (Fig. 6A and Fig. 6B).

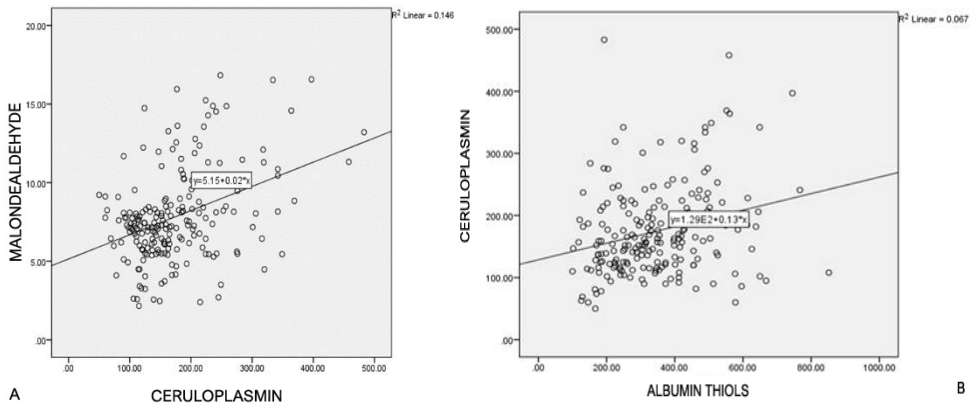


Figure 6A. Correlation between lipid peroxidation values represented by malondialdehyde and ceruloplasmin values; **6B.** Correlation between ceruloplasmin and thiol values

In the group of patients studied there was a strong correlation between the values of albumin thiols and the value of the total antioxidants ($r = 0.196$, $p < 0.005$), as a direct correlation also exists between lipid peroxidation values (default of malondialdehyde) and total thiols ($r = 0.297$, $p < 0.0001$) (Fig. 7A and Fig. 7B).

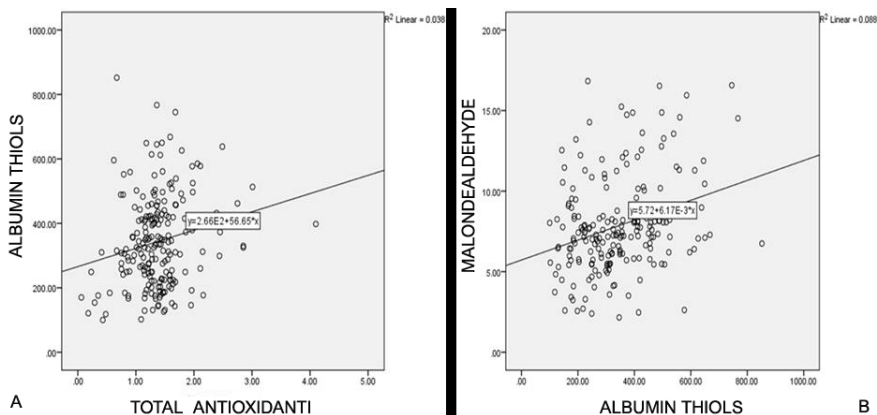


Figure 7A. Correlation between albumin thiol values and total antioxidant values; **7B.** Correlation between the value of malondialdehyde and the value of thiols

Statistically, there were no significant correlations between the values of malondialdehyde and antioxidants ($r = 0.0380$ and $p < 0.05$) and between the values of ceruloplasmin and antioxidants ($r = 0.984$, $p > 0.001$) (Fig. 8A and Fig. 8B).

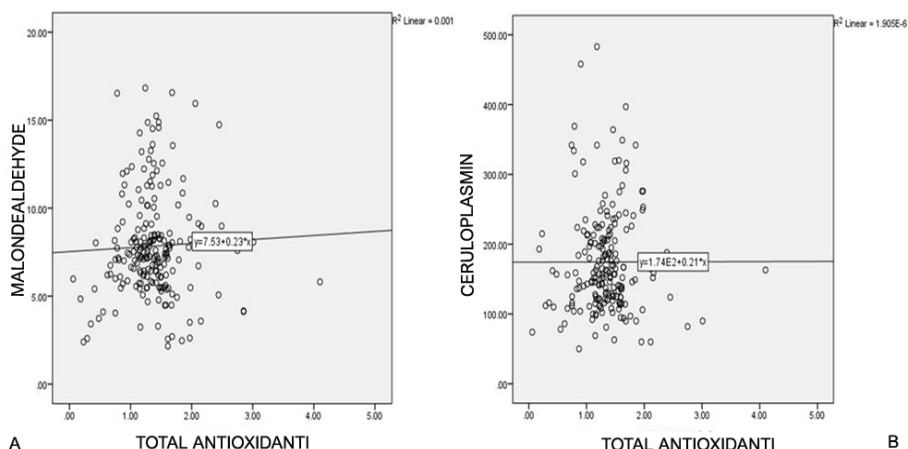


Figure 8A. Correlation between the value of malondialdehyde and antioxidants;
8B. Correlation between the value of ceruloplasmin and antioxidants

To prevent cell damage by oxidative stress, the cells of aerobic organisms have developed over time a series of extremely powerful anti-oxidant strategies. ROS may be accidentally generated as a consequence of altered cellular metabolism (eg during cellular respiration cycle), or by inflammation.

ROS have oxygen-derived molecules that are thought to be responsible for severe metabolic imbalances [10]. The main source of intracellular ROS is determined by the oxidative process in the mitochondrial respiratory chain. Normally in a healthy body oxidative stress reacts as a signal. But under pathophysiological conditions, it is a determining factor in malignant cell amplification and phenotyping [11].

Martindale and Holbrook estimated that ROS occurs in 1-2% of the oxygen used by mitochondria during oxidative phosphorylation and is therefore considered to be a normal by-product of the metabolism energy. Some common forms of ROS resulting from oxidative phosphorylation like superoxide anion ($O_2\bullet^-$), such as hydrogen peroxide (H_2O_2) and hydroxyl radicals ($OH\bullet$), act as oxidants, stealing electrons from nucleic acids, proteins and lipids. Normally the body is accustomed to elevated levels of ROS by activating the apoptotic pathways, and mechanisms that convert ROS to non-toxic products are endogenous absorption enzymes (e.g., antioxidants) [12].

ROS interferes with the body through two effects: primary and secondary. The primary effect is localized and reversible, depending on the intensity of the oxidative stress and the level of antioxidants and highlighted by a performance score 0-1 (changes in cell membrane permeability, ionic imbalances, peroxidation of fatty acids in cell membranes, changes in cellular metabolic processes because of protein alterations and the decreased energy production).

The transition to the secondary effect marks the irreversible phase and is accompanied by the appearance of clinical manifestations like cell lysis, altered biofunctions, low activity resistance, or to infections - specific for a 2-4 score. In this stage the imbalance of calcium ions that promotes the activation of hydrolytic enzymes, protease, cell lysis, vascular disorders, peroxidation of proteins and nucleic acids, altered immune reactivity, tissue damage located in one or more organs. High exercise activity causes oxidative stress only in overload training (in large volume or long-term period) and can lead to an impaired antioxidant defense [13].

Saed, Diamond and Fletcher N. in their paper established that in the cancer cell, the presence of the imbalance between the production of reactive oxygen species and the elimination of free radicals leads to a state of oxidative stress and to the destruction of some essential components of the cell [14].

M. Ryan Smith, Praveen K. Vayalil, Fen Zhou, Gloria A. Benavides in their work they demonstrated that free oxygen radicals released by the malignant tumor can be partially but not totally inhibited by the administration of antioxidants, as demonstrated by the determination of thiols and other components in their study [15].

The data presented suggest that the balance of oxidative stress is more inclined in the favor of the excess production of free oxygen radicals to the detriment of their uptake.

Weinberg and Chandel demonstrated that elevated ROS levels overwhelm the cell's ability to respond appropriately. ROS overproduction becomes a threat to nucleic acids, proteins and lipids that ultimately lead to oncogenic transformation [16].

CONCLUSIONS

The defense mechanisms represented by antioxidants cannot compensate for the fact that the tumor is an inducer of oxidative stress. The disease progression is represented by resistance to apoptosis, increased cellular mobility with the increased metastatic capacity, as well as the

conversion to anaerobic glycolysis. On the other hand, the excess production of ROS is in the detriment of cancer cell survival and proliferation, through the destructive mechanisms given by the oxidative-destructive reactions of biomacromolecules essential to life.

All of the determinations strengthen the idea that ROS overproduction and the lack of an effective compensatory body response to this imbalance, cannot be done without exogenous antioxidant support.

EXPERIMENTAL SECTION

There were studied in dynamic 113 patients with breast cancer, admitted in the Surgery Department III of the Oncology Institute of Bucharest for surgery treatment, between October 2016 and December 2018.

The patients were diagnosed with breast cancer, the results firmly confirmed by histopathological reports.

The approval of the study was obtained from the Ethics Committee of the Oncology Institute of Bucharest No. 15920/12.11.2018.

After giving their personal consent in writing, whole blood samples were collected by venous puncture. By centrifugation using a Beckman J2-J1 model (Germany, 2002), the blood serum was isolated, and then the following determinations were made:

- The lipid peroxides were evaluated by measuring the final concentration of malondialdehyde (MDA). The method is spectrophotometric and is based on the formation of a colored adduct (MDA- TBA2) that develops maximum absorption at 532nm depending on the concentration.

- The oxidative activity of ceruloplasmin. We used the Ravin method by reaction with p-phenylenediamine in acetic acid-acetate pad. The color intensity developed at 540nm is directly proportional with the concentration of the measured compound.

- The thiol-albumin groups TA were determined by reaction with the 5,5'-dithiobis (2- nitrobenzoic) acid, Ellman's reagent, which, following oxidations, develops the maximum intensity at 412 nm in accordance with the concentration of the SH groups formed.

- The total antioxidants were biochemically measured by a method that utilizes the ability of the serum to reduce iron. When the pH is low, the FeIII-tripyridyl-s-triazine complex (FeIII -TPTZ) is reduced to its ferrous form, by forming a new complex that develops an intense blue color, measurable, with a maximum absorption at 593 nm.

In order to make these determinations, the solutions were prepared using compounds of analytical purity from Merck and Sigma, the water that

has been used was genetically pure after filtering by Millipore devices (Milli-Q-Biocel, United States, 2010), and the spectrophotometric readings were carried out on a Specord 210 spectrophotometer (Germany 2005).

ACKNOWLEDGMENTS

No funding was received for this work. This research did not receive any specific grant from funding agencies in the public, commercial, or not-for-profit sectors.

REFERENCES

1. A.R. Nourazarian, P. Kangari, A. Salmaninejad; *Asian Pac J Cancer Prev.*, **2014**, *15*, 4745–4751.
2. M.A. Hossain, K. Asada; *J Biol Chem*, **1985**, *260*, 12920–6.
3. I.I.C. Chio, D.A. Tuveson; *Trends in Mol Med*, **2017**, *23*, 411–29.
4. R.C. Rose, A.M. Bode; *Biochem. J*, **1995**, *306*, 101-105.
5. V. Adler, Z. Yin, K.D. Tew, Z. Ronai; *Oncogene*, **1999**, *18*, 6104–6111.
6. L. Gate, J. Paul, G.N. Ba, K.D. Tew, H. Tapiero; *Biomedicine & Pharmacotherapy*, **1999**, *53*, 169-180.
7. D.H. Kang; *AACN Clinical Issues*, **2002**, *13*, 540-549.
8. G. Sigounas, A. Anagnostou, M. Steiner; *Nutrition and Cancer*, **1997**, *28*, 30-35.
9. S. Kiokias, M.H. Gordon; *European Journal of Clinical Nutrition*, **2003**, *57*, 1135-1140.
10. S. Sharhar, H. Normah, A. Fatimah, R.N. Fadilah, Ga. Rohi, et al; *Asian Pacific Journal of Cancer Prevention*, **2008**, *9*, 343–349.
11. R. Kumaraguruparan, S. Naghini, et al; *Clinica Chimica Acta*, 2002, *325*, 165-170.
12. J.L. Martindale, N.J. Holbrook; *J Cell Physiol*, **2002**, *192*(1), 1-15.
13. E. Mihalas, LI. Serban, D. Matei, D. Cascaval, Al. Galaction; *Studia UBB Chemia*, **2019**, *LXIV* (2), Tom I, 35-47.
14. G.M. Saed, M.P. Diamond, N.M. Fletcher; *Gynecol Oncol.*, **2017**, *145*(3), 595-602.
15. M.R. Smith, P.K. Vayalil, F. Zhou, G.A. Benavides, et al; *Redox Biol.*, **2016**, *8*, 136-48.
16. F. Weinberg, N.S. Chandel; *Ann N Y Acad Sci.*, **2009**, *1177*, 66-73.

DETERMINATION OF THE COMPOSITION AND CONTAMINATION WITH HEAVY METALS OF SOILS FROM THE SREBARNA LAKE RESERVE

METODI MLADENOV^{a*}, SPASKA YANEVA^b

ABSTRACT. The wetlands in direct contact with large rivers, such as the connection between Srebarna Lake and the Danube River, are particularly vulnerable to heavy metals. These metals can be a serious problem due to their toxicity, long persistence and bioaccumulation in the food chain, at the top of which in the wetlands are the waterfowl. For this reason, they are extremely susceptible to the accumulation and influence of heavy metals in their bodies and it is possible to come on to accumulation of significant concentrations, leading to negative effects for them. In this regard, subjects of study in this article are soils from the reserve area. Eight soil samples were tested for pH, electrical conductivity, nutrient content and heavy metals presence. The presented results show that the soils in the area have a relatively good stock in terms of carbon (humus), Ca, Mg, K and P, and although some heavy metals and metalloids have been found, their concentrations are below the permissible normatively established values.

Keywords: soil composition, bioaccumulations, nutrients, heavy metals, contamination, toxicity.

INTRODUCTION

Srebarna Lake is situated in northeastern Bulgaria, on the Bulgarian bank of the Danube, beside the village of Srebarna [1, 2]. It has coordinates: 44°07 N, 27°04 E, area of 120 ha, a depth of 1.7 to 4.7 m dependent on Danube water level, volume of 2.81-14.35 km³ and the lake status is eu-hypertrophic [3]. "Srebarna" nature reserve is one of the eleven wetlands in

^a University of Chemical Technology and Metallurgy, Department of Engineering Ecology, 8 St. Kl. Ohridski Bul, 1756, Sofia, Bulgaria.

^b University of Chemical Technology and Metallurgy, Department of Organic Chemical Technology, 8 St. Kl. Ohridski Bul, 1756, Sofia, Bulgaria.

* Corresponding author: mladenov@uctm.edu

Bulgaria, declared in 1942 like a "breeding ground" for waterfowl, and hunting in the lake was forbidden. Over the years, "Srebarna" has had undergone many changes in its status, mainly due to the different attitude of the state to its management – from inclusion in the list of endangered from strike off the UNESCO list, to granting the status of a maintained reserve and its inclusion for permanent in the list of the sites of the world cultural and natural heritage. [4, 5].

Wetlands such as Srebarna Lake are areas where water covers the soil or is present in its surface layer, year-round or seasonally. In these ecosystems, water is the main factor on which ecological conditions and related animal and plant species depend [6]. Periodic monitoring of various environmental factors and the interrelationships between them is crucial for the maintenance of ecological status and biodiversity, as the accumulation of pollutants in these ecosystems can lead to deterioration of biological living conditions and to the disruption of ecological equilibrium [7-11]. The wetlands in direct contact with large rivers, such as the connection between Srebarna Lake and the Danube River, are particularly vulnerable to heavy metals. In such type of wetland, the assessment of heavy metal content gives a more realistic idea of the actual impact of the river on the surrounding environment, as these river waters are usually severely affected by human activity [12-15].

Heavy metals, can be a serious problem due to their toxicity, long persistence and bioaccumulation in the food chain, and in high concentrations can lead to damage to animal species. They have the ability to react with the aquatic ecosystems with multiple and complex mechanisms and interactions, and can bind to different geochemical phases in sediments. They can also accumulate in the aquatic biota and have the ability to be converted into organic complexes, which may be more toxic than the simple elements. Accumulation and movement in aquatic ecosystems, when the concentration of heavy metals in the water is low, can occur along the food chain, in base of which are the soil and sediment. [11, 13, 14, 16].

Because waterfowl have a relatively long life and are at the top of the food chain in marshy systems, they are extremely susceptible to the accumulation and influence of heavy metals in their bodies. In migratory birds, even short-term contact with contaminated habitat leads to the accumulation in the body of significant amounts of the respective pollutant, which is directly related to their rapid metabolism, and it is possible to lead to the accumulation of significant concentrations leading to negative effects for them [17]. Thus, for example, Kwok and team [18] reported the bioaccumulation of non-essential elements (Cd, Hg, Pb) in various organs and tissues of Ardeid, such as feathers, liver, kidneys, muscle and eggs, such as claim some of these inorganic elements can accumulate in the egg shells, and that these shells

DETERMINATION OF THE COMPOSITION AND CONTAMINATION WITH HEAVY METALS OF SOILS FROM THE SREBARNA LAKE RESERVE

can be used as indicators of heavy metal contamination. The following figure summarizes the main heavy metals that are monitored in the environment and some of the negative effects they have on the bird population.

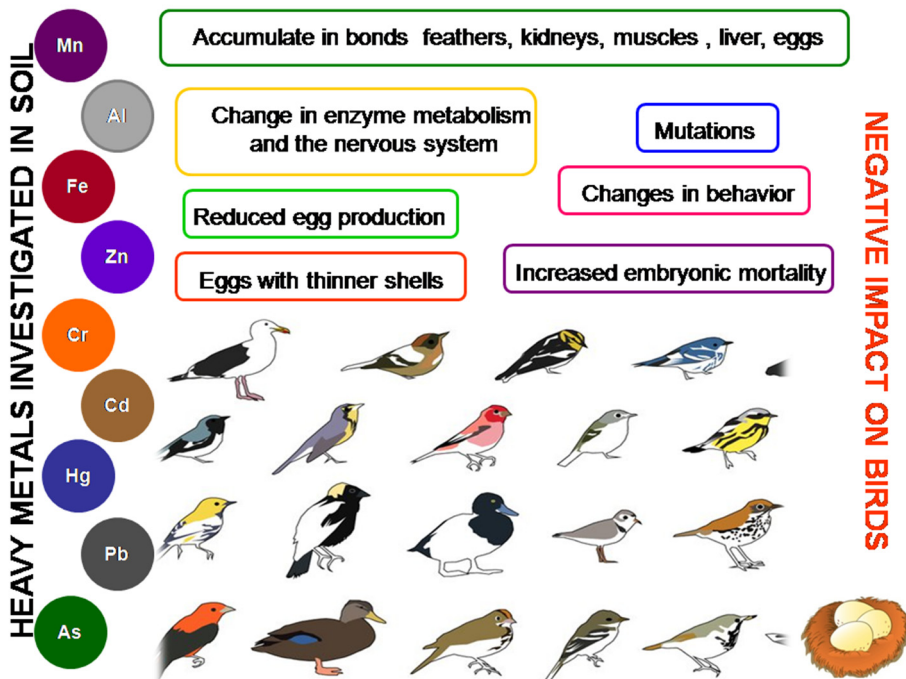


Figure 1. Accumulation of heavy metals in the avian organisms

The objectives of this study are to survey the soil composition and heavy metals content in the Srebarna Lake wetland.

RESULTS AND DISCUSSION

The reaction of soils has a significant impact on the soil formation process and on soil fertility. The vital activity of microorganisms, the direction of the ongoing biochemical processes in the soil and the availability of nutrients for plants depend to a large extent on it. The most favorable for the plants are the weakly acidic and neutral reaction of the soil, and in the conditions of low pH the solubility and migration of some of the elements significantly increase.

The established values for pH of all samples (see Table 1) are in the range pH = 6.2-7.2, which defines them as extremely favorable for the development of plant species, and the established values correspond to the data on soil acidity in wetlands. The lowest established value is for sample 6 – pH = 6.28, and the highest for sample 5 – pH = 7.11.

Table 1. Physicochemical parameters

Sample №	pH	Conductivity (mS/cm)
1	7.06	0.627±0.009
2	6.83	0.534±0.006
3	6.42	0.698±0.010
4	6.71	0.208±0.005
5	7.11	0.189±0.005
6	6.28	0.144±0.004
7	7.05	0.574±0.008
8	6.77	0.236±0.007

The determination of electrical conductivity is done in order to determine the presence of mobile forms (usually ions) of the elements in the solution and usually higher values of conductivity, indicate the presence of a large number of these mobile forms, mainly metals. The measured values for this indicator (see Table 1) characterize the studied soils as poor of mobile ions of the elements, as the highest values were found in samples 1 and 3 – 0.627 mS/cm and 0.698 mS/cm, respectively.

Plants obtain phosphorus from the soil, where it is found in the form of organic and mineral compounds in relatively small quantities – 0.05-0.25%. The amount and distribution of phosphorus compounds in the soil depend mainly on the phosphorus content of the soil-forming rock and on the conditions of soil formation. The results with respect to this element (see Table 2) show a relatively good stock in the studied soils.

Table 2. Nutritional element content, in dry matter

Sample №	Element, %						
	N	P	K	Na	Ca	Mg	C*
1	0.06±0.007	0.20±0.01	0.54±0.09	0.063±0.011	1.54±0.33	0.84±0.10	5.37±0.22
2	<0.01	0.19±0.01	0.56±0.08	0.082±0.015	1.47±0.28	0.67±0.14	2.13±0.18
3	0.01±0.004	0.21±0.02	0.75±0.09	0.072±0.012	0.74±0.17	0.77±0.11	3.61±0.15
4	<0.01	0.14±0.01	0.63±0.08	0.173±0.022	1.27±0.25	1.24±0.17	1.75±0.11
5	0.02±0.004	0.16±0.01	0.70±0.09	0.054±0.013	2.32±0.34	0.62±0.11	2.54±0.19
6	<0.01	0.10±0.01	0.42±0.07	0.058±0.014	2.73±0.37	0.86±0.12	1.17±0.16
7	0.04±0.006	0.17±0.01	0.65±0.08	0.068±0.013	2.19±0.28	0.58±0.09	3.47±0.23
8	<0.01	0.15±0.02	0.60±0.09	0.073±0.015	1.47±0.25	0.93±0.14	2.73±0.17

* expressed like a content of humus

DETERMINATION OF THE COMPOSITION AND CONTAMINATION WITH HEAVY METALS
OF SOILS FROM THE SREBARNA LAKE RESERVE

The carbon content in the soil is mostly in the form of the so-called humic compounds, because of that in practice it is accepted to determine the content of total carbon and most often this indicator of brevity is referred to as humus. The average humus content in the soils in Bulgaria is in the range of 2-4%. The comparison of the obtained results (see Table 2) with these values again shows a good stock in the studied samples. Lowest, below 2% are the values established in samples: 4 – 1.75% and 6 – 1.17%.

The results for the total content of the element nitrogen show extremely low values – below 0.1%, in all samples.

The elements Na, Ka, Ca and Mg serve as a source of cationic nutrition for plants and belong to the group of so-called exchange cations. The results of their analysis show that the content of calcium cations is predominant a characteristic feature of the soils formed under grassy and forest vegetation. The highest content (Table 2) for this element was found in sample 6 – 2.73%, and the lowest in sample 3 – 0.74%.

The results for the sodium content in all samples are in the range of 0.05-0.2% and classify them as non-saline soils. Regarding the element K, the results (see Table 2) fall in the range of 0.4-0.8% and show a good supply of this nutrient. For the element magnesium, the highest content was found in sample 4 – 1.24%, and the lowest in sample 7 – 0.58%.

The results of the analysis for heavy metal content performed by ICP-OES are given in Table. 3.

Table 3. Content of heavy metals, in dry matter

Concentration, mg.kg⁻¹	Sample №							
	1	2	3	4	5	6	7	8
Al*10 ³	25.5	28.4	27.2	32.4	25.6	26.9	22.5	28.4
Cr	50.1	57.7	52.6	74.7	53.6	44.2	47.8	56.6
Mn	491.3	567.1	697.3	681.1	491.5	593.5	447.4	631.0
Fe*10 ³	11.3	22.9	30.2	25.6	20.4	16.3	18.0	17.4
Co	9.8	10.2	10.7	14.3	12.8	11.4	11.1	12.2
Ni	31.2	24.5	34.3	45.1	27.6	32.4	21.7	24.4
Cu	33.4	50.2	56.3	63.3	28.4	33.2	30.7	37.2
Zn	70.2	68.4	79.4	89.3	62.4	60.3	51.8	68.6
As	<0.5	<0.5	<0.5	11.7	5.11	1.97	<0.5	3.5
Pb	<0.5	<0.5	<0.5	2.5	1.7	<0.5	<0.5	<0.5
Se	<0.5	<0.5	<0.5	<0.5	<0.5	<0.5	<0.5	<0.5
Bi	<0.5	<0.5	<0.5	<0.5	<0.5	<0.5	<0.5	<0.5
Cd	<0.25	<0.25	<0.25	<0.25	<0.25	<0.25	<0.25	<0.25
Sb	<0.5	<0.5	<0.5	<0.5	<0.5	<0.5	<0.5	<0.5

*Values for these elements showed with "<" represent the detection limits values

Obtained values for heavy metals contents were compared with maximum admissible concentrations (MAC) values for heavy metals in soils, for the elements for which such values are regulated in the Bulgarian legislation [19]. These values depend on the type of soil usage, the objects of preservation, the mechanical composition and pH (H₂O) of the soils. According to this regulation, the sampled soils can be classified like a permanent grass areas and the MAC values according to established pH values for them are presented in Table 4.

Table 4. MAC values for soils of permanent grass areas

<i>Element</i>	<i>As</i>	<i>Cu</i>	<i>Cr</i>	<i>Ni</i>	<i>Pb</i>	<i>Zn</i>
MAC at pH (H ₂ O) 6.0 – 7.4, mg.kg ⁻¹	30	140	250	80	130	390

The presence of Al, Co, Cu, Fe, Zn, Ni, Mn and Cr was detected in all tested samples (see Table 3), and highest values were found for the elements Al and Fe in the concentration ranges of 22000-32000 mg.kg⁻¹ and 11000-31000 mg.kg⁻¹, respectively, for which elements, however, there are no MAC values in the national legislation. The data obtained from the study also show high contents of the element manganese – in the range of 400-700 mg.kg⁻¹, for which, element also has no normative maximum values.

Significant contents were also found for the elements Zn and Cr, although below the MAC values (MAC_{Zn} = 390 mg.kg⁻¹ and MAC_{Cr} = 250 mg.kg⁻¹), respectively for Zn – 51-90 mg.kg⁻¹ and for Cr – 44-75 mg.kg⁻¹. Arsenic content was found in samples 4, 5, 6 and 8, but in concentrations significantly lower than the corresponding MAC value – 30 mg.kg⁻¹.

No dependence of the content of the determined elements on the location of the sampling points is established. Such a dependence can be allowed for the element lead, for which values have been established above the limits of determination of the apparatus used, in two of the samples (sample 4 – 2.5 mg.kg⁻¹ and sample 5 – 1.7 mg.kg⁻¹) which are located not far from automobile road.

The results of the soil surveys show that they do not appear as a source of heavy metals for the environment in the reserve. The studied soils cannot lead to a negative impact on the bird populations inhabiting the territory of Srebarna Lake reserve. Due to the connection of the lake with the Danube River and the water regimes in which the areas around the reserve are flooded periodically, it is recommended to conduct annual monitoring of soil conditions for heavy metals and other toxic substances subject to different control and monitoring regimes.

CONCLUSIONS

The established values for pH of all samples are in the range $\text{pH} = 6.2\text{-}7.2$, which defines them as extremely favorable for the development of plant species. The measured values for the conductivity characterize the studied soils as poor of mobile ions of the elements.

The analysis of the content of nutrients in the tested samples shows a relatively good stock in terms of carbon (humus), Ca, Mg, K and P and insufficient content of N, and the values for the element sodium allow the studied soils to be classified as non-saline soils.

The results of the analysis of the content of heavy metals in the studied soil samples show values many times lower than the maximum permissible concentrations established in the national legislation.

EXPERIMENTAL SECTION

Sampling and sample preparation

Sampling points are situated in the area of Srebarna Lake reserve – see Figure 2. The soil samples were taken in 2019 year, according to standard requirement [20]. The depth of sampling is 0-30 cm. Preliminary treatment for preparation for physico-chemical tests was performed according to the requirements of [21]. The sample preparation of the samples for analysis of the content of K, Na, Ca and Mg and heavy metals was performed according to the standard methodology – BNS 16174 [22].

Instrumentation and measurement conditions

Conductivity measurements and pH determinations were performed with combined pH meter PCE-PHD1 (PCE instruments), according to requirements of – BNS EN 15933 [23] and BNS ISO 11265 [24]. The Kjeldahl method was used for determination of nitrogen content [25]. Phosphorus was determined spectrophotometric [26], through UV-VIS spectrophotometer Specol-11, Carle-Tseys (Germany). The content of K, Na, Ca and Mg was determined by flame atomic-absorption spectrometry (Thermo Elemental, SOLAR – M5 AA) after decomposition in “aqua regia”. Contents of the elements Al, Co, Cu, Fe, Zn, Ni, Cd, Mn, Pb, Cr, As, Se, and Bi were determined by inductively coupled plasma optical emission spectrometry (Prodigy Teledyne, Leeman Labs) [27].

Reagents

The following reagents were used to perform the experimental work: HCl (37 % suprapur, Fluka), HNO_3 (65 % suprapur, Merck), H_2SO_4 (98 %, pure for analys, Valrus) and Milli-Q water (0,01 $\mu\text{S}/\text{cm}$).

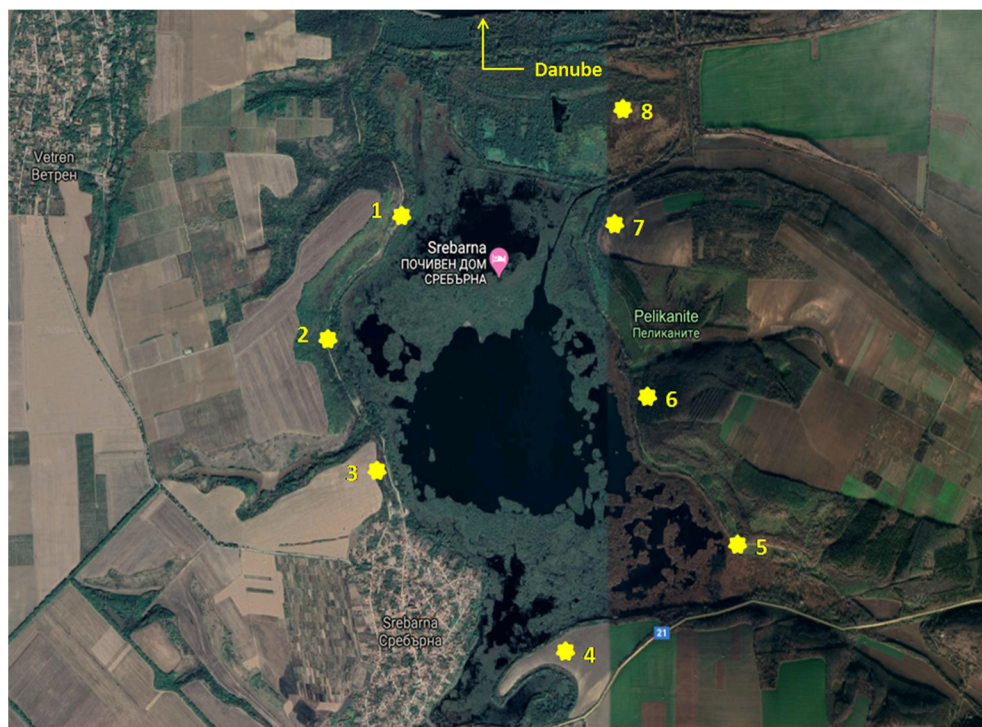


Figure 2. Map of the Srebarna Lake reserve with sampling points

ACKNOWLEDGMENTS

The authors would like to thank of Maria-Antoaneta Ivanova for the help for specifying the soil-sample points and the Science and Research Sector of the UCTM–Sofia for the financial support (Contract № 12019/2020).

REFERENCES

1. N. Petkov; *Acrocephalus*, **2006**, 27 (128-129), 37–43.
2. N. Kamburova; T. Michev; *J. Balk. Ecol.*, **2003**, 6(2), 191-199.
3. M. Beshkova; R. Kalchev; L. Pechlivanov, V. Vassilev; *Phytoplankton composition and abundance in Srebarna Lake and adjacent temporary wetlands (Bulgarian floodplain of the Lower Danube River)*, **2010**, In: 38th IAD Conference, Dresden, Germany.

DETERMINATION OF THE COMPOSITION AND CONTAMINATION WITH HEAVY METALS
OF SOILS FROM THE SREBARNA LAKE RESERVE

4. G. Zhelezov; M. Varbanov; M. Germ; A. Gaberščik; Problems of Geography, **2011**, 1-2, 107-118 (in Bulgarian).
5. M. Nikolova; R. Vatsheva; V. Nikolov; GIS Assessment of Global Change Impacts on the Dynamics of the Srebarna Lake Ecosystem, **2010**, In: 3rd International Conference on Cartography and GIS, 15-20 June, Nessebar, Bulgaria (in Bulgarian).
6. S. Nedialkov; H. Kochev; T. Michev; A. Damyanova; V. Velev; Contribution to the nesting distribution of the black kite *Milvus migrans migrans* (Boddaert, 1783) in Bulgaria, **1984**, In: International Symposium "The role of wetlands in preserving the genetic material", Srebarna, 8-12 October, Collected works, BAS, Sofia, 164-187 (in Bulgarian).
7. V. Yanchev; I. Ivanova; R. Nedkov; *J. Ecol. Eng. Env. Prot.*, **2011**, 1, 4-11 (in Bulgarian).
8. A. Simeonova; J. Bekyarova; R. Chuturkova; *J. Ecol. Eng. Env. Prot.*, **2011**, 1, 25-30 (in Bulgarian).
9. C. Baoshan; Y. Qichun; Y. Zhifeng; Zh. Kejiang; *Ecol. Engin.*, **2009**, 35, 1090–1103.
10. K. Radeva; *J. Ecol. Eng. Env. Prot.*, **2015**, 4, 15-22 (in Bulgarian).
11. N. Pourang; *Env. Monitor. Assess.*, **1995**, 35, 207-219.
12. Q. Li; Z. Wu; B. Chu; N. Zhang; C. Cai; *J. Fang; Environ. Pollut.*, **2007**, 149, 158-164.
13. M. Khan; M. Khisroon; A. Khan; N. Gulfam; M. Siraj; F. Zaidi; A. Abidullah; S. Fatima; S. Noreen; Z. Shah; F. Qadir; *BioMed. Research International*, **2018**, Article ID 1910274, 10 pages, <https://doi.org/10.1155/2018/1910274>.
14. G. Bonanno; J. Borg; V. Martino; *Sci. Total Envir.*, **2017**, 576, 796–806.
15. B. Chattopadhyay; A. Chatterjee; S. Mukhopadhyay; *Aq. Ecosyst. Health & Manag.*, **2002**, 5(2), 191–203. DOI: 10.1080/14634980290031848
16. K. Victor; M. Ladji; A. Adjiri; Y. Cyrille; T. Sanogo; *Int. J. Chem. Tech. Research*, **2016**, 9(2), 189-195.
17. E. Belyoskii; Ecology of the bird in the impact regions, **2010**, Dissertation, Ekaterinburg, Russia (in Russian).
18. C. Kwok; Y. Liang; H. Wang; Y. Dong; S. Leung; M. Wong; *Ecotoxic. Environ. Safety*, **2014**, 106, 62–67.
19. State Gazette of Republic of Bulgaria, Regulation №3 of the Ministry of Environment and Water, the Ministry of Health and the Ministry of Agriculture and Food of Bulgaria from 1 august 2008 about the permissible norms for harmful substances in the soils. State Gazete, 71, **2008** (in Bulgarian).
20. Bulgarian National Standard (BNS) 17.4.5.01, **1985**, Preservation of nature. Soil. General requirements for soil sampling (in Bulgarian).
21. BNS ISO 11464, **2012**, Soil quality. Preliminary preparation of samples for physico-chemical analysis.
22. BNS EN 16174, **2012**, Sediments, treated bio-wastes and soils. Solvation fractions and elements in "aqua regia".

23. BNS EN 15933, **2012**, Sediments, treated bio-wastes and soils. Determination of pH.
24. BNS ISO 11265, **2002**, Soil quality. Determination of the electric conductivity.
25. BNS ISO 11261, **2002**, Quality of soils. Determination of total nitrogen. Modified method of Kjeldahl.
26. BG ISO 11263, **2002**, Soil quality – Determination of phosphorus – Spectrometric determination of phosphorus soluble in sodium hydrogen carbonate solution.
27. BNS EN 16170, **2016**, Sediments, treated bio-wastes and soils. Determination of elements through ICP-OES.

DETERMINATION OF OPTIMAL EXTRACTION PARAMETERS OF POLYPHENOLS FROM *FORSYTHIA EUROPAEA* DEGEN & BALD. BLOOM USING RESPONSE SURFACE METHODOLOGY

DANIJELA KOSTIC^{a*}, BILJANA ARSIC^a, MILAN MITIC^a,
SNEŽANA MITIC^a, MARIJA MARKOVIC^b, GORDANA, STOJANOVIC^a

ABSTRACT. The study was designed to examine the influence of ethanol and acetone solvent concentration, extraction time (45-135 min) and extraction technique: maceration and ultrasound extraction on the extraction of total phenolics and flavonoids from petals of *Forsythia europaea* Degen & Bald. The highest content of total phenolics in the extracts was obtained using the pure ethanol and acetone in both the extraction processes. The differences in the content of total phenols in different compositions of the mixture for the extraction are the results of different polarities of the applied solvent systems. When ethanol solutions were used for the extraction, the optimum conditions for the extraction of phenols and flavonoids from dried petals by maceration and ultrasound extraction from *F. europaea* were 135 min and 100% ethanol. In the case of acetone solvent system, the optimum conditions for the extraction by maceration were 135 min and 98.07% acetone and for the ultrasound extraction 135 min and 88.76% acetone. The optimum conditions for the extraction of flavonoids when the acetone solvent system was used, by maceration and ultrasound extraction were 135 min and 77.95 % acetone. Obviously, ultrasonic extraction was less time consuming, and it requires for all performed extractions solvent with less percentage of acetone.

Keywords: *phenolics; flavonoids; maceration; ultrasonic extraction; response surface methodology*

^a University of Nis, Faculty of Sciences and Mathematics, Department of Chemistry, Visegradska 33, 18000 Nis, Serbia

^b University of Nis, Faculty of Sciences and Mathematics, Department of Biology, Visegradska 33, 18000 Nis, Serbia

* Corresponding author: danijelaakostic@yahoo.com

INTRODUCTION

Forsythia (*Forsythia*) is a genus belonging to the olive family (*Oleaceae*). It is a shrub characteristic by beautiful yellow flowers, but they can be pink for the plant, usually grown in Asia. This genus covers a group of plants originating mainly from Asia (China, Japan), but one species is endemic and grows in the Balkans (Balkan forsythia, lat. *Forsythia europaea* Degen & Bald.).

The Balkan or European *forsythia* (lat. *Forsythia europaea* Degen & Bald.) is an endemic species of the *Forsythia* species whose range of distribution covers northern Albania and areas of the former Yugoslavia. This species is thermophilic and heliophilic, *i.e.*, it requires heat and light.

The fruit of this herb has anti-inflammatory, antipyretic and antiviral properties and is used to treat respiratory infections. It is assumed that it can slow blood coagulation, so it should be avoided before surgery or if a person is already using a drug that has the same effect. *Forsythia* is not toxic if used in moderation. However, *forsythia* is not recommended for pregnant women. The list of poisonous plants for pets and humans does not contain *forsythia*. However, there is a difference between its non-toxicity and edibility. Some people use flowers of *forsythia* in their diet, but not in large quantities because petals can have a bitter taste.

The flowers of the plant are also used as a salad decoration. It is absolutely safe to have the *forsythia* in the garden, and it is necessary to find out more about its chemical composition and its effects on humans so that it can be used in nutrition. [1]

There are few scientific papers concerning the testing of this plant species. However, as *Forsythia suspensa* is used as a plant traditionally in China, there is a need to test its qualitative composition, as it was done by HPLC (Nucleosil C-18 column) analysis with a PDA detector. The methanolic extract was analyzed. The following components were successfully separated by this method: caffeic acid, rutin, forsythoside A, forsythin and forsythigenin. [2]

Phytochemical studies have shown that the major components of this plant, accumulated mainly in the fruit, are triterpenoids, lignans, flavonoids, phenylethanoid glycosides. Studies have shown that phenolic components, including lignans, flavonoids, phenylethanoid glycosides, are responsible for the diverse biological activity of this species. [3] Dried leaves of *F. europaea* collected at Kyoto Herbal Garden in Japan show the presence of the following compounds: phylogenin, (+)-pinorezinol, filirin, (+)-pinorezinol- β -D-glucoside, forsitiazide and rutin. [4]

The higher yields in the previous extraction kinetics studies using maceration were achieved by circulation techniques when it was concluded that the operating conditions have an influence on the extraction yield and the kinetics of the extraction. [5,6]

In the literature, there are no available data on the influence of solvent concentration, extraction time and extraction technique on the quantity of the extracted phenolic compounds from the dried bloom of *F. europaea*.

The *F. europaea* and its extracts can be used as a good source of natural plant pigment and antioxidant agents. Therefore, the aim of this work was the optimization of the extraction process in order to achieve a higher degree of extraction of phenolic compounds from the dried bloom of *F. europaea*.

RESULTS AND DISCUSSION

In Table 1 it is shown the dependence of the contents of total phenols in ethanol-aqueous extracts of mulberry fruit on time with different concentrations of ethanol-water and acetone-water (0, 50 and 100%) of maceration process and ultrasonic extraction. The process lasted 45, 90 and 145 min. Total phenol content was shown as mg gallic acid equivalents (GAE) per 100 g of dried petals.

The phenol content determines the pharmacological properties of the plant and for medicinal plants the concentration of phenol is 0.23 to 2.85 mg GAE / g fresh sample, while the phenol concentration of culinary plants is 0.26 to 17.51 mg GAE / g fresh sample [7]. Based on the literature, the highest content of phenolic compounds is found in culinary herbs of the genus *Origanum*, about 20 mg GAE /g fresh sample. [8]

The content of total phenolics in the tested extracts for maceration and ultrasonic extractions from 479.5 to 2216.2 and 598.33 to 2720.4 mg GAE/100g dried petals, respectively in ethanol-water solvent. The phenol content is low in acetone-water extracts.

In Table 2 it is shown the dependence of the contents of flavonoids in extracts of dried petals on time with different concentrations of ethanol-water and acetone-water (0, 50 and 100%) of maceration process and ultrasonic extraction. The process lasted 45, 90 and 145 min. Total flavonoid content was shown as mg catechine equivalents (CE) per 100 g dried bloom. The content of flavonoid in the tested extracts for maceration and ultrasonic extractions from 454.7 to 2000.5 and 535.5 to 2495.2 mg CE/100g dried petals, respectively in ethanol-water extracts. The flavonoid content is low in acetone-water extracts.

Higher content of phenols and flavonoids is in the extracts obtained by ultrasonic extraction. Table 1. Phenolic content (mg GAE/100g dried petals)

Table 1. Phenolic content (mg GAE/100g dried petals)

Time (min)	Water		Ethanol 50%		Ethanol 100%		acetone 50%		acetone 100%	
	maceration	Ultrasound extraction	Maceration	Ultrasound extraction	Maceration	Ultrasound extraction	Maceration	Ultrasound extraction	Maceration	Ultrasound extraction
45	479.5± 19.60	598.3± 20.12	1287.2± 39.615	1478.9± 15.511	1865.5± 12.604	1515.3± 46.111	2000± 35.51	2445.2± 42.306	1901.2± 23.206	2258± 14.62
90	548.2± 20.13	682.1± 15.06	1399.2± 41.222	1760.5± 24.202	2187.2± 25.302	1650.4± 51.203	2045.3± 44.222	2600.8± 48.905	2050.6± 26.210	2400.3± 16.903
13	591.5± 29.24	730.5± 35.22	1503± 52.61	1889.2± 27.803	2359.3± 24.915	1801.2± 61.109	2216.2± 52.312	2720.4± 60.112	2210.5± 30.214	2605.2± 20.604

Table 2. Flavonoids content (mg CE/100g dried petals)

Time (min)	Water		Ethanol 50%		Ethanol 100%		acetone 50%		acetone 100%	
	maceration	Ultrasound extraction	Maceration	Ultrasound extraction	Maceration	Ultrasound extraction	Maceration	Ultrasound extraction	Maceration	Ultrasound extraction
45	485.3± 23.22	598.33± 20.11	1478.9± 15.502	1865.5± 12.632	901.2± 23.20	2258± 14.63	1302.2± 32.205	1639.8± 30.501	1352.4± 23.601	1706.8± 25.101
90	540.5± 18.31	682.12± 15.06	1760.5± 24.211	2187.2± 25.312	2050.6± 26.201	2400.3± 16.904	1475.5± 33.603	1848.8± 29.709	1506.5± 29.303	1869.7± 26.611
13	591.2± 21.12	730.51± 35.25	1889.2± 27.803	2359.3± 24.906	2210.5± 30.205	2605.2± 20.603	1650.2± 36.612	2003.2± 33.503	1612.2± 32.805	1969.5± 32.203

Based on numerous studies, it is known that the content of polyphenolic compounds is influenced by the genotype, site and technique of cultivation, as well as differences in plant maturity.[9] Also, external factors such as light, temperature, the presence of nutrients in the soil, and altitude can affect the phenylpropanoid metabolism of the plant.[10] Phenolic compounds are thought to play the largest role in the biological activity of extracts and their presence contributes to the antioxidant activity of the plant. A large number of studies indicate that the role of flavonoids is of particular importance among phenolic compounds.

Response surface methodology and optimum conditions for the maceration and ultrasound extraction of phenols and flavonoids from dried petals from *Forsythia europaea* Degen & Bald. using the ethanol solvent system.

Response surface design and the finding of the optimum conditions for the optimization of maceration were achieved using the software JMP 15 (SAS Institute Inc., Cary, USA). Two factors were selected: time (45 min, 90 min, and 135 min) and percentage of ethanol (0%, 50%, and 100%).

DETERMINATION OF OPTIMAL EXTRACTION PARAMETERS OF POLYPHENOLS FROM FORSYTHIA EUROPAEA DEGEN & BALD. BLOOM USING RESPONSE SURFACE METHODOLOGY

The computational modeling of the response surface design and subsequent optimization gives more easily optimized conditions for the extraction of biologically active compounds, such as phenols. Maximum desirability of the extraction process by maceration and ultrasound extraction for the investigated dried petals from *F. europaea* is given in Figure 1, and the pattern in Table 3.

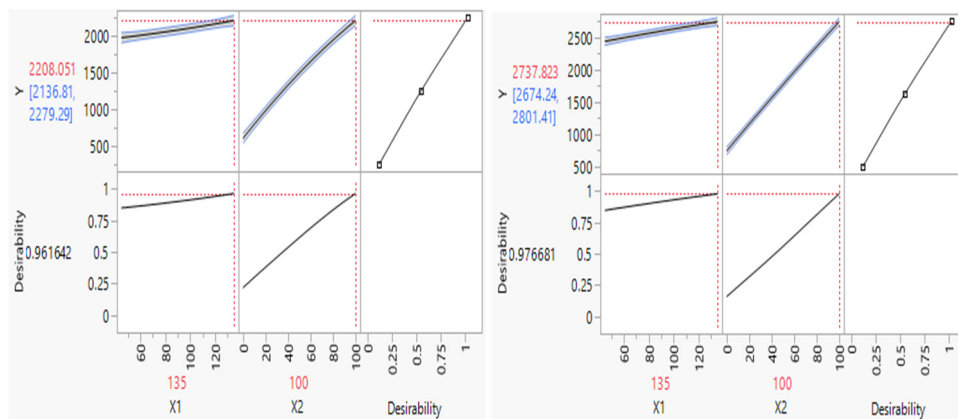


Figure 1. Maximum desirability for the extraction of phenols by maceration and ultrasound extraction using ethanol solvent system

Table 3. Response surface pattern for the extraction of phenols from dried petals of *F. europaea* using ethanol solvent system

Maceration					Ultrasound extraction				
	Pattern	Time (min)	Ethanol %	Phenol content (mg GAE/100g dried petals)		Pattern	Time (min)	Ethanol%	Phenol content (mg GAE/100g dried petals)
1	++	135	100	2216.2	1	00	90	50	1650.4
2	A0	135	50	1503	2	0A	90	100	2600.8
3	--	45	0	479.5	3	++	135	100	2720.4
4	0a	90	0	548.2	4	A0	135	50	1801.2
5	-+	45	100	2000.5	5	a0	45	50	1515.3
6	0A	90	100	2045.3	6	--	45	0	598.33
7	00	90	50	1399.2	7	0a	90	0	682.12
8	+-	135	0	591.5	8	+-	135	0	730.51
9	00	90	50	1399.2	9	-+	45	100	2445.2
10	a0	45	50	1287.2	10	00	90	50	1650.4

The script for the model was run, and the results were displayed with all statistical data. The optimum conditions regarding time and the percentage of ethanol were found using the option of a Prediction profiler and the selection of Maximize Desirability.

The optimum conditions for the extraction of phenols from dried petals by maceration and ultrasound extraction from *F. europaea* were 135 min and 100 % ethanol.

The computational modeling of the response surface design and subsequent optimization gives more easily conditions for the most efficient extraction of biologically active compounds, such as flavonoids. Maximum desirability of the extraction process by maceration and ultrasound extraction for the investigated dried petals from *Forsythia europaea* Degen & Bald. is given in Figure 2 and the pattern in Table 4.

The optimum conditions for the maceration and ultrasound extraction of flavonoids from dried petals from *F. europaea* were 135 min and 100 % ethanol.

Response surface methodology and optimum conditions for the maceration and ultrasound extraction of phenols and flavonoids from dried petals from *Forsythia europaea* Degen & Bald. using the acetone solvent system.

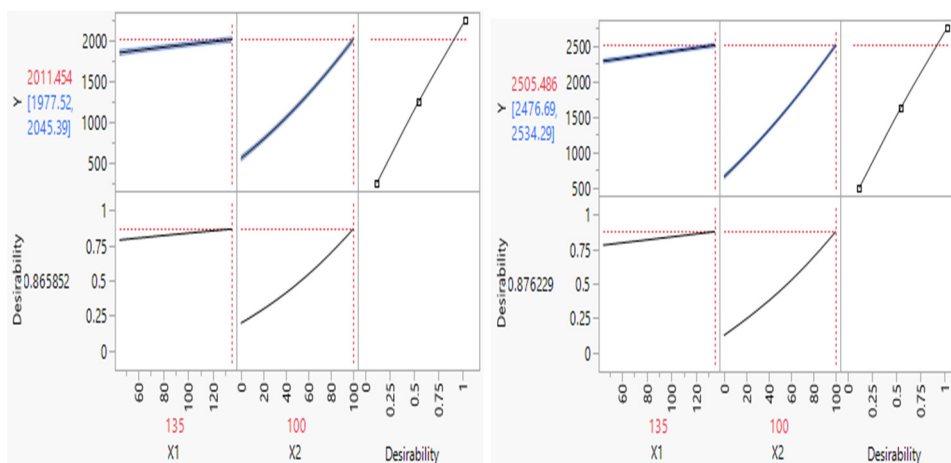


Figure 2. Maximum desirability for the extraction of flavonoids by maceration and ultrasound extraction using ethanol solvent system

Table 4. Response surface pattern for the extraction of flavonoids by maceration and ultrasound extraction using ethanol solvent system

Maceration					Ultrasound extraction				
	Pattern	Time (min)	Ethanol%	Flavonoids content (mg CE/100g dried petals)		Pattern	Time (min)	Ethanol%	Flavonoids content (mg CE/100g dried petals)
1	00	90	50	1128.2	1	0a	90	0	590.5
2	0A	90	100	1942.5	2	00	90	50	1402.1
3	00	90	50	1128.2	3	00	90	50	1402.1
4	++	135	100	2000.5	4	-+	45	100	2282.3
5	0a	90	0	502.6	5	+-	135	0	655.2
6	A0	135	50	1212.3	6	--	45	0	535.5
7	+-	135	0	550.3	7	++	135	100	2495.2
8	--	45	0	454.7	8	a0	45	50	1311.8
9	a0	45	50	1048.8	9	A0	135	50	1508.3
10	-+	45	100	1856.2	10	0A	90	100	2404.1

Response surface design and the finding of the optimum conditions for the optimization of maceration and ultrasound extraction were achieved using the software JMP 15 (SAS Institute Inc., Cary, USA). Two factors were selected: time (45 min, 90 min, and 135 min) and percentage of acetone (0%, 50%, and 100%), and one response: the content of phenols obtained by maceration and ultrasound extraction (Table 5 and Figure 3).

Table 5. Response surface pattern for the extraction of phenol by maceration and ultrasound extraction using acetone solvent system

	Pattern	Time (min)	Acetone%	Phenol content (mg GAE/100g dried petals)		Pattern	Time (min)	Acetone%	Phenol content (mg GAE/100g dried petals)
1	0a	90	0	540.5	1	++	135	100	2605.2
2	00	90	50	1760.5	2	+-	135	0	730.51
3	0A	90	100	2050.6	3	--	45	0	598.33
4	A0	135	50	1889.2	4	00	90	50	2187.2
5	--	45	0	485.3	5	0A	90	100	2400.3
6	a0	45	50	1478.9	6	a0	45	50	1865.5
7	++	135	100	2210.5	7	A0	135	50	2359.3
8	-+	45	100	1901.2	8	00	90	50	2187.2
9	00	90	50	1760.5	9	0a	90	0	682.12
10	+-	135	0	591.2	10	-+	45	100	2258

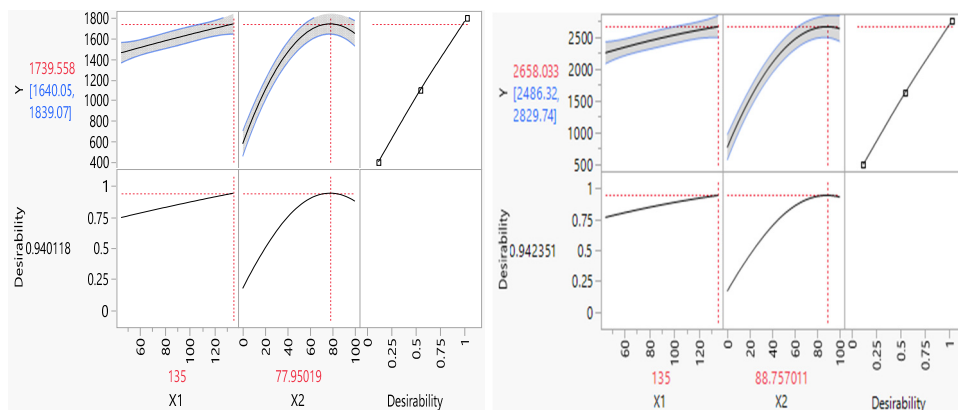


Figure 3. Maximum desirability for the extraction of phenols by maceration and ultrasound extraction using acetone solvent system

The optimum conditions for the extraction of phenols from dried petals from *F. europaea* by maceration were 135 min and 98.07 % acetone. The optimum conditions for the ultrasound extraction of phenols from dried petals from *F. europaea* were 135 min and 88.76 % acetone.

Response surface design and the finding of the optimum conditions for the optimization of maceration and ultrasound extraction of flavonoids were achieved using two factors: time (45 min, 90 min, and 135 min) and percentage of acetone (0%, 50%, and 100%), and one response: the content of flavonoids (Table 6 and Figure 4).

Table 6. Response surface pattern for the extraction of flavonoids by maceration and ultrasound extraction using acetone solvent system

	Pattern	Time (min)	Acetone%	Phenol content (mg GAE/100g dried petals)		Pattern	Time (min)	Acetone%	Phenol content (mg GAE/100g dried petals)
1	--	45	0	454.5	1	-+	45	100	1706.8
2	++	135	100	1612.2	2	00	90	50	1848.8
3	a0	45	50	1302.2	3	a0	45	50	1639.8
4	-+	45	100	1352.4	4	00	90	50	1848.8
5	A0	135	50	1650.2	5	A0	135	50	2003.2
6	0A	90	100	1506.5	6	++	135	100	1969.5
7	0a	90	0	501.5	7	--	45	0	535.5
8	00	90	50	1475.5	8	+-	135	0	655.2
9	+-	135	0	550.7	9	0A	90	100	1869.7
10	00	90	50	1475.5	10	0a	90	0	590.5

DETERMINATION OF OPTIMAL EXTRACTION PARAMETERS OF POLYPHENOLS FROM *FORSYTHIA EUROPAEA* DEGEN & BALD. BLOOM USING RESPONSE SURFACE METHODOLOGY

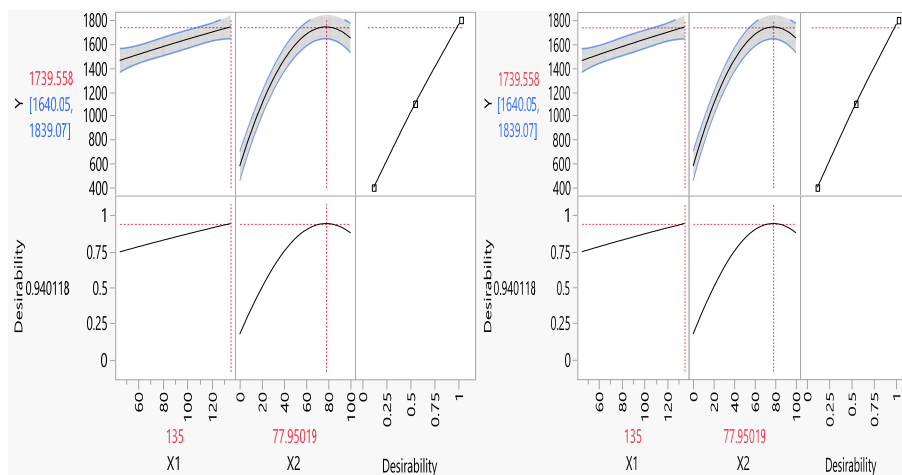


Figure 4. Maximum desirability for the extraction of flavonoids by by maceration and ultrasound extraction using acetone solvent system. The optimum conditions for the extraction of flavonoids from dried petals from *F. europaea* by maceration and ultrasound extraction were identical 135 min and 77.95 % acetone.

In our previously study we examined the influence of solvent concentration, extraction time and extraction technique on the extraction yield of phenolic compounds, flavonoids and antioxidant activity from *Morus nigra* L., *Morus rubra* L. and *Morus alba* L. fruits. The best conditions for the extraction of total phenols, flavonoids and monomeric anthocyanins by the maceration and ultrasonic extraction processes were found. [11] Obviously, ultrasonic extraction was less time consuming, and it requires for all performed extractions smaller percentage of solvent.

CONCLUSIONS

Contents of total phenols and flavonoids in extracts of dried bloom from *F. europaea* on time with different concentrations of ethanol and acetone (0, 50 and 100%) by maceration process and ultrasonic extraction. The content of total phenolics in the tested extracts for maceration and ultrasonic extractions from 479.5 to 2216.2 and 598.33 to 2720.4 mg GAE/100 g dried petals, respectively in ethanol-water extracts. The content of flavonoid in the tested extracts for maceration and ultrasonic extractions from 454.7 to 200.5

and 535.5 to 2495.2 mg CE/100g dried petals, respectively in ethanol water extracts. The phenols and flavonoid content are low in acetone-water extracts. Higher content of phenols and flavonoids is in the extracts obtained by ultrasonic extraction.

The highest content of total phenolics in the extracts obtained using the pure ethanol and acetone in both the extraction process. The differences in the content of total phenols in different compositions of the mixture for extraction are the result of different polarity of the applied solvent systems. The optimum conditions for the extraction of phenols and flavonoids from dried petals by maceration and ultrasound extraction from *F. europaea* were 135 min and 100 % ethanol.

The optimum conditions for the extraction of phenols from dried petals from *Forsythia europaea* Degen & Bald. by maceration was 135 min and 77.95 % acetone. The optimum conditions for the ultrasound extraction of phenols from dried petals from *F. europaea* was 135 min and 88.76 % acetone.

The optimum conditions for the extraction of flavonoids from dried petals from *F. europaea* by maceration and ultrasound extraction were 135 min and 77.95 % acetone.

The results show that the effect of ultrasound has a positive effect on the rate of extraction of phenolic compounds. The results indicate a high content of phenolic compounds *F. europaea* located in Southeast Serbia, which confirms their nutritional and pharmacological potential of this plant.

EXPERIMENTAL SECTION

Material: The petals of the Balkan Forsythia plant harvested from the Nis area (Cair Park) in March 2016 were used for this work. The plant was identified and recorded in the herbarium of the Faculty of Natural Sciences and Mathematics in Niš and was given a voucher number 11982 (*Forsythia europaea* Degen & Bald, 11982)

Apparatus and reagents: An Agilent 8453 UV-vis spectrophotometer (USA) was used for the absorbance measurements and spectra recording, using an optical or quartz cuvettes of 1 cm optical path. The pH measurements were made with Hanna Instruments pH-meter (USA) equipped with the glass electrode. The Folin–Ciocalteu phenol reagent and sodium carbonate were purchased from Merck Chemical Suppliers (Darmstadt, Germany). The other used chemicals including solvents were of analytical grade.

Maceration: Homogenized dried bloom and milled (2 g) was soaked into the mixture of the previously prepared solvent: ethanol-water (0%, 50%, 100%), aceton-water (0%, 50%, 100%), at a ratio of 1:50 w/v. Maceration with a solvent system was performed at 45, 90 or 135 min at 25 °C. The suspension was then filtered through a Buchner funnel and Whatman No.1 filter paper. The extracts were stored in the refrigerator and in the dark to their further use for the determination of phenolic compounds. [12]

Ultrasonic extraction: Milled plant material (2 g) was extracted with the previously mentioned solvent systems in the thermostatic ultrasonic bath (Sonic, Niš, Serbia) with the nominal power: 3×50 W; dimensions of bathrooms: 30×15×20 cm, and at a frequency of 40 kHz. The kinetics of the extraction of phenolic compounds were collected at the indicated time intervals (45-135 minutes). The extracts were separated from the plant material on Buchner's funnel with a weak vacuum and further treated according to the procedure for the determination of total phenols. [13]

Determination of total phenolics: Total phenol contents of the extracts were found by the modified Folin-Ciocalteu method. An aliquot of the extracts (1 mL) was mixed with 0.5 mL Folin-Ciocalteu reagent and 2 mL of sodium carbonate (20%). The absorbance was recorded after 10 min of the incubation at room temperature at 760 nm. The total phenolic content was expressed as mg/100 g gallic acid equivalent (GAE). The result of each assay was obtained from 3 parallel determinations. [14]

Determination of total flavonoid content Total flavonoid content was determined using a spectrophotometric method based on the formation of flavonoid complex with aluminum. Total flavonoid content was calculated as catechin (mg CE/100g) using the equation based on the calibration curve. [15]

Response surface methodology and optimum conditions for the extraction: Response surface design and the finding of the optimum conditions for the optimization of maceration and ultrasonic extractions were achieved using the software JMP 14.0.1 (SAS Institute Inc., Cary, USA) [16] Two factors were selected: time (45 min, 90 min, 145 min) and % ethanol (0%, 50%, and 100%), acetone (0%, 50%, and 100%), and three responses: total phenols, flavonoids, and the Central Composite Design with 2 central points. The script for the model was run, and the results were displayed with all statistical data. The optimum conditions regarding time and the solvent system were found using the option of Prediction profiler and the selection of Maximize Desirability. The average value of the optimum time and the solvent system was found from three measurements.

ACKNOWLEDGMENTS

The authors acknowledge the Ministry of Education, Science and Technological Development of Serbia for the financial support 451-03-68/200124

REFERENCES

1. Q. Zhang C; Jia H.; Xu Y.; Wang M.; Zhang C.; Huo Q.; S Shi; Z. Yu; *Mini-Rev. Org. Chem.*, **2012**, 9(3),303-318(16).
2. Y.Y. Cui; S.Y. Feng; G. Zhao; M.Z. Wang; *Yao. Xue. Xue. Bao.*, **1992**, 27(8), 603-608.
3. B. Yang; A. Kotani; K. Arai; F. Kusu; *Anal. Sci.*, **2001**,17, 599-604.
4. S. Kitagawa; S. Nishibe; R. Benecke; H. Thieme; *Chem. Pharm. Bull.* **1988**, 36(9), 3667-3670.
5. D. Milenovic; V. Veljkovic; T. Todorovic; M. Stankovic; *Chem. Ind.* **2002**, 56(2), 54-60.
6. Lj. P. Stanojević; M.Z. Stanković; M.D. Cakić; V.D. Nikolić; Lj. B. Nikolić; D.P. Ristić; *Chem. Ind.*, **2009**, 63, 79–86.
7. W. Zheng; S.Y. Wang; *J. Agricul. Food Chem.*, **2001**, 49(11), 5165–5170.
8. G. Cervato; M. Carabelli; S. Gervasko; A. Cittera; R. Cazzola; C. Benvenuto; *J. Food Biochem.* **2000**, 24(6), 453-465.
9. D. Orhan; A. Hartevioğlu; E. Küpeli; E. Yesilada ; *J. Ethnopharm.*, **2007**, 112,394-400.
10. R.A. Dixon; N.L. Paiva; *Plant Cell.* **1995**, 7, 1085-1097.
11. E. Kostić; B. Arsić; M. Mitić; D. Dimitrijević; E. Pecev Marinkovic; *Not. Bot. Horti. Agrobot. Cluj Napoca*, **2019**, 47(3),629-633.
12. J.R. Dean; *Extraction techniques in analytical sciences (Vol. 34)*. John Wiley & Sons, Ltd. 2009.
13. M. Vinatoru; *Ultrason. Sonochem.* **2015**, 25, 94-95.
14. V.L. Singleton; J.A. Rossi; *Am. J. Enol. Viticul.* **1965**,16(3),144-158.
15. B. Stojanovic; S. Mitic; G. Stojanovic; M. Mitic; D. Kostic; D. Paunovic; B. Arsic, *Not. Bot. Horti. Agrobot. Cluj Napoca.* **2016**, 44(1), 175-182.
16. W. Mietlowski; *J. Biopharm. Stat.* **2008**, 18(3), 590-594

DOXEPIN AS CORROSION INHIBITOR FOR COPPER IN 3.5 wt. % NaCl SOLUTION

SIMONA VARVARA^{a*}, ROXANA BOSTAN^a, MARIA POPA^a,
LUIZA GAINA^b, FLORIN POPA^c

ABSTRACT. The effect of 3-(dibenzo[*b,e*]oxepin-11(6H)-ylidene)-N,N-dimethylpropane-1-amine (doxepin) on the corrosion behaviour of copper in 3.5 wt.% NaCl solution was investigated by electrochemical techniques, SEM-EDX and quantum chemical calculations. Polarization curves indicate that doxepin acts as a mixed-type inhibitor. Impedance data also prove the anticorrosive proprieties of doxepin, due to its adsorption on the copper surface. The inhibition efficiency of doxepin increases with increasing its concentration, reaching a maximum value of 88.8% at 5 mM. SEM-EDX analysis revealed that doxepin is able to prevent the formation of the oxides on the copper surface. Quantum chemical calculations are in agreement with the results obtained by electrochemical measurements.

Keywords: *corrosion, copper, doxepin, electrochemical impedance spectroscopy, polarization curve, SEM-EDX, quantum chemical calculations*

INTRODUCTION

Due to its high electrical and thermal conductivity, mechanical workability, and malleability [1], copper is widely used in a variety of fields, including construction, electronics, piping system, transportation, artworks etc. Although copper has good corrosion resistance, when exposed to aqueous media containing high chloride concentrations (*i.e.* HCl, NaCl), it undergoes severe degradation, leading to important economic losses [2]. Starting from '60s [3] up to now, various organic substances containing heteroatoms (*i.e.* N,

^a Department of Cadastre, Civil Engineering and Environmental Engineering, "1 Decembrie 1918" University of Alba Iulia, 15-17 Unirii St., 510009 Alba Iulia, Romania

^b Babeş-Bolyai University, Faculty of Chemistry and Chemical Engineering, 11 Arany Janos St., RO-400028, Cluj-Napoca, Romania

^c Materials Science and Engineering Department, Technical University of Cluj-Napoca, 103-105 Muncii Avenue, 400641, Cluj-Napoca, Romania

* Corresponding author: svarvara@uab.ro

S, or P), π bonds, phenyl rings and/or conjugated double bonds were proved to play an important role in the control and mitigation of copper corrosion. Some recent papers review the classes of organic inhibitors for copper corrosion [4, 5], drawing attention to the possibility of using pharmaceutical compounds [5] for effective protection of copper-based materials against corrosion. According to Geethamani and Kasthuri [6], this area of research is important because the expired pharmaceutical drugs are inexpensive, readily available [7] and, in some cases, ecologically acceptable. A literature survey reveals that the levetiracetam [8], ibuprofen [9], metronidazole [10], itraconazole [11], montelukast sodium [12], myclobutanil and hexaconazole [13] and various antibiotics [14-16] have been studied as promising inhibitors for copper corrosion. The inhibition action of these drugs was attributed to blocking the surface *via* the formation of copper complexes on the metallic surface.

The aim of the present paper is to study the inhibiting properties of doxepin drug on copper corrosion in 3.5% wt. NaCl solution. Doxepin is a medication used to treat depressive and anxiety disorders, chronic hives, and trouble sleeping. Potentiodynamic polarization, electrochemical impedance spectroscopy, and scanning electron microscopy coupled with energy dispersive X-ray spectrometry (SEM-EDX) were the main investigation methods. Molecular parameters of doxepin were determined by quantum chemical computations.

RESULTS AND DISCUSSION

Potentiodynamic polarization measurements

Figure 1 shows the cathodic and anodic polarization scans recorded for copper in 3.5% NaCl solution, in the absence and presence of various concentrations of DOX.

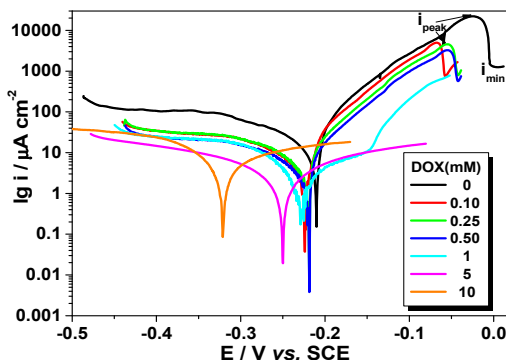


Figure 1. Tafel polarization curves for copper in NaCl 3.5% solution, in the absence and presence of different concentrations of DOX

The anodic behaviour of copper in NaCl solution is well described in the literature [17-20]: first, due to the oxidation of Cu to Cu⁺, the current density increases continuously to the peak value (i_{peak}). Then, under the attack of the aggressive Cl⁻ ions, Cu⁺ is rapidly transformed in an insoluble film of CuCl, which leads to a decrease of the current density from i_{peak} to the minimal value (i_{min}). Finally, due to the poor stability of the passive film, CuCl is transformed into soluble cuprous complex CuCl₂⁻ and the current density starts increasing again. As illustrated in Fig. 1, a small passivation domain could be noticed on the polarization curves obtained in the absence and in the presence of low concentrations of DOX (< 1mM). The addition of the inhibitor, even in low concentrations, decreases the passivation current densities with respect to the blank NaCl solution. However, the anodic current peak disappears, and broad current plateaus are visible in the presence of higher concentrations of DOX (> 1 mM). It should be noted that the anodic dissolution of copper in 3.5 % NaCl solutions containing high concentrations of DOX does not obey the Tafel's law.

As depicted in Fig. 1, both anodic and cathodic current densities decrease with the addition of doxepin as compared to the blank solution. The reducing trend of the current density values is more pronounced as the concentration of the inhibitor increases. A negative shift of the corrosion potentials could be also noticed in the presence of increasing DOX concentrations. These results suggest that doxepin is able to slow down the kinetics of both the anodic dissolution of copper and cathodic oxygen reduction, acting as a mixed-type inhibitor. The anticorrosive properties of doxepin may be related to its adsorption on the copper surface and the formation of a barrier film, impeding the cathodic and the anodic sites, as well.

The values of corrosion parameters, such as the corrosion potential (E_{corr}) and the corrosion current density (i_{corr}) obtained from the polarization curves are summarized in Table 1.

Table 1. Corrosion parameters obtained from the polarization curves of copper in 3.5% NaCl solution, in the absence and in the presence of different concentrations of DOX

DOX (mM)	E_{corr} (mV vs. ESC)	i_{corr} ($\mu\text{A cm}^{-2}$)	IE (%)
0	-165.3	24.10	-
0.10	-223.9	12.56	47.9
0.25	-219.1	7.92	67.1
0.50	-219.2	7.73	67.9
1	-228.5	3.92	83.7
5	-250.2	2.77	88.5
10	-320.8	16.42	65.3

The values of inhibition efficiency (IE), also presented in Table 1, were calculated according to the following equation:

$$IE = \frac{i_{\text{corr}}^0 - i_{\text{corr}}}{i_{\text{corr}}^0} \times 100 \quad [\%] \quad (1)$$

where i_{corr}^0 and i_{corr} are the values of the corrosion current densities in absence and in presence of DOX, respectively.

As shown in Table 1, the values of the corrosion current density, i_{corr} decrease with increasing doxepin concentration up to 5 mM. At higher concentrations of inhibitor, a slight increase of the i_{corr} value could be noticed in Table 1, but it remains lower with respect to the blank solution. These results confirm the ability of doxepin to retard the copper corrosion process.

At low concentrations, doxepin exhibits rather a moderate anticorrosive effect on the copper, but the IE values gradually increase with the inhibitor concentration and attain the maximum value of 88.5 % in the presence of 5 mM DOX. A further increase in the DOX concentration to 10 mM leads to a decrease of the IE value at 65.3 %.

Electrochemical impedance spectroscopy

Figure 2 presents the Nyquist diagrams for copper corrosion after 1-h immersion in 3.5% NaCl solution, in the absence and in the presence of various concentrations of doxepin.

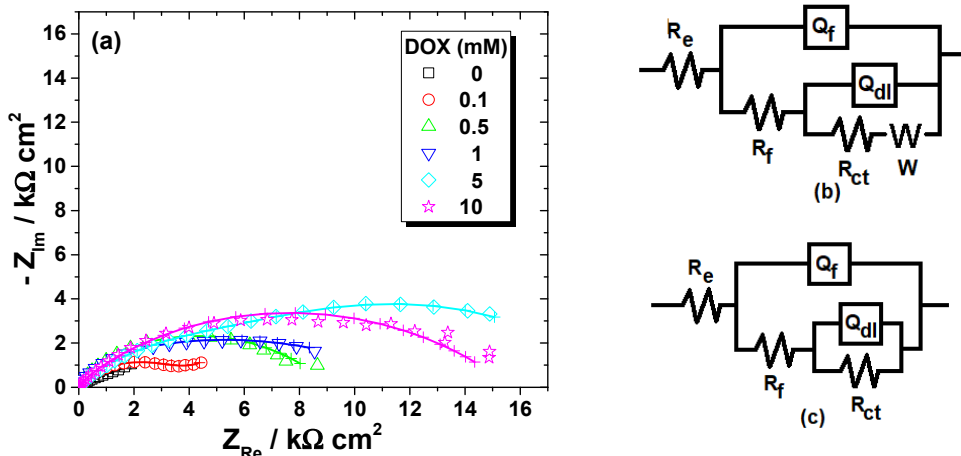


Figure 2. Nyquist diagrams recorded for copper after 1-h immersion in 3.5% NaCl solution, in the absence and in the presence of various concentrations of DOX (a). The equivalent electrical circuits used to fit the EIS data (b, c). Symbols represent the experimental data and lines with cross (—+—) correspond to the simulated spectra.

For the blank solution and in the presence of low concentrations of DOX (< 0.5 mM), a capacitive behaviour could be noticed in high and medium frequency region, followed by a straight line at the low frequency, which might be due to the diffusion of the corrosion reactants and products towards or away from the copper surface [21]. In these cases, the corrosion process is mixed-controlled by the charge-transfer and the diffusion. Although not clearly seen in Figure 2a, two-time constants and a Warburg impedance are necessary to suitably reproduce the experimental data obtained in 3.5% NaCl solution without and with the addition of low concentrations of DOX. Therefore, the corresponding EIS data were interpreted in terms of the equivalent electric circuit depicted in Figure 2b.

As the concentration of DOX increases, the Warburg impedance disappears, and a capacitive behaviour could be noticed over the whole frequency range. The attempts to represent the EIS data of copper exposed to 3.5% NaCl solution containing higher concentrations of DOX (≥ 0.5 mM) by one-time constant circuit did not allow a satisfactory agreement between the model and experimental results. Thus, two-time constants were used for these data simulation, according to the equivalent electrical circuit from Figure 2c.

In the equivalent circuits from Figure 2, R_e represents the electrolyte resistance, the high-frequency parameters, $R_f - Q_f$ correspond to the corrosion product film/inhibitor film [22], while the parameters, $R_{ct} - Q_{dl}$ are attributed to the charge transfer resistance and double layer capacitance. W stands for the Warburg impedance.

As illustrated in Figure 2, the used equivalent electrical circuits reproduce properly the experimental impedance, since a good overlapping between the measured and calculated data was obtained.

The capacitive contributions of the impedance plots were simulated using constant phase elements, represented by the terms Q and n instead of pure capacitors, due to the non-ideal behaviour of the metal surface. The semicircle depression is often explained by the heterogeneity of the surface, caused by roughness, inhibitor adsorption, porous layers formation, the presence of impurities [23].

The impedance of CPE is given by [24]:

$$Q = Z_{CPE(\omega)} = [C(j\omega)^n]^{-1} \quad (2)$$

where Q represents a pre-exponential factor, which is a frequency-independent parameter with dimensions of $\Omega^{-1} \text{ cm}^{-2} \text{ s}^n$; j is an imaginary number; $\omega = 2\pi f$ is the angular frequency in $\text{rad} \cdot \text{s}^{-1}$; n is the exponent which defines the character of frequency-dependence ($-1 \leq n \leq 1$).

The values of the pseudo-capacitances (C) associated with constant phase elements were recalculated using the equation:

$$C = (R^{1-n}Q)^{1/n} \quad (3)$$

The R-Q electrochemical parameters obtained by the fitting procedure are given in Table 2.

The inhibition efficiency (IE) was calculated from EIS measurements according to the following equation:

$$IE(\%) = \frac{R_{ct} - R_{ct}^0}{R_{ct}} \times 100 \quad (4)$$

where R_{ct} and R_{ct}^0 are the values of the charge transfer resistance, in presence and in absence of DOX, respectively.

Table 2. Electrochemical parameters of copper corrosion in 3.5 wt% NaCl solution obtained in the absence and in the presence of different concentrations of doxepin

DOX (mM)	R_f ($k\Omega cm^2$)	Q_f ($\mu F s^{n-1} cm^{-2}$)	n_f	C_f ($\mu F cm^{-2}$)	R_{ct} ($k\Omega cm^2$)	Q_{dl} ($\mu F s^{n-1} cm^{-2}$)	n_{dl}	C_{dl} ($\mu F cm^{-2}$)	W ($\Omega^{-1} cm^{-2} s^{1/2}$)	IE (%)
0	0.1	144.8	0.80	51.4	2.2	807	0.51	1400	0.0026	-
0.1	0.5	34.7	0.86	17.5	3.6	1438	0.57	87.4	0.0065	38.9
0.5	0.7	30.2	0.87	16.9	8.5	93.8	0.51	76.1	-	74.1
1	1.0	31.5	0.84	16.2	11.6	80.0	0.50	74.2	-	81.0
5	1.5	11.9	0.70	2.1	19.7	53.8	0.40	58.5	-	88.8
10	0.6	1.7	0.87	0.60	8.4	31.1	0.52	8.8	-	73.8

As could be noticed in Table 2, the film capacitance, C_f values decrease, while simultaneously the film resistances, R_f increase, as the inhibitor concentration increases up to 5 mM. These results suggest that the protective surface film formed in the presence of DOX becomes progressively thicker and less permeable to the aggressive Cl^- ions from the solution.

The charge-transfer resistance, R_{ct} presents larger values in the presence of DOX, confirming its inhibiting effect on copper corrosion, most likely due to the inhibitor absorption on the metallic surface. The decrease of the C_{dl} values in the presence of DOX as compared to its absence could be due to a smaller exposed surface area and/or to a decrease in the local dielectric constant, from which it can be assumed that the water molecules

are gradually replaced by the adsorbed inhibitor molecules [25]. As a result, the inhibition efficiency increases with increasing the doxepin concentration and reaches the highest value of 88.8 % at 5 mM DOX. The decrease of the IE value at higher concentrations of inhibitor (*i.e.* 10 mM), agrees with the outcomes of the potentiodynamic polarization measurements. Similar results were previously reported for other inhibitors [26–29] and were attributed to the deterioration or dissolution of the adsorbed layer on the copper surface.

Surface characterization

SEM micrographs and the corresponding EDS spectra of the copper specimens after 24 h of immersion in 3.5% NaCl solution in the absence and in the presence of 5mM DOX are shown in Figure 3.

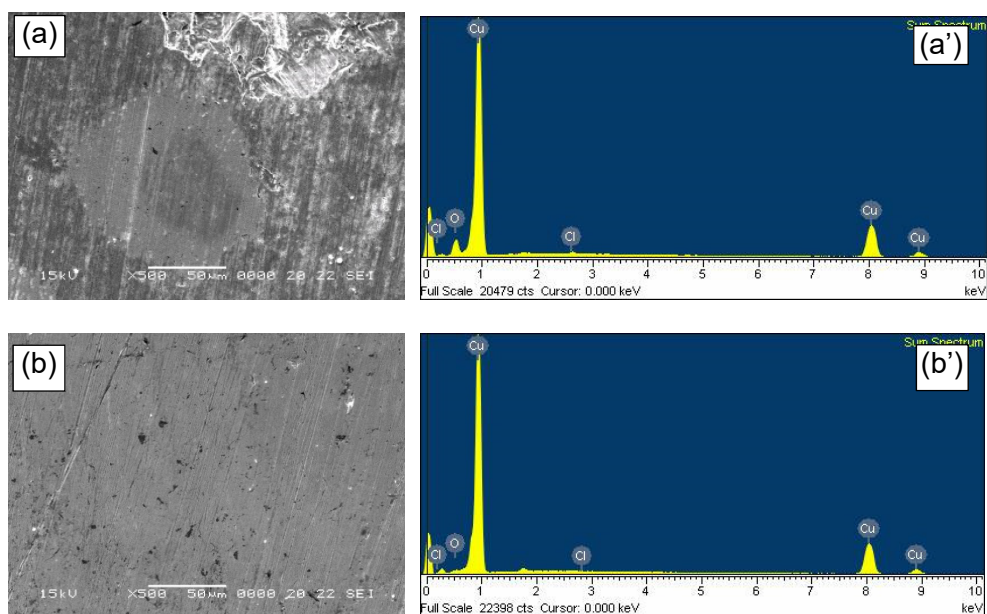


Figure 3. SEM micrographs and EDX spectra of the copper surface after 24 h exposure to 3.5% NaCl solution in absence (a, a') and presence of 5mM DOX (b, b')

In the absence of DOX, the SEM micrograph reveals a severe attack of the copper surface by the aggressive Cl^- ions from the electrolyte (Figure 3a). The EDX spectrum reported in Figure 3a' shows the characteristic peaks of copper and a marked presence of the oxygen atoms, together with the chloride atoms.

In the presence of DOX, the copper dissolution process was significantly retarded, and almost no corrosion products are visible on the metallic surface (Figure 3b). Moreover, the amount of oxygen on the copper surface is markedly reduced, as revealed in Figure 3b', confirming that the doxepin adsorption prevents to some extent the formation of oxides on the copper surface.

Quantum chemical calculation

For better understanding the inhibition mechanism of doxepin on copper, quantum chemical calculations and molecule geometry optimization were performed using Spartan'06, followed by semi-empirical (PM3) and 6-31G(d) B3LYP DFT. The generated lowest energy conformers were further used in order to calculate the quantum molecular parameters, such as E_{HOMO} , E_{LUMO} , energy gap, ΔE ($E_{\text{HOMO}} - E_{\text{LUMO}}$) and the dipole moment, both in vacuum and water (Table 3).

It is well known that copper is a d type transition metal, characterized by a pronounced tendency to form coordination complexes with donor molecules. It was supposed that the inhibition process is based on the formation of an insoluble and highly adherent donor-acceptor (DA) complex between doxepin and copper. The formation of DA complex involves the electron donation from the HOMO orbitals of doxepin into the vacant copper orbitals, accompanied by backdonation from the metal to the LUMO orbitals of the inhibitor.

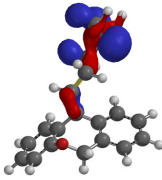
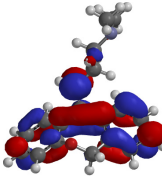
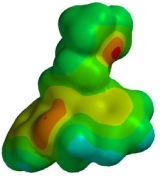
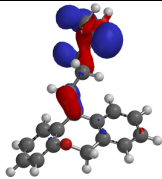
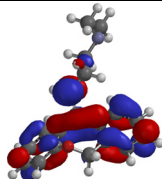
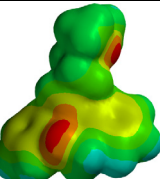
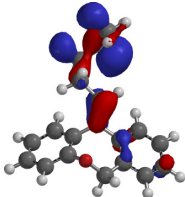
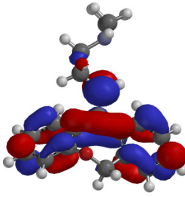
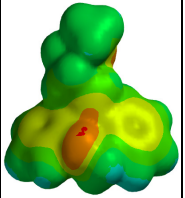
The examination of the frontier molecular orbitals for both isomers E, Z of Doxepin (Table 3) reveals that HOMO orbital overlays the alkene chain preponderantly on the amino group, while LUMO orbital covers the heteroaromatic ring.

Based on the theoretical calculation, it was assumed that the nitrogen atom of doxepin is mainly involved in the electron donation to copper unoccupied orbitals.

CONCLUSIONS

The inhibiting behaviour of 3-(dibenzo[*b,e*]oxepin-11(6H)-ylidene)-N,N-dimethylpropane-1-amine (doxepin) on copper corrosion in 3.5 wt.% NaCl solution was investigated using electrochemical methods (potentiodynamic polarization and electrochemical impedance spectroscopy) surface analysis (SEM-EDX) and quantum chemical calculations. Based on the obtained results, the following conclusions may be drawn:

Table 3. Calculated quantum chemical parameters, repartition of HOMO, LUMO and electrostatic potential map of (E)-3-(dibenzo[b,e]joxepin-11(6H)-ylidene)-N,N-dimethylpropane-1-amine (a. vacuum; b. water) and (Z)-3-(dibenzo[b,e]joxepin-11(6H)-ylidene)-N,N-dimethylpropane-1-amine (c. vacuum)

E [au]	E _{HOMO} [eV]	E _{LUMO} [eV]	Dipole [Debye]	HOMO	LUMO	Electrostatic potential map
-866.604337 ^a	-5.71 ^a	-0.63 ^a	1.01 ^a			
	ΔE [eV]					
	5.08 ^a					
-866.616426 ^b	-5.99 ^b	0.80 ^b	1.30 ^b			
	ΔE [eV]					
	5.19 ^b					
-866.606396 ^c	-5.73 ^c	-0.57 ^c	1.08 ^c			
	ΔE [eV]					
	5.06 ^c					

(1) Doxepin presents inhibiting properties for copper corrosion in NaCl solution; its inhibition efficiency increases with increasing the drug concentration up to an optimum value of 5 mM.

(2) Polarization curves indicate that doxepin acts as a mixed-type inhibitor.

(3) Impedance data revealed the anticorrosive proprieties of doxepin, most likely due to its adsorption on the copper surface, as proved by the decrease of the double layer capacitance in presence of DOX.

(4) SEM-EDX analysis showed that doxepin is able to prevent to some extent the corrosion products formed on the copper surface.

(5) Quantum chemical calculations agree with the results obtained by electrochemical measurements.

EXPERIMENTAL SECTION

The corrosive blank solution containing 3.5 wt.% NaCl was prepared by dissolving the analytical grade NaCl (Merck, Germany) in distilled water.

For the corrosion studies, tablets of 25 mg doxepin (DOX) purchased from a local drug store were used. The active substance from doxepin is 3-(dibenzo[*b,e*]oxepin-11(6H)-ylidene)-*N,N*-dimethylpropane-1-amine).

The molecular structures of the two isomers of doxepin are presented in Figure 4.

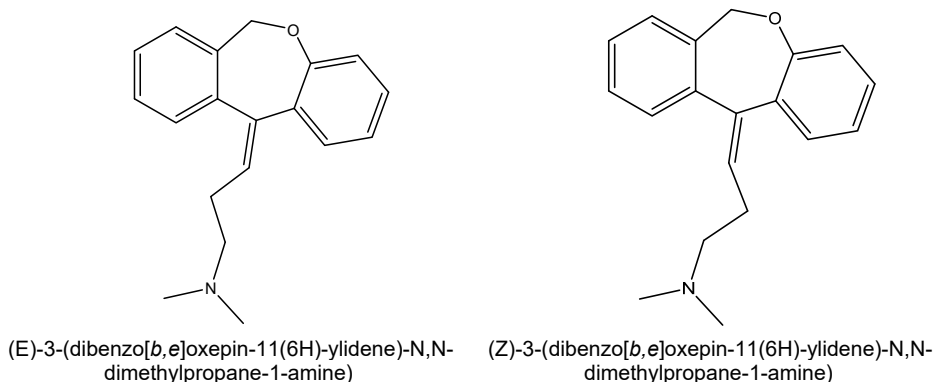


Figure 4. Molecular structure of the two isomers of 3-(dibenzo[*b,e*]oxepin-11(6H)-ylidene)-*N,N*-dimethylpropane-1-amine)

The drug was dissolved in the 3.5 wt.% NaCl electrolyte, in order to obtain various concentrations of DOX, in the range of 0.1 mM to 10 mM.

The electrochemical investigations were carried out at room temperature using a conventional three-electrode cell. The working electrode was a pure copper disk embedded in epoxy resin, with an exposed surface area of 0.38 cm². A saturated calomel electrode (SCE) and a large area platinum electrode were used as reference and counter electrodes, respectively.

Prior to all measurements, the copper electrode was grounded using successive grades of silicon carbide paper up to 4000, washed thoroughly with distilled water and degreased with ethanol.

Electrochemical measurements were carried out using PAR 2273 potentiostat controlled by computer. Polarization measurements were performed after 1-h immersion of the copper electrode in the test solution, at a scan rate of 10 mV/min, in the potential range of ± 200 mV vs. open circuit potential.

Electrochemical impedance spectroscopy measurements (EIS) were carried out at open circuit potential, after 1-h immersion of the working electrode in the corrosive solution. The impedance spectra were acquired in the frequency range of 10 kHz to 10 mHz, at 5 points per hertz decade, with an AC voltage amplitude of ± 10 mV. The impedance data were interpreted using ZSimpWin V3.21 software.

For morphological studies, the copper samples were immersed for 24 hours in 100 mL of 3.5 % NaCl solution, in the absence and presence of 5 mM DOX. Then, the copper electrodes were carefully washed with distilled water, dried at room temperature and further analysed by scanning electron microscopy, using a Jeol JEM 5510 LV electron microscope coupled with an EDX analyser (Oxford Instruments, INCA 300).

In an attempt to determine the most stable geometry of the inhibitor molecule, the minimum energy was evaluated starting with molecular mechanics optimization of the conformers generated within the Confanal module of Spartan'06 [30], followed by semi-empirical (PM3) and 6–31G(d) B3LYP DFT calculations [31–33] on all such obtained conformers.

REFERENCES

1. M. Shabani-Nooshabadi; F.S. Hoseiny; Y. Jafari; *Metall. Mater. Trans. A*, **2015**, *46*, 293–299.
2. D.S. Chauhan; M.A. Quraishi; C. Carrière; A. Seyeux; P. Marcus; A. Singh; *J. Mol. Liq.*, **2019**, *289*, 111–113.
3. I. Dugdale; J.B. Cotton; *Corros. Sci.*, **1963**, *3*, 69–74.
4. M.M. Antonijević; M.B. Petrović; *Int. J. Electrochem. Sci.*, **2008**, *3*, 1–28.
5. A. Fateh; M. Aliofkhaezaei; A.R. Rezvanian; *Arab. J. Chem.*, **2020**, *13*, 481–544.
6. P. Geethamani; P.K. Kasthuri; *J. Taiwan. Inst. Chem. E.*, **2016**, *63*, 490–499.
7. N. Vaszilcsin; V. Ordodi; A. Borza; *Int. J. Pharm.*, **2012**, *431*, 241–244.
8. G. Karthik; M. Sundaravadivelu; *Egypt. J. Pet.*, **2016**, *25*, 481–493.
9. Z.Z. Tasić; M.B. Petrović Mihajlović; A.T. Simonović; M.B. Radovanović; M.M. Antonijević; *Sci. Rep.*, **2019**, *9*, 1–14.
10. A. Samide; B. Tutunaru; A. Dobrițescu; P. Ilea, A.C. Vladu; C. Tigae; *Int. J. Electrochem. Sci.*, **2016**, *11*, 5520–5534.
11. Z. Gong; S. Peng; X. Huang; L. Gao; *Materials*, **2018**, *11*, 1–17.
12. B. Tan; S. Zhang; Y. Qiang; L. Feng; C. Liao; Y. Xu; S. Chen; *J. Mol. Liq.*, **2017**, *248*, 902–910.
13. W. Li; L. Hu; S. Zhang; B. Hou; *Corros. Sci.*, **2011**, *53*, 735–745.
14. R. Ganapathi Sundaram; G. Vengatesh; M. Sundaravadivelu, *J. Bio. Tribo. Corros.*, **2017**, *36*, 3–13.

15. R. Farahati; S. Morteza Mousavi-Khoshdel; A. Ghaffarinejad; H. Behzadi; *Prog. Org. Coat.*, **2020**, *142*.
16. G. Gece; *Corros. Sci.*, **2011**, *53*, 3873–3898.
17. G. Kear; B.D. Barker; F.C. Walsh; *Corros. Sci.*, **2004**, *46*, 109–135.
18. A. Shaban; E. Kálmán; J. Telegdi; *Electrochim. Acta.*, **1998**, *43*, 159–163.
19. K.F. Khaled; M.A. Amin; *Corros. Sci.*, **2009**, *51*, 2098–2106.
20. C. Rahal; M. Masmoudi; M. Abdelmouleh; R. Abdelhedi; *Prog. Org. Coat.*, **2015**, *78*, 90–95.
21. Y. Qiang; S. Zhang; S. Yan; X. Zou; S. Chen; *Corros. Sci.*, **2017**, *126*, 295–304.
22. H. Tian; W. Li; K. Cao; B. Hou; *Corros. Sci.*, **2013**, *73*, 281–291.
23. A. Popova; M. Christov; A. Vasilev; *Corros. Sci.*, **2011**, *53*, 1770–1777.
24. I.D. Raistrick; J.R. MacDonald; D.R. Franceschetti; *The electrical analogs of physical and chemical processes. Impedance Spectroscopy Emphasizing Solid Materials and Systems*, John Wiley & Sons, J.R. MacDonald (Ed.), New York, **1987**, pp. 27–84.
25. Y. Qiang; S. Zhang; L. Guo; X. Zheng; B. Xiang; S. Chen; *Corros. Sci.*, **2017**, *119*, 68–78.
26. R. Bostan; S. Varvara; L. Găină; L.M. Mureșan; *Corros. Sci.*, **2012**, *63*, 275–286.
27. S. Varvara; R. Bostan; O. Bobiș; L. Găină; F. Popa; V. Mena; R.M. Souto; *Appl. Surf. Sci.*, **2017**, *426*, 1100–1112.
28. K. Barouni; L. Bazzi; R. Saghi; M. Mihit; B. Hammouti; A. Albourine; S.E. Issami; *Mat. Lett.*, **2008**, *62*, 3325–3327.
29. K.M. Ismail; *Electrochim. Acta.*, **2007**, *52*, 7811–7819.
30. SPARTAN'06 Wavefunction, Inc., Irvine, CA.
31. D.J. Becke; *Chem. Phys.*, **1993**, *98*, 5648–5652.
32. P.J. Stephens; J. Devlin; C.F. Chabalowski; M.J. J Frisch; *Phys. Chem.*, **1994**, *98*, 11623–11627.
33. C. Lee; W. Yang; R.G. Parr; *Phys. Rev. B.*, **1988**, *37*, 785–789.

CORROSION RESISTANCE OF CERIUM-CONVERSION COATINGS FORMED FROM CERIUM(III) SALTS ON ALUMINIUM ALLOY 7075-T6

PETER RODIČ^a and INGRID MILOŠEV^{a,*}

ABSTRACT. Cerium conversion coatings were explored as an alternative to chromium conversion coatings for corrosion protection of aluminium alloy 7075-T6. Conversion coatings were formed in a conversion bath of 0.05 M cerium salt and 0.25 M hydrogen peroxide at room temperature. Various cerium salts were used: Ce(III) acetate, Ce(III) nitrate and Ce(III) chloride. The conversion process from Ce³⁺ to Ce⁴⁺ was followed by UV-VIS spectroscopy. The conversion of cerium coatings on alloy surface was monitored by measuring open circuit potential. To investigate the corrosion properties of uncoated and coated samples, the linear polarization and electrochemical potentiodynamic curves were recorded in 0.1 M NaCl. Additionally, salt spray chamber testing was carried out. Samples were characterized by scanning electron microscopy. Results revealed that the cerium conversion and corrosion resistance were dependent on the type of cerium salt and conversion time in the conversion bath. The most compact and uniform cerium conversion coatings were produced from solution of cerium(III) acetate, but better protection was obtained in nitrate and, especially, chloride solutions due to thicker coatings.

Keywords: aluminium alloy 7075-T6, corrosion, cerium conversion coatings, cerium salts

INTRODUCTION

Aluminium alloys are used in many applications because of their excellent physical characteristics, such as small density, and the high strength-to-weight ratio [1]. Some alloys are heterogeneous and contain numerous intermetallic particles (IMPs) added to increase the strength of aluminium. IMPs are mainly more cathodic (more noble) than aluminium matrix covered by native oxide; the electrochemical heterogeneity increases the susceptibility

^a Jožef Stefan Institute, Department of Physical and Organic Chemistry, Jamova c. 39, SI-1000 Ljubljana, Slovenia

* Corresponding author: ingrid.milosev@ijs.si

of the alloys to corrosion in aggressive environments. 7xxx wrought aluminium alloys contain zinc as a major addition, along with magnesium and copper in combinations that develop various levels of strength. The alloys, which contain copper, have the highest strengths and have been used for more than 50 years as construction materials, primarily in aircraft applications.

Aluminium oxide is stable in aqueous solution in the pH range of 4.0 – 9.0 [2]. At $\text{pH} > 9$, aluminium or aluminium – rich oxide will form AlO_2^- (aluminate ions), while at $\text{pH} < 4$ it will dissolve to form Al^{3+} ions. The copper-containing alloys, such as AA7075-T6, have lower resistance to general and localized corrosion than those of the series that do not contain copper [2]. Pitting is the most common type of corrosion attack on aluminium alloy. Pits form at localized discontinuities in the oxide film on aluminium exposed to the aggressive environment. The chloride ions are known to facilitate the breakdown of the aluminium oxide film. The resistance of aluminium to pitting depends significantly on its purity. The reason is the presence of IMPs, especially those with higher copper contents which act as abundant cathodic sites and increase the overall rate of corrosion.

For the protection of aluminium alloys under service conditions, various coatings systems are employed. Chemical conversion coatings are successfully employed for both improving the pitting corrosion resistance and enhancing paint chemical adhesion [3, 4]. For many decades, chromate conversion coatings (CCCs) have been used for that purpose. CCCs are particularly effective since chromium species are present in two oxidation states, Cr(III) and Cr(VI). The chromium Cr(III) species provide a barrier protective effect, and the Cr(VI) species are responsible for “self-repair” effect. The latter is based on the reduction of Cr(VI) species at the coating defect to form the passivating Cr(III) oxide (Cr_2O_3). Unfortunately, the exposure to hexavalent chromium is carcinogenic, and it is now prohibited due to its toxicity, mandating more viable alternatives [5].

Hitherto, alternative chromate-free, systems are unable to match the standards provided by the chromate-containing system, but the results are improving in the last years [6, 7]. The corrosion resistance of cerium-based conversion coatings (CeCCs) as an environmentally benign alternative to CCCs is being investigated in the last decades. It is well accepted that the inhibition effect of cerium salts on corrosion of aluminium and aluminium alloy is achieved by the protection of cathodic sites for oxygen reduction reaction by cerium oxide/hydroxide precipitates transformed from cerium salts [8, 9]. Hydrogen peroxide (H_2O_2) is a strong oxidant and its presence in the cerium salt solution can promote oxidation and dissolution of the substrate, which in turn, accelerates the precipitation of the conversion layer [10, 11]. Hydrogen peroxide can also cause the oxidation of Ce(III) to Ce(IV), thus affecting the ratio between these species and, consequently, the structure and properties of CeCCs.

Inhibition mechanism of CeCCs formed from CeCl_3 and $\text{Ce}(\text{NO}_3)_3$ solutions onto aluminium alloy substrates was studied [12–15]. The local increase in pH up to 8.5-9 due to cathodic reaction of oxygen reduction establishes the conditions under which the precipitation of $\text{Ce}(\text{OH})_3$ takes place [8, 9]. This insoluble precipitate blocks the cathodic sites and thus diminishes overall corrosion rate. During this process, oxidation of Ce(III) to Ce(IV) species occurs as well leading to the mixture of both oxidation states in the final product. In the presence of H_2O_2 , the oxidation is facilitated.

The purpose of this paper is to investigate the inhibition of corrosion by formation CeCCs. The formation of conversion coating is similar as reported [12]. In our previous studies, we have investigated in detail two methodologies of preparation of rare-earth conversion coatings on aluminium alloys: (i) immersion of metal sample directly in NaCl solution with rare-earth salts added [16–20], and (ii) preparation of conversion coating separately in a conversion bath containing rare earth salt [21,22]. The addition of hydrogen peroxide was studied as well [22]. Our investigations were focused on rare earth salts differing in cation (cerium and lanthanum) [18, 21, 22] and anion (chloride, nitride, acetate, sulphate) [17]. In the present study, we aimed to investigate the conversion coatings prepared from three types of cerium salts in the presence of H_2O_2 and deposited on aluminium alloy 7075-T6. The conversion process was followed using UV-VIS spectroscopy. The electrochemical and corrosion properties of coated and uncoated samples were investigated in NaCl solution. The optimal CeCCs coatings were additionally tested in the salt spray chamber, and the surface was characterized by scanning electron microscopy coupled with energy dispersive X-ray spectroscopy (SEM/EDS).

RESULTS AND DISCUSSION

UV-VIS spectroscopy of cerium salts solution

The conversion of various solutions containing cerium(III) salts after the addition of H_2O_2 to conversion bath to stimulate the oxidation of cerium(III) ions to cerium(IV) ions was followed by UV-VIS spectroscopy. Cerium(III) salts are in the form of a white powder or colourless crystals. Their water solutions are colourless; consequently, these solutions do not absorb visible light, but only UV light (UV-A and UV-B) under 350 nm. In contrast, cerium(IV) salts are coloured and their water solutions absorb visible light under 600 nm. The water solutions of cerium(IV) are yellow to orange or even brown. Solution transparency and its colour depends on the type of cerium species formed and on the presence of other anions.

The kinetics of the conversion was followed for conversion bath containing 0.05 M $\text{Ce}(\text{OAc})_3$, $\text{Ce}(\text{NO}_3)_3$ and CeCl_3 and 0.25 M H_2O_2 (Figure 1). Before the addition of H_2O_2 , all solutions absorbed only under 330 nm. After the addition of H_2O_2 , the oxidation process occurred within several minutes (3 min), as noticed by increasing intensity of plateau at wavelengths above 350 nm. The oxidation of Ce(III) to Ce(IV) ions was reflected in a change of solution colour from transparent to orange (red). Moreover, the important difference in the kinetics of conversion was noticed. The fastest was in $\text{Ce}(\text{OAc})_3$ solution, which is observed as a sudden (after 3 min) change of colour from transparent to non-transparent red coloured (insert in Figure 1a). On the other hand, the conversion is much slower in $\text{Ce}(\text{NO}_3)_3$ and CeCl_3 solutions (inserts Figures 1b, c). After 3 min, the solution became slightly yellow coloured. After 20 minutes, the difference in the spectra during the conversion was much smaller, but it still slowly continued. After 4 hours, the conversion of CeCl_3 was more pronounced than $\text{Ce}(\text{NO}_3)_3$, but both still remained lower compared to the conversion of $\text{Ce}(\text{OAc})_3$ obtained only after 3 minutes. This result indicated that the conversion of cerium(III) salts in the presence of H_2O_2 is strongly related to the associated anions in cerium salt.

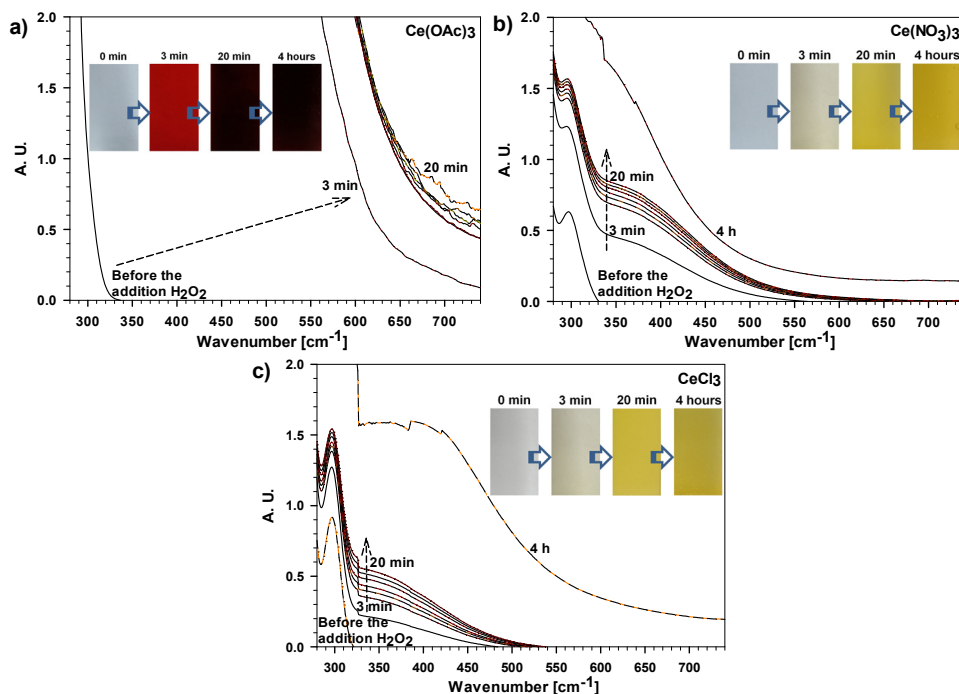


Figure 1. UV-VIS spectra of conversion bath containing 0.05 M Ce(III) salt and 0.25 M H_2O_2 : (a) $\text{Ce}(\text{OAc})_3$, (b) $\text{Ce}(\text{NO}_3)_3$ and (c) CeCl_3 . The inset figures show the changes of the solutions colours in the cuvettes during conversion.

Electrochemical measurements

CeCC formation

CeCCs were deposited on AA7075-T6. Before deposition, the substrates were ground with emery papers. The samples were then immersed in 0.05 M cerium salt, Figure 2. Immediately after, hydrogen peroxide (H_2O_2) as an oxidation reagent was added to the solution to obtain 0.25 M concentration. Samples were immersed in conversion bath at room temperature for different periods of time (from 3 min to 4 h) (Figure 2).

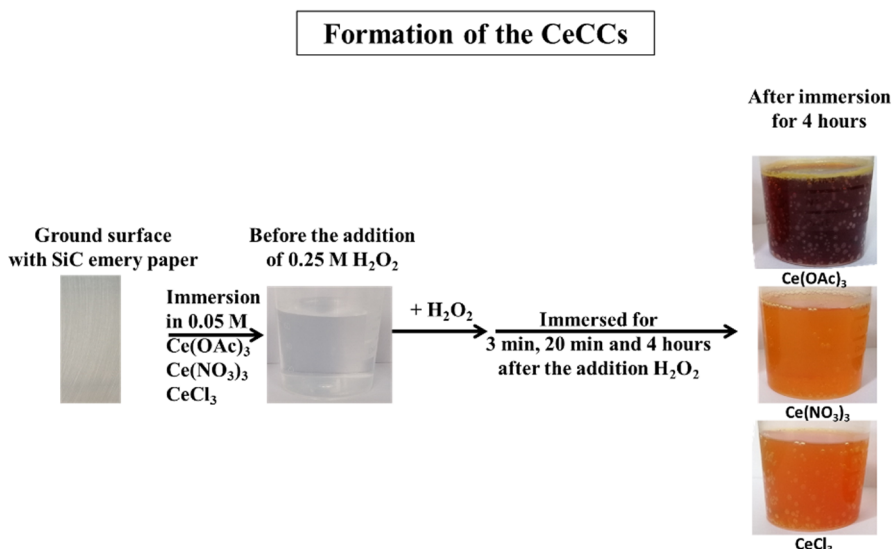


Figure 2. Schematic presentation of CeCCs formation during immersion of AA7075-T6 in conversion bath containing 0.05 M of Ce(III) salt ($Ce(OAc)_3$, $Ce(NO_3)_3$ or $CeCl_3$) and 0.25 M H_2O_2 .

The formation of cerium conversion coatings on AA7075-T6 surface as a function of immersion time in a solution containing $Ce(OAc)_3$, $Ce(NO_3)_3$ and $CeCl_3$ was monitored using open circuit potential, ($E_{oc\ form}$), Figure 3. $E_{oc\ form}$ in cerium solution depends on cerium salt. The most negative value was obtained in $Ce(OAc)_3$ solution. This confirmed the importance of the anions present in the solution, where OAc^- and Cl^- ions are more aggressive for AA7075-T6 compared to NO_3^- . The pH values of cerium salts solutions (pH_{sol}) are neutral ($Ce(OAc)_3$; $pH_{sol}=7.2$) or slightly acidic ($Ce(NO_3)_3$ $pH_{sol}=5.2$ and $CeCl_3$ $pH_{sol}=5.2$), Figure 3a. However, after addition H_2O_2 into solution, $E_{oc\ form}$ rapidly increased for a few hundreds mV to less negative values and after 3 minutes of

immersion, reached the first maximum (Figure 3a). This indicated the start of the formation of cerium film on the aluminium surface. After the addition H_2O_2 , pH decreased to much lower pH values (solution became acidic), where the passive aluminium film is not stable. At the beginning of conversion, the pH was between 2.8 and 3.3 (insert Figure 3b). Such conditions accelerate the formation of cerium film on the surface. During the course of the conversion, the pH slightly decreased for CeCl_3 CeCC, increased for $\text{Ce}(\text{OAc})_3$ CeCC, and remained unchanged for $\text{Ce}(\text{NO}_3)_3$ CeCC. After 20 minutes of immersion, the $E_{\text{oc form}}$ for CeCl_3 , become more constant confirming the formation of more stable (thicker) cerium conversion film. However, the formation continued at longer immersion time, but after 4 hours, the $E_{\text{oc form}}$ became constant in all immersed solutions (Figure 3b). The colours of the final solutions are shown in Figure 2 and are comparable with colours monitored with UV-VIS (Figure 1). It can be concluded that the conversion of cerium in water solution is mainly related to the presence of H_2O_2 in the conversion bath.

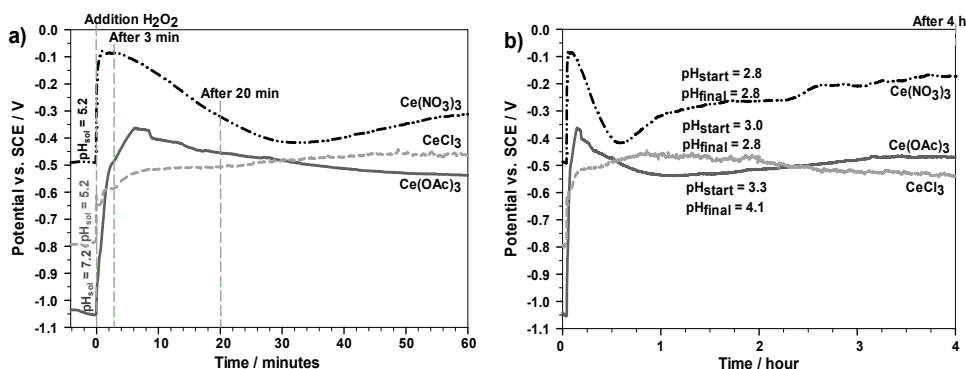


Figure 3. Open circuit potentials of AA7075-T6 during CeCCs formation for various conversion times (a) first hour and (b) up to 4 hours in conversion bath of 0.05 M of different cerium salts with 0.25 M H_2O_2 added. The inserted values represent the pH of the cerium solution (pH_{sol}) and pH values of the conversion solution after addition H_2O_2 (pH_{start}) and after 4 hours of immersion in conversion bath (pH_{final}).

After immersion of the aluminium sample in conversion bath, the colour of the aluminium surface was changed from metallic grey to orange-green due to the formation of cerium conversion coating on its surface (Figure 2). The precipitation of cerium (III) and cerium(IV) oxide/hydroxide islands at the metal surface has been presented in the literature [10, 18, 21, 22] and in our previous studies [16, 17, 20, 22]. Herein the mechanism of cerium conversion on aluminium alloy is presented schematically in Figure 4.

CORROSION RESISTANCE OF CERIUM-CONVERSION COATINGS FORMED
FROM CERIUM(III) SALTS ON ALUMINIUM ALLOY 7075-T6

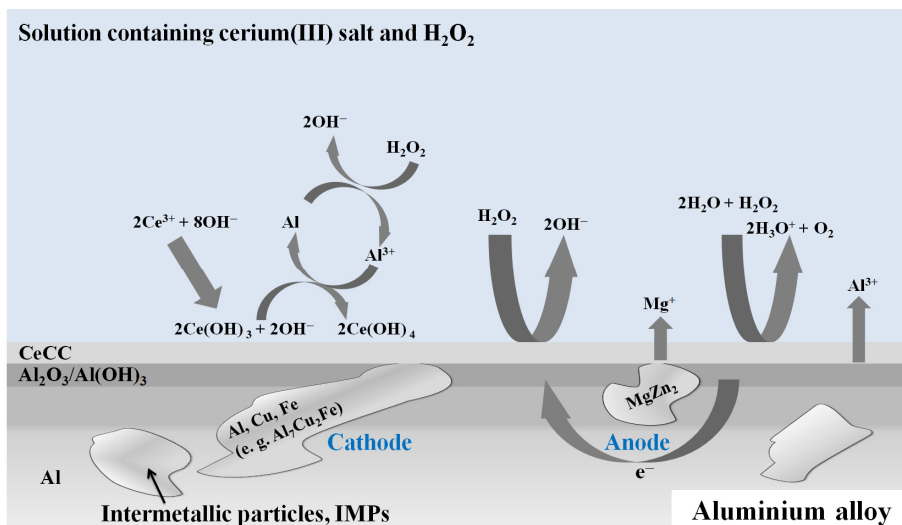


Figure 4. Schematic presentation of formation CeCCs on aluminium alloy.

Briefly, the cerium conversion coating is formed due to the oxidation of Ce^{3+} into Ce^{4+} in the presence of OH^- ions formed locally on the aluminium alloy surface. The process is accelerated in the presence of H_2O_2 , where the OH^- ions are also formed due to its decomposition. The critical impact in the formation of the film presents the intermetallic particles, IMPs. Therefore, the film formation starts at the cathodic sites of these IMPs and later (after more extended conversion) throughout the whole aluminium surface.

Corrosion testing

Once the AA7075-T6 samples were coated, they were subject to the electrochemical measurements. First, samples were allowed to rest for one hour of immersion in the corrosive medium of 0.1 M NaCl. The electrochemical measurements were performed on conversion coatings formed for different periods of immersion in cerium conversion solution (3 min, 20 min and 4 hours) (Figure 2). The electrochemical corrosion parameters determined from potentiodynamic polarization measurements for bare and coated AA7075-T6 samples are presented in Table 1 and polarization curves are presented in Figure 5. Polarization curve of bare sample consists of cathodic part related to

oxygen reduction and anodic part related to the dissolution of Al [16,19,23]. Bare AA7075-T6 shows poor corrosion resistance, as reflected in small R_p , large j_{corr} and immediate rise in current density following the E_{corr} . In the absence of the coating, the chloride solution is in contact with the metal surface (mainly cathodic intermetallic particles) and the porous aluminium oxide surface film.

When coated, the improvement of corrosion characteristics is dependent on the type of cerium salt and time of immersion in the conversion bath. The porous layer, especially the cathodic sites, is additionally protected by the precipitated cerium-based layer.

Table 1. Electrochemical parameters in 0.1 M NaCl for non-coated AA7075-T6 and coated with different CeCCs formed for various conversion times in conversion bath of 0.05 M of cerium salt with 0.25 M H₂O₂ added.

	R_p [kΩ cm ²]	j_{corr} [nA/cm ²]	E_{corr} [V]	E_{pit} [V]	ΔE [mV]	
Ground AA7075-T6	1	1 860	-0.70	-0.69	10	
Conversion time 3 min	R_p [kΩ cm ²]	j_{corr} [nA cm ²]	E_{corr} [V]	E_{pit} [V]	ΔE [mV]	IE [%]
Ce(OAc) ₃	8	199	-0.70	-0.69	10	87.5
Ce(NO ₃) ₃	3	1636	-0.69	-0.68	10	66.7
CeCl ₃	27	64	-0.69	-0.68	10	96.3
Conversion time 20 min	R_p [kΩ cm ²]	j_{corr} [nA cm ²]	E_{corr} [V]	E_{pit} [V]	ΔE [mV]	IE [%]
Ce(OAc) ₃	32	324	-0.77	-0.68	90	95.3
Ce(NO ₃) ₃	3	1827	-0.67	-0.66	10	66.7
CeCl ₃	34	394	-0.78	-0.69	90	97.0
Conversion time 4 h	R_p [kΩ cm ²]	j_{corr} [nA cm ²]	E_{corr} [V]	E_{pit} [V]	ΔE [mV]	IE [%]
Ce(OAc) ₃	13	551	-0.98	-0.69	290	76.9
Ce(NO ₃) ₃	248	122	-0.67	0.23	900	99.4
CeCl ₃	555	70	-0.52	-0.01	510	99.7

For CeCl₃ and Ce(NO₃)₃ CeCCs, the conversion time has a decisive role on the improvement of corrosion parameters (Figure 5). For shorter conversion times, up to 20 min, the polarization curves did not differ considerably compared to that of bare alloy; j_{corr} was smaller and the E_{corr} shifted somewhat more negative, but no passive range was established. The inhibition efficiency (IE) was below 97 %. However, after 4 h conversion, both CeCl₃ and Ce(NO₃)₃ CeCCs exhibited different curves with strongly reduced

CORROSION RESISTANCE OF CERIUM-CONVERSION COATINGS FORMED
FROM CERIUM(III) SALTS ON ALUMINIUM ALLOY 7075-T6

j_{corr} and E_{corr} shifted to more positive direction giving ΔE of 0.5 V and 0.9 V, respectively. The extension of ΔE reflects significantly improved resistance of the coated surface to initiation of pitting corrosion. These coatings act like mixed inhibitors with a stronger effect on the anodic part.

The $\text{Ce}(\text{OAc})_3$ CeCC showed improved corrosion parameters only after 4 h conversion time; the E_{corr} was shifted more negative and passive plateau was established but the E_{pit} did not exceed that of uncoated alloy. Despite faster conversion in the presence of H_2O_2 , the cerium coating formation is slow. The cerium ions rather precipitate into solution instead of forming the film on the aluminium surface. In contrast to chloride and nitrate CeCCs, acetate CeCC shows less corrosion protection ability and acts as a cathodic inhibitor, i.e. opposite to former two, which show strong anodic inhibition.

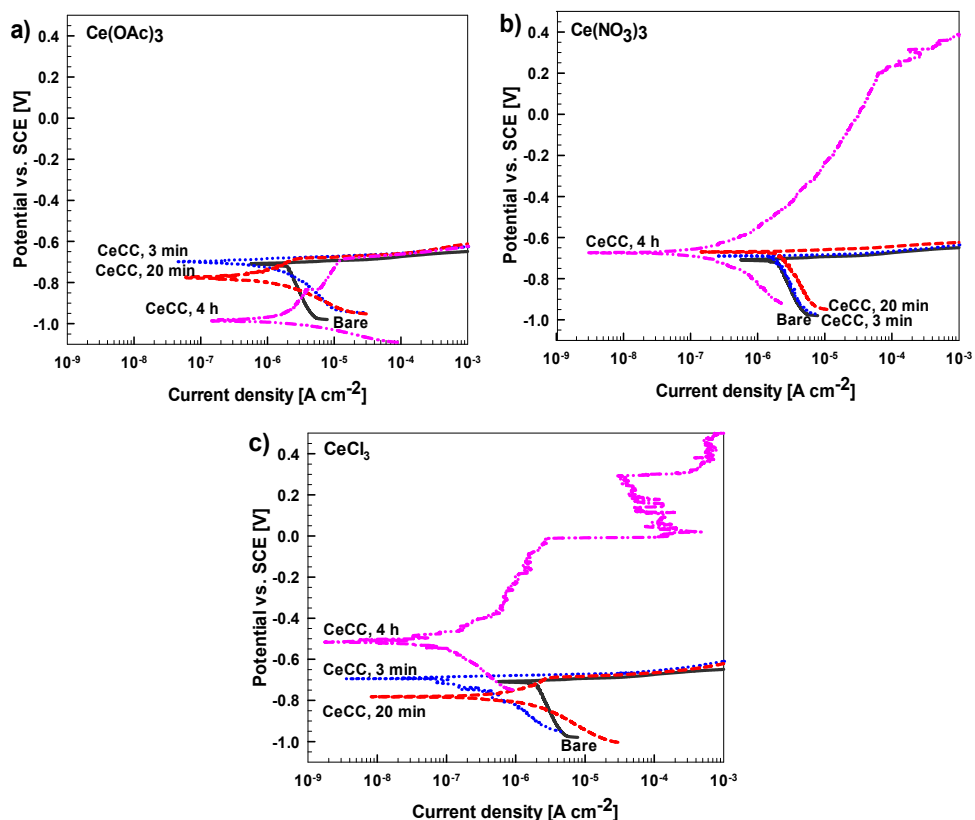


Figure 5. Electrochemical polarization curves recorded in 0.1 M NaCl for bare AA7075-T6 and coated with CeCCs formed for various conversion times in conversion bath of 0.05 M of different cerium salts with 0.25 M H_2O_2 added. Stabilization at the E_{oc} was 1 h.

did not benefit from prolonged conversion time. Comparing CeCl_3 and $\text{Ce}(\text{NO}_3)_3$ CeCCs, the former show better characteristics: nitrate CeCC exhibits broader ΔE range but the current densities are greater and progressively increase. In terms of inhibitions efficiency IE, CeCl_3 and $\text{Ce}(\text{NO}_3)_3$ CeCCs reach the highest value, more than 99 %.

Test in salt spray chamber

Good corrosion properties of selected CeCCs were confirmed with salt spray test. The images of uncoated and coated AA7075-T6 samples after different times of exposure in salt spray chamber were compared in Figure 6. The CeCCs were formed in 0.05 M $\text{Ce}(\text{OAc})_3$, $\text{Ce}(\text{NO}_3)_3$ and CeCl_3 solutions with addition 0.25 M H_2O_2 and conversion time of 4 h. This procedure was selected based on the most efficient results obtained from potentiodynamic measurements (Figure 5).

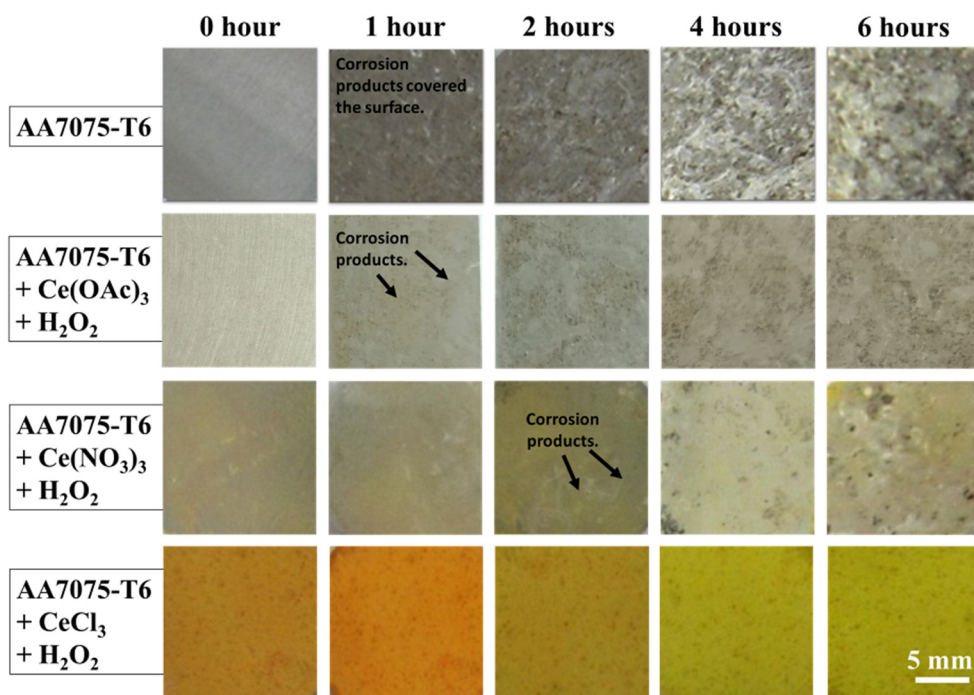


Figure 6. Surface appearance after salt spray test at different periods of time for bare AA7075-T6 and coated with CeCCs formed for conversion time of 4 h in $\text{Ce}(\text{OAc})_3$, $\text{Ce}(\text{NO}_3)_3$ and CeCl_3 solutions after the addition of 0.25 M H_2O_2 .

AA7075-T6 is not stable in chloride media and corrosion products covering the whole surface can be seen after only 1 hour. The amount of products increase during the extended exposure time (Figure 6). The protection with CeCCs improved the corrosion resistance. $\text{Ce}(\text{OAc})_3$, $\text{Ce}(\text{NO}_3)_3$ and, especially, CeCl_3 CeCCs were oxidized to cerium Ce(IV) which is evident from the yellow colour characteristic of the presence of cerium in oxidation state (IV). However, the difference in the coating durability was noticed. Slight improvement in corrosion resistance of the formed film was obtained for $\text{Ce}(\text{OAc})_3$ CeCC. The first corrosion products are observed after 1 hour, but the amount of them is lower compared to bare AA7075-T6. Better corrosion protection was obtained for $\text{Ce}(\text{NO}_3)_3$ CeCC because first corrosion products were observed after 2 hours. However, both $\text{Ce}(\text{OAc})_3$ and $\text{Ce}(\text{NO}_3)_3$ CeCCs were not resistant after longer exposure (4, 6 hours) and the corrosion products were formed on the surface. The most durable protective was obtained for CeCl_3 CeCC, where corrosion products were not observed even after 6 hours. From the effectiveness point of view, the use of conversion coatings based on CeCl_3 and $\text{Ce}(\text{NO}_3)_3$ is justified.

SEM/EDS characterization

SEM/EDS was used to characterize surface morphology of AA7075-T6 prior to and after coated with CeCCs (Figure 7). Chemical composition determined at different spots at the sample surface is presented in Table 2. The matrix of bare AA7075-T6 consists of Al, and some other metal elements mainly Zn, Mg and Cu, which are dispersed in the structure (Figure 7a, spot 1). Bare sample also contains Cu- and Fe-based IMPs (spots 2,3) which present cathodic spots relative to aluminium oxide matrix (spot 1).

The changes in the surface morphology can be noticed after immersion AA7075-T6 during 4 hours formation CeCCs. Coatings largely differ in morphology: acetate coating seems to be much thinner but much more homogeneous compared to nitrate and chloride CeCCs (Figure 7b). Cerium was detected at the coating surface (spot 5). Some defects were noted where the coating was delaminated and revealed bare alloy surface (spot 4). Nitrate coating seemed thicker than acetate coating but cracked (Figure 7c). However, cerium was detected at the surface of the coating and within the cracks (points 6 and 7). As for acetate, for nitrate coatings the formation of

Ce-coating was related to Cu-based IMPs. Some defects were observed at the surface. Chloride coating appeared even more cracked and thicker

(Figure 7d). Chloride coating contained a large amount of Ce (point 8) and no Al was detected, indicating that the alloy surface was fully covered with few micrometres thick CeCC.

Cracks may form during exposure of the coatings to vacuum within the microscope chamber but may also be related to the inherent properties of the coatings due to its large thickness and consequent internal stress. The cracks initiation is dependent on a number of factors; conversion time, type of cerium ions and hydrogen peroxide concentration and pH of the conversion solution affect the composition and morphology of the coatings formed, which is also reflected on corrosion properties. Another important parameter is the evaporation of the water during the drying process. Thus, the coating with large thickness will be more susceptible to cracking.

Table 2. EDS analysis results performed on the marked areas in Figure 7 on (a) ground AA7075-T6 and coated with CeCCs formed from 0.05 M (b) Ce(OAc)₃, (c) Ce(NO₃)₃ and (d) CeCl₃ solution in the presence of 0.25 M H₂O₂.

Elements, given in weight percentage (wt. %)							
Spots	Zn	Mg	Fe	Cu	O	Ce	Al
1	7.4	2.2	-	2.5	0.9	-	87.0
2	1.4	-	11.1	32.0	4.2	-	51.3
3	-	-	10.4	30.7	4.7	-	54.2
4	5.6	1.6	-	1.4	25.2	-	66.2
5	5.4	1.9	-	1.5	25.9	1.6	63.7
6	-	0.8	-	2.7	14.5	16.7	65.3
7	-	1.1	-	5.8	19.2	17.5	56.4
8	-	-	-	-	13.9	86.1	-

CORROSION RESISTANCE OF CERIUM-CONVERSION COATINGS FORMED FROM CERIUM(III) SALTS ON ALUMINIUM ALLOY 7075-T6

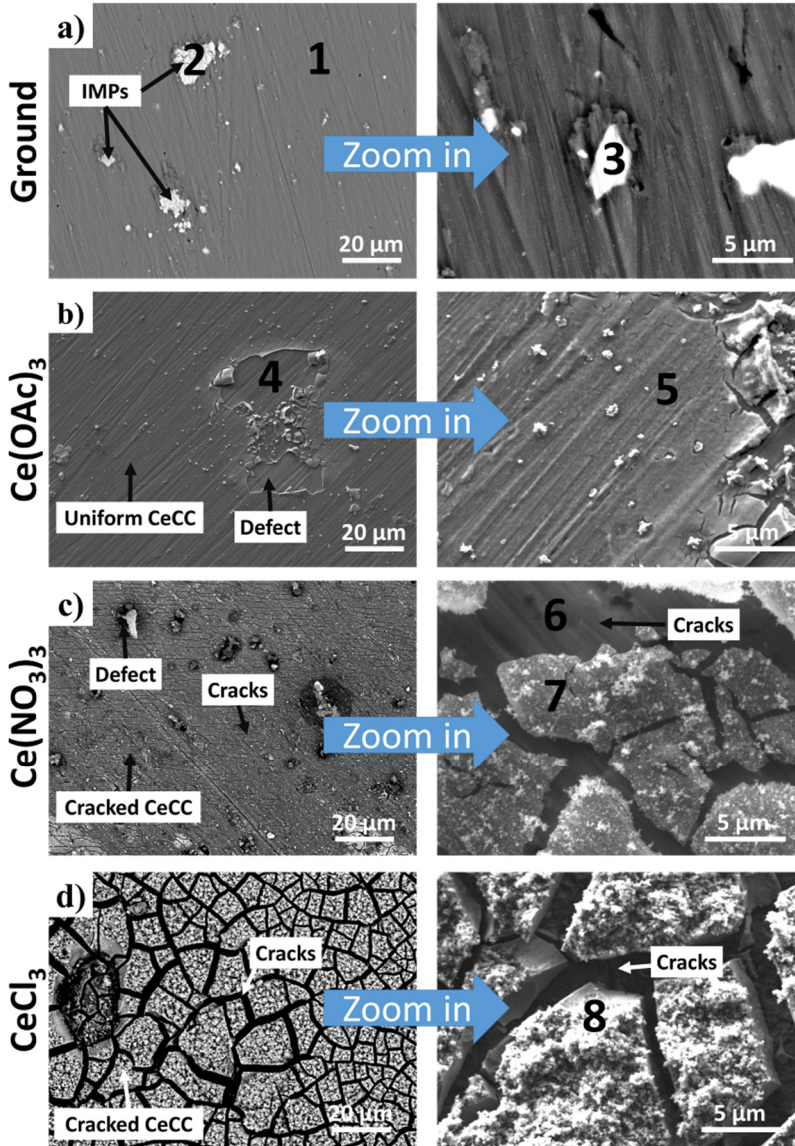


Figure 7. Backscattered SEM images (COMPO) mode of (a) ground AA7075-T6 and coated with CeCCs formed from (b) 0.05 M $\text{Ce}(\text{OAc})_3$, (c) 0.05 M $\text{Ce}(\text{NO}_3)_3$ and (d) 0.05 M CeCl_3 solutions. All coatings were formed with 0.25 M H_2O_2 added and conversion time was 4 hours. SEM images were taken at lower (1000 \times , left column) and higher magnification (5000 \times , right column). The arrows note the intermetallic particles (IMPs), CeCC, cracks in the coating and defects.

CONCLUSIONS

Cerium conversion coatings (CeCCs) were formed by deposition of cerium oxide/hydroxide from the water-based solution of different Ce salts on AA7075-T6 substrates. The conversion was carried out in 0.05 M solution of Ce salts (chloride, nitrate and acetate) for different conversion times in the presence of H_2O_2 as oxidant agent.

The corrosion protection the uncoated and coated AA7075-T6 was studied by electrochemical measurements in 0.1 M NaCl solution and salt spray chamber test in 5 wt.% NaCl. Both $CeCl_3$ or $Ce(NO_3)_3$ CeCCs showed similar performance in terms of electrochemical and salt spray chamber results. When longer conversion time of 4 h was used to deposit coatings on AA7075-T6, the nitrate and chloride-based CeCCs act as strong anodic inhibitors, and acetate-based CeCC acts as cathodic inhibitor in chloride solution. Salt spray test confirmed low protective ability of acetate, better in nitrate and the best in chloride-based CeCCs.

The morphology of the coatings is abundant; in the case of acetate CeCC the surface was uniformly covered, whereas nitrate- and chloride-based coatings were susceptible to cracking, probably due to larger thickness.

To conclude, selected cerium conversion coatings showed the ability to protect AA7075-T6 under moderate, non-rigorous corrosive conditions. Coatings are relatively easy to prepare, are low-cost and non-toxic.

EXPERIMENTAL SECTION

Materials and chemicals

Metal substrates

Aluminium alloy 7075-T6, in the form of 0.5 mm thick sheet supplied by Kaiser Aluminum, USA, was used as a substrate. Sheets were cut into disks of 15-mm diameter. Before deposition, the substrates were ground with 2400- and 4200-grit SiC emery papers (Struers, The Netherlands), rinsed with distilled water and cleaned ultrasonically in ethanol for 10 minutes.

Chemicals and procedure for formation of conversion coatings

A 50 mL volume of 0.05 M cerium salt was prepared in a 100 mL beaker serving as a conversion bath. Then the sample was positioned at the bottom of the beaker with the ground surface facing up. Immediately after, hydrogen peroxide (H_2O_2 , 30 %, AppliChem) as an oxidation reagent was added to the solution to obtain 0.25 M concentration (Figure 2).

Samples were immersed in conversion bath at room temperature for different periods of time (from 3 min to 4 h) and then taken out, rinsed with distilled water for ten minutes and dried with a jet of compressed air.

Cerium conversion coatings were formed from various cerium(III) salts were used: Ce(III) acetate ($\text{Ce}(\text{OAc})_3 \cdot \text{Ce}(\text{CH}_3\text{COO})_3 \times 2\text{H}_2\text{O}$, 99.9 %, Aldrich), Ce(III) chloride ($\text{CeCl}_3 \times 7\text{H}_2\text{O}$, 99.9 %, Aldrich) and Ce(III) nitrate $\times \text{H}_2\text{O}$ ($\text{Ce}(\text{NO}_3)_3$, 99.5 %, Fluka). The content of crystal-bound water in cerium(III) acetate was calculated from the thermogravimetric analysis.

Methods

UV-VIS spectroscopy

UV-VIS spectra were recorded with a Perkin-Elmer Lambda 25 UV-VIS spectrophotometer. Samples were immersed in a 1 cm wide disposable plastic makro cuvettes (Ratiolab GmbH, Dreieich, Germany) then placed in the holder in the UV spectrometer. Spectra were measured between a wavelength from 700 nm to 280 nm as absorbance spectra. The spectra were recorded every 3 minutes and are presented as absorbance units (A. U.).

Corrosion measurements

Electrochemical measurements

Electrochemical measurements were performed in a three-electrode standard corrosion cell (Parstat – Corrosion Cell Kit, model K0047, volume 1 L) at 25°C. Bare, uncoated AA7075-T6 samples coated by conversion coatings were embedded in a Teflon holder (model K0105 Flat Specimen Holder Kit) served as a working electrode. An area of 0.95 cm² was exposed to the corrosive solution. A saturated calomel electrode (SCE, Hg/Hg₂Cl₂, 0.242 V vs. saturated hydrogen electrode) was used as reference electrode together with reference electrode bridge tube and carbon rods as a counter electrode. All potentials in the text refer to the SCE electrode. Electrochemical experiments were carried out with an Autolab PGSTAT 12 (Metrohm Autolab, Utrecht, The Netherlands) potentiostat/galvanostat and controlled by Nova 2.1 software.

During the formation of CeCC in the conversion bath, the open circuit potential was measured as a function of time prior and after addition of H₂O₂ until a steady-state value was achieved, referred to as $E_{\text{oc form}}$.

The corrosion performance of uncoated and coated samples was investigated in 0.1 M NaCl solution (NaCl, AppliChem > 99.5%) of pH = 5.2. Solution was prepared using Milli-Q Direct water with the resistivity of 18.2 MΩ cm at 25 °C (Millipore, Billerica, MA).

Prior to measurements, the samples were allowed to stabilize under open circuit conditions for approximately 1 h. During that time, the open circuit potential was measured as a function of time until a steady potential was achieved (referred to as E_{oc}). Following stabilization at the E_{oc} , the electrochemical measurements were carried out. The linear polarization measurements were performed in a potential range of ± 10 mV vs. E_{oc} , using a 0.1 mV/s potential scan rate. The values of polarization resistance (R_p) were deduced from the slope of fitted current density vs. potential lines using Nova software. Potentiodynamic measurements were performed using a 1 mV/s potential scan rate, starting -250 mV to E_{oc} . The potential was then increased in the anodic direction. For each sample, measurements were performed at least in triplicate and the representative measurement was chosen to be presented in graphs. Related electrochemical corrosion parameters (corrosion potential (E_{corr}), corrosion current density (j_{corr})) were obtained from polarization curves by Tafel approximation. The difference between the pitting potential (E_{pit}) and E_{corr} was denoted as a passive span and calculated as $\Delta E = |E_{pit} - E_{corr}|$. Some polarization curves with not well defined anodic Tafel region were extrapolated by inspecting only a linear fit of the cathodic Tafel curve, which intersects the E_{corr} .

The corrosion inhibition efficiency (IE) was determined from linear polarization and calculated using the equation:

$$IE = \frac{R_p^* - R_p}{R_p^*} \quad [1]$$

where R_p^* and R_p are polarization resistance measured on coated and uncoated samples.

Salt spray test

Salt spray testing was carried out in a salt spray chamber of the capacity 0.17 m³ (ASCOTT, Staffs, Great Britain). Testing was carried out according to the International Standard Organization (ISO) standard 9227-2006 »Corrosion tests in the artificial atmosphere«. The concentration of sodium chloride solution was 50 g/L (5 ± 1 %).

The device for spraying the salt solution comprised a supply of clean air, of controlled pressure and humidity. The temperature of the hot water in the saturation tower was 46 °C and the overpressure was 85 kPa. The temperature in the salt spray chamber was set to 35 °C \pm 2 °C. The test lasted 6 hours.

The samples were taken from the chamber every few hours and photographed in order to follow the progress of the corrosion process with time. Micrographs were taken by a digital camera.

SEM characterization

A scanning electron microscope (SEM) JSM-7600F (JEOL) and an energy dispersive X-ray spectrometer (EDS) Inca 350 (Oxford Instruments) were used to analyse the morphology and chemical composition of bare and coated AA7075-T6 substrates. Prior analysis, the samples were coated with a thin layer of carbon. SEM analysis was performed in a backscattered electron (BSE) mode with beam energy of 5 or 15 kV. EDS analysis were performed in point mode and the carbon was omitted from quantitative analysis.

ACKNOWLEDGMENTS

The financial support by Slovenian Research Agency is kindly acknowledged (core projects No. P2-0393 and No. P1-0134). This work is a part of the micro-grant Key enabling technology for clean production (abbreviation KET4CP) "Surface treatment process implementation for aluminium sealing to improve anti-corrosion properties", agreement No. KET4CP-SME2019-06-No-01". The authors thank Barbara Kapun for performing SEM/EDS analysis.

REFERENCES

1. J.E. Hatch, *Aluminum: Properties and Physical Metallurgy*, ASM International, **1984**.
2. J.R. Davis, *Corrosion of Aluminum and Aluminum Alloys*, ASM International, **1999**.
3. P.L. Hagans; C.M. Haas; *Surf. Eng.* **1994**, *5*, 405–411.
4. M. Kendig; S. Jeanjaquet; R. Addison; J. Waldrop; *Surf. Coat. Technol.*, **2001**, *140*, 58–66.
5. ECHA European Chemicals Agency, Chromium VI compounds - ANNEX XVII TO REACH - Conditions of restrictions, <https://echa.europa.eu>.
6. I. Milošev; *Acta Chim. Slov.*, **2019**, *66*, 511–533.
7. O. Gharbi; S. Thomas; C. Smith; N. Birbilis; *Npj Mater. Degrad.*, **2018**, *12*, 1–8.
8. B.R.W. Hinton, D.R. Arnott, N.E. Ryan; *Met. Forum*, **1984**, *7*, 211–217.
9. B. Hinton; *Corrosion*, **2010**, *66*, 085001-085001–15.
10. F.H. Scholes; C. Soste; A.E. Hughes; S.G. Hardin; P.R. Curtis; *Appl. Surf. Sci.*, **2006**, *253*, 1770–1780.

11. M. Forsyth; B. Hinton; *Rare Earth-Based Corrosion Inhibitors*, Elsevier, **2014**.
12. C.-S. Lin; W.-J. Li; *Mater. Trans.*, **2006**, *47*, 1020–1025.
13. A. Decroly; J.-P. Petitjean; *Surf. Coat. Technol.*, **2005**, *194*, 1–9.
14. M. Dabalà; L. Armelao; A. Buchberger; I. Calliari; *Appl. Surf. Sci.* **2001**, *172*, 312–322.
15. T.G. Harvey; *Corros. Eng. Sci. Technol.*, **2013**, *48*, 248–269.
16. P. Rodič; I. Milošev; *J. Electrochem. Soc.* **2016**, *163*, C85–C93.
17. I. Milošev; P. Rodič; *Corrosion*, **2016**, *72*, 1021–1034.
18. B. Volarič; I. Milošev; *Corros. Eng. Sci. Technol.*, **2017**, *52*, 201–211.
19. P. Rodič; I. Milošev; *Corros. Sci.* **2019**, *149*, 108–122.
20. P. Rodič; I. Milošev; M. Lekka; F. Andreatta; L. Fedrizzi; *Electrochim. Acta.* **2019**, *308*, 337–349.
21. I. Milošev; B. Volarič; *Corrosion*, **2017**, *73*, 822–843.
22. B. Volarič; A. Mazare; S. Virtanen; I. Milošev; *Corrosion*, **2020**, *76*, 18–38.
23. F. Andreatta; M.M. Lohrengel; H. Terryn; J.H.W. de Wit; *Electrochim. Acta*, **2003**, *68*, 3239–3247.

MORPHOLOGICAL AND STRUCTURAL INVESTIGATION OF THE POLY(VINYL CHLORIDE) / GRAPHENE OXIDE COMPOSITES

LUIZA STINGESCU^a, CALIN CADAR^{b,c}, LIVIU COSMIN COTET^{b,c},
LUCIAN BAIA^{c,d,e}, KATA SASZET^{d,e}, KLARA MAGYARI^{d,e},
ALIN GRIG MIHIS^{b,c}, CARMEN IOANA FORT^{b,c}, MALVINA STROE^a,
ELENA MATEI^a, ANDREEA NILA^a, ION ANGHEL^f, MONICA BAIA^{c,d},
MIHAELA BAIBARAC^a, VIRGINIA DANCIU^{b,c,*}

ABSTRACT. The morphological and structural properties of the poly(vinyl chloride)/graphene oxide (PVC/GO) composites are reported. By the mixture of the two constituents, the PVC/GO composite membranes with a concentration of the GO sheets varying from 0 wt.% to 0.5, 1, 2, 3, 4 and 5 wt.% were prepared. Using scanning electron microscopy (SEM) and the analysis of the atomic force microscopy (AFM) images we observed that as increasing the GO concentration in the PVC mass from 0 wt.% to 5 wt.%, the average surface roughness decreases from 235 μm to 227 μm . Using Raman scattering, we report that as increasing the GO concentration in the PVC mass, the ratio between the relative intensities of the Raman lines situated in the spectral ranges 600-650 and 2850-3000 cm^{-1} ($I_{600-650}/I_{2850-3000}$) increases as a consequence of the change of GO carbon atoms hybridization from sp^2 to sp^3 . An increase in the number of C-C bonds, simultaneous with the appearance of O-C=O bonds and the decrease of the chlorine concentration, when the GO concentration increases in the PVC weight is reported by X-ray photoelectron spectroscopy (XPS). The down-shift of the main diffraction signal from 24° to 26° when the GO concentration

^a National Institute of Materials Physics, Lab. Optical Process in Nanostructured Materials (LOPNM), 405 A Atomistilor str., Bucharest-Magurele, Romania

^b Babes-Bolyai University, Faculty of Chemistry and Chemical Engineering, Department of Chemical Engineering, 11 Arany Janos str., RO-400028, Cluj-Napoca, Romania

^c Babes-Bolyai University, Institute of Research-Development-Innovation in Applied Natural Sciences, 30 Fantanele str., RO-400294, Cluj-Napoca, Romania

^d Babes-Bolyai University, Faculty of Physics, 1 M. Kogalniceanu str., RO-400084 Cluj-Napoca, Romania

^e Babes-Bolyai University, Interdisciplinary Research Institute on Bio-Nano-Sciences, Nanostructured Materials and Bio-Nano-Interfaces Center, 42 T. Laurian str., RO-400271, Cluj-Napoca, Romania

^f "Alexandru Ioan Cuza" Police Academy, Fire Officers Faculty, 3 Morarilor str., Bucharest, Romania

* Corresponding author: vdanciu@chem.ubbcluj.ro

increases in the PVC/GO composite mass from 0 wt.% to 5 wt.%, confirms the incorporation of GO in the polymeric matrix and the modification of the original PVC sample structure. Using transmission electron microscopy (TEM), no agglomerations of the GO structures within the PVC/GO matrix contrast limit were observed.

Keywords: *poly(vinyl chloride), graphene oxide, membranes*

INTRODUCTION

Due to the ease of processing, low cost, good physical, chemical and corrosion properties, poly(vinyl chloride (PVC) is a widely used polymer. As estimated in the PVC market report [1], the global PVC market stood at US\$ 57.06 billion in 2015. It is expected a tremendous rise during the period from 2015 to 2021, the revenue in this PVC market reaching to US\$ 78.90 billion by the end of the forecasted period of time and it is forecast to increase even more to 88.02 Billion USD by 2027 [2]. The main available products in the PVC market are flexible and rigid PVC. The flexible PVC has applications in medical equipment, signage, electrical cable insulation, plumbing, and inflatable items, while rigid PVC is used across construction sectors. However, PVC has several disadvantages such as poor processability, thermal stability and weatherability. Moreover, PVC without plasticizers or fillers is typically brittle and is not suitable in many fields [3-5].

Recently, the improvement in thermal, electrical and mechanical properties of PVC matrix with graphene derivatives has been reported in many related papers [6-9]. As filler material, graphene oxide (GO) is inexpensive, it has hydrophilic character and it contains epoxy, alcohol, carbonyl and carboxyl groups [10, 11]. Additionally, GO can be homogeneously dispersed in organic solvents such as tetrahydrofuran (THF) and N,N'-dimethylformamide (DMF), which allows a good interfacial adhesion between polymer and GO, also inducing significant changes to the composite properties. Due to the lone pairs of electrons at the chlorine atom of the PVC, and respectively the dipole-dipole interaction between hydrogen and chlorine atom which can stiffen the polymer backbone, the PVC/GO composites are of particular interest. In addition, GO can interact with PVC chlorine atoms and become an active site that allows anchoring of other functional groups thus improving the properties of the composite. Deshmukh and Joshi [7] reported that the strong interaction between PVC and GO increased thermal stability of the composites.

The objective of this work is to prepare PVC/GO composite membranes by mixing of GO with PVC dissolved in THF and DMF. The morphological and structural characteristics of the PVC/GO composites were investigated.

RESULTS AND DISCUSSION

By microscopic investigation, (Fig. 1a, b), 2D GO nanosheets with surfaces of tens of micrometers and thicknesses that reach up to atomic layer of carbon can be observed. These can build 3D structures of tens of micrometers thickness (Fig. 1c). Details about structural characterization of GO used for this study for the preparation of PVC/GO composites, including XRD, Raman, FTIR, DLS and XPS measurements, were presented in an research article published by Cotet et al. [12].

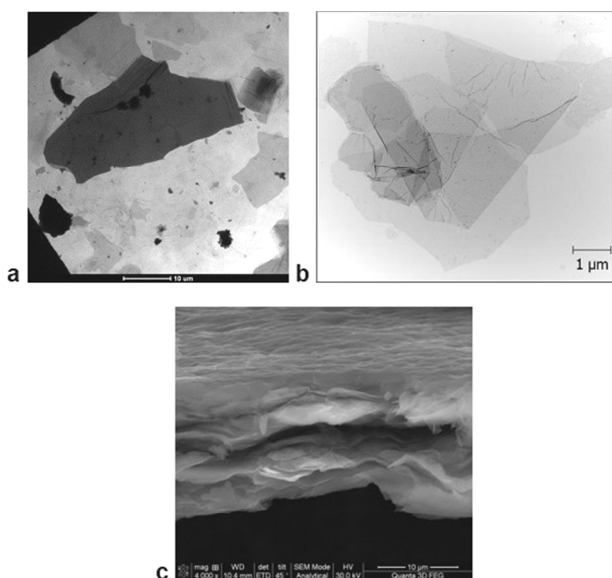


Figure 1. TEM (a), SPM (b) and (c) SEM micrographs for GO.

A selection of SEM images of PVC membranes is shown in Fig. 2. It is observed that in the case of PVC/GO composites with 3 and 5 wt.% GO, the membrane surface becomes rougher, in good agreement with the observations reported in Ref. [13] and confirmed by our studies. In this context, the surface properties of the samples have been analyzed by atomic force microscopy (AFM) using the WsxM5.0 software.

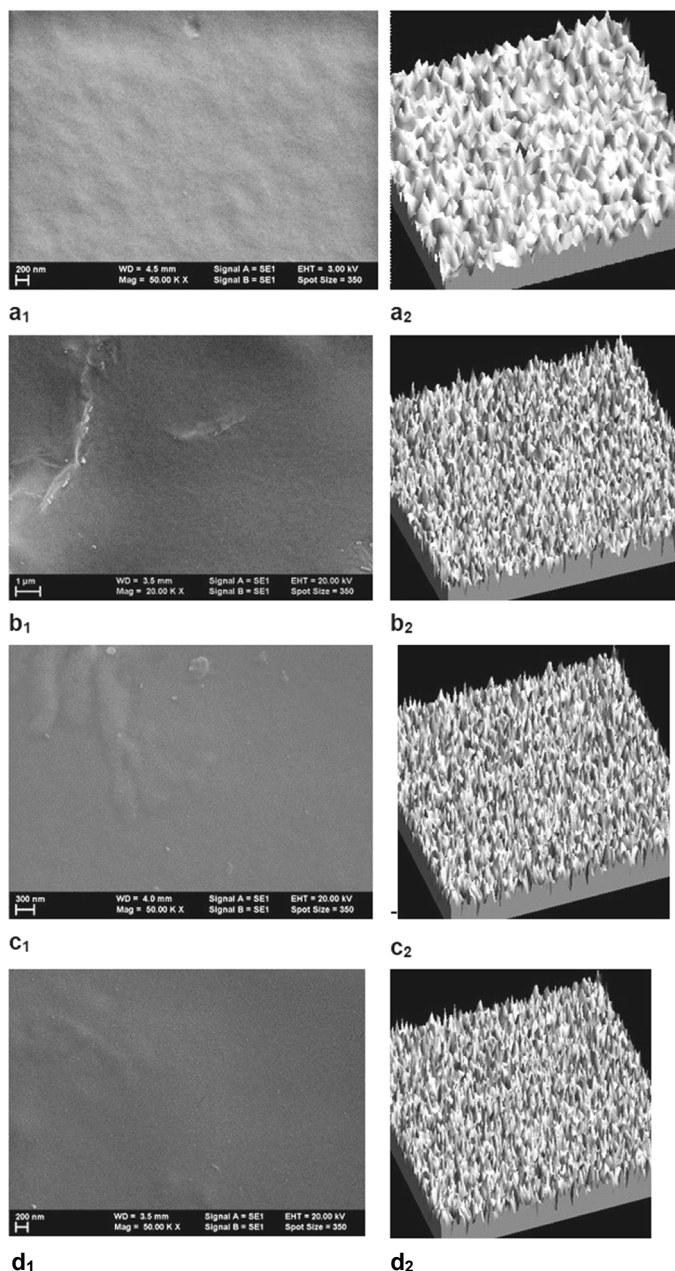


Figure 2. SEM images for the following membranes: PVC 0 wt.% GO (a₁), PVC 0.5 wt.% GO (b₁), PVC 3 wt.% GO (c₁), and PVC 5 wt.% GO (d₁). AFM images of the membranes: PVC 0 wt.% GO (a₂), PVC 0.5 wt.% GO (b₂), PVC 3 wt.% GO (c₂), and PVC 5 wt.% GO (d₂).

From AFM images the following values for roughness average and Root Mean Square (RMS) roughness are reported: i) 235 μm and 281 μm in the case of the PVC membrane; ii) 233 μm and 278 μm in the case of the PVC membrane having 0.5 wt.% GO; iii) 230 μm and 277 μm in the case of the PVC membrane having 3 wt.% GO and iv) 227 μm and 275 μm in the case of the PVC membrane having 5 wt.% GO.

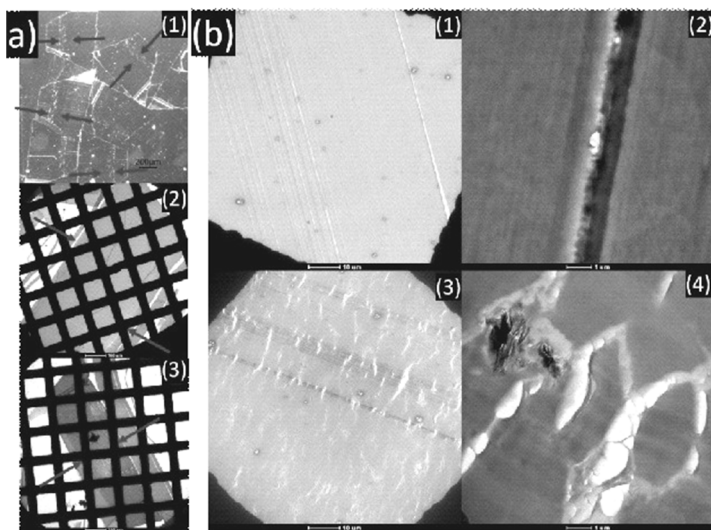


Figure 3. (a) Optical microscopy and TEM micrographs showing transversal cross-sections of (1) PVC 3 wt.% GO, (2) PVC 0 wt.% GO and (3) PVC 4 wt.% GO membranes with the membrane-resin boundary indicated with arrows. (b) Textural particularities induced by the presence and absence of GO filler as observed in the multi-scale TEM micrographs for (1-2) PVC 0 wt.% GO and (3-4) PVC 4 wt.% GO.

In order to gain a deeper understanding regarding the GO dispersion in the PVC matrix, a cross-sectional analysis was performed as presented in Fig. 3. Slices of the resin embedded membranes were investigated using optical microscopy and TEM. The cross-section of the PVC sample reveals a homogeneous aspect with some texture imperfections given by the irregularities of the glass blades used during sample sectioning. The sample containing GO indicates some additional features presented as microscale discontinuities, probably even more emphasized by the mechanical stress induced during the sample sectioning. Moreover, the observed irregularities found in the analyzed sections of the PVC 4 wt.% GO indicate a homogeneous distribution

at the microscale. At larger magnifications, morphological features specific to both individual and agglomerated graphene sheets are observed in the intimate vicinity of the irregularities. The results suggest that GO disperses throughout the entire volume of the membrane leading towards the formation of a nano-scale network. The parameters of the GO filler-based network (i.e. connectivity and percolation threshold) are considered to be strongly correlated with the synthesis parameters and filler concentration and to further influence the electric and thermal properties of the composite.

The FTIR spectra of the PVC samples and the PVC/GO composites are shown in Fig. 4.

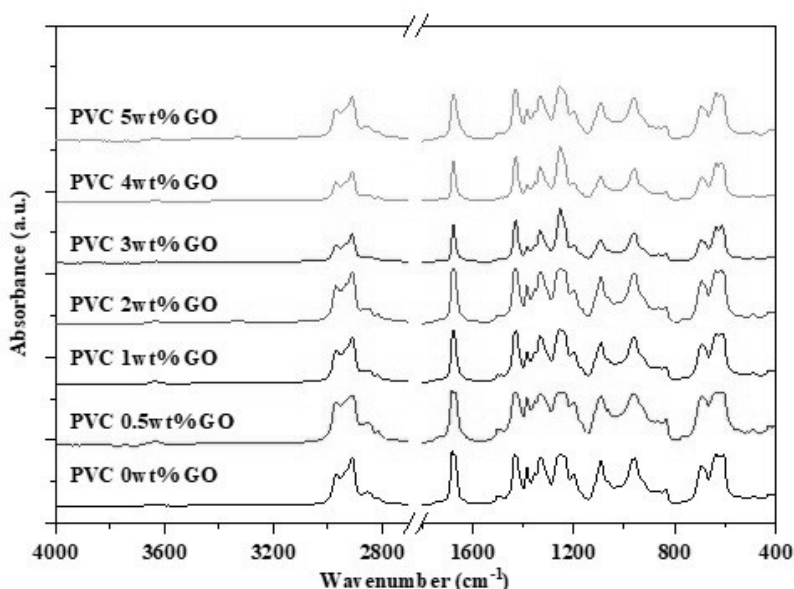


Figure 4. FTIR spectra of PVC and the following PVC/GO composites: PVC 0.5 wt.% GO, PVC 1 wt.% GO, PVC 2 wt.% GO, PVC 3 wt.% GO, PVC 4 wt.% GO and PVC 5 wt.% GO wt.%.

The absorption bands from 2981 cm^{-1} are attributed to the stretching vibration of the C-H bond, those from 2822 cm^{-1} to the asymmetrical stretching vibrations, and those from 1668 cm^{-1} to the stretching vibration of C=O, which are attributed to CO_2 from the background. At the absorption band at 1426 cm^{-1} , the deformation vibrations in plane of the CH groups can be identified, at 1340 cm^{-1} those of the deformation in plane of CH_2 , and at 1251 cm^{-1} the twisting vibrations of the CH. [14] At the same time, at 1091 cm^{-1} , the stretching

vibrations of the CH₂-Cl groups are observed, at 970 cm⁻¹ the rocking vibration of the CH in the cis position, at 695 cm⁻¹ the stretching vibration of the C-Cl, at 614 cm⁻¹ elongation vibrations of C-Cl and at 612 cm⁻¹ rocking vibrations of CH in trans position were identified. [14] The absorption bands related to PVC have been identified being consistent with the results found in related studies. Analyzing the spectra of the composites, the specific PVC bands, but no significant differences between the spectra can be observed and the presence of the characteristic bands for GO cannot be identified with certainty. Therefore, this analysis shows that FTIR spectroscopic technique is not sufficiently sensitive to highlight the presence of GO in the used concentration range.

In all diffractograms of the samples presented in Fig. 5 one large and two smaller, broad signals can be observed, suggesting the amorphous structure of the materials [14, 15]. In the case of pure PVC, these signals appear at 2θ ~18°, 24° and 40°, all characteristic for PVC according to previous literature. These amorphous reflections shift proportionally with the GO content, reaching ~ 20°, 26°, 42° in the case of PVC 4 wt.% GO. In the case of the PVC 5 wt.% GO sample there is no further shifting in the reflections, the diffractogram is dominated by an amorphous signal around 2θ ~ 25°.

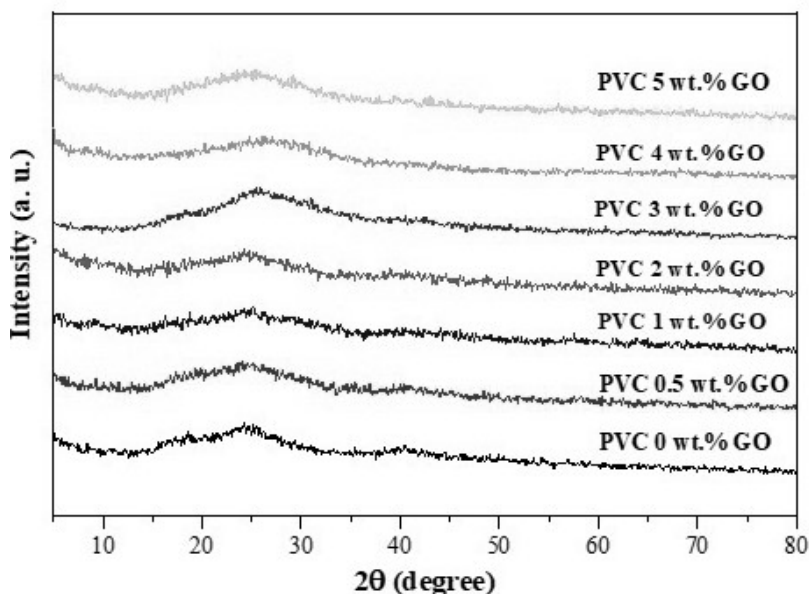


Figure 5. XRD results for pure PVC and the following PVC/GO composites: PVC 0.5 wt.% GO, PVC 1 wt.% GO, PVC 2 wt.% GO, PVC 3 wt.% GO, PVC 4 wt.% GO and PVC 5 wt.% GO.

These displacements may suggest the incorporation of GO into the polymeric matrix, that is altering the original structure of the PVC sample. The characteristic reflection of GO at $\sim 2\theta = 10^\circ$ cannot be clearly observed in any of the samples. [16] Apart from the shift of the above-mentioned reflections, no other significant differences were observed. This could mean that the amount of GO added in PVC/GO composites is too small to be detected by XRD measurements.

The Raman spectra of PVC and its GO composites recorded using the 514 nm excitation wavelength are shown in Fig. 6.

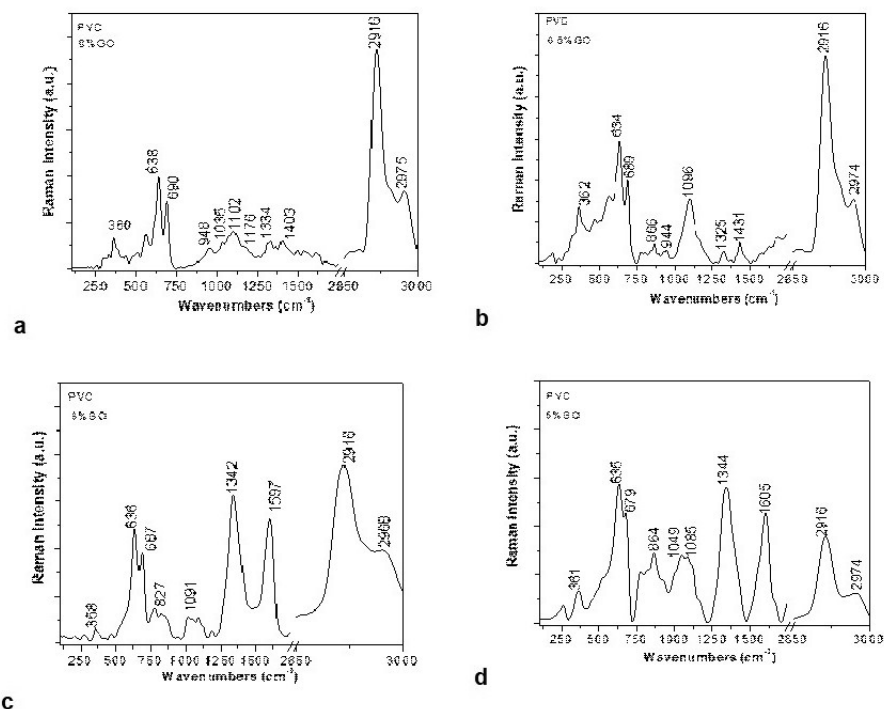


Figure 6. Raman spectra of the membranes: PVC 0 wt.% GO (a), PVC 0.5 wt.% GO (b), PVC 3 wt.% GO (c), and PVC 5 wt.% GO (d).

The main Raman lines of PVC are situated in the spectral ranges 300-500, 600-750, 950-1200, 1334, 1403-1430 and 2850-3000 cm⁻¹, being associated to the vibrational modes: C-Cl bond in the trans configuration of the polymer, C-Cl stretching [17, 18] C-C stretching, CH₂ symmetrical stretching (2915-2920 cm⁻¹) and the CH₂ asymmetric stretching (2970 cm⁻¹) [19]. Figure 6a

highlights that the ratio between the relative intensities of the Raman lines in the spectral domains 600-650 and 2850-3000 cm^{-1} ($I_{600-650}/I_{2850-3000}$) has a value equal to 0.41. As increasing of GO concentration in the mass of the polymer, a modification of the $I_{600-650}/I_{2850-3000}$ ratio is observed. According to Fig. 6d in the case of PVC/GO composite with a 5 wt.% GO concentration, the $I_{600-650}/I_{2850-3000}$ ratio becomes equal to 1.63. The gradual decrease of the relative intensity of the Raman line of PVC from 2916 cm^{-1} in the presence of GO indicates the generation on the macromolecular chain of PVC of some structural units of the type Cl-CH=CH- and/or $-\text{CH=C-Cl-}$. The formation of such structural units indicates the partial dehydrogenation of the macromolecular compound which should result in the formation of new C-H and C-OH bonds on the GO surface. Formation of new C-H and C-OH bonds on the surface of the GO sheets originates in breaking C-O-C bonds from GO epoxy groups. In contrast with the GO sheets characterized by the I_D/I_G ratio equal to 0.9⁹, in the case of PVC/GO membrane composites having a GO concentration equal to 5 wt.%, the I_D/I_G ratio is equal to 1.23. This higher value of the I_D/I_G ratio indicates the formation of C-H bonds as a consequence of the conversion of carbon atoms with sp^2 hybridization (related to C=C bonds) to carbon atoms with sp^3 hybridization.

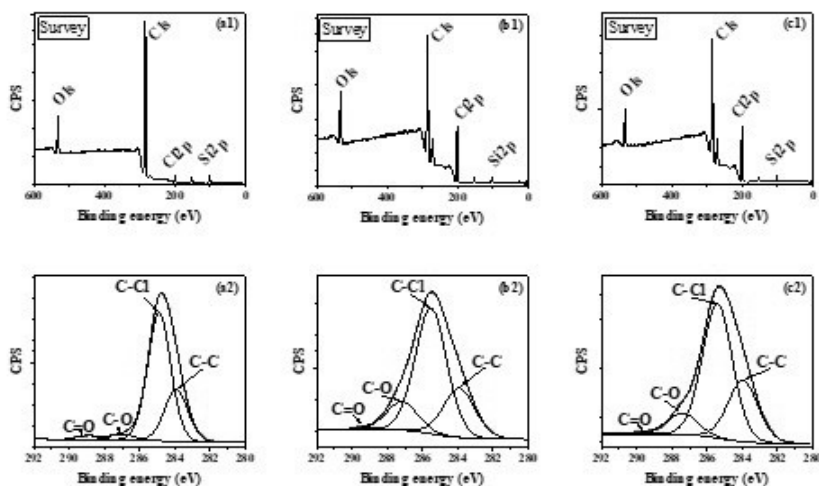


Figure 7. XPS spectrum selection, survey and C1s component (high resolution spectrum), for PVC (a1 and a2), PVC 0.5 wt.% GO (b1 and b2), PVC 5 wt.% GO (c1 and c2) samples.

The XPS spectra of the PVC/GO samples and a selection thereof are shown in Fig. 7 to highlight the influence of the presence of GO in the PVC/GO composite. Based on the literature, the C1s PVC line can be divided into two components, [20] at ~ 284 eV (C-C and C-H), ~ 285 eV (C-Cl). In addition to the C-C and C-Cl bonds, there are also the C-O bonds at 286.9 eV (2-3%) and C=O 288.5 eV (2-3%). With the addition of GO (PVC with 0.5 wt.% GO and PVC with 5 wt.% GO) the C1s peak is modified (Fig. 7b, c), suggesting that the synthesis was successful. In PVC with 0.5 wt.% GO, the C-O concentration is 13% and in PVC with 5 wt.% GO it is 10%. The analysis of the high-resolution spectrum of C1s shows that the concentration of C-C bonds increased with GO concentration suggesting that GO covers PVC (it is clearly the change of the C-C and C-Cl lines intensities ratio). The XPS measurements also show a decrease in chlorine concentration with increasing GO content.

CONCLUSIONS

This work reports about new results concerning the morphological and structural properties of the composites based on PVC and the GO sheets, obtained by mixing of two constituents when free membranes were resulted. The analysis of SEM and 3D images of the prepared PVC/GO membranes highlight a roughness for all six samples, with increasing the GO concentration in the PVC mass from 0 to 5 wt.%, the roughness average decreased from 235 to 227 μm . On the other hand, both SEM and TEM images proved that there are no agglomerations of the GO structures within the PVC/GO matrix contrast limit. XRD diffractograms revealed a down-shift of the main diffraction signal from 24° to 26° when the of GO concentration increases in the PVC/GO composite mass from 0 to 5 wt.%, the fact that certified the incorporation of GO in the polymeric matrix and the modification of the original PVC sample structure. In the FTIR spectra no significant difference is observed between the samples, but there are differences in the Raman lines and the XPS spectra. However, the Raman spectra analysis revealed that as increasing the GO concentration in the polymer mass, the ratio between the relative intensities of the Raman lines situated in the spectral ranges 600-650 and 2850-3000 cm^{-1} ($I_{600-650}/I_{2850-3000}$) increases as a consequence of the change of the GO carbon atoms hybridization from sp^2 to sp^3 . The analysis of the high-resolution XPS spectrum of C1s further showed an increase in the number of C-C bonds, the appearance of O-C=O bonds and the decrease of the chlorine concentration as the GO concentration increased.

EXPERIMENTAL SECTION

Materials

Natural graphite (Fluka; purum powder, <0.1 mm) powder (GF), H₂SO₄ 85% (SC Nordic Invest SRL, Cluj-Napoca), H₃PO₄ 85% (Merck), KMnO₄ (Merck, 99%), H₂O₂ 3% solution (SC "Hippocrates 2000" SRL, București), HCl 37% (SC Nordic Invest SRL, Cluj-Napoca), absolute ethanol (SC Nordic Invest SRL, Cluj-Napoca) were used for the synthesis of GO. Hydroxyethyl cellulose (HEC), lauryl peroxide (LPO), N,N'-dimethylformamide (DMF), poly(vinyl chloride) (PVC with Mw = 48.000, density = 1 g/mol at 25 °C) used for preparation of PVC membranes and composites were purchased from the Aldrich-Sigma company, these being used without further purification.

a) Synthesis of GO

The synthesis of GO was based on a three-step method. In the first step H₂SO₄ and H₃PO₄ (83 mL) were mixed in a 9/1 volume ratio [12, 21]. After 5 min. of mixing, 7.5 g of graphite was added at room temperature under stirring. The suspension was stirred for 10 min. and the as-prepared mixture was placed in an ice bath and after 20 min., 33 g of KMnO₄ was added gradually, maintaining the same stirring conditions. The mixture was removed from the ice bath after 2 h and kept under stirring at room temperature for 2 days. In the second step, the mixture was placed again in an ice bath and 550 mL of H₂O₂ was added gradually under stirring. After 1 h, the mixture was centrifuged (at 5000 rpm for 15 min.) and the supernatant was decanted. The remained solid material was then washed successively with 550 mL of H₂O (bidistilled), 275 mL of 37% HCl and 275 mL of absolute ethanol. The last two washes were repeated twice. During each wash, the solution was sonicated for 15 min. (using Bandelin Sonorex ultrasonic bath, model RK-510-H; P: 160/640W; f: 35 KHz) and centrifuged (at 5000 rpm for 15 min.). In the third step, the resulting solid was dispersed in 550 mL bidistilled water and sonicated for 15 min. A homogeneous dark brown suspension was obtained and kept in a sealed vessel for 5 days. Then, approximately 500 mL of this initial GO suspension was harvested by pipetting from the top of the vessel, poured and spread on a glass wafer and dried at room temperature. Mechanical exfoliation from the substrate was used to obtain a GO membrane (i.e. unsupported GO film). These membranes have been morpho-structurally characterized and used to obtain PVC/GO composites.

b) Preparation of the membranes of PVC and its composites with the GO sheets

To obtain the PVC membranes, 0.4 g PVC was dissolved in 10 mL THF and 10 mL DMF. The obtained solution was poured into a Petri dish and then deposited on a hob at 60 °C in order to evaporate the solvents. After one hour, the PVC membrane was dried under vacuum for another 6 hours until constant mass. In order to obtain PVC/GO composites, two solutions were prepared, the first containing 0.4 g PVC in 10 mL THF, and the second containing 1, 2, 4, 6, 8 and respectively 10 mg GO in 10 mL DMF. The two solutions were mixed and then the same procedure described for obtaining the PVC membranes was followed.

Characterization techniques

X-ray diffraction (XRD) was carried out on a Shimadzu XRD 6000 diffractometer using CuK α radiation ($\lambda=1.54$ Å), equipped with a graphite monochromator. The diffractograms were recorded in 2θ range from 10° to 80° with a speed of 2°/min.

IR absorption spectra were recorded with a FTIR Vertex 80 spectrometer, from Bruker, at room temperature, in the 400–4000 cm⁻¹ range, with a spectral resolution of 4 cm⁻¹, by using the well-known KBr pellet technique.

Raman spectra were recorded with a Raman spectrophotometer, T64000 model, from Horiba Jobin Yvon endowed with an Ar laser (the excitation wavelength being 514 nm). The Raman spectra were recorded with a spectral resolution of 1 cm⁻¹.

Transmission electron microscopy (TEM) investigations were performed on the GO flakes and polymer composites. The nanomaterial was dispersed in ethanol and deposited on the surface of carbon coated Cu grids. The composites were embedded in LR white resin and ultramicrotomed using glass blades. The slices were deposited on Cu grids for TEM investigations and on glass slides for optical microscopy studies. A FEI Tecnai G2 F20 X-Twin TEM operating at 200 kV was used in bright field mode. The SEM analysis were performed using a tabletop microscope Hitachi TM4000 plus (Hitachi High-Technologies, Japan), equipped with an energy-dispersive X-ray system (AZtec One EDS, Oxford Instruments Analytical Ltd., UK), at an accelerating voltage of 5 kV.

The SEM analysis of the GO flakes was performed using a tabletop microscope Hitachi TM4000 plus (Hitachi High-Technologies, Japan), equipped with an energy-dispersive X-ray system (AZtec One EDS, Oxford Instruments Analytical Ltd., UK), at an accelerating voltage of 5 kV.

SEM pictures of the PVC/GO composite membranes were recorded with Zeiss Gemini 500 scanning electron microscope. An analysis of the roughness parameters of these composites membranes was carried out using WSxM5.0 develop 9.3 software.

X-ray photoelectron spectroscopy (XPS) spectra were recorded with a PHI 5600ci Multi Technique system employing a monochromatic Al-K α source (1486.6 eV), a hemispherical analyzer and charge neutralization device. Samples were carefully fixed on a double-sided carbon tape to ensure that the sample particles covered the tape. Experiments were performed by operating the X-ray source with a power of 200 W, while the pressure in the analyzer chamber was in the range of 10⁻⁹-10⁻¹⁰ mbar. The binding energy scale was charge referenced to the C1s at 284.6 eV. Elemental composition was determined from survey spectra acquired at pass energy of 60 eV. High resolution spectra were obtained using analyzer pass energy of 20 eV. Analysis of the data was carried out with CasaXPS software. A Shirley background was used for all curve-fitting along with the Gaussian/Lorentzian product form (70% Gaussian and 30% Lorentzian).

The SPM data was processed with MountainsMap 7.4 software from Digital Surf as contact atomic force microscopy (AFM).

ACKNOWLEDGMENTS

This work was supported by a grant of the Romanian Ministry of Research and Innovation, CCCDI – UEFISCDI, project number PN-III-P1-1.2-PCCDI-2017-0350 / 01.03.2018 (Graphene4Life), within PNCDI III.

REFERENCES

1. Z.M. Research; PVC Market (Rigid PVC And Flexible PVC) by Application (Pipes & Fittings, Wires & Cables, Films & Sheets, Bottles and Others) For Automotive, Electrical & Electronics, Construction, Packaging And Other End-User: Global Industry Perspective, Comprehensive <http://www.zionmarketresearch.com/report/pvc-market> (accessed Dec 18, 2019).
2. John Watson (Reports And Data); Polyvinyl Chloride (PVC) Market To Reach USD 88.02 Billion By 2027 <https://www.globenewswire.com/news-release/2020/02/13/1984885/0/en/Polyvinyl-Chloride-PVC-Market-To-Rreach-USD-88-02-Billion-By-2027-Reports-And-Data.html> (accessed Sep 18, 2020).

L. STINGESCU, C. CADAR, L.C. COTET, L. BAIA, K. SASZET, K. MAGYARI, A.G. MIHIS, C.I. FORT, M. STROE, E. MATEI, A. NILA, I. ANGHEL, M. BAIA, M. BAIBARAC, V. DANCIU

3. J. Hu; X. Jia; C. Li; Z. Ma; G. Zhang; W. Sheng; X. Zhang; Z. Wei; *J. Mater. Sci.*, **2014**, *49*, 2943–2951.
4. A. Godínez-García; D.D. Vallejo-Arenas; E. Salinas-Rodríguez; S. A. Gómez-Torres; J. C. Ruiz; *Appl. Surf. Sci.*, **2019**, *489*, 962–975.
5. F. Mindivan; M. Gökteş; *Polym. Bull.*, **2020**, *77*, 1929–1949.
6. H.J. Salavagione; G. Martínez; *Macromolecules*, **2011**, *44*, 2685–2692.
7. K. Deshmukh; G.M. Joshi; *Polym. Test.*, **2014**, *34*, 211–219.
8. S. Vadukumpully; J. Paul; N. Mahanta; S. Valiyaveetil; *Carbon N. Y.*, **2011**, *49*, 198–205.
9. K. Deshmukh; S.M. Khatake; G.M. Joshi; *J. Polym. Res.*, **2013**, *20*, 286, pp. 1-11.
10. V. Singh; D. Joung; L. Zhai; S. Das; S. I. Khondaker; S. Seal; *Prog. Mater. Sci.*, **2011**, *56*, 1178–1271.
11. S. Sava; C. Sarosi; B. Stanca; A. Tonea; C. Alb; D. Dudea; *Stud. Univ. Babeş-Bolyai Chem.*, **2015**, *60*, 71–80.
12. L.C. Cotet; K. Magyari; M. Todea; M. C. Dudescu; V. Danciu; L. Baia; *J. Mater. Chem. A*, **2017**, *5*, 2132–2142.
13. S.M. Hosseini; E. Jashni; M. Habibi; M. Nemati; B. Van der Bruggen; *J. Memb. Sci.*, **2017**, *541*, 641–652.
14. N. Ahmad; A. Kausar; B. Muhammad; *J. Plast. Film Sheeting*, **2016**, *32*, 419–448.
15. C. Nicolăescu; L. Olar; R. Stefan; M. Todica; C.V. Pop; *Stud. Univ. Babeş-Bolyai Chem.*, **2018**, *63*, 63–70.
16. Y. Feng; C. He; Y. Wen; Y. Ye; X. Zhou; X. Xie; Y.W. Mai; *Compos. Part A Appl. Sci. Manuf.*, **2017**, *103*, 74–83.
17. K.A. Prokhorov; D.A. Aleksandrova; E.A. Sagitova; G.Y. Nikolaeva; T.V. Vlasova; P.P. Pashinin; C.A. Jones; S.J. Shilton; In *Journal of Physics: Conference Series*; 2016; p 012001.
18. F. Qiu; G. He; M. Hao; G. Zhang; *Materials (Basel)*, **2018**, *11*, 2139, pp. 1-15.
19. J.M. Hankett; C. Zhang; Z. Chen; *Langmuir*, **2012**, *28*, 4654–4662.
20. K. Artyushkova; J.E. Fulghum; *Surf. Interface Anal.*, **2001**, *31*, 352–361.
21. A. Pérez Del Pino; E. György; C. Cotet; L. Baia; C. Logofatu; *RSC Adv.*, **2016**, *6*, 50034–50042.